Western University
Scholarship@Western

Digitized Theses | Digitized Special Collections

1994

Early Proterozoic Birimian Gold Mineralization Of The Bogosu And Prestea Districts Of The Ashanti Gold Belt, Ghana, West Africa

A Hamid Mumin

Follow this and additional works at: https://ir.lib.uwo.ca/digitizedtheses

Recommended Citation
Mumin, A Hamid, "Early Proterozoic Birimian Gold Mineralization Of The Bogosu And Prestea Districts Of The Ashanti Gold Belt, Ghana, West Africa" (1994). *Digitized Theses*. 2374.
https://ir.lib.uwo.ca/digitizedtheses/2374

This Dissertation is brought to you for free and open access by the Digitized Special Collections at Scholarship@Western. It has been accepted for inclusion in Digitized Theses by an authorized administrator of Scholarship@Western. For more information, please contact tadam@uwo.ca, wlswadmin@uwo.ca.

EARLY PROTEROZOIC BIRIMIAN GOLD MINERALIZATION OF THE BOGOSU AND PRESTEA DISTRICTS OF THE ASHANTI GOLD BELT, GHANA, WEST AFRICA

by

A. Hamid Mumin

Department of Earth Sciences

Submitted in partial fulfillment
of the requirement for the degree of
Doctor of Philosophy

Faculty of Graduate Studies
The University of Western Ontario
London, Ontario
September 1993

© A. Hamid Mumin 1994

Acknowledgements

The writer extends his sincere appreciation and gratitude to all the individuals and organizations that contributed in many ways to the completion of this project. Foremost, credit goes to Dr. M. E. Fleet for thoughtfully and efficiently guiding this study to a successful conclusion, and for his support and help throughout the research.

Dr. F. J. Longstaffe made a major contribution through his encouragement and funding of the stable isotope studies. The author is grateful to Dr. S. Chryssoulis and C. Weisener of Surface Science Western for providing the SIMS analyses, and for their valuable review and comments on the results. R. Barnett and D. Kingston provided all the help and assistance required to complete the EMP analyses, P. Middlestead was invaluable for his help with the stable isotope analyses, J. Forth and G. Wood prepared the sections, and C. Wu performed the whole-rock geochemical analyses. The writer is grateful for the valuable discussions and assistance received from many other faculty, staff and students in the Department of Geology. Thanks are also given to Dr. E. T. C. Spooner, who helped in many ways to initiate this project.

The assistance given to the writer during his stay in Ghana by many personnel from Sikaman Gold Resources Limited, Billiton International Metals BV, Billiton Bogosu Gold (formerly CBR), Prestea Goldfields Limited and Ashanti Goldfields Corporation is gratefully acknowledged.

Funding and support for this research was provided by the operating and research grants of Dr. M. E. Fleet, Dr. F. J. Longstaffe and Dr. S. Chryssoulis,

Abstract

Mesothermal gold ores of the Bogosu and Prestea concessions of southwestern Ghana are hosted by Birimian (2.1 Ga) carbonaceous sedimentary rocks. Gold mineralization is post-peak metamorphism, and occurs within dilatant zones of the Ashanti Structural Belt. Host sedimentary and mafic lithologies have been altered to an assemblage containing abundant ankerite, siderite and sericite.

Deeper portions of the gold system are exposed on the Prestea concession, and higher-level ores at Bogosu. Crack-seal quartz veins and carbonaceous shear-zones are the common ore types in the brittle-ductile rocks at Prestea. Tectonically-disrupted sediments with smaller zones of carbonate-altered mafic dikes are the common ore types at Bogosu.

Pyrrhotite was the first sulphide to precipitate; however, increase in pH and fO_2 resulted in its alteration to marcasite and pyrite. This was followed by precipitation of arsenian pyrite and arsenopyrite. In-situ analysis and ion mapping by SIMS suggest that most of the gold may have precipitated in solid-solution with the arsenian pyrite and arsenopyrite. However, gold was subsequently redistributed, concentrated and crystallized as colloidal and microscopic particles within voids, microfractures and at grain boundaries of the arsenian pyrite, arsenopyrite and trace amounts of other sulphides.

Ankerite-siderite and arsenopyrite geothermometers indicate that mineral deposition occurred from about 400 to 145°C. The lower limit of carbonate formation temperatures suggest that the ambient country-rock temperatures at the time of mineralization were about 145 and 215°C for Bogosu and Prestea

ores, respectively. Peak metamorphic temperatures are estimated at ≈ 375°C.

Calculated oxygen and carbon-isotope values for the hydrothermal fluid ($\delta^{18}O \approx 11.8 \pm 1.5‰$, $\delta^{13}C \approx -12.7 \pm 2.2‰$) are consistent with the generation of a metamorphic ore fluid in equilibrium with the Birimian sedimentary rocks. However, lower calculated fluid $\delta^{18}O$ and $\delta^{13}C$ values of $8.1 \pm 2.0‰$ and $-13.8 \pm 3.3‰$, respectively, for quartz and carbonates in mineralized samples suggest that phase separation of the ore fluid to a CO_2-rich gas phase and a residual ore fluid occurred prior to mineralization.

Geological and geochemical evidence suggest that the Ashanti Gold Belt formed in a sediment-dominated accretionary prism similar to the southern coast of Alaska.

Acknowledgements

The writer extends his sincere appreciation and gratitude to all the individuals and organizations that contributed in many ways to the completion of this project. Foremost, credit goes to Dr. M. E. Fleet for thoughtfully and efficiently guiding this study to a successful conclusion, and for his support and help throughout the research.

Dr. F. J. Longstaffe made a major contribution through his encouragement and funding of the stable isotope studies. The author is grateful to Dr. S. Chryssoulis and C. Weisener of Surface Science Western for providing the SIMS analyses, and for their valuable review and comments on the results. R. Barnett and D. Kingston provided all the help and assistance required to complete the EMP analyses, P. Middlestead was invaluable for his help with the stable isotope analyses, J. Forth and G. Wood prepared the sections, and C. Wu performed the whole-rock geochemical analyses. The writer is grateful for the valuable discussions and assistance received from many other faculty, staff and students in the Department of Geology. Thanks are also given to Dr. E. T. C. Spooner, who helped in many ways to initiate this project.

The assistance given to the writer during his stay in Ghana by many personnel from Sikaman Gold Resources Limited, Billiton International Metals BV, Billiton Bogosu Gold (formerly CBR), Prestea Goldfields Limited and Ashanti Goldfields Corporation is gratefully acknowledged.

Funding and support for this research was provided by the operating and research grants of Dr. M. E. Fleet, Dr. F. J. Longstaffe and Dr. S. Chryssoulis,

and from Sikaman Gold Resources Limited, Billiton International Metals BV, University of Western Ontario entrance scholarships, an Ontario Graduate Research Scholarship, a University of Western Ontario Graduate Research Fellowship, several teaching assistantships, a research assistantship and the Laboratory for Stable Isotope Studies in Resource Geology and Environmental Geochemistry.

TABLE OF CONTENTS

LIST OF TABLES

LIST OF FIGURES

LIST OF PHOTOGRAPHIC PLATES

LIST OF APPENDICES

The author of this thesis has granted The University of Western Ontario a non-exclusive license to reproduce and distribute copies of this thesis to users of Western Libraries. Copyright remains with the author.

Electronic theses and dissertations available in The University of Western Ontario's institutional repository (Scholarship@Western) are solely for the purpose of private study and research. They may not be copied or reproduced, except as permitted by copyright laws, without written authority of the copyright owner. Any commercial use or publication is strictly prohibited.

The original copyright license attesting to these terms and signed by the author of this thesis may be found in the original print version of the thesis, held by Western Libraries.

The thesis approval page signed by the examining committee may also be found in the original print version of the thesis held in Western Libraries.

Please contact Western Libraries for further information:
E-mail: libadmin@uwo.ca
Telephone: (519) 661-2111 Ext. 84796
Web site: http://www.lib.uwo.ca/

Chapter 1: Introduction

Gold has been recovered from the Early Proterozoic Birimian rocks (2.3 to 1.9 Ga) of West Africa for the last one thousand years, and production dominated the world gold supply from the 14th to the 18th centuries. The geology of this major auriferous province remains little known in the western world, largely due to difficulties in accessing both the tropical areas of the south and the arid regions to the north. The Birimian is approximately the size of Ontario, and includes parts of Guinea, Liberia, Cote d'Ivoire, Ghana, Burkina Faso and Mali, with small outliers in Mali, Senegal and Guinea (Figure 1.1). In spite of minimal exploration and development, several world-class ore deposits are known in the Birimian, and there is potential for many other significant discoveries.

The Ashanti Gold Belt of southwestern Ghana is by far the most important gold-bearing structure of the Birimian. This thesis investigates a 33 km segment of the Ashanti Gold Belt known as the Bogosu and Prestea mining concessions (Figure 2.2), located in the Western Region of southern Ghana.

The Bogosu concession was awarded to Denison Mines Ltd. of Toronto in 1985 by the Government of Ghana. In 1986, Denison entered into a Joint Venture agreement with Sikaman Gold Resources Ltd. (40.5%), Denison Mines Ltd. (40.5%), the Government of Ghana (10%), and the International Monetary Fund (9%) for the exploration and possible development of the concession. The author joined the project in February of 1988, as Chief Geologist and subsequently Site Manager, and worked on site in Ghana through the exploration, feasibility and pre-development phases of the project. By mid 1988, Billiton International Metals BV joined the project, eventually acquired

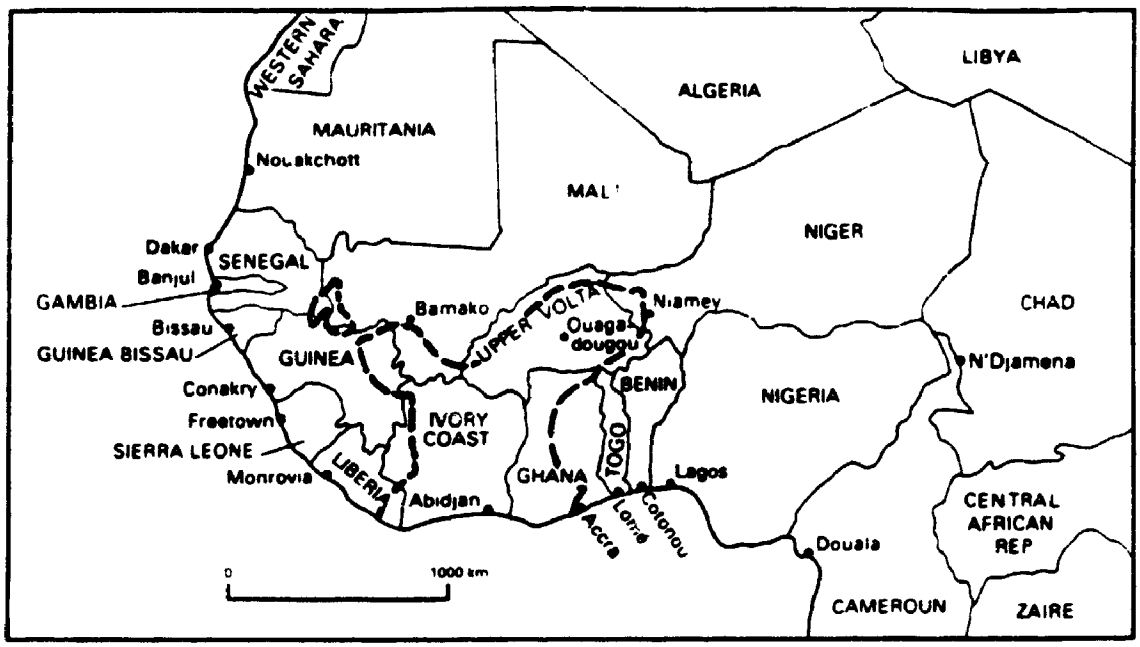

Figure 1.1: Political map of West Africa showing the outline (dashed) of Early Proterozoic (≈ 2.1 Ga) Birimian rocks.

the controlling interest and developed the concession as the most important new gold mine in West Africa. First gold at the new mine was produced in late 1990.

Prior to this thesis, no geological investigations had been conducted on the Bogosu concession, other than reconnaissance surveys and those directly related to mining. Only one petrological thesis (Adjimah, 1988) has been written on the geology at Prestea.

This thesis reviews the literature on West African geology as it relates to the Birimian, reports on the geology, structure and mineralogy of the Bogosu and Prestea concessions, and comments on the whole-rock geochemistry of important lithologies, ore mineralogy, chemistry of hydrothermal minerals, distribution of gold, and ^{13}C and ^{18}O isotope systematics. These observations permit a reconstruction of the physico-chemical evolution of this major gold system within the proposed regional tectonic setting of a sediment-dominated accretionary prism. Gold mineralization post-dated the early stages of deformation of the Ashanti Structural Belt and the peak metamorphism. However, the gold-bearing hydrothemal fluids that were focussed along dilatant structures appear to have been derived from subsequent metamorphism of Birimian lithologies below the zone of mineralization. The new information presented here is used to model the Birimian tectonics of southwestern Ghana, and hints at new insights into mechanisms of gold deposition and evolution in mesothermal gold deposits. Based on samples and analyses from other mining areas, the implications of this research are believed to extend beyond the Bogosu and Prestea regions, to the Ashanti Belt as a whole.

Chapter 2: The Early Proterozoic Birimian of West Africa

Introduction to the Birimian

The African continent is the second largest land mass of Earth and is also the most tectonically stable. Phanerozoic mobile belts are restricted to the extreme north-west (Atlas mountains) and to the southern tip of South Africa. The continent contains small Archean nuclei centered near: 1) Liberia and Mauritania in the west, 2) Congo, Angola and Tanzania in the central regions, and 3) Zimbabwe and the Transvaal in the south. These nuclei are surrounded or bordered by larger, Early Proterozoic volcano-sedimentary-plutonic terrains, which in turn were followed by several tectono-orogenic events of lesser significance. Finally, stabilization of the continent as we now know it concluded with the major Pan-African event at ≈550 Ma. Very little tectonic activity has occurred since that time.

The southern portion of the Precambrian West African craton encompasses a broad section of geological time, from the Archean Liberian platform in the west (≈3200 Ma), to the Pan-African (≈550 Ma) Togo thrust belt in the east. These two terrains are separated by the Early Proterozoic Birimian terrain (≈2100 Ma), which is overlain in its eastern portion by the sedimentary rocks of the Late-Middle Proterozoic (≈1100 Ma) Volta Basin (Figure 2.1).

The Archean Nucleus of the West African Craton

The Archean nucleus covers most of Sierra Leone, southern Guinea, northern Liberia and a portion of north-western Cote d'Ivoire. It has a basement structure of gneiss-migmatite-granulite rocks with strong N-S and

Figure 2.1: Synoptic map of the main geological units of West Africa (Wright et al., 1985). The Ashanti Gold Belt is located in the southeast corner of the Proterozoic terrain, about 200 km west of Accra.

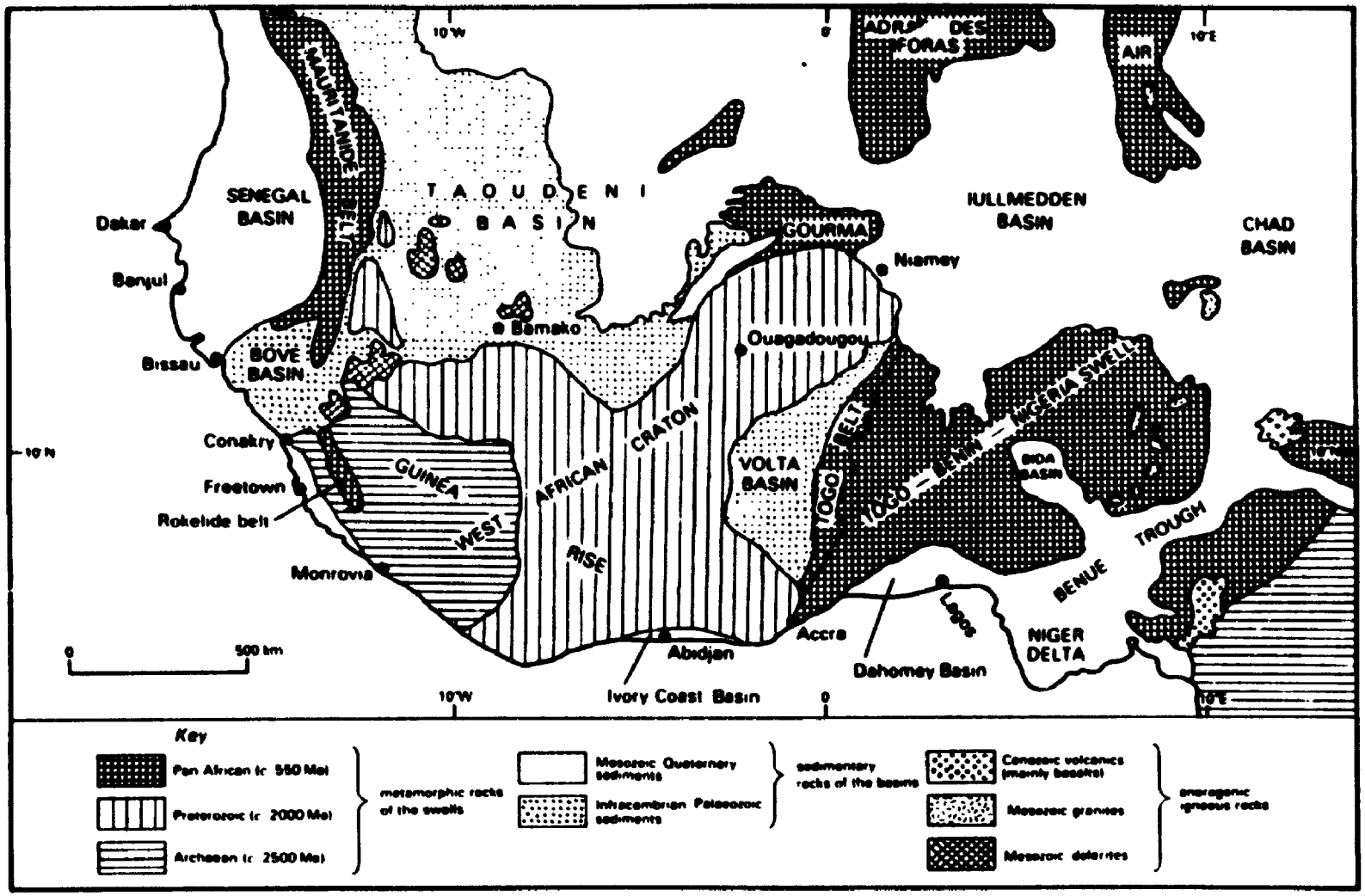
10°W
0
10°E
10°N
SENEGAL BASIN
MAURITANIDE BELT
TAOUDENI BASIN
ADRAR DES FORAS
AIR
IULLMEDDEN BASIN
CHAD BASIN
GOURMA
Niamey
Dakar
Banjul
Bissau
BOVE BASIN
Bamako
Ouagadougou
Conakry
Freetown
Rokelide belt
GUINEA
WEST
AFRICAN
CRATON
RISE
VOLTA BASIN
TOGO BELT
TOGO — BENIN — NIGERIA SWELL
BIDA BASIN
BENUE TROUGH
Monrovia
Lagos
Accra
Abidjan
NIGER DELTA
Dahomey Basin
Ivory Coast Basin
0
500 km
Key
Pan African (c 550 Ma)
Proterozoic (c 2000 Ma)
Archaean (c 2500 Ma)
metamorphic rocks of the swells
Mesozoic Quaternary sediments
Infracambrian Palaeozoic sediments
sedimentary rocks of the basins
Cenozoic volcanics (mainly basaltic)
Mesozoic granites
Mesozoic dolerites
anorganic igneous rocks

NE-SW structural fabrics. The northern and western areas are predominantly N-S trending, while in the south and eastern portions there is a shift in structural fabrics to NE-SW. This N-S, NE-SW fabric is ubiquitous throughout the study area and spans the entire sequence of rocks up to the Pan-African.

Numerous supracrustal belts follow the structural trend. They are in the form of narrow, schistose, linear remnants of greenstones and metasedimentary rocks, ranging from 10 to 130 km in length. Their compositions are similar to greenstone belts elsewhere in the world, with a lower sequence of mafic/ultramafic volcanic and intrusive rocks. These are overlain by tholeiitic amphibolite lavas and sills and minor sedimentary rocks, with an upper sequence of clastic metasedimentary rocks, greywacke, turbidites, iron formation, and a subordinate metavolcanic component with mafic through felsic rocks (Wright et al., 1985; Hawkes, 1972). Liberian age (≈2750 Ma) granites intrude the central basement complex in a northwest trending belt.

Liberian rocks have ages ranging back to about 3200 Ma (Cahen et al., 1984). These dates have been interpreted variously, but it is generally accepted that several orogenic events affected the area, namely: 1) initial formation of Archean crust at 3200 Ma), 2) pre-Leonian at >3100 Ma (Man Charnockite, Mt. Douan formation), 3) Leonian orogeny at ≈2950 Ma (gneiss-migmatite-granulite basement), and 4) Liberian event at ≈2750 Ma with broadly contemporaneous deposition of supracrustal sequences and intrusion of granitoids.

The eastern boundary of Archean rocks is the Sassandra-Mt. Trou fault zone, which marks the beginning of the Proterozoic Birimian terrain of southern West Africa.

The Proterozoic Accretion

The Proterozoic of West Africa is better defined and studied than the neighbouring Archean, but most of this work is of a general nature and conclusions regarding the geological make-up are sometimes based upon preliminary information. This uncertainty reflects the difficulties of working in the region, which include: 1) tropical rain forests along the coast and the remoter Sahel (arid) regions to the north, and 2) episodic, abysmal political and economic situations over long periods of time which tend to destroy any pre-existing technical infrastructure. Consequently, geological interpretations vary and sometimes conform to political and ethnic boundaries.

The Birimian consists of three main units: volcanic greenstone belts, metasedimentary belts, and intrabelt granitoid intrusions. These occur in tectonically controlled belts following the same N-S or NE-SW lineaments as in the Archean rocks. The most dominant feature is the west-dipping marine metasedimentary rocks composed of phyllitic argillites and turbidites, greywackes, slates and schists. The sedimentary rocks are referred to as flysch by French geologists, and the term is generally used within Cote d'Ivoire (Junner, 1946; Cahen et al., 1984; Luebe et al., 1986, 1990). Mafic volcanics overlie the sedimentary package in the east (Ghana) and north (Burkina Faso), while in the west (Cote d'Ivoire) the sedimentary rocks are considered to be erosional products of the same volcanic belts. The boundary between the two interpretations conforms to the political boundary between Cote d'Ivoire and Ghana. This appears to be a French-English controversy.

Major structural lineaments are often exposed near the boundaries of

parallel volcanic belts. This is particularly evident in southwest Ghana (Figure 2.2). The Ashanti thrust belt (1 km wide and 250 km in exposed length) has always been reported to be located along the contact between metasedimentary rocks and metavolcanic rocks. However, current mapping (this project) did not locate any volcanic rocks along the Ashanti structural zone. On the basis of exposures from Prestea in the southwest to Konongo in the northeast, most of the rocks that have been labelled "volcanics" are thought mostly to be tabular intrusions of variable but mainly mafic compostion. They may be dike-like feeders for overlying volcanics that took advantage of crustal weaknesses along the structural belts. In these areas, volcanic rocks immediately overlying the intrusions must have been eroded away, although large areas in flanking zones remain. The Ashanti belt is by far the most studied area of West Africa, and yet, even here the true nature of some of the geology is still under question.

Within and flanking the volcanic belts are later Tarkwaian clastic sedimentary rocks that unconformably overlie older rocks (Figure 2.2). The Tarkwaian is a shallow marine to sub-aerial sequence composed of conglomerates, quartzites, sandstones and phyllites. The main belt of Tarkwaian rocks occurs within the Ashanti volcanic belt; however, Tarkwaian rocks have been documented in association with almost all Birimian greenstones (Luebe et al., 1986, 1990; Wright et al., 1985; Sestini, 1973).

Granitoid intrusions are generally concordant with structural trends and are often foliated. The deposition of these granitoids in linear and quasi-linear belts has been well documented in Cote d'Ivoire by Angoran and Kadio (1983), and in Ghana by Luebe et al., (1986), (Figure 2.2). They occupy large regions between volcano-sedimentary terrains. The intrusions took place during the main Eburnean orogenic episode, when Birimian sedimentary rocks and

Figure 2.2: Modified geology of central and western Ghana (Luebe et al., 1986). (**B** = Bogosu and Prestea districts).

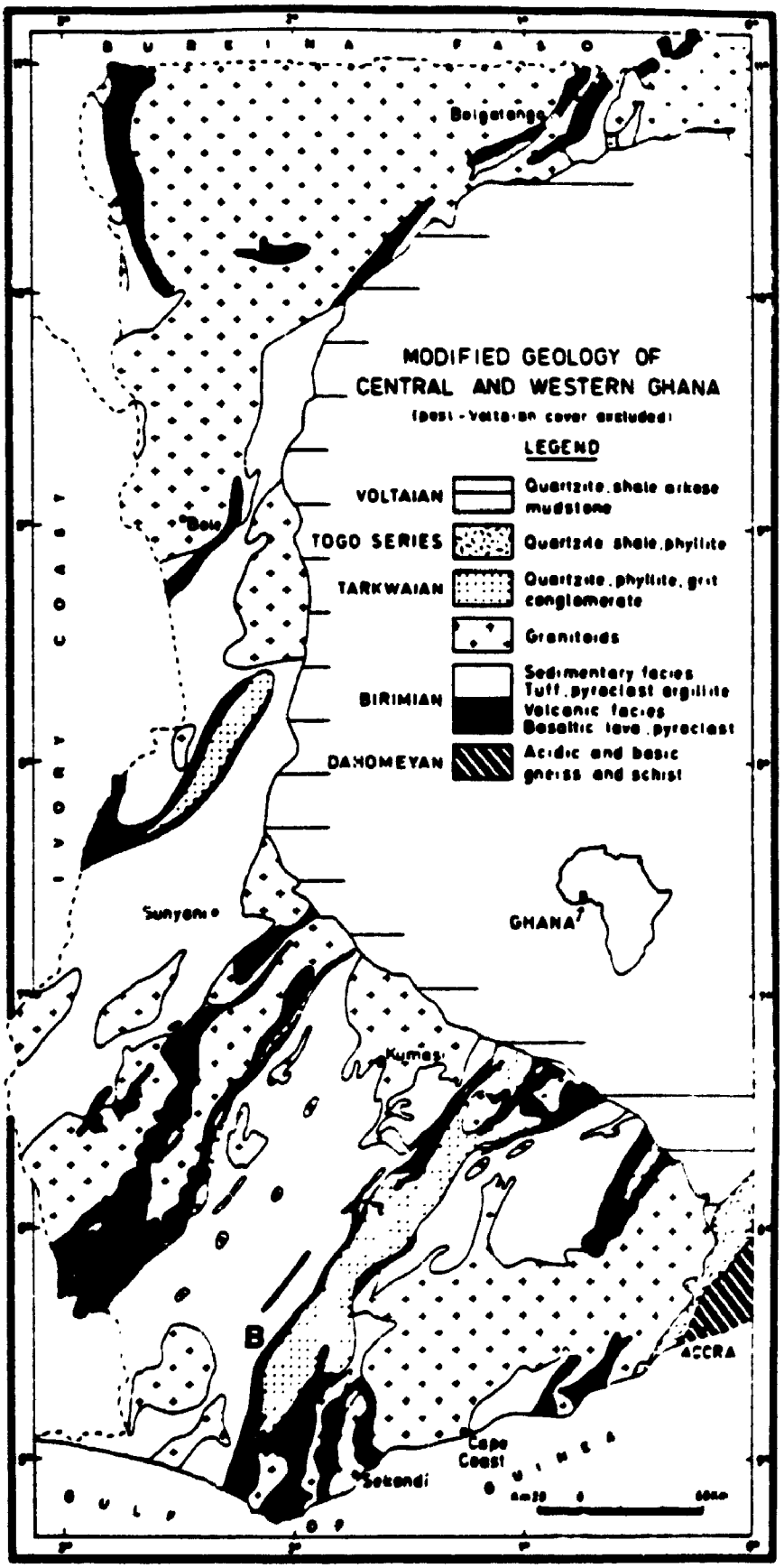
MODIFIED GEOLOGY OF
CENTRAL AND WESTERN GHANA
(post-Voltaian cover excluded)
LEGEND
VOLTAIAN
Quartzite, shale arkose mudstone
TOGO SERIES
Quartzite shale, phyllite
TARKWAIAN
Quartzite, phyllite, grit conglomerate
Granitoids
BIRIMIAN
Sedimentary facies
Tuff, pyroclast argillite
Volcanic facies
Basaltic lava, pyroclast
DAHOMEYAN
Acidic and basic gneiss and schist
GHANA
Bolgatanga
Bole
Sunyani
Kumasi
B
ACCRA
Cape Coast
Sekondi
BURKINA FASO
IVORY COAST
GULF OF GUINEA

volcanics were isoclinally deformed. Granodioritic compositions predominate, but, large syntectonic batholiths are often two-mica granites or biotite-hornblende-bearing varieties. Also, there is a late tectonic to post-tectonic suite of granitoid intrusions that are much smaller, typically unfoliated and sub-rounded in outcrop. These latter intrusions have a wider range of composition, from hornblende and biotite-bearing granites to diorites, monzonites and syenites (Wright et al., 1985; Angoran and Kadio, 1983; Luebe et al., 1986, 1990).

A general time correlation for Early Proterozoic stratigraphy and Eburnean orogenic events in the Birimian has been prepared by Cahen et al. (1984). Three major orogenic episodes correlate with the formation of the lower Birimian (2270 Ma), upper Birimian (2130 Ma) and Tarkwaian (2030 Ma). However, it should be noted that there is a wide variety of ages preserved within both the Archean and Proterozoic terrains of West Africa, and considerable controversy exists with respect to the timing of orogenic events.

Origin of the West African Craton

The important features to be considered before discussion of models for the origin of the West African Craton are: 1) progressive eastward younging of the rocks from 3200 Ma (oldest Archean) to 550 Ma (Pan African), with a wide range of ages preserved from ≈3200 Ma to ≈1600 Ma (Cahen et al., 1984; Caen-Vachete, 1988; Caen-Vachete et al., 1984; Clauer et al., 1982; Onstott and Dorbor, 1987; Kone et al., 1988; Toure et al., 1987; Abouchami et al., 1990; Hirdes et al., 1992; Taylor et al., 1992), 2) sub-parallel tectonic structures controlling the distribution of supracrustals, granitoids and sedimentary rock sequences with a crude regularity to their spacing, 3) deformation to a steep

isoclinal sequence that generally dips to the west, and 4) planar parallelism between volcanic rocks, intrusions, metasedimentary rocks and major structural breaks. These are features common to both the Archean and Proterozoic, with the main differences being the small size of preserved supracrustal relics, and a metamorphosed basement complex of unknown origin in the Archean. It should also be noted that the area considered in this study is only part of the craton as it existed in Early Proterozoic times. The full extent covers a larger area to the north as well as a segment of northern South America where good correlations have been made by many investigators (e.g. Caen-Vachette, 1988; Molina, 1988; Bonhomme and Bertrand-Sarfati, 1982).

Models for development of the West African craton include: 1) crustal reactivation with downwarping of pre-existing crust, sediment accumulation in the basins and finally compressional tectonics to fold and deform the intracratonic belts (e.g. Wright et al., 1985), 2) intracratonic rift models where extensional tectonics create rift environments. Volcanic rocks were extruded along the major boundary faults and provided source material for intra-rift sedimentation. Compressional tectonics then deformed and folded the rift belts (e.g. Luebe et al., 1986, 1990; Hastings, 1982), (Figure 2.3), 3) simultaneous development of ensialic and ensimatic basins through plate tectonics and subduction under continental crust with later uplift and erosion (Wright et al., 1985), (Figure 2.4), and 4) more recent suggestions requiring accretion of an allochthonous terrain to the craton (Abouchami et al., 1990; Taylor et al., 1992).

In all models presented there are two major problems: 1) they all require pre-existing continental crust, and 2) with the exception of the Leube et al., (1986) model (Figure 2.3), they all depict the Birimian as anticlinal basins. In

Figure 2.3: Intracratonic rifting model for the evolution of the Birimian (Luebe et al., 1986).

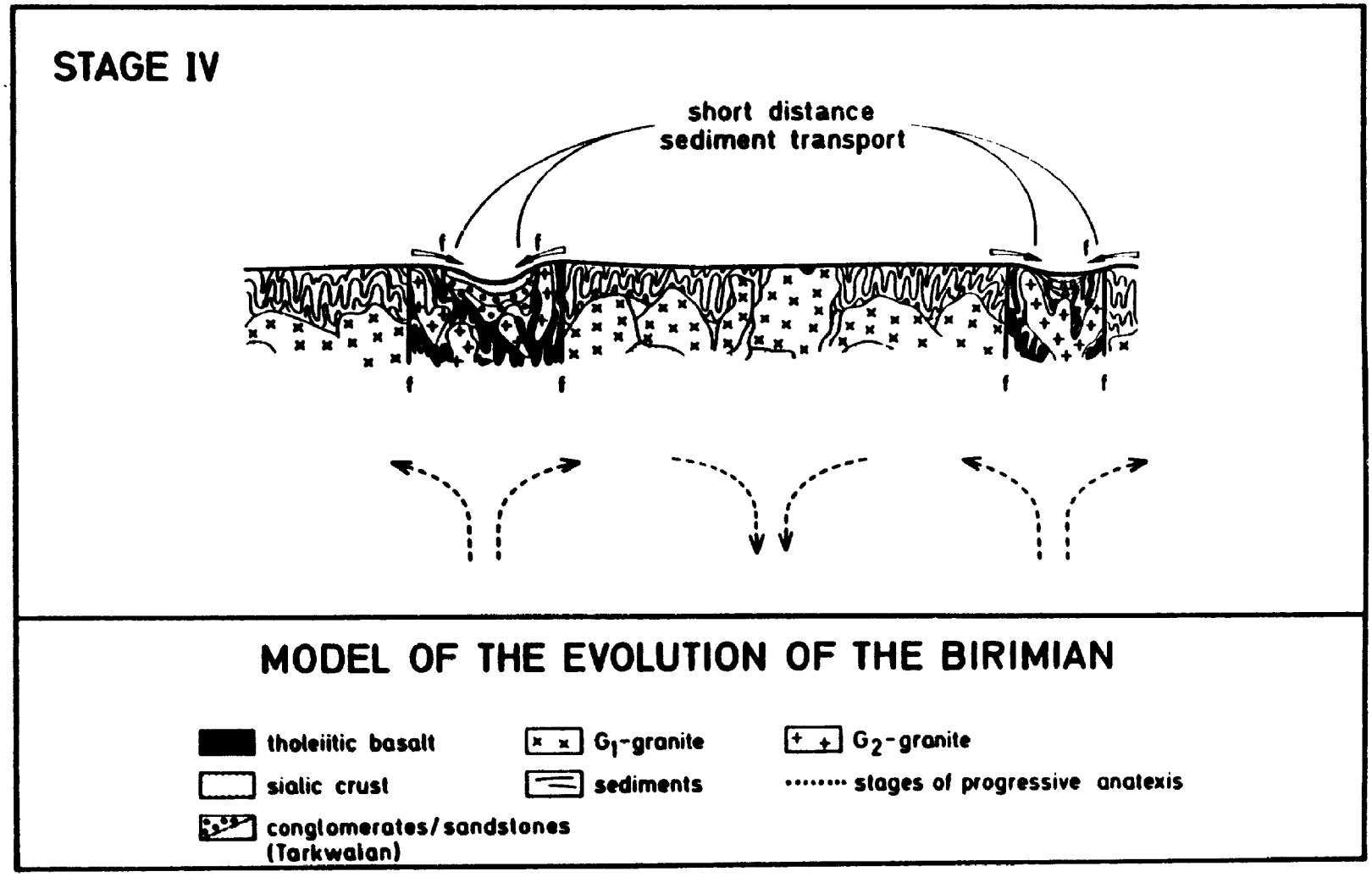
STAGE IV
short distance
sediment transport
f
f
f
f
f
f
MODEL OF THE EVOLUTION OF THE BIRIMIAN
tholeiitic basalt
sialic crust
conglomerates/sandstones
(Tarkwaian)
G1-granite
sediments
G2-granite
stages of progressive anatexis

Figure 2.4: Subduction driven ensialic and ensimatic rift and basin model for the development of the Birimian (Wright et al., 1985).

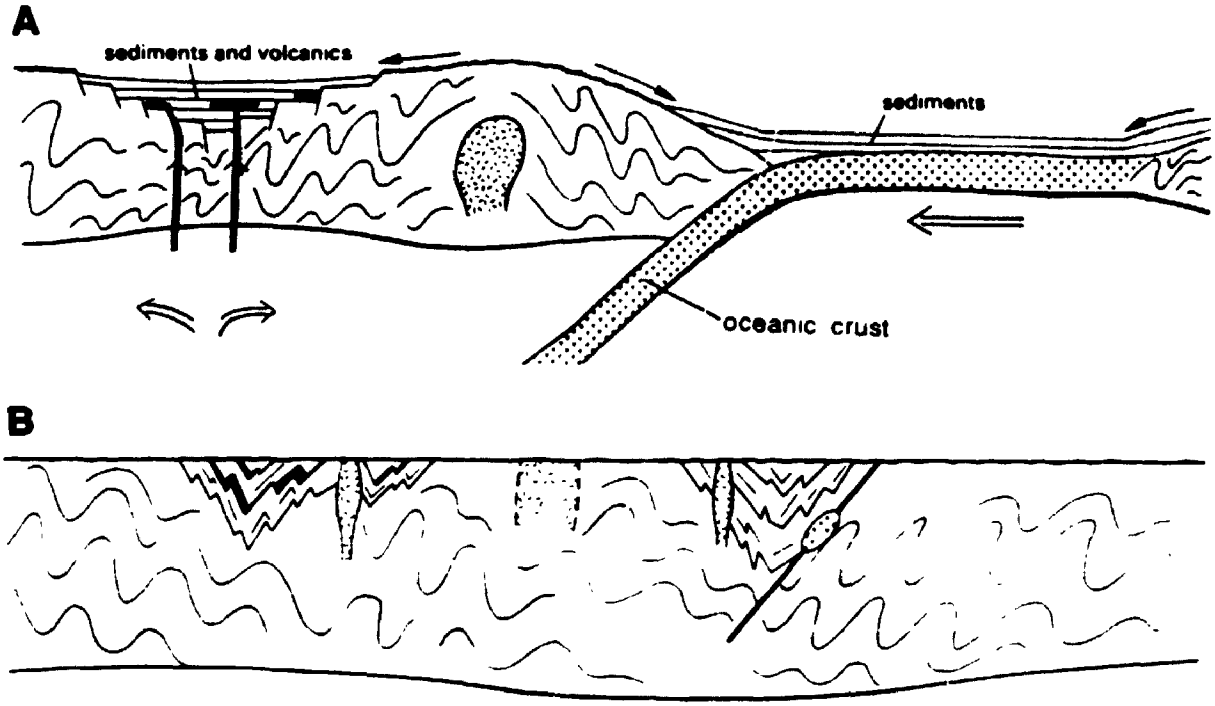
A
sediments and volcanics
sediments
oceanic crust
B

the Birimian today, there is little or no evidence for pre-existing continental crust or for anticlinal basins with the exception of late Tarkwaian-type clastics. Although the Leube et al. (1986) model arrives at a reasonable facsimile of the modern Birimian, simultaneous development of as many rifts and basins within sialic crust as are required to constitute the Birimian (≈ 20) seems unlikely.

The subduction process suggested by Wright et al. (1985) (Figure 2.4a) may be closer to what actually happened; however, their end product (Figure 2.4b) does not resemble the current make-up of the Birimian. One geological model that may be a close analogue for what is observed in southwest Ghana is the accretionary complex developing along the southwest coast of Alaska. There are close correlations between the marine sedimentary rocks, late clastics, volcanic belts, granitoids, structural fabrics and thrust belts. The Birimian and Archean rocks of West Africa have a wide range of ages that are difficult to accommodate within discrete event models. However, through westward subduction under the craton and progressive eastward accretion of the rocks, the entire Proterozoic Birimian (± Archean) may have developed through time by episodic periods of: 1) subduction-driven accretion of sedimentary rocks, and 2) intrusion of granitoids and volcanic belt forming magmas into zones of relaxation from subduction-generated melts. This process could produce the wide range of ages recorded in the rocks, as well as the regional geological patterns depicted in Figures 2.2 and 3.2. A close resemblance to actual geology and structures in the Birimian sedimentary rocks occurs in a cross-section through the geology of the southwest coast of Alaska (Sample and Moore, 1987). This section through part of a sediment-dominated accretionary wedge illustrates repetitive reverse faulting, sedimentary rocks uniformly dipping toward older rocks, steep to gently dipping zones of stratal disruption, volcanic rocks and felsic intrusions. All are standard features of the Birimian of

southwest Ghana.

Gold Mineralization

West Africa was the world's leading supplier of gold from the 14th century to the turn of the 18th century. Virtually all of this gold came from Birimian rocks. Prior to the 16th century the main trade routes were caravans through the Sahara to North Africa, and from there to the rest of the world. With the beginning of the 15th century, the Europeans travelled along the west coast of Africa and gradually displaced the northern trade. Several historical West African empires were based on the wealth, power and prestige of gold (Knopf, 1988), and this symbolism is still woven into the culture of the Ashanti Kingdom of Ghana.

Historical gold production was carried out by thousands of Africans washing gravels from innumerable stream beds throughout the tropical and semi-tropical rain forest regions along the south-west coast, as well as in drier regions of the Sahel to the north. They also worked primary quartz-vein deposits in near surface, saprolitic rocks by carefully chipping away at the higher-grade, free-milling gold. This material would be hand-crushed, sieved, washed in the nearest stream to separate out heavy minerals, amalgamated and finally refined in blacksmith-type hearths. This same practice continues today (often illegally on the doorsteps of modern mines) by uncounted thousands of "Galamsey" workers throughout southern and western Ghana, and in parts of Cote d'Ivoire, Burkina Faso, Mali, Sierra Leone and Liberia.

Primary Lode Deposits

Primary lode gold deposits occur along linear structural belts associated with volcanic/sedimentary interfaces. The type locality where most of the modern gold comes from is the Ashanti Gold Belt, southwestern Ghana (Figure 2.5). This is a major thrust-fault zone within greywackes, turbidites and argillaceous phyllites intruded by many tabular dikes of variable, but mainly mafic composition. Primary gold deposits occur along the length of the belt as: 1) massive, fractured or crack-seal type quartz veins; e.g. Prestea (Figure 4-7), Ashanti and Konongo mines, 2) quartz stockworks in sheared sedimentary rocks and carbonate altered intrusions; e.g. Bogosu (Figures 3-1 and 3-11) and Konongo-Obenemasi mines along the Ashanti belt and Syama in Mali, and 3) "crush zones" which are sheared and fragmented quartz stockworks in carbonaceous sedimentary rocks; e.g. the Bogosu mine and undeveloped deposits at the Prestea concession (Figures 3-1, 3-2 and 3-11).

Free-milling native gold occurs in rich lodes as disseminated flecks and veinlets within the larger quartz vein systems, but rarely in other ore types. The remaining gold occurs as microscopic inclusions and lattice-bound gold in pyrite, arsenopyrite and to a lesser extent in other sulphide minerals. Disseminated sulphides occur in narrow bands and mylonite fissures flanking major quartz veins, and in zones up to 50 meters wide associated with quartz stockworks, altered intrusions and sheared sedimentary rocks. Minor primary lodes that follow the general tectonic fabric are also found in innumerable unrecorded veins, located throughout Birimian sedimentary rocks.

Along the Ashanti belt, economic mineralization can be more or less continuous in en-echelon lenses over great strike lengths (e.g., 30 km at

Figure 2.5: Gold and manganese occurrences in central and western Ghana (Luebe et al., 1986).

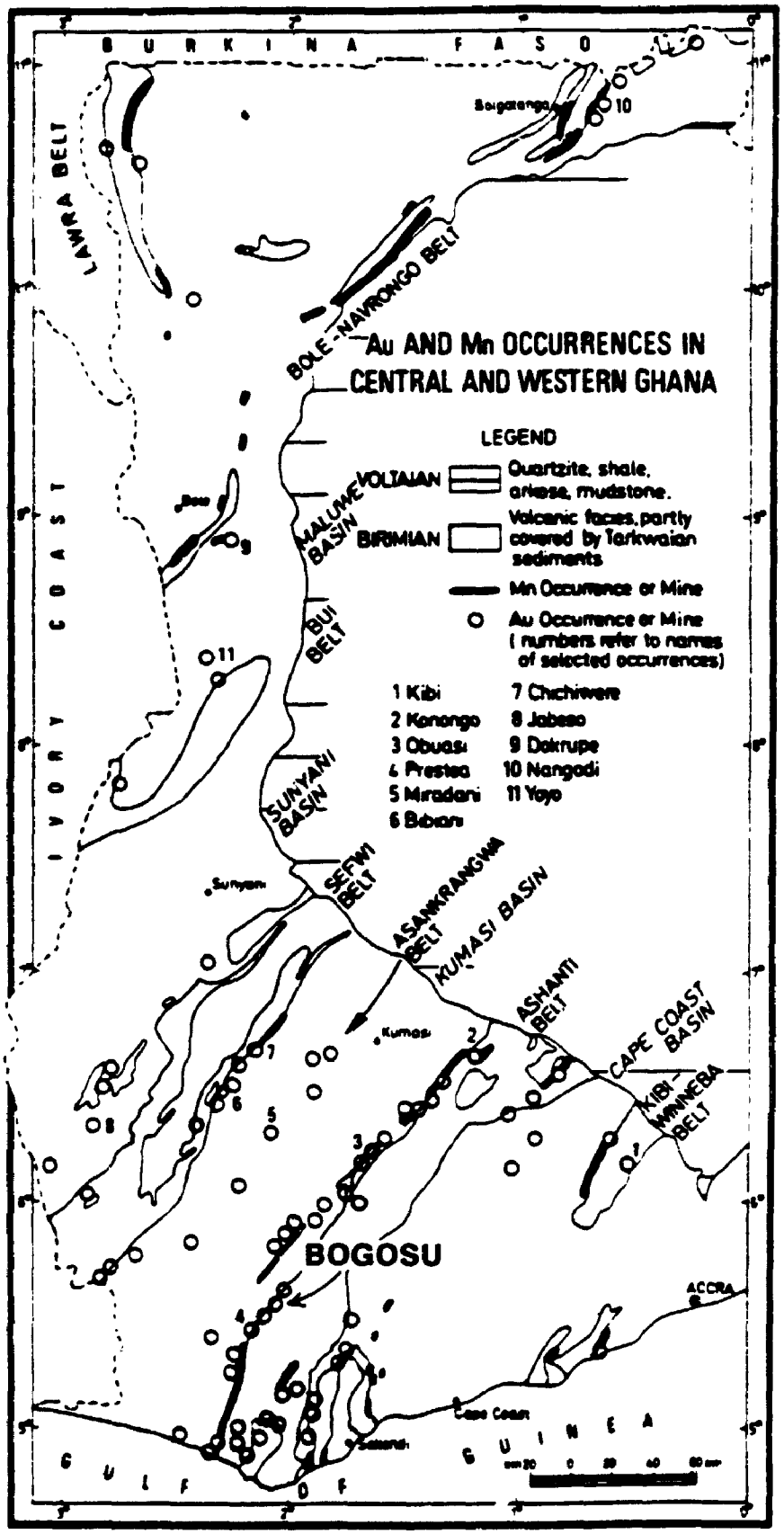
Au AND Mn OCCURRENCES IN
CENTRAL AND WESTERN GHANA
LEGEND
VOLTAIAN
Quartzite, shale, arkose, mudstone.
BIRIMIAN
Volcanic facies, partly covered by Tarkwaian sediments
Mn Occurrence or Mine
Au Occurrence or Mine
(numbers refer to names of selected occurrences)
1 Kibi
2 Konongo
3 Obuasi
4 Prestea
5 Miradani
6 Bibiani
7 Chichiwere
8 Jabesa
9 Dokrupa
10 Nangodi
11 Yoyo
BURKINA FASO
IVORY COAST
LAWRA BELT
BOLE-NAVRONGO BELT
MALUWE BASIN
BUI BELT
SUNYANI BASIN
SEFWI BELT
ASANKRANGWA BELT
KUMASI BASIN
ASHANTI BELT
CAPE COAST BASIN
KIBI-WINNEBA BELT
BOGOSU
ACCRA
GULF OF GUINEA

Bogosu-Prestea). Within individual mines, several of the ore types mentioned above are usually present, with variations laterally, vertically and across strike. Some of these deposits are quite large (see Chapters 3 and 4), and considerable additional potential exists throughout much of West Africa.

Various theories have been used to explain the origin of primary lode deposits along the Ashanti and related belts. Early geologists from the Gold Coast Geological Survey (now Ghana Geological Survey Department) recognized the important structural control over the deposits and speculated on a deep, hydrothermal source for the mineralization (e.g. Junner 1932, 1935). Recently, some investigators have suggested that much of the Ashanti Belt gold mineralization was syn-sedimentary in origin, and was subsequently metamorphically remobilized into major fault zones (e.g., Hirdes and Luebe, 1989; Ntiamoah-Agyakwa, 1979). However, the present thesis presents compelling evidence suggesting these deposits formed through tectonic and metamorphic processes within a sediment-dominated accretionary prism.

Paleoplacer Deposits

The second major gold deposit type of the Birimian is Witwatersrand-type quartz-pebble conglomerate ores of the Tarkwaian clastic sequence. The type deposits for this category occur within the Ashanti belt at Tarkwa, approximately 20 to 30 km east of the Prestea and Bogosu mining districts (Figure 2.5). The clastic sedmentary rocks occupy a linear band 15 to 30 km wide running the length of the Ashanti belt. They are situated in the region between the major structural break hosting the lode gold deposits, and the volcanic sequences of the Ashanti belt (Figure 2.2 and 3.2). The Tarkwaian rocks have a maximum thickness of 2.5 km at Tarkwa (Sestini, 1973).

Conglomerates, quartzites, sandstones and phyllites dominate the sequence. Quartz-pebble conglomerates with associated cross-bedded sandstones carry detrital hematite, pyrite and gold within the banket series conglomerates. The deposits are laterally extensive and display similar features to Witwatersrand quartz-pebble conglomerate deposits (Minter et al., 1986; Pretorius, 1981) with the following notable exceptions documented by Sestini (1973): 1) detrital iron in the Tarkwaian is mostly hematite rather than pyrite. Interestingly, this is consistent with current weathering of primary rocks, which converts sulphides to oxides prior to detrital concentration in the stream gravels, 2) there is no uranium in the Tarkwaian deposits, and 3) the Tarkwaian banket has conglomerate ores ranging from 1 meter to 15 meters in thickness compared to an average 1 meter thickness in the Witwatersrand (e.g. current mining widths at Tarkwa Goldfields Limited are 2 meters to 3 meters on the main reef, with a second hanging wall reef of 4 to 5 meters thickness not yet mined. Ore widths in some prospects of the southern portion of the Tarkwa basin are on the order of 10 to 12 meters, and these are being developed as lower grade, surface oxidized, open pit mines (Greer et al., 1988)).

Smaller amounts of gold have been won from Tarkwaian rocks in other parts of the belt (Kesse, 1985), and Tarkwaian clastic sequences (some with minor gold showings) have been reported associated with all volcanic belts in Ghana (Luebe et al., 1986, 1990; Hirdes and Luebe, 1989), as well as in other parts of West Africa (Wright et al., 1985). However, outside of the immediate Tarkwa area, the rocks remain virtually unexplored. Sestini (1973) adequately documented the paleo-placer origin of these deposits, and several investigators have suggested that the source of the Tarkwaian gold is the nearby primary lode deposits of the Ashanti belt.

Modern Placer Deposits

The third significant gold resource type of West Africa is the modern placer. This type of gold deposit is widely distributed in the numerous stream and river beds of the tropical to subtropical region to the south, as well as in arid regions to the north (Angoran and Kadio, 1983; Ghana Geological Survey, 1969; Kesse, 1985; Olade, 1980; Umeji, 1983). The gold source is primary lodes and paleoplacers, which typically occur along hillsides due to the erosional resistance of quartz and associated intrusions. Rapid tropical weathering of these hills is a very efficient mechanism for releasing gold into the secondary environment. The rock is altered to clays, leaving a surface accumulation of quartz fragments and ironstones composed of quartz, hematite, limonite and goethite lying at the top of a thin laterite unit. This in turn overlies 20 to 100 meters of saprolite. Quartz fragments and ironstones gradually make their way down slope through creep, mass wasting and tropical rain washing to accumulate in the river and stream beds, along with heavy minerals and gold. Here, the material is reworked until relatively pure quartz-pebble and sand deposits form, with gold and other heavy minerals concentrated at the base of mature gravels.

Gold in these placers is recovered with dredges, shovel or dragline and washplant operations, small-scale panning and washing ventures, and by "mining" along the river terraces. This "mining" is accomplished by the local Galamsey who hand-dig a series of close-spaced pits and connect them by tunnels in an approximately 1 meter thick room-and-pillar type operation. The profile through the gravel layers in these river terrace operations is similar to that found in Tarkwaian paleoplacers. Similarities in areal distribution between the Tarkwaian paleo-placers and modern placers have been documented by

Sestini (1973). Loose-packed, matrix-supported, poorly-rounded quartz-pebble layers carry little or no gold, while tightly-packed, mature gravels can be very rich. A number of new placer operations have recently come to production in Ghana and elsewhere in West Africa, and many more are under development (e.g. Kibi belt, Sefwi belt and Ankobra river in Ghana, Figure 2.5; southwest Cote d'Ivoire and northeast Guinea).

One of the more interesting aspects of Ashanti gold belt mineralization is the inter-relationship between the three major gold types. Modern placers can be witnessed in the making, and some of these are demonstrably similar to the 2000 Ma paleoplacers of the Tarkwaian. Furthermore, the total gold content of the Ashanti primary lode gold deposits, when considering all types of gold mineralization (economic to background) is more than sufficient to form paleoplacer deposits of Witwatersrand proportions. For example, considering the entire width of the Ashanti structural belt (±1 km), the Bogosu-Prestea belt averages at least 50 ppb of gold along ≈30 km strike length, with proven vertical depths of at least 5,500 feet at the Prestea mine. The majority of this gold occurs at subeconomic to background levels and is of no economic interest. However, this is equivalent to the release of about 130, 000, 000 ounces of gold for every kilometer depth of erosion, and this gold becomes available for reconcentration as placer deposits. This is believed to be a conservative estimate based on work at the Bogosu concession (> 20,000 meters of surface trench, underground adit and drill core assaying) and visits to the developed and undeveloped resources of the adjacent Prestea concession.

Economic Minerals Associated with Gold

Two main economic minerals are associated with gold in West Africa. Manganese mineralization occurs within sedimentary rocks in linear belts near the interface with volcanic rocks. Regionally, the manganese deposits parallel and sometimes correlate with the gold belts. Some investigators such as Ntiamoah-Agyakwa (1979) have suggested that gold and manganese were deposited syngenetically and simultaneously as chemical sedimentary rocks. He suggests that the gold was later metamorphically remobilized into structural zones. No convincing evidence was found to support this idea. The two elements occur in separate and distinct environments, and only occasionally are there minor examples of gold ore associated with manganese-rich sedimentary rocks (eg., Akanko mine, Ghana, De Kun, 1963). These appear to be cases where manganese-rich sedimentary rocks were later tectonized, thereby allowing introduction of gold from exotic sources.

The second elemental association of economic interest is the occurrence of gold and diamonds together in alluvial gravels (e.g., Birim and Bonsa rivers, Ghana; Aredor mine, Guinea). As with manganese, there is no direct genetic link between the two, rather a more fortuitous one whereby kimberlite pipes and dikes appear to have taken advantage of some of the same crustal breaks that host lode gold in the Birimian. Subsequent erosional processes concentrated the gold and diamonds together in placer deposits. However, regionally, manganese, gold and diamonds may be linked to a common tectonic process as discussed in the concluding chapter of this thesis.

Summary of the Birimian

The Birimian is composed of 4 major units: marine sedimentary rocks, volcanic greenstone belts, granitoid intrusions and later clastic sedimentary rocks. All units are aligned in N-S to NE-SW structural belts. The Birimian of southwestern Ghana is presently thought to have formed by subduction-driven accretion of sedimentary rocks onto the West African craton. Intrusion of granitoids and mafic magmas that formed the volcanic belts occurred in zones of relaxation from melts generated by the subduction process. Primary gold lodes were deposited in major and minor structural lineaments parallel to volcanic belts, while Witwatersrand-type paleoplacers and modern placers were the result of erosion and reconcentration of primary deposits.

Chapter 3: Regional Geology of the Bogosu and Prestea Concessions

The Prestea and Bogosu mining concessions are located in southwestern Ghana approximately 60 to 90 km northeast of the Atlantic coast line at Axim (Figures 2.2 and 2.5). The Ashanti gold belt strikes through the centre of these concessions for 33 km; 15 km in the Prestea property and 18 km in the Bogosu concession immediately to the northeast. This region is the southern-most of three major mining districts along the Ashanti gold belt which includes in addition to the Prestea and Bogosu districts, the Obuasi area in the central portion, which is mined by Ashanti Goldfields Limited and has produced to date over 20 million oz Au, and the Konongo district, about 250 km northeast of the coast near the northeastern-most extremity of the belt (Figure 2.5).

The geology of the Bogosu and Prestea districts is dominated by two major sedimentary rock sequences, an abundance of mafic intrusions and a major crustal lineament hosting the ores. Consequently these features are discussed in further detail in this section.

Tarkwaian Sedimentary rocks

The geology of the Bogosu and Prestea concessions is dominated by two major sedimentary rock sequences striking to the northeast. The eastern portion consists of Tarkwaian clastic sedimentary rocks, while deeper-water Birimian turbidites and greywackes dominate in the west (Figures 2.2, 3.1 and 3.2). The Tarkwaian rocks are comprised of a shallow marine sequence of clastic sedimentary rocks. These rocks vary from course conglomerates to moderately carbonaceous phyllites, as a result of shallow-marine or deeper-water deposition, respectively. Polymictic conglomerates of subrounded

Figure 3.1: Geology of the Bogosu concession. The Ashanti structural zone runs through the length of the concession just west of the Birimian-Tarkwaian boundary. The structural belt hosts numerous gold deposits within both the Bogosu and Pretsea concessions.

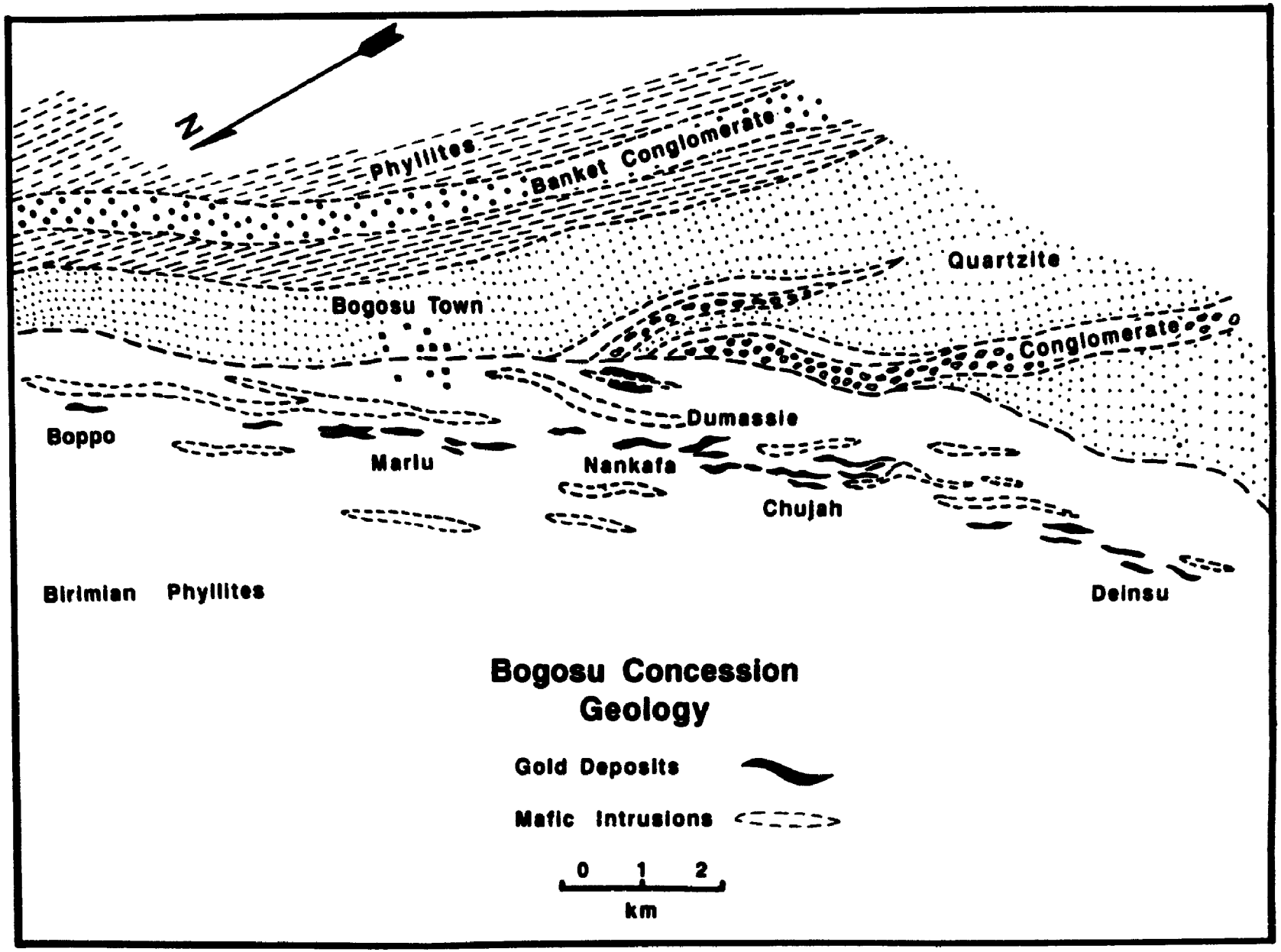
N
Phyllites
Banket Conglomerate
Quartzite
Bogosu Town
Conglomerate
Dumassie
Boppo
Mariu
Nankafa
Chujah
Birimian Phyllites
Deinsu
Bogosu Concession
Geology
Gold Deposits
Mafic Intrusions
0 1 2
km

Figure 3.2: Schematic cross-section through the Bogosu-Prestea district of the Ashanti Gold Belt. This crustal lineament is host to intrusive rocks and gold mineralization. Erosion of the primary gold deposits is believed to be the source of gold for the Tarkwaian paleo-placer deposits, as well as supplying abundant gold for numerous modern placers.

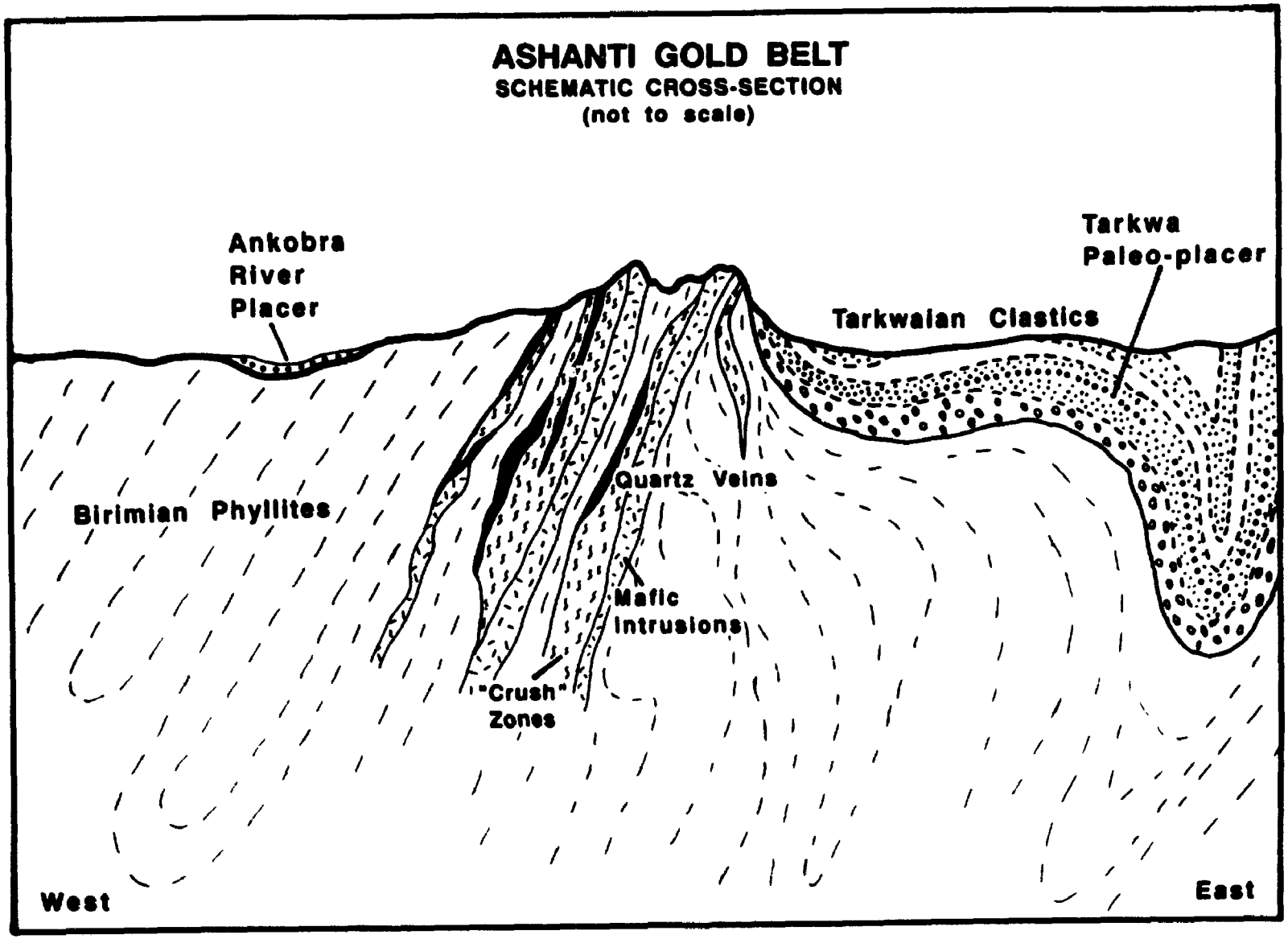
ASHANTI GOLD BELT
SCHEMATIC CROSS-SECTION
(not to scale)
Ankobra
River
Placer
Tarkwa
Paleo-placer
Tarkwaian Clastics
Birimian Phyllites
Quartz Veins
Mafic
Intrusions
"Crush"
Zones
West
East

pebbles and cobbles form the basal Kawere unit. These have been altered by greenschist facies metamorphism and metasomatism. Source materials for the conglomerates were dominantly volcanic rocks from the Ashanti belt and Birimian sedimentary rocks, with a minor granitic component. The upper, and probably faulted contact of the Kawere conglomerate is locally intruded by mafic rocks. These intrusions separate the Kawere group from the overlying Huni quartzite. In the south-central region of the Bogosu concession, the stratigraphy of the basal conglomerate, mafic intrusion and quartzite are repeated due to a southwesterly directed overthrust (Figure 3.1). The Huni quartzite is a thick sandstone unit which in turn is overlain by fine-grained phyllitic sedimentary rocks. This completes an upward-fining transgressive sequence which is then followed by a regression through to shallow-water clastic sedimentary rocks of the Banket series. The Banket is a sequence of quartzites whose most important features are cross-bedded sandstones intercalated with hematite and gold-bearing quartz-pebble conglomerates that are similar to Witwatersrand deposits (Sestini, 1973). The Banket series hosts the significant paleoplacer ores found in the nearby Tarkwa region to the east (Figures 3.1 and 3.2). The sequence again fines to phyllitic sedimentary rocks in the easternmost portion of the Bogosu concession.

Birimian Sedimentary Rocks

West of the Tarkwaian-Birimian contact lies a monotonous sequence of turbidites, greywackes and other carbonaceous sedimentary rocks. In the Bogosu concession they are metamorphosed to low-grade greenschist facies shaly-phyllites. However, in the Prestea concession to the south the rocks are more indurated and often have slaty cleavage. These rocks may best be described as slaty phyllites. The most striking sedimentary rock types at

Bogosu are turbidites that are finely banded on a mm to cm scale (Plate 4.1B). Each individual layer consists of a fine-grained clastic base that grades upwards to an aphanitic and carbonaceous top. The clastic base is dominated by quartz with lesser amounts of siderite, albite, sericite, chlorite, ± ankerite and calcite. The carbonaceous shaly portions are metamorphosed to predominantly sericite with subordinate albite, carbonates, quartz, chlorite and graphite (Table 3.1 and Plate 3.1A). Most sedimentary rocks on the concession are similar to the banded turbidites, except that the scale of individual beds from clastic base to carbonaceous top may vary from below visual resolution to tens of meters in thickness. The thicker beds are noticeably graded, and some have clastic bases composed of detrital grains up to 5 mm in diameter. These units fine upwards and invariably have carbonaceous tops that sometimes are < 1 mm thick, but are always present. The fining direction of Birimian sedimentary rocks on the Bogosu consession consistently indicates that younging of these rocks is towards the west.

Common field names used to describe the rocks result from variations in the turbidites. Thicker beds with coarser clastic material near the base and only minor carbonaceous partings are termed "greywackes". However, when the sedimentary rocks are dominantly fine-grained with only minor carbonaceous material they have been designated as "argillites" by local geologists. Carbonaceous units with little clastic material are widespread. These have shaly textures on the Bogosu concession and are called "graphitic phyllites". Based on observations at Bogosu, it is an interesting feature of this area that all of the rocks seem to be variations of banded turbidites. Differences in grain size, thickness of individual beds and the ratio of clastic component to carbonaceous component dictate the rock classification given to any particular unit.

Table 3.1: Average modal mineralogy of Bogosu and Prestea sedimentary rocks (%).

Mineral	Least Altered	Bogosu Ores	Prestea Ores
Quartz	40	46	28
Chlorite	2.5	2	2.5
Sericite	30	14	11
Calcite	1		
Ankerite	5	17	22
Siderite	14	3	5
Albite	2	10	18
Epidote	tr		tr
Rutile	0.5	0.4	0.8
Ilmenite	tr	tr	
Apatite		tr	
Monazite		tr	
Graphite	2	3	2
Pyrite	1.5	4	7
Arsenopyrite	tr	0.5	3
Pyrrhotite	tr	tr	1
Chalcopyrite	tr	tr	tr
Tetrahedrite	tr	tr	tr
Marcasite	tr		tr
Sphalerite	tr		tr
Gold		1-30 ppm	1-30 ppm
n=	11	7	4

tr = trace

PLATE 3.1

A: Photomicrograph of the carbonaceous, shaly top of a turbidite layer from the Bogosu concession. The sericitic matrix is host to carbonate veining and minor amounts of quartz, albite, chlorite and graphite. The crenulation texture is part of the regional deformation: Ser-sericite; Cb-carbonate; scale bar is 0.2 mm.

B: Photomicrograph of a carbonceous layer from a greywacke-turbidite bed in the Bogosu concession. The sericite-rich and chlorite-rich matrix has bedding-parallel quartz-carbonate veins, crenulation cleavage and tension gashes forming an S_1 fabric, and graphitic micro-shear planes: scale bar is 2 mm.

C: Photomicrograph of a spotted, carbonaceous phyllite from the Prestea mine. Augen porphyroblasts of intergrown ankerite and siderite include graphitic layers from an earlier foliation. The graphitic layers show minor rotational deformation from further shearing: scale bar is 0.5 mm.

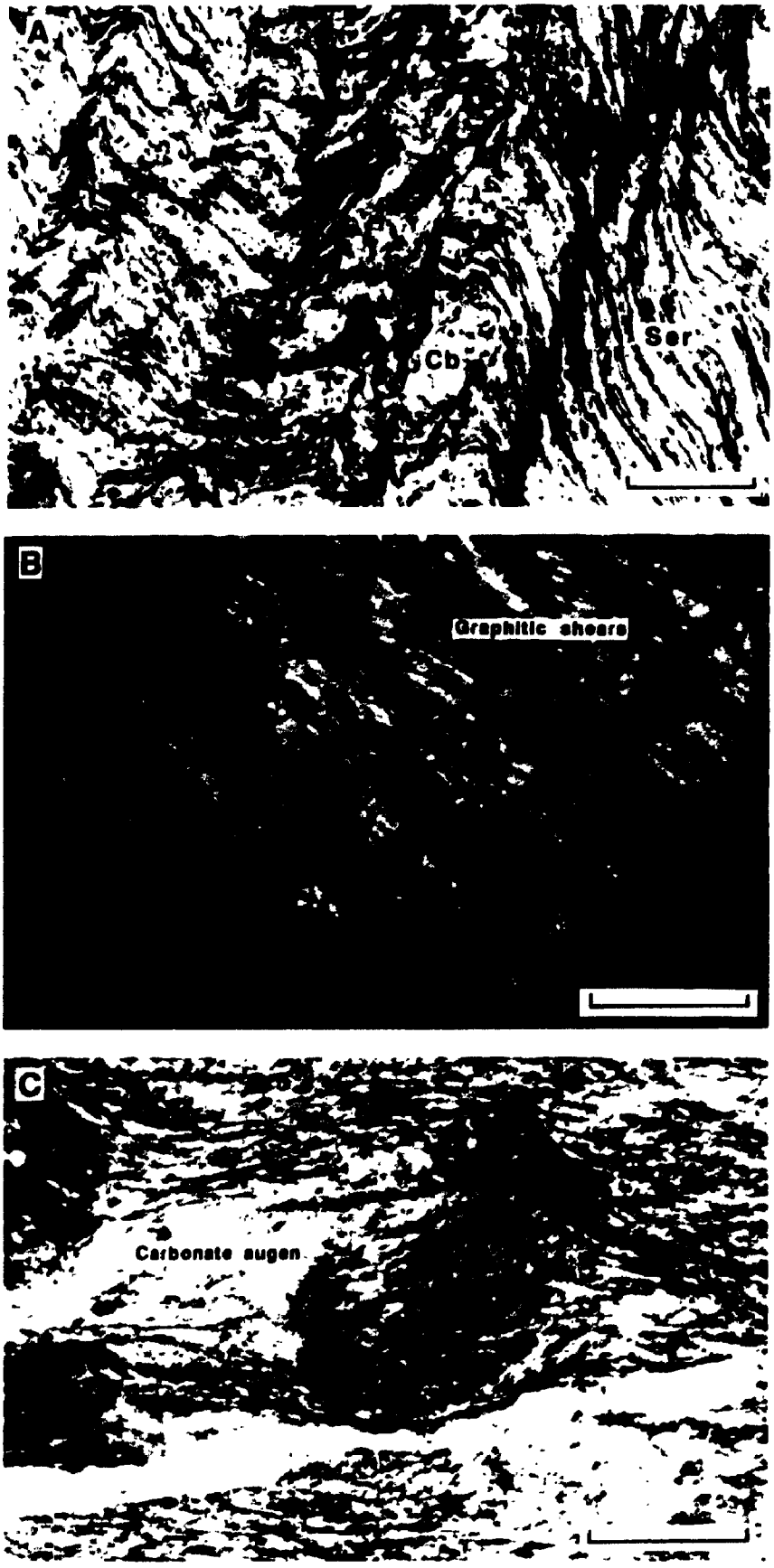
A
Cb
Ser
B
Graphitic shears
C
Carbonate augen

Birimian sedimentary rocks on the Prestea concession have been described by Adjimah (1988) as siliceous, tuffaceous, carbonaceous and spotted phyllites, with intercalated metamorphosed arenites and wackes (Figure 3.3). Current observations suggest that these rocks are lateral facies equivalents of sedimentary rocks occurring on the Bogosu concession, with two main distinctions. Rocks exposed in those underground workings that were available for mapping lack the striking banded turbidite textures which are common on the Bogosu concession. Also as mentioned earlier, Prestea rocks are more indurated indicating a slightly higher grade of greenschist facies metamorphism than at Bogosu.

Spotted phyllites of the Prestea concession are well foliated, carbonaceous rocks that contain augen porphyroblasts of intergrown siderite and ankerite up to 5 mm in diameter (Plate 3.1C). These porphyroblasts are elongated parallel to the foliation, enclose remnants of previously altered and foliated rocks such as veinlets of phyllosilicates and/or quartz-carbonates, and may have been further rotated by shearing (Adjimah 1988). Some large grains enclose smaller porphyroblastic carbonates and others have an outer rim of carbonate that does not preserve the tectonic foliation of the host rocks. Similar carbonate textures have been observed in Bogosu rocks where, however, the porphyroblasts are typically less than 1 mm in diameter. At Bogosu, they are most easily seen in some of the mafic rocks where they give a spotted appearance to an otherwise massive texture. They occur also in Bogosu sedimentary rocks and transgress lithological boundaries. This carbonate porpyroblastic texture is a syn-tectonic feature that is believed to be the result of contact metamorphism ± metasomatism. It occurs predominantly in narrow zones within and adjacent to mafic lithologies, suggesting that the mafic rocks have intruded into the sedimentary rocks, and are a source of localized metamorphism. Further

Figure 3.3: Cross-section through the geology of the Prestea mine (Adjimah 1988). Metavolcanic rocks are currently interpreted to be altered mafic intrusions. Current mining is mainly along the quartz lenses and adjacent graphitic fissures.

A: South wall of the 2400 level - 300 south crosscut (≈ 1 km depth).

B: South wall of the 2500 level - 302 south crosscut (≈ 1 km depth).

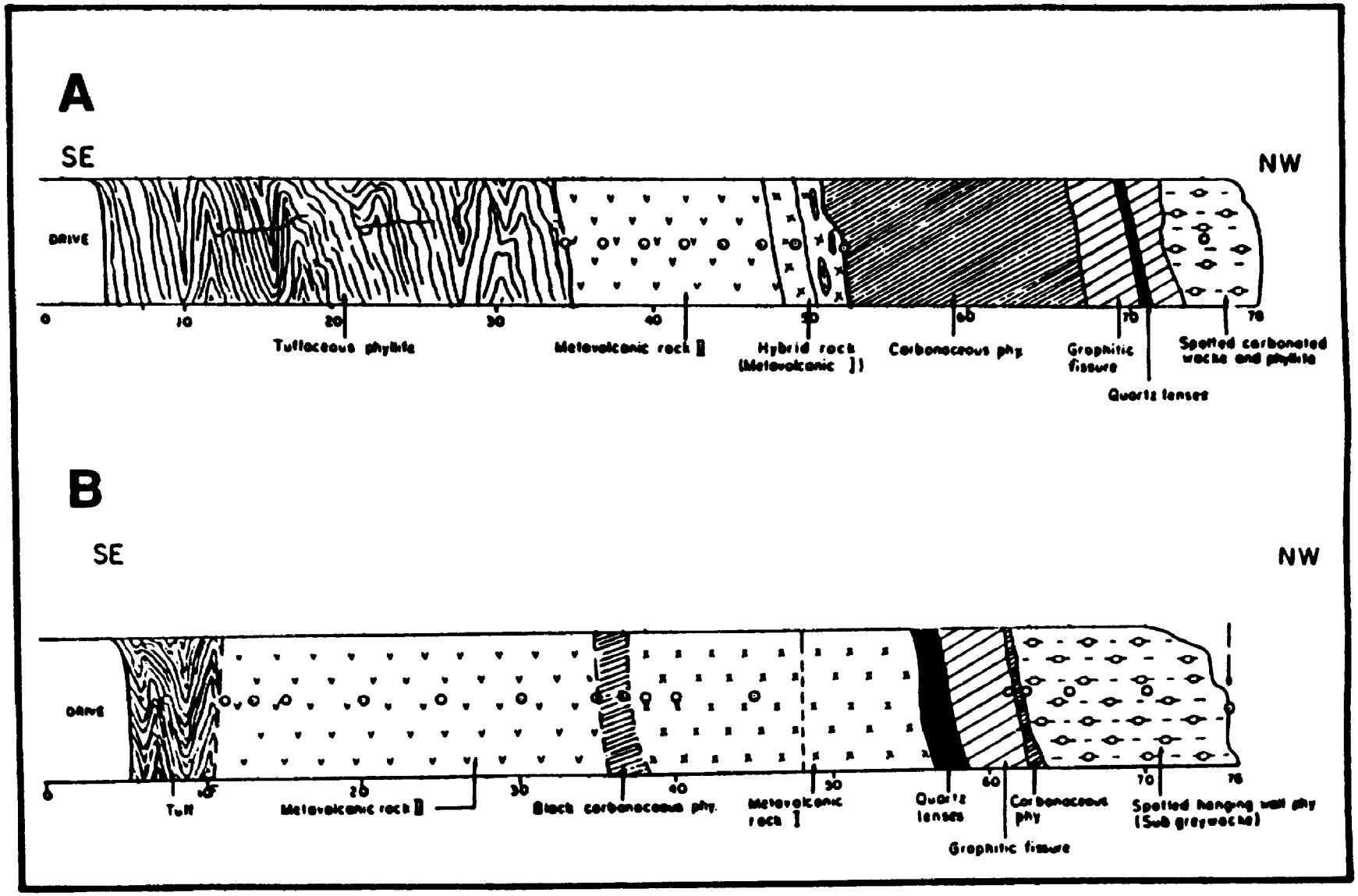
A
SE
NW
DRIVE
0
10
20
30
40
50
60
70
78
Tuffaceous phyllite
Metavolcanic rock II
Hybrid rock (Metavolcanic I)
Carbonaceous phy
Graphitic fissure
Quartz lenses
Spotted carbonated wacke and phyllite
B
SE
NW
DRIVE
0
Tuff
20
Metavolcanic rock II
30
Black carbonaceous phy.
40
Metavolcanic rock I
50
Quartz lenses
60
Carbonaceous phy
Graphitic fissure
70
Spotted hanging wall phy (Sub greywacke)
78

evidence for minor contact metamorphism is provided by the stable isotope patterns documented in Chapter 9.

Mafic Intrusive Rocks

Mafic rocks are found throughout the whole of the Ashanti structural belt. Along with occasional compositional variations ranging from dacitic to ultramafic, they constitute the only significant non-sedimentary rocks in the Bogosu-Prestea region. Current literature groups them as part of the belt volcanics and it is stated that the gold ores occur near the contact of Birimian sedimentary rocks and these volcanic rocks (e.g. Luebe et al., 1990; Hirdes and Luebe, 1989; Kesse, 1985). However, current mapping in the Bogosu-Prestea region clearly demonstrates that these gold-bearing lithologies are isolated within Birimian sedimentary rocks, with known occurrences being restricted to the structural zones (Figures 3.1 and 3.2).

In the study area mafic rocks are fine-grained, massive, tabular units that are from 1 to 100 m thick and up to several km long. They lack any evidence of volcanic textures such as pillows, amygdules or pyroclastic shards, etc. They occur within the same structures that have deformed Birimian sedimentary rocks and host gold. Consequently, they are conformable and sub-conformable to both stratigraphy and the regional structure. At Bogosu and Prestea they are always found in the immediate or very-close hanging wall and/or footwall of the gold lodes (Figures 3.2, 3.3 and 3.4). Sometimes the mafic units occur within the gold lodes, in which case they may be hydrothermally altered and form excellent ores of the disseminated sulphide and quartz stock-work varieties. Often, large tabular lenses of mafic rock host ores at their contact with gold-mineralized sedimentary rocks ("crush zones") and grade

Figure 3.4: Geological cross-section through the Chujah deposit, Bogosu concession, from diamond drilling and surface mapping. The economic mineralization mainly occurs in sheared sedimentary rocks and carbonate-altered dikes. Prior to development, the geological reserve for this deposit was about 4.5 million tonnes grading ≈ 5 g/t Au to an estimated open pit depth of 150 meters.

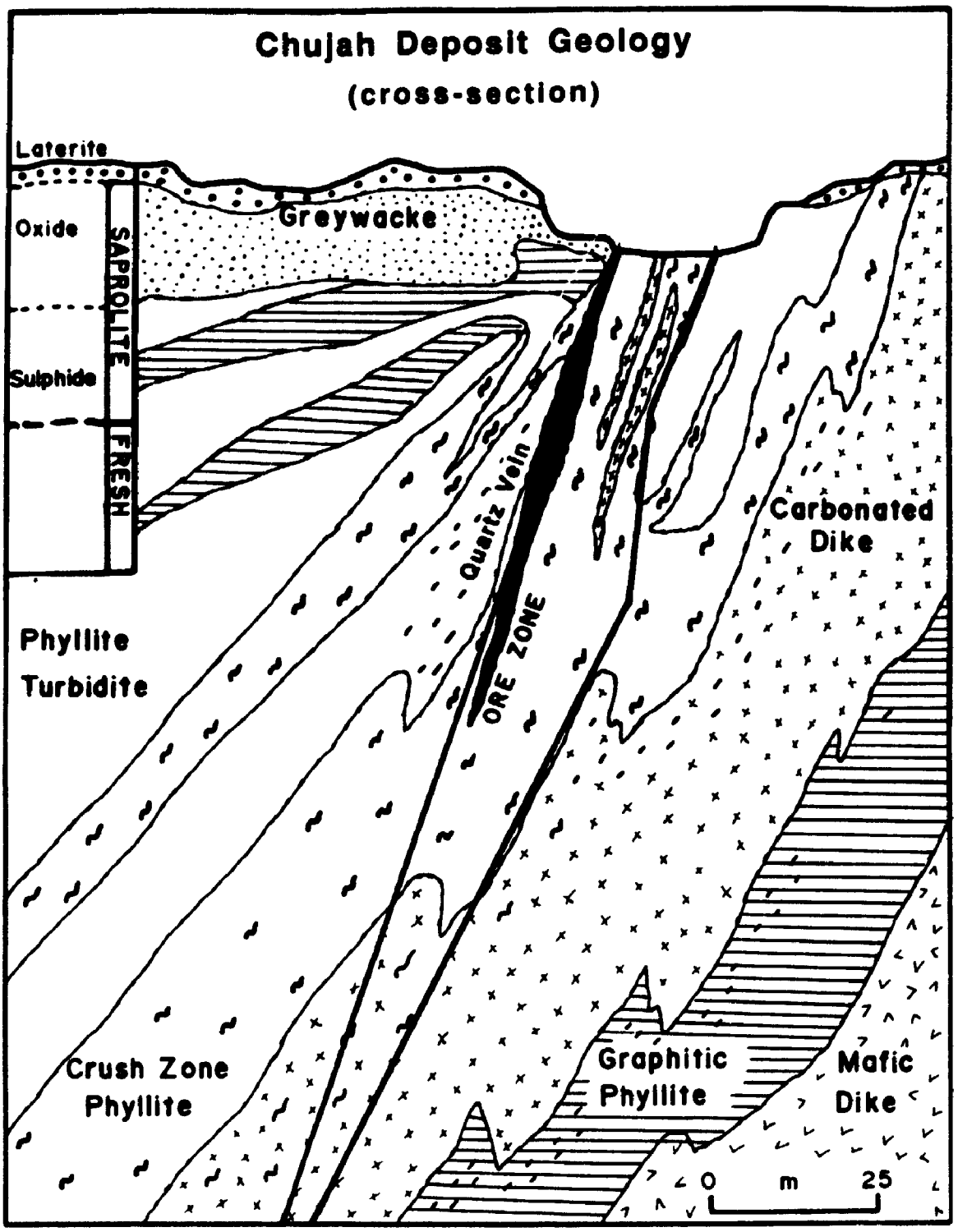
Chujah Deposit Geology
(cross-section)
Laterite
Oxide
SAPROLITE
Sulphide
FRESH
Greywacke
Quartz Vein
ORE ZONE
Carbonated Dike
Phyllite Turbidite
Crush Zone Phyllite
Graphitic Phyllite
Mafic Dike
0 m 25

progressively into less altered rock away from the lithological contact. In some locations (e.g., Chujah 3 deposit) the least-altered mafic rocks unconformably transect the ore zone, while other mafic rocks are variably altered through to high-grade ores.

In some localities such as the Chujah 3 pit, fault contacts with the host sedimentary rocks and other mafic units are clearly visible. Chilled margins and progressive increase in grain size from fine-grained marginal portions to medium-grained cores of mafic units have been observed (e.g., Chujah deposit drill core). These characteristics along with the lack of volcanic features, fine-grained massive texture, restricted occurrence to structural zones and local nonconformable nature are evidence that these rocks are part of a series of dikes intruded along the Ashanti structural belt. Some of the dikes have zones with abundant carbonate porphyroblasts (up to 1 mm in diameter) set in a chloritic matrix. These textures are similar to spotted phyllites at Prestea, and preceed both pervasive carbonation and mineralization of the dikes. The spotted alteration is believed to be caused by minor contact metamorphism from some of the larger intrusions in the Ashanti structural zone. Varying stages of alteration and mineralization within separate intrusive phases sometimes occur in a single ore zone (e.g., Chujah 3). Here, least-altered varieties cut across or intrude conformably other dikes with varying degrees of mineralization, suggesting a syntectonic emplacement of the mafic magmas.

Structural Geology

Two principal structural domains are identifiable along the Ashanti gold belt. Regional low-strain terrains form the country rocks and local high-strain zones contain the gold-bearing lineaments of the Ashanti gold belt, as well as

other belt-marginal gold-bearing structures (e.g. Sefwi belt, Figure 25).

A penetrative SW-NE trending subvertical foliation pervades low-strain rocks of both the Birimian and Tarkwaian sequences (Eisenlohr, 1992). This foliation generally lies subparallel to stratigraphy due to isoclinal folding of Birimian sedimentary rocks during the main deformational events. However, in Bogosu rocks the foliation occasionally varies from parallel to perpendicular to the bedding planes. This is attributed to local variations in the attitude of Birimian sedimentary rocks from sub-horizontal to sub-vertical near the structural zones. The deformation is best studied in aphanatic, carbonaceous sedimentary rocks for which it is most easily observed in thin section. Tension veins lie in the plane of bedding with tension gashes aligned with the S_1 fabric and orthogonal to the veins. Crenulation cleavages that follow the S_1 fabric are visible, and these are displaced moderately by black, carbonaceous shear planes orthogonal to the S_1 fabric (Plates 3.1A and 3.1B). In the vicinity of ore, the dominant foliation is parallel to the main structures, and may be superimposed on earlier deformation fabrics.

The high-strain zones contain the major gold-bearing structures that occur along the margins of the volcanic belts, particularly the northwest margin of the Ashanti belt. On the Bogosu and Prestea concessions turbidite sedimentary rocks and greywackes are host to the structural deformation. The structural zone is up to one kilometer wide, and is located in the middle of the concessions immediately west of the Birimian-Tarkwaian boundary (Figure 3.1). However, within the structure, major shearing is restricted to en-echelon bands ranging from less than a meter to over 100 meters in width. The structures dip steeply to the west from 65° to 80° at Bogosu, and are up to subvertical at Prestea. Consequently, they are generally sub-parallel to the bedding planes of the host-

rocks. Many of the narrow shear zones are located in the southern portion (Prestea), while in the north, wide zones of tectonically disrupted sedimentary rocks (crush zones) are common.

Shearing along the Ashanti gold belt is restricted to Birimian sedimentary rocks and does not appear to affect the Tarkwaian rocks. However, it is not known whether the structural belt continues further eastwards beneath the clastic sedimentary rocks of the Tarkwaian. Confirmation that the Ashanti Belt lineament is a major tectonic feature comes from geophysical mapping. A steep gravity gradient is delineated along the northwest margin of the belt, indicating large amounts of vertical movement (Hastings, 1982).

According to Eisenlohr (1992), the foliaton in the high-strain rocks is accompanied by a southwest-plunging stretching lineation formed by contact with the bedding planes; but in low-strain rocks this lineation is sub-horizontal. However, the extent of his data base is unknown, and at least in the Bogosu-Prestea region, these lineations vary from southwest plunging to northeast plunging. The implication from the latter observation is that deformation associated with high-strain zones was not a single uniform event, but occurred episodically over time with moderate variations in attitude (Figure 3.4). Much of the variation is due also to tectonic disorientation of previously sheared rocks. However, the overall sense of motion is moderately oblique to near-vertical thrusting (Hastings, 1982; Eisenlohr, 1992).

Some of the above mentioned features are well preserved in some deposits, including the Dumassie East deposit which is located near the center of the Bogosu concession. Subhorizontal bedding in this area is repeatedly faulted by regional thrusting related to the Ashanti Gold Belt, and tends to force the

stratigraphy into alignment with the plane of faulting. Frequency and intensity of the deformation increase toward the main zone of structural deformation, culminating in a zone of tectonically disrupted sedimentary rocks. These strongly deformed zones contain quartz veining and sulphide and gold mineralization.

The oblique over-thrust relationship between Birimian and Tarkwaian rocks is supported by, 1) similar penetrative fabrics in both units, 2) a tectonized contact between Tarkwaian and Birimian rocks, 3) repetition of Tarkwaian stratigraphy near the Birimian contact, and 4) overturned bedding (Eisenlohr, 1992). It is interesting to note that on the Bogosu concession Tarkwaian rocks young to the east, while Birimian rocks young to the west. As will be explained later, this should not be confused with overturned bedding. The conclusion of Eisenlohr (1992) that the Birimian is overthrust onto the Tarkwaian may be attributed to the reversal of younging directions; however, almost all previous investigators (e.g., Leube et al., 1990) observe the opposite relationship. Current information from the Bogosu concession is consistent with the earlier investigators, indicating the Tarkwaian overlies the Birimian along a thrust contact.

Even though Tarkwaian sedimentary rocks unconformably overlie Birimian rocks and form a tectonized and overthrust contact, some controversy exists with respect to the depositional timing of these two units. Increasingly precise dating and geological evidence from tectonic and intrusive relationships suggest that the time span between their deposistional events may be geologically negligible (Eisenlohr 1992). Most explanations of Birimian tectonics suggest separate depositional and deformation events for Birimian and Tarkwaian rocks. The first event (Eburnean orogeny) is believed to have deformed

Birimian rocks with the erosional products filling basins and grabens to form the Tarkwaian clastic rocks. A second event of renewed folding and gravity tectonics simultaneously deformed both units (Ledru et al., 1988; Leube et al., 1990). However, more recent structural analysis by Eisenlohr (1992) suggests that the two sequences were simultaneously and progessively deformed in an event accompanied by greenschist facies metamorphism. This latter suggestion is perhaps the most important contribution from Eisenlohr (1992), and is consistent with findings from this study as will be discussed in the final section.

The deformation features described above are the result of northwest-southeast directed compression. Sedimentary strata have been isoclinally folded so that the bedding is normal to the compressional stresses. Further compression intensified deformation such that stress release occurred along belt-marginal lineaments in planes sub-normal to the principal stress. This caused the reverse thrust faulting and/or oblique thrusting in a transpressional environment responsible for the Ashanti structural deformation (Eisenlohr, 1992; Colvine et al., 1988; Simpson, 1986; Sibson, 1977, 1983). The important results are that both stratigraphy and major structural lineaments have been forced into: 1) planar parallelism normal to the principal tectonic stress, and 2) dipping toward older rocks of the craton.

Chapter 4: Geology of Gold Lodes in the Bogosu and Prestea Districts of the Ashanti Gold Belt

The Bogosu and Prestea region is an historical gold producing area with recorded production dating from at least the West African empires of the 11th to 18th centuries. However, the modern era of production commenced near the beginning of the 20th century when European explorers were attracted to indigenous alluvial ventures and surface workings on high-grade quartz veins. This quickly led to development of the Ariston, Bondai, and other gold mines at Prestea which are still in production as Prestea Goldfields Limited. Total recorded production from this mine is well over 6 million oz gold (Hooper, 1989; Kesse, 1985), with large reserves as yet undeveloped.

The modern era of mining on the Bogosu concession began in 1934. Marlu Gold Mining Areas produced gold from higher-grade pockets of oxidized ores scattered along a 14 km segment of the Ashanti Belt. Total production was 934,000 oz of gold from 6,940,000 tonnes at a recovered grade of ≈ 4.5 g/t. During this period, Marlu extracted the near-surface, oxidized portions of the gold lodes. The mine shut down in 1954. Production on the concession was resumed in 1990 by an international consortium led by Billiton International Metals BV. Open pit methods are still being used, but the focus is on larger disseminated sulphide lodes found beneath the near-surface oxidized ores.

Gold mineralization in the Bogosu and Prestea concessions is in semi-continuous enechelon bands for about 30 km of strike length. The gold lodes are defined on the basis of economic grade, which delineates individual ore lenses from the ubiquitously gold-enriched Ashanti Structural Belt. The Ashanti Belt deformation zone is host to several different ore types within the

concessions. The four most important categories are quartz-vein lodes, sedimentary rock hosted ores, mineralized dikes and weathered ores. A description of these ores and variations within them will be presented in this section.

Sedimentary-Rock Hosted Ores

The most important sedimentary-rock hosted ores are known locally by the term "graphitic crush zones" (Plate 4.1C). They occur as shear zones up to 50 m wide throughout the Bogosu concession and in the northern Prestea area. These lodes are characterized by cataclastic deformation of the host sedimentary rocks and contain abundant quartz-albite-ankerite stockwork veins, breccia cementation and tension veins and gashes (Plate 4.3).

Crush zones occur within the major structural lineament and they all have the same general strike of N 40°E and dip of between 65° and 80° to the northwest. The bedding planes of the majority of the host sedimentary rocks strike also at N 40° E and have steep northwest dips bringing the majority of sedimentary rocks into subparallel alignment with the tectonic and structural fabrics of the ores. Due to local variations in the attitude of bedding planes as well as tectonic disorientation of the host rocks, shearing also has occurred at high angles to the stratigraphic layering. This has resulted in distinct brecciation and cross-cutting vein relationships.

However, shearing is more often sub-parallel to bedding planes such that movement has occurred as slippage along phyllosilicate-rich bands. Primary bedding-textures are well preserved in some of these rocks even though they may be abundantly mineralized, sheared and altered. In rocks with bedding-

PLATE 4.1

A: Photograph of the contact between a weathered, moderately graphitic turbidite-greywacke (saprolite) and the overlying laterite. Up to three meters of mottled, red-brown and buff coloured laterite cover the mineralized rocks of the Bogosu and Prestea concessions.

B: Photograph of a typical weathered turbidite (saprolite) exposed in a road cut through the Bogosu concession.

C: Photograph of a weathered graphitic crush zone (saprolite) exposed near an adit entrance southwest of the Chujah area.

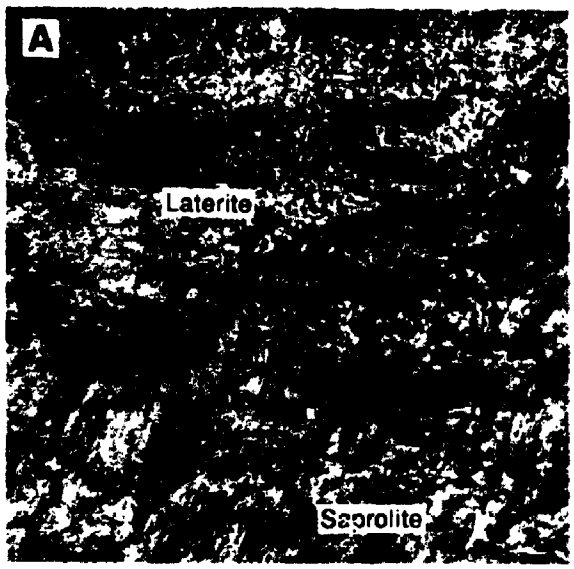
A
Laterite
Saprolite

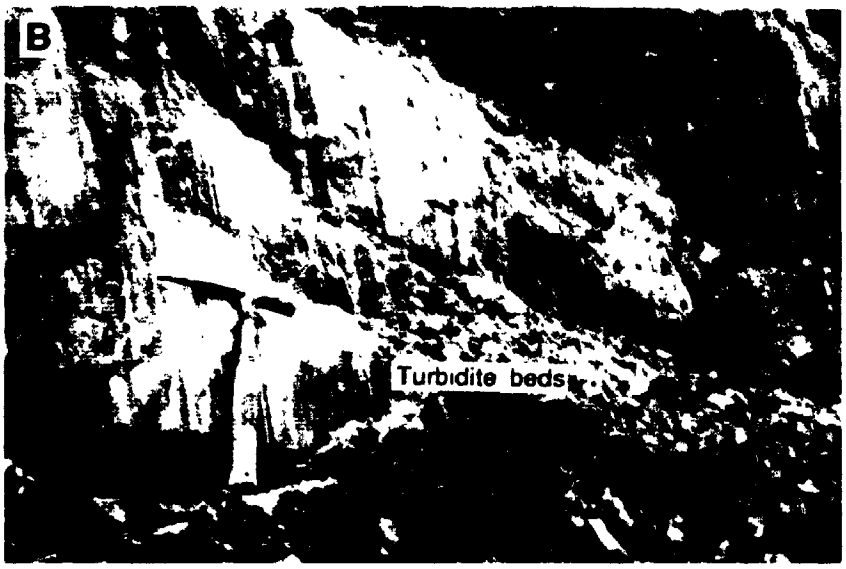
B
Turbidite beds

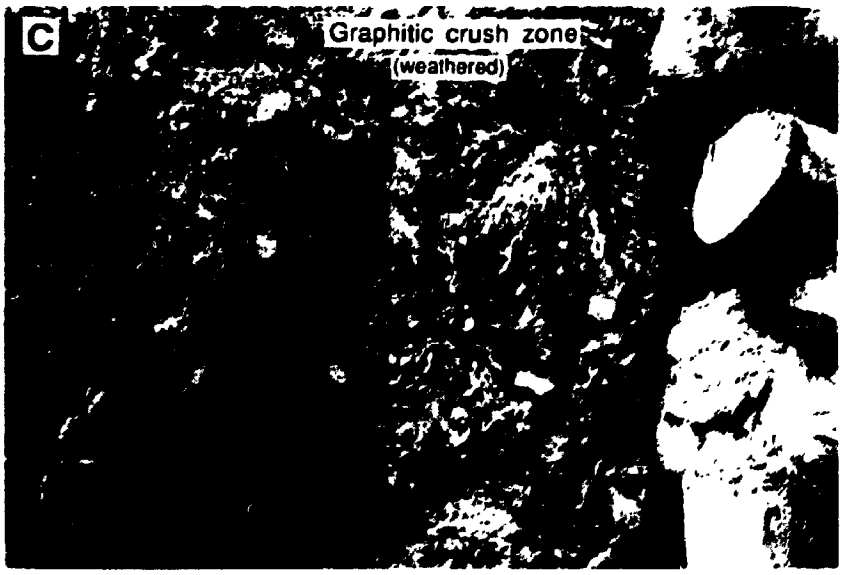
C
Graphitic crush zone
(weathered)

PLATE 4.2

A: View of the old Chujah South pit (looking SW). Previous mining (1934 to 1954) on the Bogosu concession stopped at the water table which is the lower limit of sulphide-mineral oxidation.

B: Photograph of a weathered and fractured quartz vein exposed in a road-cut southwest of the Chujah deposits, Bogosu concession.

C: Photograph of a weathered, carbonated dike exposed in the wall of the Chujah deposit. The dark bands are quartz veins with a coating of secondary iron oxides.

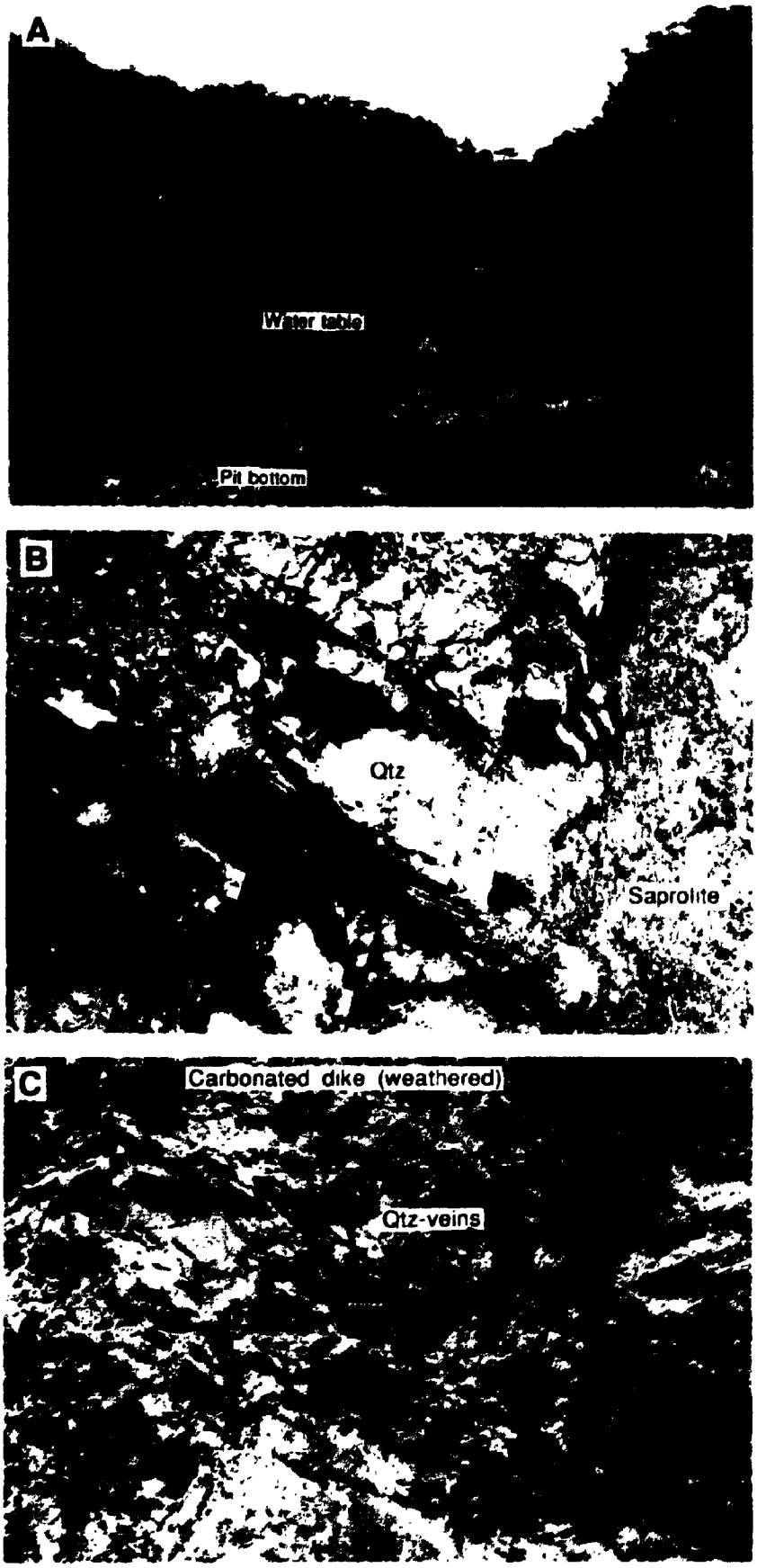
A
Water table
Pit bottom
B
Qtz
Saprolite
C
Carbonated dike (weathered)
Qtz-veins

parallel shears only tension gashes cut across bedding planes at a high angle (Plate 4.3A). Sulphide mineralization occurs as fine veinlets and disseminated grains along the sheared bedding planes. In banded turbidites, disseminated mineralization is concentrated in the clastic layers, while the relatively impermeable carbonaceous tops contain only minor disseminated sulphides, or sulphides along shear planes. Preservation of this type of bedding-parallel shearing and mineralization is generally not common, although local occurrences along the Ashanti Gold Belt have caused some investigators to suggest a syn-sedimentary rock origin for the gold ores. In most cases, graphitic crush zone ores have multiple stages of shearing and mineralization. Typically, early bedding-parallel shears are further brecciated, sheared and mineralized until a classic "crush zone" develops (Plate 4.3C).

Quartz fragments in the crush zone ores range from a fraction of a millimeter to several centimeters in size, and are embedded in a foliated matrix of phyllosilicates, carbonates and quartz. The quantity of quartz vein fragments is highly variable, ranging from a few percent in some well-bedded ores to over 30% in some crush zones. In some parts of the Bogosu concession, as in the Nankafa deposit, there is a distinct gradient in the degree of silicification of the ores. Parts of the upper portions are pervasively silicified and veined with as much as 80% quartz in the rock (Table 5.4 #75). Mass-balance calculations (Table 5.5) confirm that on average there was a 41% net increase in SiO_2 in the ores compared to host sedimentary rocks, and for silicified ores the increase in SiO_2 may exceed 140%. Silicification is the main reason for mass and volume increases of 34% and 33%, respectively, in typical crush zone ores. This mass/volume increase together with textural and structural evidence for open-space fracture filling such as comb-textured quartz ± ankerite ± albite growing orthogonally into vein cavities (Plate 8.1B and 8.1E) indicate mineralization

PLATE 4.3

A: Polished section of drill core showing a mineralized banded turbidite from the Dumassie deposit, Bogosu concession. Primary bedding is still visible although highly sheared. Quartz veinlets fill tension gashes sub-perpendicular to bedding and shearing. This sample contains about 5% pyrite as tiny veinlets and disseminated grains along sheared bedding planes (sulphides are not visible in the photograph due to the grey-black colour of the rock and the fine-grained nature of the sulphides): scale bar is 3 cm.

B: Polished section of drill core showing cataclastic deformation of graphitic crush zone ore from the Dumassie deposit, Bogosu concession. This sample contains about 10% pyrite and arsenopyrite as finely disseminated grains along micro-fractures, shear planes and quartz veinlets, and in the carbonaceous sedimentary-rock matrix (sulphides are not visible in the photograph due to the grey-black colour of the rock and the fine-grained nature of the sulphides): scale bar is 3 cm.

C: Polished section of drill core showing the typical texture of "classic" crush zone from the Dumassie deposit, Bogosu concession. The pebbly texture is caused by the fragmentation of quartz stockwork-veins in the sheared, carbonaceous matrix. This sample contains 3 to 4% fine-grained disseminated pyrite and arsenopyrite (sulphides are not visible in the photograph due to the grey-black colour of the rock and the fine-grained nature of the sulphides): scale bar is 3 cm.

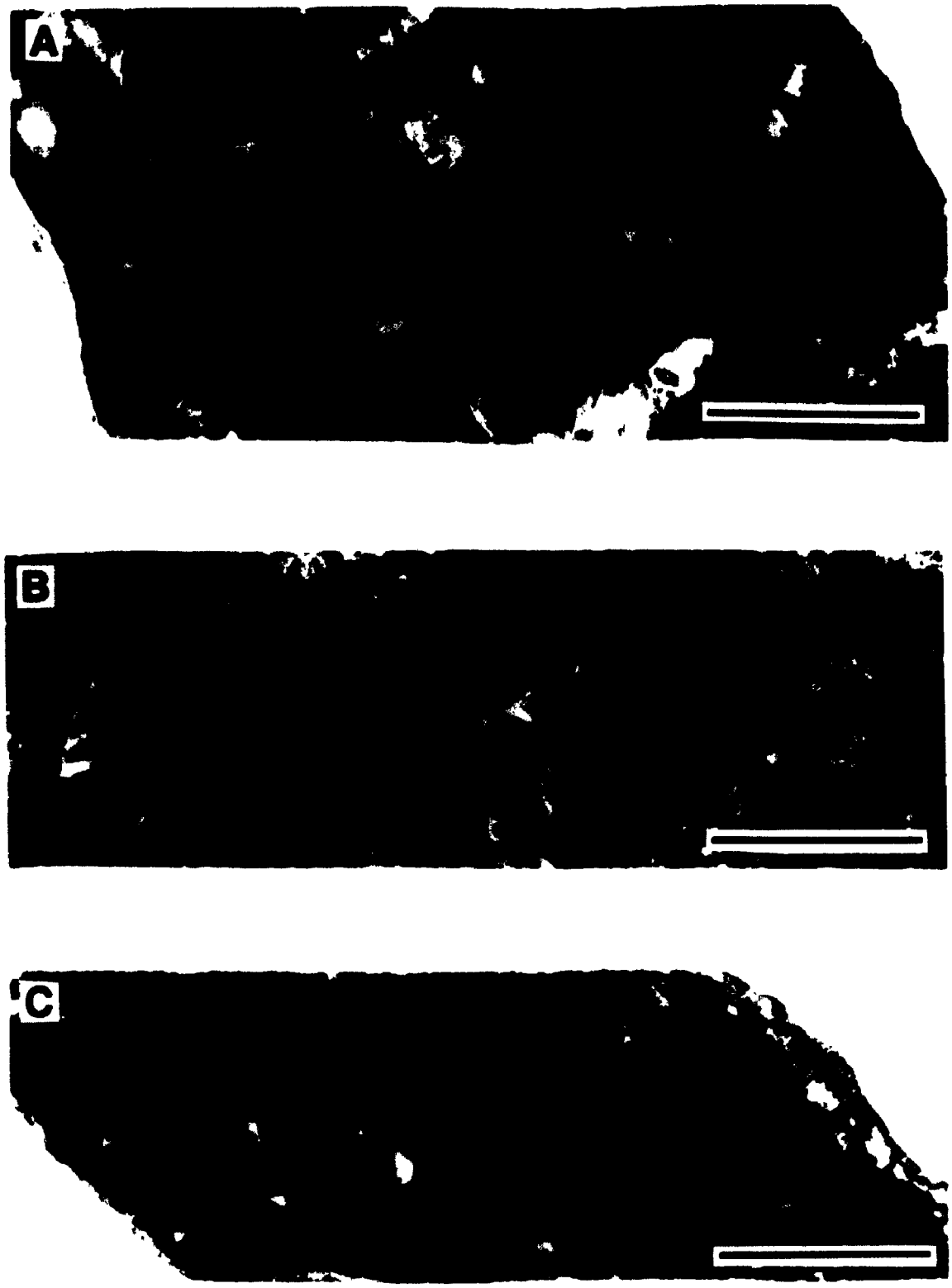
A
B
C

occurred in an extensional environment.

Two types of sedimentary-rock hosted ores are associated with the major quartz lodes at the Prestea concession. The most important are narrow, carbonaceous "fissure zones", that typically are less than 2 m in total width. These are zones of severely sheared and crushed carbonaceous sedimentary rocks with prominent black, carbon-rich (<10% C) shear planes. The fissures generally consist of bifurcating, en-echelon lenses aligned subparallel or parallel to the host stratigraphy. Fissure zones are commonly found on the footwall, and/or hanging wall of the quartz veins, and sometimes transect a quartz vein from one side to the other. They occur also in the host sedimentary rocks. These fissure zones are continuous throughout the Prestea workings and beyond, and are believed to be lateral equivalents of the graphitic "crush zone" ores of the Bogosu concession. However, shearing along the fissures is noticeably more ductile than at Bogosu, and many of these rocks have been ground to mylonites.

A more recent discovery in the Prestea gold mine is the presence of wider zones of mineralized sedimentary rocks that may occur in footwall and/or hanging wall rocks to the quartz lodes. At the time of investigation these mineralized zones had not been systematically documented at Prestea since the primary target had always been the free-milling ores of the large quartz lodes. They are more similar to Bogosu crush zone ores, except that deformation is more ductile with development of a strong foliation. Brecciation, silicification and stockwork veining common to Bogosu ores are not as prominent in these mineralized sedimentary rocks at Prestea. As with the graphitic fissures, the mineralized sedimentary rocks are thought to be lateral equivalents of the Bogosu ores.

In general, arsenopyrite exceeds pyrite in Prestea ores by a factor of at least 2 : 1, whereas pyrite dominates at Bogosu. Arsenopyrite dominates in the large quartz lodes, graphitic fissures ores and in mineralized dikes. The one exception at Prestea seems to be in mineralized sedimentary rocks where pyrite was more common in the samples investigated. Even at Bogosu where pyrite dominates all ores, the pyrite / arsenopyrite ratio is highest in the sedimentary-rock hosted ores.

There is a distinct gradation to the textural and mineralogical variations observed in the sedimentary-rock hosted ores of the Bogosu and Prestea districts. Laminated mylonitic fissures and brittle-ductile shearing at Prestea are replaced by breccias and cataclastic ores at Bogosu, and these grade further into local zones of pervasive silicification. In relationship to the generalized ore zone of Colvine et al. (1988), the Prestea rocks can be placed in the brittle-ductile regime (Sibson, 1977, 1983; Simpson, 1986). By contrast, breccias and cataclastic ores from Bogosu would occur only in the upper brittle deformation zone. Furthermore, the zones of pervasive silicification suggest that these areas are near the upper limits of potential mineralization for mesothermal lode gold systems. Overall, the textures of Prestea ores indicate higher ambient temperatures and/or confining pressures during formation, than occurred at Bogosu.

Carbonated-Dike Ores

Intrusive rocks are common in all regions of the Ashanti Structural Belt. Often they contain quartz stockworks, disseminated sulphides and gold mineralization. Most of the dikes related to ore are Fe-rich tholeiites (Chapter

5), although variations ranging from dacite to ultramafic have been observed. Even the least-altered dikes of the Bogosu and Prestea area have been subjected to an early lower-greenschist metamorphic / hydrothermal event. The dikes are massive, aphanitic rocks with little textural variation except for a very-fine foliation consistent with the deformation fabric of the Ashanti structural zone. This foliation is uniplanar and varies from imperceptible to barely detectable in least-altered varieties. It is considerably less-developed than the fabrics in host sedimentary rocks which have been subjected to lengthy and progresssive deformation of the sedimentary rock pile. The weak planar fabric of the dikes becomes progressively more pronounced parallel to the plane of the gold-bearing structures with increasing proximity to ore and structural zones. This suggests that the dikes were late additions to the sedimentary-rock pile, after the sedimentary rocks had already been isoclinally deformed. Subsequent deformation of the dikes was then controlled almost entirely by the Ashanti Structural Belt.

Mineralization of the dikes is non-selective compositionally, and occurs only when they have been tectonized and sheared by the Ashanti structures such that they were made permeable to the mineralizing fluids. Those dikes which are entirely within tectonized zones may be completely altered and mineralized; however, most are found adjacent to the main lodes, and show progessive decreases in alteration and mineralization away from the center of the ore zone. With increasing proximity to ore, the dikes are progressively carbonated with conversion of chlorite, albite, calcite and epidote to coexisting siderite and ankerite, disseminated throughout the matrix. This is accompanied by development of quartz-ankerite stockwork veining in an orthogonal fracture pattern of up to cm-sized veins (Plate 4.2C and 4.4B). Creation of fractures for the introduction of veins at this stage may have been enhanced by slight volume

PLATE 4.4

A: Polished face of a sample of crack-seal quartz-vein ore from the Prestea mine. The black bands are thin slivers of the altered, carbonaceous sedimentary host-rock. Very-fine-grained arsenopyrite, pyrite, chalcopyrite, sphalerite, tetrahedrite and trace amounts of other sulphide minerals and gold are concentrated along the slices of wall rock material (sulphides are not visible in the photograph due to the grey-black colour of the rock and the fine-grained nature of the sulphides): scale bar is 3 cm.

B: Polished section of drill core showing carbonated-dike ore from the Dumassie deposit, Bogosu concession. The dark and white areas are predominantly quartz ± albite veins. The intermediate, grey areas are fragments of the carbonated dike. This sample contains about 15% pyrite and arsenopyrite mostly disseminated along microfractures and in the matrix of the carbonated-dike fragments (sulphides are not visible in the photograph due to the grey-black colour of the rock and the fine-grained nature of the sulphides): scale bar is 3 cm.

A

B

reduction during carbonate alteration (Chapter 5). This contrasts with only very-fine veinlets of calcite in least altered-dikes.

Sulfidation of some siderite to pyrite almost immediately followed the carbonation of the dikes; however, total pyrite is generally <1% during early stages of carbonation. This stage of alteration may be accompanied by minor increases in shearing, or none at all may be detectable. The pervasive nature of the carbonation and lack of increased shearing or quartz stockwork development suggest an early phase of hydrothermal alteration that preceeds mineralization. This was most likely caused by outward migration of hydrothermal fluids from central conduits into tectonically-undisturbed host rock. The reasons for early carbonate alteration of dike rocks are discussed in greater detail in Chapter 9.

Carbonation of the dikes was followed by increasingly severe shearing and alteration until the rock was entirely converted to siderite, ankerite, quartz, sericite, rutile ± chlorite ± pyrite ± arsenopyrite (Table 5.2). The entire rock and any early stockwork veining were fractured and brecciated with increased shearing. However, later generations of veins may be preserved. Fragments of the original host-rock are strongly foliated in this zone due to the shearing (Plate 4.4B).

In the mineralized portions of the dikes, shearing is accompanied by quartz - ankerite ± albite stockwork veining, often with comb-textured ankerite growing orthogonally into the vein cavities (Plates 8.1B and 8.1E). A selvage of pyrite and/or arsenopyrite often developed in the host rock at the margins of veins, and sometimes within the veins (Plates 8.1A and 8.1E). However, the vast majority of sulphide mineralization was caused by sulphidation of siderite ±

ankerite within the carbonated-rock matrix. The iron content and consequently the siderite-ankerite content of the carbonated dikes is quite high, averaging ≈ 13 wt% and 56 modal%, respectively (Tables 5.1 and 5.2). Consequently, these dikes can be very rich in sulphide mineralization which locally exceeds 25 wt% pyrite plus arsenopyrite. The sulphides are generally disseminated and in small foliation-parallel veinlets throughout the matrix of quartz-carbonate-sericite-albite fragments in the brecciated ores. Where mineralized, these carbonated and tectonized dikes usually make good ores, with individual one meter assay intervals ranging from 2 to over 30 g/t Au. To date they have been mined as ores only at Bogosu, where they constitute generally less than 25% of any given gold deposit.

The mineralized dikes have generally been ignored in the first 100 years of production at the Prestea mine. However, during visits to several mine levels between the 9th and 30th levels (-400 m to -1375 m vertical depth), between the Main and Bondai shafts it was noted that carbonate altered, tectonized and arsenopyrite + pyrite bearing dikes occurred ubiquitously. In fact, the main haulage drifts about 15 to 30 m into the footwall from the main quartz reef on the levels visited are driven in part through these mineralized lithologies. In places they also occur in the immediate footwall of the quartz reefs and graphitic fissures that were being mined. Those observed were typically a few meters in width with unknown strike distances, but assumed to be quite extensive since they were observed in all areas visited. All samples of these arsenopyrite and pyrite-bearing dikes that were investigated microscopically contained identifiable gold grains (Table 7.1). However, no information was available at the time of investigation on average gold contents of this material at Prestea.

The mineralized Prestea dikes are very similar to dike ores at Bogosu with a few notable exceptions. Both pyrite and arsenopyrite crystals are larger in the Prestea dikes than in Bogosu ores. Arsenopyrite is present as euhedral, acicular crystals up to 5 mm in length, but typically in the range of 1 mm to 3 mm. Pyrite is either an agglomerate of small euhedral to subhedral grains smeared out along shear planes, or later subhedral to euhedral porphyroblastic grains often intergrown with the arsenopyrite. Deformation of Prestea dikes is distinctly more ductile than at Bogosu. These rocks have an aphanitic texture, are well foliated and lack the cataclastic fragments that make up the Bogosu ores. Some examples of Prestea dikes can be classified as mylonites, whereas Bogosu dikes form cataclastic breccias comprised of quartz-carbonate-albite veins and finely sheared and laminated carbonate-rich matrix fragments. It is clear from the deformation textures as well as slight differences in mineralogy that the dikes at Prestea were subjected to a somewhat higher grade of metamorphic conditions than their counterparts exposed near surface on the Bogosu concession.

Quartz Lodes

Large quartz lodes are the most important of four main ore types in the Bogosu and Prestea districts, and of the Ashanti Gold Belt in general. To date the vast majority of production has come from quartz reefs at the Ashanti (Obuasi), Prestea and Konongo mines, although major production efforts in all three areas are shifting towards the other ore types.

The large quartz reefs at Prestea and Obuasi extend through the mine workings in discontinuous lenses up to 15 m thick. These ores extend for 8 and 10 km along strike, respectively, and are over 1.5 km in vertical depth. The

lodes are similar to Archean crack-seal veins, with bands of carbonaceous wall-rock (Plate 4.4A) that have been altered to carbonates, albite, sericite and minor graphite that gives them a jet-black appearance. Sometimes they form massive quartz veins without any obvious wall-rock inclusions. However, these tend to be much lower in grade or are barren. Locally, streaks of visible gold in small veinlets may extend for several meters in the quartz, and these are not uncommon in some of the higher-grade lodes. However, the vast majority of gold is associated with sulphide mineralization along the thin bands of wall rock that give the quartz its banded appearance. The sulphide mineralization is dominated by arsenopyrite and lesser amounts of pyrite, although at Prestea, accessory chalcopyrite, sphalerite and tetrahedrite may be important constituents of the ores.

At the Prestea concession the quartz veins are fractured, brecciated and occasionally boudinaged. Considerable movement along the veins is evident from some of the carbonaceous shear planes that have well-developed striations from shear gouging. Flakes of carbonaceous material from one of the shear planes were analysed microscopically and by powder X-ray difraction (PXRD). The results showed that in spite of the jet-black appearance only about 5 to 10% graphite is actually present in this material, the remainder being finely comminuted quartz, ankerite, sericite and albite.

Even though quartz in the veins is highly deformed, most of it is annealed and recrystallized, suggesting deformation in the brittle-ductile transition zone. Quartz veins occur only in association with the graphitic fissure zones which flank the veins and occassionly transect them from nanging wall to footwall or vice versa. However, quartz lodes occur semi-continuously to sporadically whereas the fissure zones are continuous throughout the area. Some quartz

lodes have late tension gashes with open-space filling by late euhedral ankerite ± sulphides.

At Bogosu to the north, quartz lodes form an insignificant portion of the overall ores, generally not exceeding 2 to 5% of total ore in any deposit (Figure 3.4). The larger quartz veins at Bogosu are generally less than 1 m in width, although veins exceeding 3 m in width have been observed. They seldom are longer than 150 m in length. They are most often located at the hanging wall or footwall contact of the crush zone lodes (Figures 3.2 and 3.4), but they may also occur within the lodes themselves. They follow strictly the plane of shearing of the ore-bearing structures. Crack-seal textures are observed at Bogosu also, but to a much lesser extent than at Prestea. Massive quartz is more common, but it invariably has been subjected to severe deformation causing intense fracturing and brecciation of the veins (Plate 4.2B). In spite of this deformation, the larger quartz veins are moderately annealed and generally remain intact.

Discontinuous bands and wispy fragments of wall rock material host pyrite and arsenopyrite mineralization in these veins. The sulphides in turn host the gold which grades sporadically from 0 to 100 g/t over 1 m assay intervals. However, on the Bogosu concession quartz veins are too small and insignificant to form targets for modern methods of mining, and are only recovered when included within the other ore types.

The structural features described in this section suggests that these types of crack-seal quartz lodes form along major tectonic fracture zones simultaneous with active shearing. The mineral deposition into open-space fractures and overall volume increase in ore zones (Chapter 5) indicate that mineralization must have occurred either in localized areas of extension, or during regional

relaxation of the principal tectonic stress.

Weathered Ores

A range of hills 30 to 300 m in height marks the entire length of the Ashanti Gold Belt due to high but differential rates of tropical erosion. Carbonaceous turbidites and greywackes are easily weathered and form low-lying areas. The greater resistance of intrusive rocks and adjacent quartz lodes within the structural belt, has caused them to stand out as a range of hills. Quartz veins are often the only primary rocks exposed at surface, with the exception of some areas where relatively pure quartzites outcrop in adjacent Tarkwaian rocks.

Surface weathering has created a lateritic covering which is only 1 to 3 m thick along the hillsides that contain the gold lodes. This laterite thickens towards the base of the hills and in low-lying areas may exceed 3 m; however, little information was available to confirm this. The laterite forms a reddish-brown to orange-buff, mottled covering of clay that hides virtually all Birimian rocks (Plate 4.1A).

Tropical weathering on the concession was observed to be extremely efficient at releasing gold into the secondary environment. Lying on the surface of the laterite is a thin layer of scattered fragments of quartz and ironstone pebbles. The quartz is released from barren and gold-bearing veins and stockworks during weathering. Ironstones are composed of secondary limonites and goethite that may or may not be cemented to quartz fragments. They form during weathering and oxidation of sulphides and iron-bearing minerals such as siderite, ankerite, chlorite and epidote. This quartz and ironstone rubble eventually ends up in the stream valleys between and along the hillsides due to

mass wasting and runoff during tropical rainstorms. In the streams it is further worked to form numerous sand and gravel placer deposits. Most of these placer deposits contain gold and many areas have been worked both mechanically and manually. Diamonds have been recovered also, with or without gold in some placer deposits of the Bonsa and other streams in the Tarkwa region, and elsewhere in Ghana. Of particular interest is the Ankobra river which runs along side both the Bogosu and Prestea concessions and cuts across the Ashanti Gold Belt in the Prestea concession. About one million ounces of recorded production have been mechanically dredged from this river during the period 1903 - 1920 and 1938 - 1957 (Kesse, 1985). In 1988, the United Nations Development Program estimated about 125,000,000 cubic meters of workable gravels at 1.5 g/m^3, or 6 million ounces of placer gold remain to be recovered from this river (UNDP 1988).

Beneath the capping of laterite lies a saprolite zone, in which the primary rocks have been weathered in situ to clays (Plate 4.1A). Primary textures such as bedding and foliation are generally well preserved in the saprolite, often making identification of the original rock type fairly easy (Plate 4.1B). Quartz veins and stockworks remain intact so that structures can be identified also (Plates 4.1C, 4.2B and 4.2C). The saprolite zone extends for up to 100 m depth on the Bogosu concession. The upper part from the surface downward to the water table is completely weathered with conversion of all minerals to clays and iron oxides. Due to the tropical rain forest environment at Bogosu, the water table level is quite high, and consequently, it is at or within several meters of the base of the hills (Plate 4.2A). From the water table downward to the lower limits of saprolite development, which is typically another 10 to 40 m, sulphide minerals remain fresh and unweathered, with arsenopyrite somewhat more resistant to weathering than pyrite. The width of the transition zone between

weathered and unweathered sulphides appears to coincide with the average annual fluctuation in the water table level. It is generally quite sharp and occurs over a depth of one to several meters (cf. Figure 3.4).

Early mechanized mining on the Bogosu concession recovered oxidized saprolite ores only. Consequently the bottoms of old pits from Marlu Gold Mining Areas (1934-1954) coincide with the base of the hills and the water table level. The depth of ore that could be mined was controlled essentially by topography, with the height of hills dictating the depth of sulphide mineral oxidization (Plate 4.2A).

Mechanical dispersion of gold was observed in the laterite capping overlying the ore zones, and this may have led to some enrichment within the uppermost layer of the saprolite. However, assay results show similar distribution patterns for gold in unweathered ores and in saprolites, suggesting that very little redistribution of gold within the saprolite zone was caused by weathering. Rather, the gold appears to remain in place as microscopic particles contained within the secondary iron oxides. A significant amount of indirect gold concentration has occurred due to leaching and removal of other elements during the weathering process. Unweathered ores have a specific gravity of approximately 2.80 g/cm^3, while weathered ores average about 1.9 g/cm^3. This alone is enough to increase the residual gold grade by up to 50%, assuming all gold remains within the saprolite.

Tropical weathering has made a further important contribution to mining in Ghana by exposing quartz veins at surface and converting surface rocks to clays. This has made it relatively easy for local miners to hand dig through the saprolite in order to follow and chip away at the higher-grade portions of these

veins. Without exception, these local workings have been the forerunners of every modern gold mine in Ghana. "There has never been a gold mine in Ghana that was not previously worked by the local citizens", (UNDP Report, Gold and Diamonds in Ghana, 1988). However, there remains the possibility that some gold lodes may come to surface in low-lying areas, and thus remain undetected and not sought after.

Chapter 5: Geochemistry and Hydrothermal Alteration of Mafic Dikes and Sedimentary Rocks

Representative samples from the different categories of host and mineralized rocks in the Bogosu and Prestea districts were selected from unweathered drill cores for geochemical analysis. Whole-rock major oxide and trace element compositions were determined by XRF using a Philips PW 1450 Automatic Sequential Spectrometer at the University of Western Ontario.

Whole-rock Geochemistry of Mafic Dikes

Twelve samples of mafic dike rocks were analysed. Although they are only a small sampling of all intrusive rocks in the study area, on the basis of field mapping and petrographic observations most of the intrusive rocks associated with ore have mafic compositions. Minor amounts of dike rocks of other composition were observed, and these ranged from dacite through to ultramafic, but only one sample of the latter was collected. It is a bleached, carbonate-altered rock from a large intrusive unit in the footwall of the Prestea mine, known locally as the footwall quartzite (i.e. thought to be a Tarkwaian quartzite). The mafic dikes analyzed here were selected from the Bogosu and Prestea regions to represent hydrothermal variations from least-altered dikes to well-mineralized dike ores. The results are listed in Table 5.1, and will be compared to average Birimian volcanic rocks of Ghana. It is important to note that the least-mobile-element data used for these comparative analyses have apparently preserved the original rock classification, regardless of the degree of hydrothermal alteration affecting Bogosu and Prestea dikes.

Leube et al. (1990) demonstrated that 81% of metavolcanic rocks

Table 5.1: Whole-rock geochemistry of mafic rocks (wt%; trace elements in ppm).

Sample category	#	SiO2	TiO2	Al2O3	Fe2O3	MnO	MgO	CaO	K2O	P2O5	Na2O	L.O.I.	TOTAL
Tholeiites	*	48.7	1.2	13.7	13.8	0.21	6.5	9.4	0.3	0.15	2.5	2.8	99.3
Least-altered dike	19	43.9	1.2	11.4	14.1	0.19	6.1	10.1	0.0	0.11	1.7	10.5	99.3
Least-altered dike	2	50.8	0.8	12.7	9.7	0.18	4.3	9.4	0.0	0.09	3.3	8.5	99.8
Least-altered dike	38	44.4	1.3	12.2	14.5	0.15	5.6	7.1	0.0	0.12	2.7	11.7	99.6
Least-altered dike	42	44.5	1.3	12.0	14.9	0.18	5.5	10.1	0.0	0.11	1.3	9.0	98.9
Carbonated dike	44	40.6	1.0	11.5	12.9	0.13	5.9	6.6	0.8	0.09	1.6	18.7	100.0
Carbonated dike	15	36.5	1.8	11.7	17.5	0.18	4.9	6.2	0.4	0.19	2.1	18.5	100.0
Carbonated dike	45	42.7	1.7	12.6	12.0	0.13	4.8	6.1	0.4	0.16	2.7	16.1	99.4
Carbonated dike	46	42.1	1.2	11.4	13.3	0.15	5.2	5.8	0.2	0.09	2.1	17.6	99.2
Carbonated-dike ore	8	42.5	1.3	14.1	13.7	0.17	3.8	6.0	0.4	0.12	5.3	11.2	98.5
Carbonated-dike ore	13	41.0	1.3	12.1	14.2	0.13	3.5	6.7	0.5	0.06	5.7	14.2	99.3
Carbonated-dike ore	47	43.7	0.9	13.1	9.9	0.14	5.1	7.3	0.8	0.04	5.2	13.0	99.1
Carbonated-dike ore	43	36.2	1.2	12.6	13.1	0.20	4.9	9.9	0.9	0.10	1.8	18.3	99.2

Sample category	#	Nb	Zr	Y	Sr	Rb	Ga	Ba	Pb	Zn	Cu	Ni	Co	Cr	V
Least-altered dike	19	4	80	26	126	1	12	5	2	100	61	72	40	72	276
Least-altered dike	2	1	84	23	212	3	15	5	2	80	40	33	48	42	148
Least-altered dike	38	1	85	23	125	1	15	5	2	113	72	88	61	76	284
Least-altered dike	42	3	86	25	199	4	12	5	2	115	61	89	58	75	263
Carbonated dike	44	3	71	23	166	45	13	170	2	107	64	79	45	110	235
Carbonated dike	15	8	122	40	281	9	16	140	2	132	55	61	56	35	342
Carbonated dike	45	11	88	12	386	12	16	134	2	96	95	98	51	152	189
Carbonated dike	46	1	81	24	192	1	17	45	2	97	65	69	45	70	260
Carbonated-dike ore	8	5	85	24	335	14	14	135	2	81	86	77	58	87	314
Carbonated-dike ore	13	2	70	14	601	18	11	202	2	71	67	70	76	92	262
Carbonated-dike ore	47	4	55	14	449	27	14	207	2	76	74	86	69	170	230
Carbonated-dike ore	43	2	74	20	520	45	15	154	2	92	68	67	52	85	281

see Appendix 9.2 for sample descriptions.

* = Average of 66 Birimian tholeiites from Ghana (Luebe et al., 1990).

investigated from the Birimian of Ghana (N=129) plot in the basalt field according to the least-mobile-element classifications (SiO_2 vs Zr/TiO_2 and Zr/TiO_2 vs Nb/Y) of Winchester and Floyd (1977), and the Jenson (1976) cation plot (Figure 5.1) further demonstrates that the majority of the analyses do lie within the tholeiite field. All dike rocks investigated from the Bogosu and Prestea concessions plot in the high-Fe tholeiite field (Figure 5.1). Further examination of the Birimian tholeiite suite by Leube et al. (1990) (Ti vs Zr and Nb vs Zr) shows a MORB-like affinity, with most of the data clustering near the Primordial Mantle line (Zr/Nb=18) and in the field of depleted N-MORB. The Bogosu and Prestea data plot similarly and fall directly within the MORB field on the Pearce diagram (Figure 5.2).

The data presented above demonstate a direct correlation between mafic intrusive rocks along the Ashanti Structural Belt (this study) and the extrusive volcanic suite examined by Luebe et al. (1990). Considering their occurrence in a major tectonic lineament, it is reasonable to suggest that these dikes were feeders for the Birimian tholeiites. The volcanics are now eroded away in the vicinity of ores, although they are well preserved in other areas of the Ashanti Belt. This does not rule out the possibility that some of the mafic rocks along the Ashanti Structural Belt are syn-sedimentary volcanic lavas or pyroclastic rocks; however, no evidence was found to support this in the study area. Certainly, most of the mafic lithologies along the Ashanti Structural Bone in the Bogosu and Prestea region are intrusive rocks. As indicated by their similarities, the origin of the Bogosu and Prestea dikes must be similar to the Birimian tholeiites as a whole.

Figure 5.1: Jenson (1976) cation plot showing Birimian tholeiite and pyroclastic rock data (Luebe et al., 1990). The field for Bogosu and Prestea dikes (BP) is shown within the dashed line.

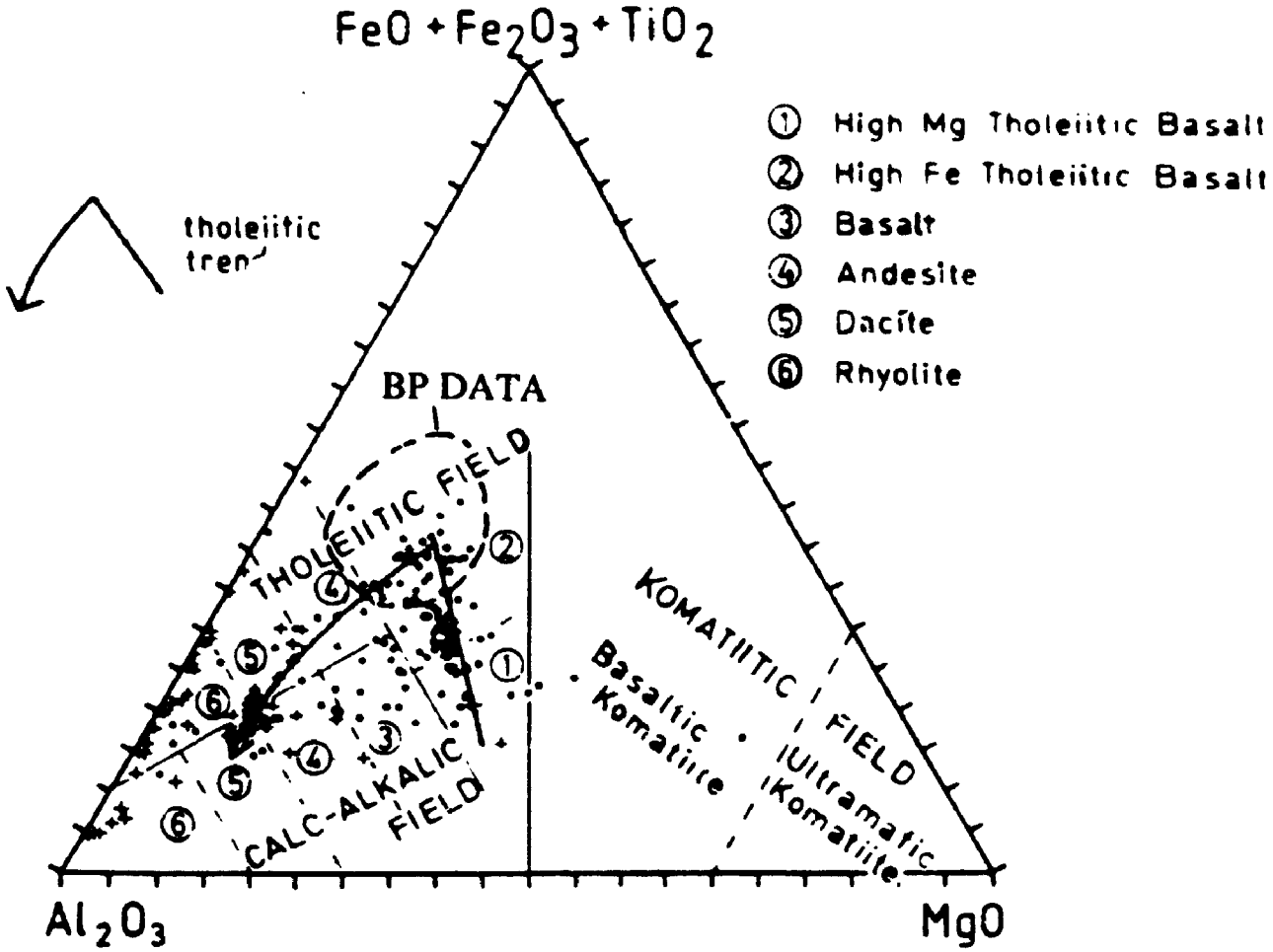
FeO + Fe2O3 + TiO2
① High Mg Tholeiitic Basalt
② High Fe Tholeiitic Basalt
③ Basalt
④ Andesite
⑤ Dacite
⑥ Rhyolite
tholeiitic trend
BP DATA
THOLEIITIC FIELD
KOMATIITIC FIELD
Basaltic Komatiite
Ultramafic Komatiite
CALC-ALKALIC FIELD
Al2O3
MgO

Figure 5.2: Ti-Zr diagram of Pearce (1982) showing the plot of 66 Birimian tholeiites (Luebe et al., 1990). The field for Bogosu and Prestea (BP) dikes is shown within the dashed line.

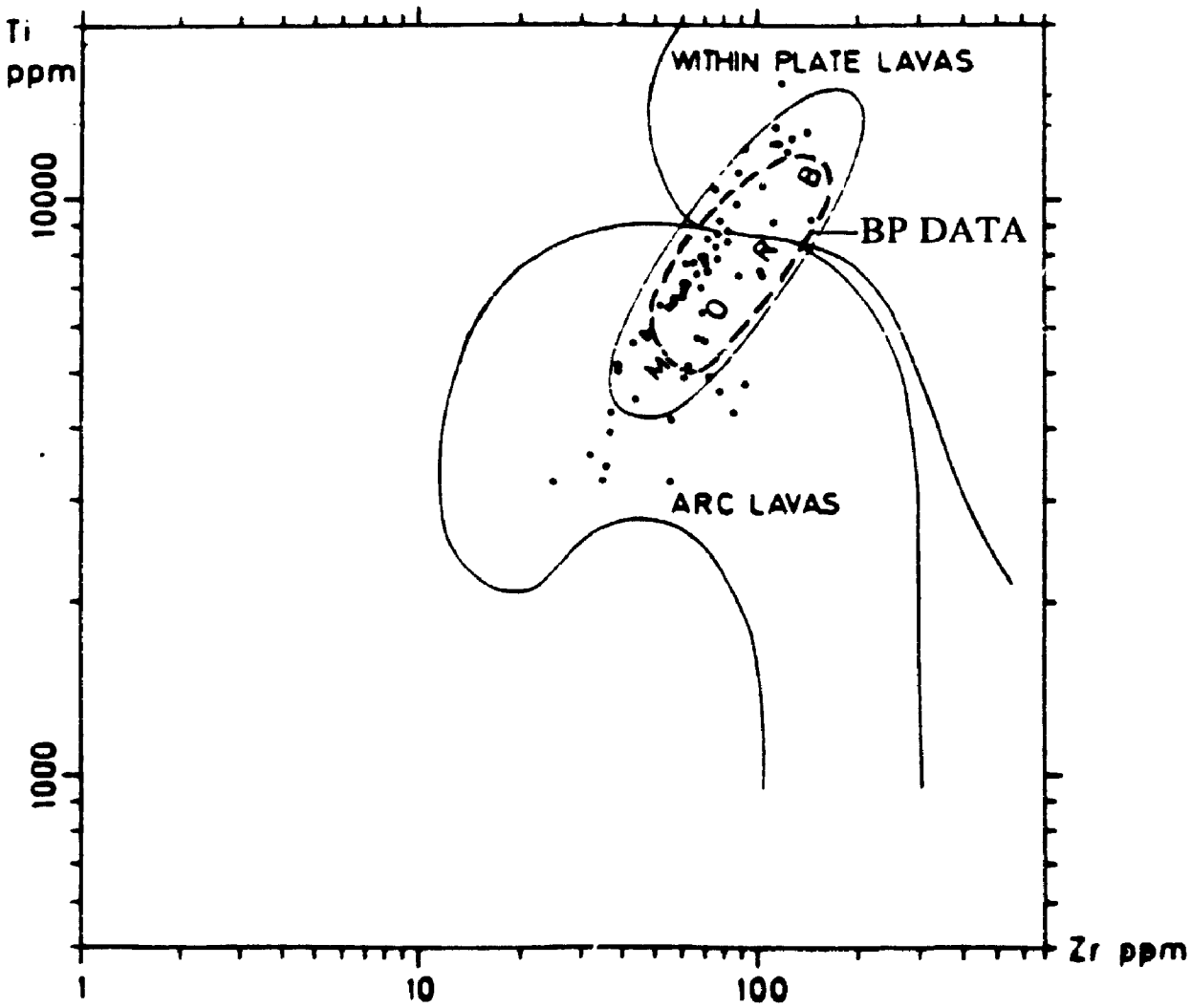
Ti
ppm
10000
1000
WITHIN PLATE LAVAS
BP DATA
ARC LAVAS
1
10
100
Zr ppm

Hydrothermal Alteration Patterns in the Mafic Dikes

The mafic dikes are considerably more homogenous, both texturally and compositionally, than the host sediments. Consequently, they are better indicators of some aspects of the hydrothermal metasomatism. Texturally and mineralogically they can be divided into 3 distinct categories: 1) least-altered dikes with a greenschist facies assemblage of chlorite, calcite, quartz and rutile, ± epidote, magnetite, sericite and trace amounts of pyrite and chalcopyrite, 2) pervasively carbonatized dikes consisting of siderite, ankerite, quartz, muscovite, rutile and pyrite with trace amounts of arsenopyrite and chalcopyrite, ± pyrrhotite, tetrahedrite, magnetite, ilmenite and chlorite, and 3) mineralized dikes with ankerite ± siderite, quartz, albite, sericite, rutile, pyrite, arsenopyrite and trace amounts of chalcopyrite, pyrrhotite, tetrahedrite, chlorite, magnetite, ilmenite, sphalerite, galena, titanite, apatite, boulangerite, cobaltite, gersdorffite and stibnite (Table 5.2). Least-altered dikes are fine-grained massive rocks often lacking evidence of the regional deformation fabric. Pervasively carbonatized dikes are bleached equivalents of the above with minor to moderate quartz-carbonate veining. The well mineralized dikes are severely sheared and have well developed quartz-ankerite-albite stockwork veining.

However, on the basis of both geochemistry and mineralogy, it seems that the least-altered dikes were previously subjected to significant hydration and carbonation reactions in addition to greenschist facies metamorphism [L.O.I. = 9.9% (n=4), compared to 2.8% for related Birimian tholeiites, Table 5.1]. Therefore, it is important to examine the metasomatic changes that affected these dikes prior to mineralization. This can be done by comparison with average Birimian tholeiites whose relationship to the dikes has already been

Table 5.2: Mineral abundances in Bogosu and Prestea dikes (modal %).

Mineral	Least altered	Carbonate alte.ed	Dike ores	Veins in ores
Quartz	21	28	38	45
Chlorite	51	3.3	<1.0	
Sericite		8	5.4	
Calcite	23			
Ankerite	tr	36	35	48
Siderite	tr	20	<4	
Albite	5	<2.0	4	7
Epidote	<2.5		<1.0	
Rutile	1.3	0.9	1.2	
Ilmenite		tr	tr	
Titanite	tr		tr	
Sphene	tr	tr		
Apatite				tr
Magnetite	tr	tr	tr	
Hematite		tr	tr	
Pyrite	< 0.3	1.7	7	
Arsenopyrite		tr	2.3	
Pyrrhotite		tr	tr	
Chalcopyrite	tr	tr	tr	
Tetrahedr .e		tr	tr	
Covellite		tr	tr	
Sphalerite			tr	
Galena			tr	
Stibnite			tr	
Cobaltite			tr	
Gersdorffite			tr	
Boulangerite			tr	
Gold		tr	3-30 ppm	
n=	8	15	10	

tr = trace

demonstrated.

Elemental depletions and additions for 21 major oxides and trace elements were incrementally tested between progressive alteration zones and compared to the average compostion of Birimian tholeiites. The procedure used was the Grant (1986) isocon method as a solution to Gresens' (1967) equations for metasomatic alteration. This method takes into consideration mass and volume changes before calculation of net elemental additions or depletions. Based on a graphical plot of whole-rock geochemical data for an unaltered reference sample versus data for the altered equivalent, assumptions can be made as to whether constant volume or mass has been retained during alteration, or whether an element or oxide such as Al_2O_3 has remained immobile. Changes in mass are then factored into the equation for a more accurate estimate of gains and losses. For this study, constant Al_2O_3 seems most appropriate, and even if Al_2O_3 does not behave completely immobile in all instances this does not significantly alter the conclusions. A line drawn through the origin and the plot of Al_2O_3 concentration defines an isocon on the graph along which no change in elemental concentration has occurred, and has the equation:

$$C^A = (M^o/M^A)\, C^o$$

where, C^A= concentration of component in the altered sample

C^o= concentration of component in the reference sample

M= mass (or concentration of immobile phase if constant Al_2O_3 or other element is assumed)

The net change in mass is then the inverse of the slope of the Al_2O_3 isocon and:

$$\Delta \text{ Mass } (\%) = \left[\frac{\text{Concentration of } Al_2O_3 \text{ in reference sample}}{\text{Concentration of } Al_2O_3 \text{ in altered sample}} - 1 \right] \times 100\%$$

The percent gain or loss of any component (i) in the system is calculated as:

$$\Delta C_i (\%) = \left[\frac{C_i^A + C_i^o}{C^A_{Al2O3} + C^o_{Al2O3}} - 1 \right] \times 100 \%$$

Consequently, all components that plot above the reference isocon (Al_2O_3 for this study) have undergone net additions during alteration, and all components plotting below the reference isocon have experienced net losses. The volume change is calculated by multiplying the mass change by the ratio of any difference in density measured before and after alteration, and is given by the following equation:

$$\text{Vol difference } (\Delta V) = \left[\frac{\text{density of the parent rock}}{\text{density of the altered rock}} \times \frac{C^O_{Al2O3}}{C^A_{Al2O3}} - 1 \right] \times 100\%$$

Calculated compositional gains and losses are listed in Table 5.3, and are graphically depicted in Figures 5.3 to 5.5 for incremental steps in progressive alteration from average Birimian tholeiites to dike ores. Data for the isocon diagrams are listed in Table 5.6. Due to uncertainties of original rock composition and small sample size, the degree of error may exceed 20% for some analyses. However, most of the calculations are significant in terms of loss or gain.

Comparison of Bogosu and Prestea dikes and average Birimian tholeiites reveals an early Stage 1 alteration that caused massive hydration and

Table 5.3: Summary of elemental gains and losses (wt%; trace elements in ppm) for mafic rocks from Bogosu and Prestea. Mass-balance is calculated for both incremental stages in progressive alteration, and for progressive stages of alteration compared to Birimian tholeiites.

Phase	Stage 1 alteration	Stage 2 alteration	Stage 3 alteration	Stages 1 and 2 alteration	Stages 2 and 3 alteration	Stages 1 to 3 alteration
SiO2	7	-12	-8	-4	-19	-12
TiO2	6	41	-22	35	6	6
Al2O3	0	0	0	0	0	0
Fe2O3	10	10	-11	17	-2	2
MnO	-3	-24	9	-20	-17	-14
MgO	-7	-4	-22	-7	-25	-30
CaO	11	-37	17	-24	-27	-11
K2O	-97	3513	47	48	5220	114
P2O5	-17	32	-43	1	-27	-43
Na2O	4	3	79	1	85	84
L.O.I.	307	78	-21	644	40	482
Cr	-59	88	2	-42	69	-42
Ni	-28	64	-6	-19	44	-24
V	-6	10	5	0	18	-2
Co	-5	17	20	-7	40	11
Cu	-29	46	-4	-14	31	-18
Zn	14	14	-29	23	-19	-15
Zr	32	10	-25	45	-18	7
Ba	-91	1910	34	45	2632	93
Sr	18	73	66	87	184	196
Y	-19	-9	7	-15	-10	-22
Δ Mass %	14	0	-7		-7	8
Δ Volume %		-2	-9		-11	
Isocon Fig.#	5.3				5.4	5.5

Stage 1 alteration = least-altered dikes vs Birimian tholeiites
Stage 2 alteration = carbonated dikes vs least-altered dikes
Stage 3 alteration = carbonated dike ore vs carbonated dikes
Stages 1 and 2 alteration = carbonated dikes vs Birimian tholeiites
Stages 2 and 3 alteration = carbonated dike ore vs least-altered dikes
Stages 1 to 3 alteration = carbonated dike ore vs Birimian tholeiites
Δ Mass % = mass change of the rock during alteration
Δ Volume % = volume change of the rock during alteration

Table 5.4: Whole-rock geochemistry of sedimentary rocks (wt%).

Rock category	#	SiO2	TiO2	Al2O3	Fe2O3	MnO	MgO	CaO	K2O	P2O5	Na2O	L.O.I.	TOTAL
Sedimentary rock	26	61.9	0.6	17.6	7.6	0.1	2.3	0.2	2.5	0.1	1.7	4.9	99.5
Sedimentary rock	61	64.8	0.6	15.1	5.6	0.1	1.9	2	2.8	0.1	1	5.1	99
Sedimentary rock	70	55.4	0.7	18.1	7.6	0.1	2.8	2.8	2.4	0.1	3	7.3	100.3
Sedimentary rock	71	69.1	0.3	9.3	4.3	0.1	1.9	1.8	1.3	0.1	0.7	10	99
Sedimentary rock	41	57.5	0.5	14.4	6.3	0.1	3.1	3.6	1.6	0.1	2.8	9.9	99.8
Sedimentary rock	54	58.8	0.6	15.3	5.8	0.1	2.7	3.1	1.5	0.2	3.7	8.4	100
Sedimentary rock	59	50.2	0.6	19.3	7.1	0.1	2.8	3.4	1.4	0	5	9.8	99.7
Sedimentary rock	73	60.3	0.6	15.5	6.2	0.1	2.3	2	1.8	0.1	1.6	10	100.5
Sedimentary-rock ore	72	61	0.4	11.6	6.1	0.1	2.5	5.1	1.6	0.1	0.2	10.2	98.9
Sedimentary-rock ore	28	63	0.5	10.5	5.8	0.1	2.2	3.6	0.3	0	5.7	8.6	100.2
Sedimentary-rock ore	34	38.8	0.9	24.1	8.9	0.1	2.3	3.4	4	0	2.8	12.1	97.5
Sedimentary-rock ore	34	39.4	0.9	24.6	9.4	0.1	2.4	3.4	4.1	0	2.8	12.5	99.4
Sedimentary-rock ore	30	62.5	0.4	13	3.9	0.1	2.3	4.6	1.4	0.4	6.7	7.7	99.8
Sedimentary-rock ore	74	57.3	0.5	14.4	6.3	0.1	1.7	2.8	0.4	0	8.4	8.3	100.1
Sedimentary-rock ore S	75	74.8	0.4	8.9	4.1	0	1.2	1.2	0.1	0	5.8	3.9	100.4

# see Appendix 9.2 for sample descriptions.
S = silicified.

Table 5.5: Whole-rock compositional data and mass-balance calculations for sedimentary-rock ores (graphitic crush zone ores).

Phase	Sedimentary rocks	Sedimentary rock ores	Δ Concentration (wt%)
0.25 x SiO_2	14.5	15.2	41
10 x TiO_2	6.1	4.5	-1
Al_2O_3	16.6	12.4	0
Fe_2O_3	6.7	5.5	11
10 x MnO	0.9	0.7	2
MgO	2.6	2.2	13
CaO	2.5	4.0	114
K_2O	2.0	0.9	-39
Na_2O	2.8	4.5	112
10 x P_2O_5	1.7	1.3	1
L.O.I.	7.6	8.7	55
Δ Mass %			34
Δ Volume %			33
* n =	6	4	

Δ Mass % = mass change during alteration.
Δ Volume % = volume change during alteration.
Δ Concentration (%) = net change in concentration for each component in the rock.
* Compostions of some sedimentary rocks are highly variable, consequently, those with obviously anomalous compositions were not used for the mass balance calculations.

Table 5.6: Whole-rock compositional data of mafic dikes for isocon diagrams (wt%, trace elements in ppm).

Phase	Birimian Tholeiites	Least-altered Dikes	Carbonated-dike Ores
0.5 x SiO_2	24.4	22.9	20.4
TiO_2	1.2	1.2	1.2
Al_2O_3	13.7	12.1	13.0
Fe_2O_3	13.8	13.3	12.7
10 x MnO	2.1	1.8	1.7
MgO	6.5	5.4	4.3
CaO	9.4	9.2	7.5
10 x K_2O	3.4	0.1	6.6
10 x P_2O_5	1 5	1.1	0.8
Na_2O	2.5	2.2	4.5
L.O.I.	2.8	9.9	14.2
0.1 x Cr	18.4	6.6	10.7
0.2 x Ni	22.2	14.1	15.9
0.1 x V	29.9	24.3	27.2
0.2 x Co	12.4	10.4	12.8
0.2 x Cu	18.8	11.7	14.8
0.1 x Zn	10.2	10.2	8.0
0.2 x Zr	14.4	16.8	14.2
0.1 x Ba	9.8	0.8	17.5
0.05 x Sr	8.0	8.3	21.4
0.5 x Y	17.0	12.1	11.5
n =	66	4	4

Table 5.7: Density determinations* for some representative rocks of the Bogosu and Prestea districts.

	Host Turbidites	GCZ Ores	Mafic Dikes	Carbonated Dikes	Dike Ores
Density (g/cm^3)	2.75	2.77	2.76	2.89	2.89
n =	2	3	3	2	2

GCZ = graphitic crush zone ores

* Density determinations were made by weighing the rock samples in air and in water.

Figure 5.3: Isocon diagram showing elemental gains and losses for least-altered dikes from the Bogosu and Prestea region compared to average Birimian tholeiites of Luebe et al. (1990) (Stage 1 alteration). Constant Al_2O_3 has been assumed. Those components plotting above the Al_2O_3 isocon have increased their concentration during alteration, while those plotting below have been depleted. Calculated gains and losses are listed in Table 5.3.

Figure 5.4: Isocon diagram showing elemental gains and losses for carbonated-dike ores compared to least-altered dikes (Stages 2 and 3 alteration). Constant Al_2O_3 has been assumed. Those components plotting above the Al_2O_3 isocon have increased their concentration during alteration, while those plotting below have been depleted. Calculated gains and losses are listed in Table 5.3.

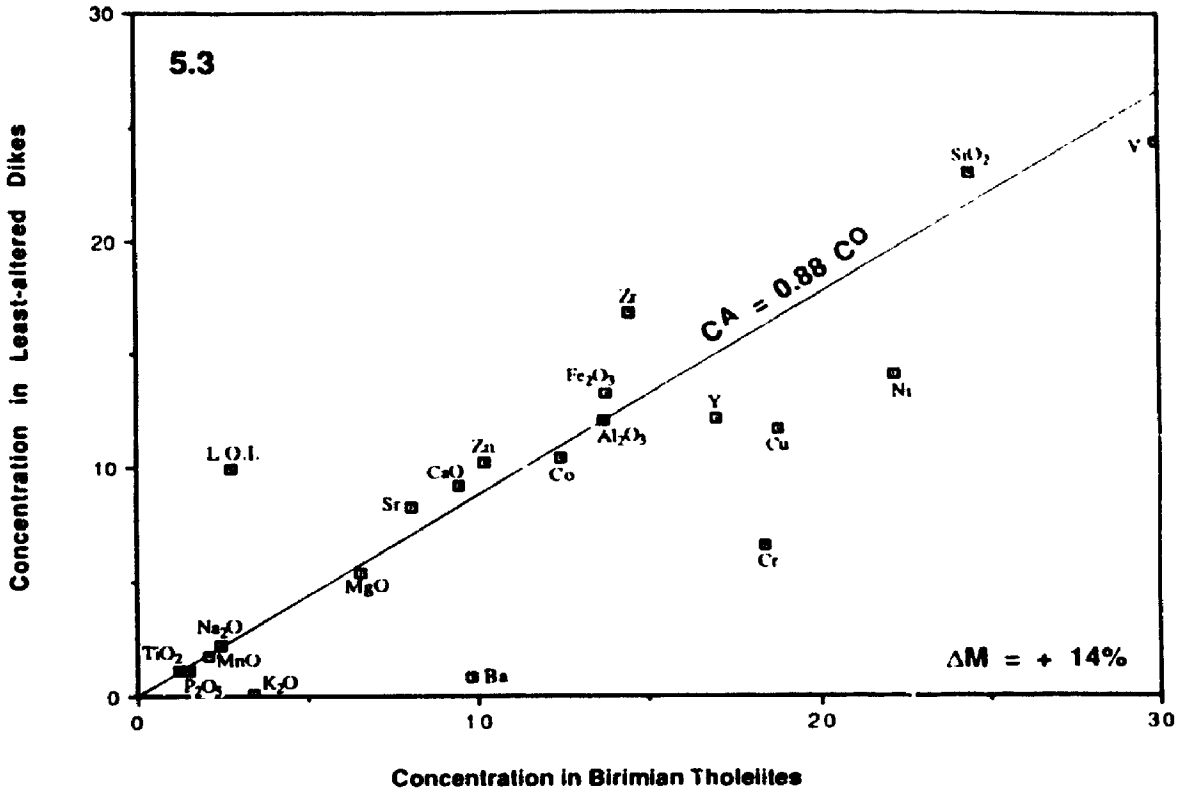
5.3
CA = 0.88 CO
ΔM = + 14%
Concentration in Least-altered Dikes
Concentration in Birimian Tholeiites
L.O.I.
SiO2
Zr
Fe2O3
Al2O3
Y
Ni
Cu
Zn
CaO
Co
Sr
Cr
MgO
Na2O
TiO2
MnO
P2O5
K2O
Ba
0
10
20
30

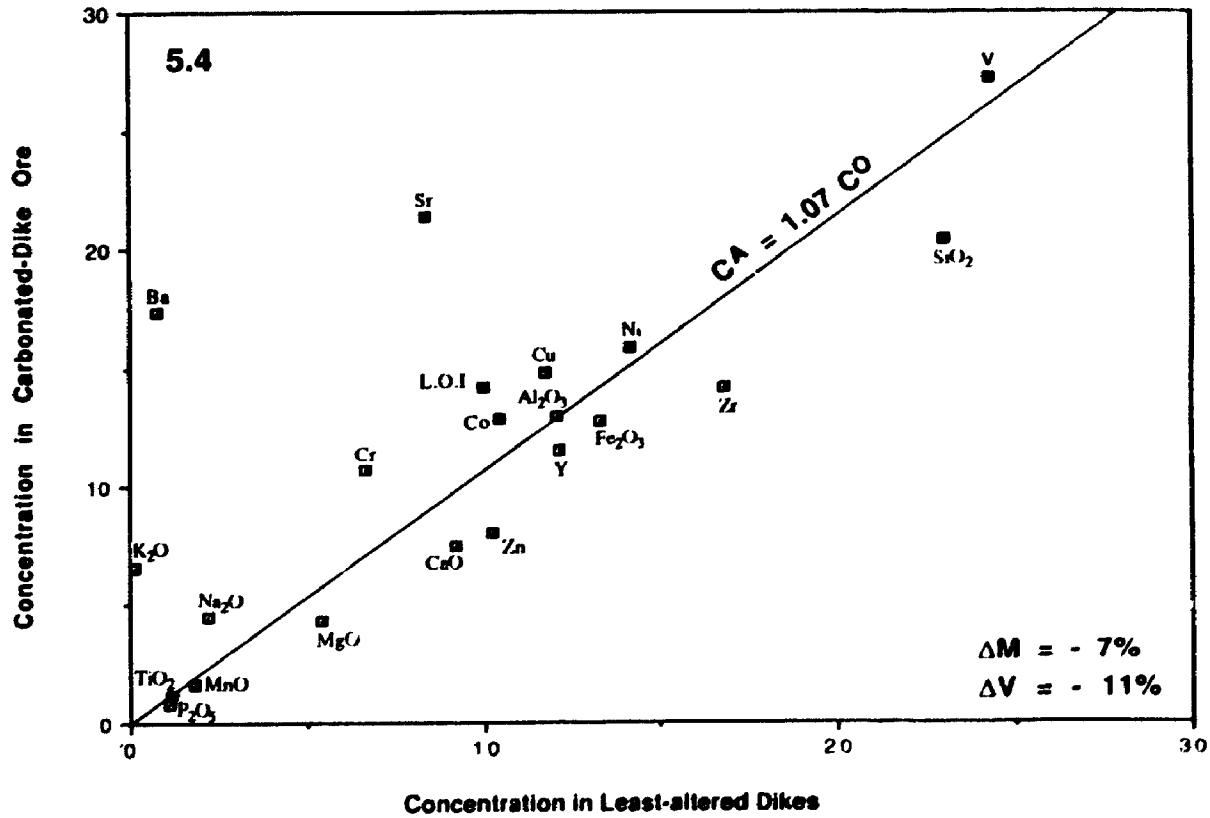
5.4
CA = 1.07 CO
ΔM = - 7%
ΔV = - 11%
Concentration in Carbonated-Dike Ore
Concentration in Least-altered Dikes
V
Sr
SiO2
Ba
Ni
Cu
L.O.I
Al2O3
Zr
Co
Fe2O3
Cr
Y
Zn
CaO
K2O
Na2O
MgO
TiO2
MnO
P2O5
0
10
20
30

Figure 5.5: Isocon diagram showing elemental gains and losses for carbonated-dike ores compared to average Birimian tholeiites of Luebe et al. (1990) (Stages 1 to 3 alteration). Constant Al_2O_3 has been assumed. Those components plotting above the Al_2O_3 isocon have increased their concentration during alteration, while those plotting below have been depleted. Calculated gains and losses are listed in Table 5.3.

Figure 5.6: Isocon diagram showing elemental gains and losses for sedimentary-rock ores compared to least-altered sedimentary rocks. Constant Al_2O_3 has been assumed. Those components plotting above the Al_2O_3 isocon have increased their concentration during alteration, while those plotting below have been depleted. Calculated gains and losses are listed in Table 5.5.

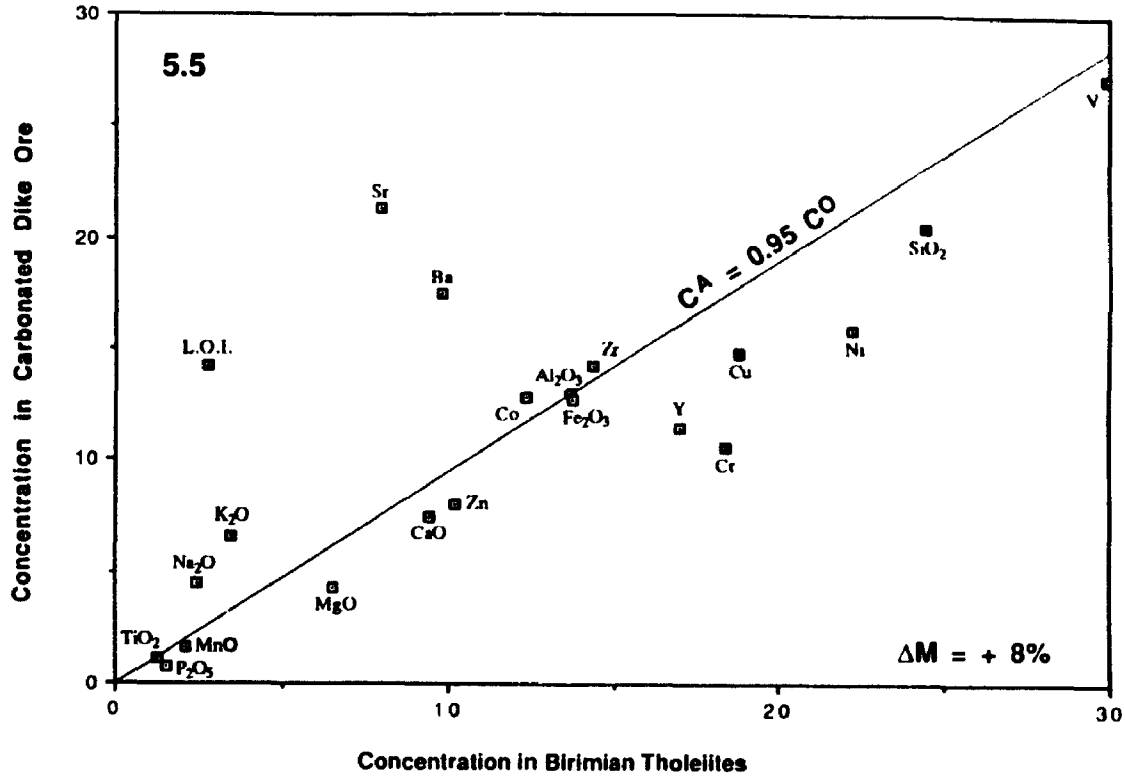
5.5
CA = 0.95 CO
ΔM = + 8%
Concentration in Carbonated Dike Ore
Concentration in Birimian Tholeiites
V
Sr
Ba
SiO2
L.O.I.
Zr
Al2O3
Co
Fe2O3
Cu
Ni
Y
Cr
Zn
CaO
K2O
Na2O
MgO
TiO2
MnO
P2O5
0
10
20
30

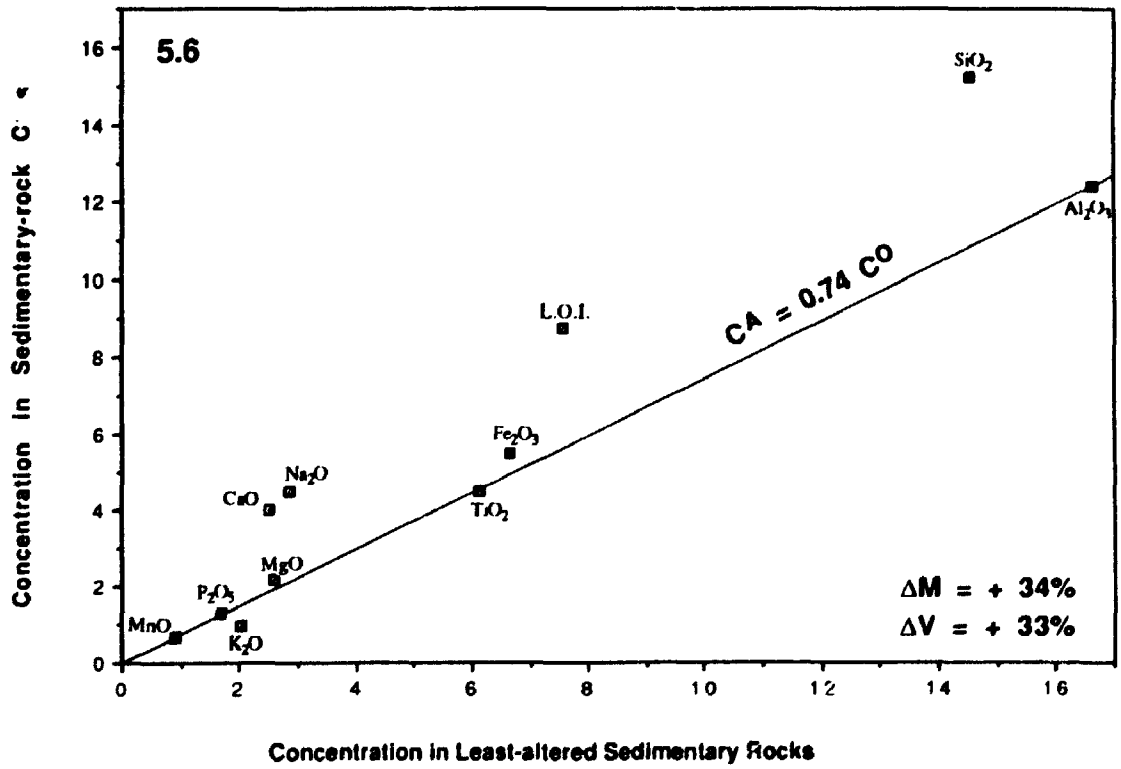
5.6
CA = 0.74 CO
ΔM = + 34%
ΔV = + 33%
Concentration in Sedimentary-rock C
Concentration in Least-altered Sedimentary Rocks
SiO2
Al2O3
L.O.I.
Fe2O3
Na2O
CaO
TiO2
MgO
P2O5
MnO
K2O
0
2
4
6
8
10
12
14
16

carbonation of the rock. A large increase in volatiles (Δ L.O.I. = +310%) was complemented by a net mass increase of ≈14% (Figure 5.3, Table 5.3). This was accompanied by almost total loss of K_2O (-97%) and most Ba (-91%). Significant losses are also indicated for Cr, Cu, Ni, Y and P_2O_5. Gains of between 10% and 32% are indicated for Fe_2O_3, CaO, Zr, Sr and Zn.

The later-stage alterations associated with mineral deposition are more meaningful since altered Bogosu and Prestea rocks can be compared to their well defined, less-altered equivalents. Due to minor differences in original rock compositions, Bogosu altered rocks are compared to least-altered equivalents found nearby and Prestea altered dikes are compared to least-altered dikes from the Prestea mine. The results were averaged, with a 2:1 weighting in favour of Bogosu for which there are more data, and discussed below.

Stage 2 alteration resulted in pervasive bleaching and carbonation of the least-altered dikes (Table 5.3). On a relative basis, very large increases occurred in K_2O (+3500%) and Ba (+1900%). Further significant gains are recorded for Cr, Ni, Cu, Sr and TiO_2 (88%, 64%, 47%, 73% and 41%, respectively). Moderate gains are suggested for Co, Zn, Zr, V and Fe_2O_3 (17%, 14%, 10%, 10% and 10%, respectively). Notable losses are restricted to CaO, MnO and SiO_2 (-37%, -24% and -12%, respectively). However, no change in mass was evident at this stage of alteration. The large increase in volatiles (Δ L.O.I. = +78%) is due mainly to carbonation of the rock, as ferromagnesian minerals (mostly chlorite) break-down to form large amounts of siderite and ankerite (Table 5.2). The K_2O increase is due to stabilization of white micas (sericite). Loss in CaO is associated with transformation of calcite to siderite and ankerite. Interestingly, the loss of MnO from the system during this stage of alteration contradicts any suggested direct genetic relationship

between gold and manganese in the Birimian of West Africa (e.g. Ntiamoah-Agyakwa, 1979).

The final step in progressive alteration, Stage 3, leads to mineralizaton of the carbonated dikes (Figures 5.4 and 5.5, Table 5.3). The most significant gains in major oxides are for Na_2O and K_2O. The increase in Na_2O is related to albitization of the rock and the increase in K_2O to further stabilization of white mica. Increase in trace elements are indicated for Sr, Ba and Co (66%, 34% and 20%, respectively). At this stage of alteration the system underwent a net mass loss of approximately 7%, with losses for P_2O_5, MgO, TiO_2, Fe_2O_3, volatiles, Zn and Zr of -43%, -22%, -22%, -11%, -21%, -29% and -25%, respectively. The losses in TiO_2, Fe_2O_3 and Zr during this final stage balance previous gains for very little change overall compared to the original composition of Birimian tholeiites (Figure 5.5, Table 5.3). Loss on ignition from the mineralized dikes includes significant sulphur from pyrite and arsenopyrite in addition to H_2O from mica and CO_2 from carbonates. However, the significant decrease in volatiles at this stage of alteration (Δ L.O.I. = -21%) is mostly the result of CO_2 loss, as siderite $\pm$ ankerite is sulphidized to form the 5 to 20% pyrite and arsenopyrite present in these samples.

It is worth noting the loss of 8% SiO_2 during Stage 3 alteration ($\approx$4% of overall sample weight). For these analyses, samples were chosen to be matrix material devoid of noticeable quartz stockwork veins to prevent a bias toward excessive SiO_2. However, mineralized dikes may contain 10-25% quartz-albite-ankerite veins. Consequently, suggested SiO_2 losses are almost certainly accounted for by the material in the stockwork veining.

There is an important volume reduction in the rocks caused by the progressive alteration of mafic dikes. Calculated reductions are 2% and 9% for Stage 2 and Stage 3 alteration, respectively. This enhances rock permeability by a maximum of 11% of the total altered-rock volume. However, this increase in permeability is not likely to occur at one time since open-space fractures caused by the volume reduction will be progressively filled by the precipitation of hydrothermal minerals.

Geochemical Evolution of the Mafic Dikes

Stage 1 alteration of the mafic dikes is the most widespread and is characteristic of all least-altered dikes examined in this study. The fact that the least-altered dikes represent a distinctly altered subset of average Birimian tholeiitic rocks precludes the possibility that this alteration is a regional phenomenon. Rather, it seems that this type of alteration of mafic rocks may be restricted to the Ashanti Structural Belt (with a known width of about 1 km in the Bogosu region) and adjacent country rocks. However, considerably more sampling would be required to precisely define its limits. The dikes within the Ashanti Structural Belt solidified at depth, and were subjected to greenschist facies alteration and metasomatism. By comparison, the Birimian tholeiites documented by Luebe et al. (1990) are postulated to be the extrusive equivalents, and clearly would not have been subjected to the same degree of alteration that affected the Bogosu and Prestea dikes.

There are some interesting negative geochemical correlations between the Birimian tholeiites and altered dikes. Near total depletions of K_2O and Ba in Stage 1 alteration contrast with significant increases during Stage 2 and 3 metasomatism. This is also true for Cr, Ni, V, Co and Cu, although to a lesser

degree. It is therefore possible that Stage 1 rocks represent source material for these elements which are subsequently enriched in Stage 2 and 3 altered rocks. Juxtapositioning of Stage 1 potential source-rocks with the altered and mineralized zones suggests that mass transfer may have taken place through lateral migration into the main structural conduits. However, this possibility is not consistent with evidence from geothermometry, mineral chemistry and stable isotopes presented in Chapters 8 and 9. In the later chapters, it will be demonstrated that initial alteration of the dikes was an early event, taking place at depth below the ore zones.

Stage 2 alteration is the first phase that can be directly related to the onset of gold mineralization. It resulted from an outward diffusion of hydrothermal fluids from the structural conduits into the host rock, thereby causing pervasive carbonation. However, gold deposition did not occur until Stage 3 alteration. The dikes contain abundant Fe (10% to 15% total Fe as Fe_2O_3, Table 5.1) which makes them potential chemical traps for alteration of Fe-bearing minerals to sulphides and arsenides through reaction with the hydrothermal fluids. At this stage, siderite ± ankerite reacted to form pyrite and arsenopyrite, and it is possible that previous carbonation of the rock either greatly facilitated, or was a prerequisite for these reactions to proceed.

The presence of large, tabular mafic dikes caused a significant competency contrast with the host sedimentary rocks. This is particularly true where highly carbonaceous and easily sheared sedimentary rocks are found adjacent to mafic rocks (cf. Figures 3.2, 3.3 and 3.4). This rheological contrast appears to have induced localized shearing, fracturing and development of permeable structures at and near the contacts of dikes with the host sedimentary rocks. The tectonic fracturing is complemented by a 9% volume loss during Stage 3 alteration.

This rock shrinkage during alteration is believed to contribute significantly to open-space fracturing in the rock, and hence to formation of the quartz-albite-ankerite stockwork veins that are related to introduction of gold, arsenopyrite and pyrite.

The whole-rock geochemical evidence for magmatic activity in an extensional environment is convincing. However, on geological grounds it is certain that these rocks are not mid-ocean ridge basalts even though they plot within the MORB field (Figure 5.2). On the basis of Rb-Sr, Pb-Pb and Sm-Nd isotopic analyses of igneous rocks, Taylor et al. (1992) state that the Birimian formed during the Early Proterozoic by differentiation from a depleted mantle source. Similar analyses were conducted by Abouchami et al. (1990) from Proterozoic terrains elsewhere in West Africa. They concluded that oceanic flood basalts, which later accreted to the continent as allochthonous terrains, are the most acceptable analogue for many of the Proterozoic basalts. However, it is not certain how applicable their work is to the Birimian of southwest Ghana. Crustal contamination and/or formation in a subduction-related (island-arc) environment have been suggested as possible reasons for the observed N-MORB least-mobile-element patterns (Leube et al., 1990). Relatively flat REE patterns (Luebe et al., 1990) and an epsilon Nd value of +2.0 (Taylor et al., 1988) further suggest that crustal contamination affected the Birimian tholeiites. This possible contamination is corroborated by evidence presented here for their syntectonic intrusion through the Ashanti Structural Belt, a major crustal lineament.

Geochemistry and Hydrothermal Alteration of Sedimentary Rocks

Geochemical analyses for whole-rock major oxide concentrations were

performed on fourteen samples of carbonaceous sedimentary rocks from the Bogosu and Prestea concessions. Carbonaceous turbidites and greywackes are the main host-rocks for the Bogosu and Prestea ores. However, on mineralogical grounds, only two distinct alteration zones were identified in the sedimentary rocks, which are least-altered host-rocks and sedimentary-rock ores. Consequently, only these two zones can be compared while testing for whole-rock geochemical additions and depletions caused by hydrothermal alteration.

The average volatile content of least-altered sedimentary rocks is quite high at between 5 and 12 wt% L.O.I. (Table 5.4), indicating that these rocks had already been affected by a hydrothermal / metamorphic event before the hydrothermal alteration related to gold mineralization took place. This is not obvious in hand specimen since the primary bedding, regional tectonic foliation described earlier and other rock textures are well preserved. Nevertheless, both mineralogy (Table 3.1) and geochemistry demonstrate significant hydration and carbonation of the host sedimentary rocks. This early alteration extends to at least 100 meters laterally away from the main ore zones, which is the maximum distance sampled normal to the plane of the mineralized structures. This appears to be an early, pervasive pre-mineralization alteration that also affected the intrusive rocks of the district. The origin of this early alteration is discussed in part in the previous section on geochemistry of mafic rocks, for which there is better control on the alteration history and geochemical data. However, it cannot be discussed fully until the evidence from mineral chemistry and stable isotopes is presented in the final chapters of this thesis.

The carbonaceous sedimentary rocks have moderate Fe contents with 4 to 8

wt% total Fe expressed as Fe_2O_3, accounted for mostly by siderite-rich carbonates with the remainder in disseminated pyrite and minor chlorite. Alumina contents are enriched with respect to source volcanic rocks, which is consistent with weathering of sedimentary rocks. MgO is consistently within the range of 2 to 3 wt% and MnO is negligible at ≤ 0.12 wt%. CaO, K_2O and Na_2O have variable concentrations that reflect both primary variations and metasomatic alteration (Table 5.4). Although there was some variation in the composition of these sedimentary rocks, the least-altered varieties and mineralized ores were averaged and plotted against each other on an isocon diagram. The solution is graphically depicted on Figure 5.6 with the isocon data and calculated changes in mass balance listed in Table 5.5.

Mass balance was calculated for the assumption of constant Al_2O_3, which was supported also by minimal changes in TiO_2, MnO and P_2O_5.

The equation for the Al_2O_3 isocon is;

$$C^A_{Al2O3} = 0.74\, C^O_{Al2O3}$$

where: C^A_{Al2O3} = concentration of Al_2O_3 in altered sample
C^O_{Al2O3} = concentration of Al_2O_3 in parent sample

and mass change is:

$$\Delta M = (1 \div 0.74 - 1) \times 100\%$$
$$= +34\%$$

The change in mass is quite high at about +34% for typical sedimentary rock-hosted ores (i.e. graphitic crush zones) and is accompanied by a minimal change in density of from 2.75 g/cm^3 for least-altered turbidites to 2.77 g/cm^3 for

graphitic crush zone ores (Table 5.7). The volume change was calculated by multiplying the mass change by the ratio of density measured before and after alteration, and is given by the following equation:

volume difference $\Delta V = [2.75 \div 2.77 \times 1.34 - 1] \times 100\%$

$= +33\%$

The reported values are average mass and volume changes for typical graphitic crush zone ores; however, they vary considerably depending on the amount of vein material present and the degree of silicification. The increases in mass and volume contrast with the depletions calculated for mafic dikes. However, only matrix material was considered in the dike calculations, whereas the whole sample (matrix and vein material) was analyzed for the sedimentary rocks. Thus, dike rock analyses yield more accurate estimates of compositional variations for most elements, but the sedimentary rock calculations give much better estimates of total mass and volume changes within the hydrothermal system.

A sample of highly silicified graphitiic crush zone ore from the Nankafa deposit (NK-204-9, Bogosu concession) was calculated to have mass and volume increases of about 88% and 91%, respectively. These large increases are caused by the introduction of quartz ± albite ± ankerite stockwork veining and pervasive silicification. Calculated increases in SiO_2 were +41% and +142% for typical graphitic crush zone ores and silicified ores, respectively. It is evident that an extensional environment must have been created in order to accommodate such large mass and volume increases.

The only significant elemental loss during alteration of sedimentary rocks

was for K (-39%), which was lost in the conversion of white micas to albite during the hydrothermal alteration associated with mineralization (Table 3.1). There is no change in MnO concentration during mineralization, which is further evidence for a lack of a direct genetic link between Mn and gold mineralization in Ghana. Major elemental gains in concentration are recorded for both Na_2O and CaO, which are incorporated into the structure of albite and ankerite, respectively, during metasomatism related to gold mineralization. Gains were also calculated for MgO (in ankerite) and volatiles (Δ L.O.I. = +55%).

A moderate increase in Fe_2O_3 is suggested by the data; however, this may be an artifact of the variability of sedimentary rock compositions. Overall there is little change in total Fe concentration during mineralization for both sedimentary rocks and dikes. This indicates that the amount of sulphide and arsenide minerals that formed during mineralization was restricted by the pre-existing Fe content of the host-rocks.

Chapter 6: Sulphide / Arsenide Paragenesis and Mineral Chemistry

Paragenesis of Sulphide and Arsenide Minerals

Sulphide / arsenide minerals are intimately associated with gold deposition throughout the Bogosu-Prestea region. They are particularly important since the majority of gold occurs within, or attached to, sulphide / arsenide grains. Consequently, documentation of their mode of occurrence and paragenesis is a valuable aide toward constraining some of the physical and chemical conditions during the evolution of the gold system, and is necessary to properly interpret geochemical data presented in the following chapters.

The least-altered sedimentary rocks and dikes contain the first recognizable generation of sulphides. They consist of minor disseminated pyrite that is often accompanied by trace amounts of chalcopyrite. The origin of this phase of mineralization cannot be traced since the host rocks have already been subjected to several stages of deformation, diagenesis and metamorphism / metasomatism.

However, what is most important to this study is the formation and subsequent transformation of sulphides associated more directly with the gold-producing event. The earliest sulphide mineral to form at the onset of hydrothermal activity associated with mineralization (early Stage 2 alteration) was pyrrhotite (Table 6.1). Generally, pyrrhotite precipitated along with chalcopyrite, and in some cases its formation may have been nucleated by pre-existing chalcopyrite and pyrite grains. Although present in many rock types, pyrrhotite is most common in the carbonaceous sedimentary rock ores at Prestea, where it is well preserved. Occasional examples of pyrrhotite-chalcopyrite-marcasite-pyrite intergrowths are preserved, although more often

SULPHIDE PARAGENESIS

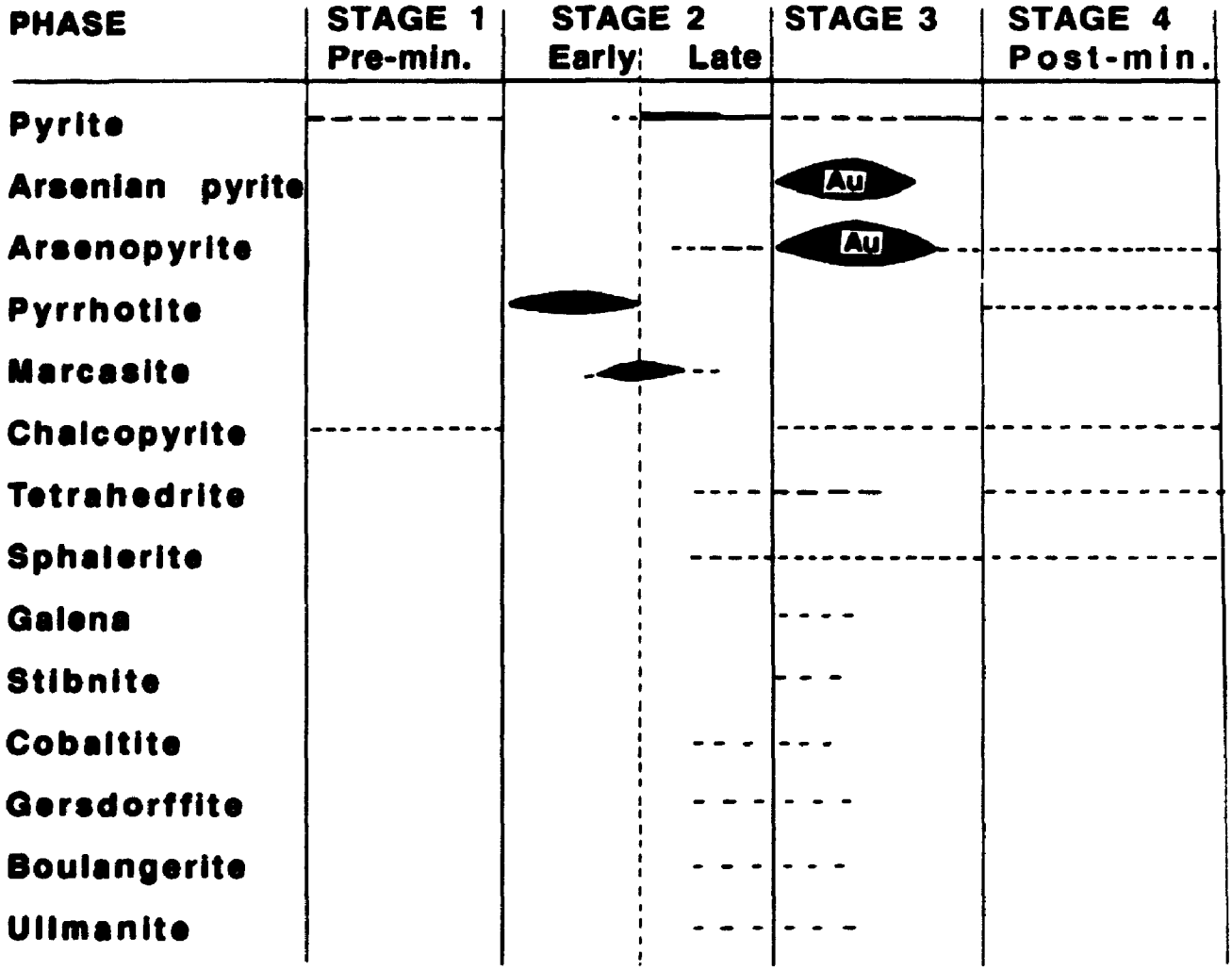

Table 6.1: The paragentic sequence for sulphide and arsenide minerals in Bogosu and Prestea ores and host-rocks.

STAGE 1: Early sulphide minerals that pre-date hydrothermal alteration related to mineral deposition.

STAGE 2: Sulphide minerals that precipitated from the gold-bearing hydrothermal fluids prior to gold deposition.

STAGE 3: Sulphide minerals that co-precipitated with gold.

STAGE 4: Sulphide minerals that formed after gold precipitation ceased.

only marcasite intergrown with pyrite remains. Often the early pyrrhotite is partially converted to marcasite and pyrite. Evidence for this sulphidation comes from the textural intergrowth of these minerals. Where pyrrhotite is no longer visible, its former presence is suggested by the relatively large, abundant (up to 32 modal percent) and random pore spaces in the product pyrite or marcasite (Plate 6.1A), as well as from random orientation of the product crystals, pyrite and marcasite (Murowchick, 1992). Based on textural observations it is not certain if marcasite and pyrite were simultaneously reprecipitated from pyrrhotite. However, almost all marcasite observed is in the process of alteration to pyrite. In some quartz-vein ores at Prestea there is good textural evidence for marcasite and/or pyrite alteration to vuggy arsenopyrite crystals. These were later rimmed by normal arsenopyrite, forming euhedral crystals with seive-textured cores (Plate 7.2A).

Apparently, the conversion of pyrrhotite to pyrite and marcasite was by a solution-precipitation mechanism rather than from sulphidation in the solid state, as is evident from the random product crystal orientations (Murowchick, 1990; Schoonen and Barnes, 1991a, 1991b). This process will proceed very efficiently at temperatures below 200°C to 250°C, where the solubility product of pyrite is six to ten orders of magnitude less than for pyrrhotite (Naumov et al., 1974). Hence, re-precipitation of pyrite will occur almost immediately upon dissolution of pyrrhotite when accompanied by a slight oxidation of the sulphide to polysulphide. If the pH is below 5, marcasite will form rather than pyrite (Murowchick and Barnes, 1986; Murowchick, 1992). The pyrrhotite and its conversion products described above are an early phase of mineralization, and have not been observed to contain gold.

An early generation of hydrothermal pyrite is associated with Stage 2

PLATE 6.1

EMP back-scattered electron images of polished sections from Bogosu and Prestea ores: Asp-arsenopyrite; Cpy-chalcopyrite; Po-pyrrhotite; Py-pyrite; Py-(As)-arsenian pyrite; Py-(s.t.)-pyrite seive-textured.

A. Compostional zoning in an arsenian pyrite grain from carbonated-dike ore from the Chujah deposit (sample C-11). The sieve-textured core is believed to be an alteration from pyrrhotite and marcasite. Numbers 11 to 13 are the locations of EMP analyses listed in Table 6.3.

B: Intergrown pyrite, acicular arsenopyrite and gold in a sample (P-30) of graphitic fissure ore from the Prestea mine.

C: Intergrown pyrite, arsenopyrite, chalcopyrite, and pyrrhotite from a sample (DM-11) of carbonated-dike ore from the Dumassie deposit. Abundant microscopic gold grains are believed to form after recrystallization of arsenian pyrite containing gold in solid-solution.

D: A compositionally zoned arsenopyrite grain containing microscopic gold grains. This sample (C-11) is from a carbonated-dike ore from the Chujah deposit, Bogosu concession.

E: Rythmic compositional zoning arsenian pyrite. This sample (P-2) is from the Main Reef quartz vein in the Prestea mine.

F: Rythmic compositional zoning in arsenian pyrite. Numbers 37 to 53 are the locations of EMP analyses listed in Table 6.3. This sample (P-19) is from a graphitic fissure ore adjacent to the Main Reef quartz vein in the Prestea mine.

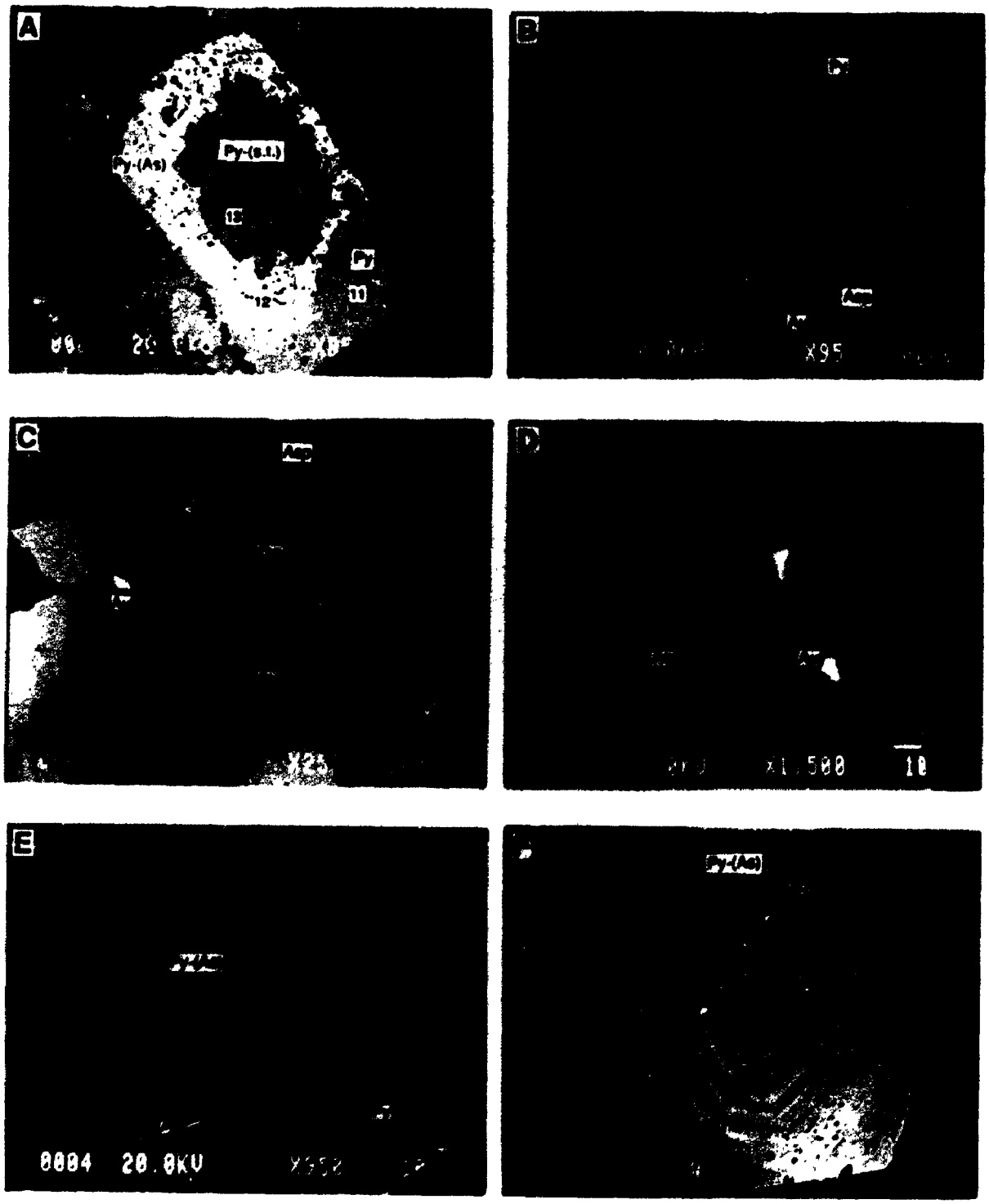
A
Py-(S.I.)
Py-(As)
B
X95
C
D
x1,500
10
E
0004 20.0KV

alteration and the carbonatization of country rocks adjacent to the gold lodes. This is most readily observed in the mafic dikes (Table 5.2) but is also true for the host sedimentary rocks. Back-scattered electron images taken with the electron microprobe show disseminated pyrite microcrystals dusting intergrowths of siderite and ankerite. Pyrite microcrystals are also found in the quartz-albite matrix as an alteration from former micron-size carbonates. This pyrite formed primarily as a result of sulphidation of siderite and to a lesser extent ankerite. With increased sulphidation, larger subhedral to euhedral grains of pyrite crystallized. Nucleation of the pyrite microcrystals occurred mostly along microfractures and vugs, where hydrothermal fluids were in direct contact with the carbonate. This stage of sulphide mineralization was accompanied by the addition of trace amounts of arsenopyrite, sphalerite, tetrahedrite and some rarer sulphides such as cobaltite and gersdorffite, attributable to the presence of cobalt and nickel in the mafic dikes. It is an interesting and important feature of these gold deposits that carbonation preceeded sulphidation, and that abundant sulphides do not occur in non-carbonate altered rocks. Indeed, carbonate alteration may be a necessary preliminary step prior to sulphide and gold mineralization in these types of deposits, rather than only a secondary aspect of wall-rock alteration. This is particularly important considering that the whole-rock geochemistry indicates that essentially no new iron was added to the system. The early sulphides discussed above do not contain gold.

The main sulphide mineralization event occurred along with Stage 3 alteration (Table 6.1). Abundant sulphides formed due to conversion of most of the remaining siderite to pyrite (1 to 15 modal% pyrite) and arsenopyrite (0.5 to 5 modal% arsenopyrite). Pyrite occurs in several textural variations from micron-sized, anhedral and euhedral grains to large (>1 mm) porphyroblastic

crystals. In sedimentary rock ores the pyrite porphyroblasts often contain inclusions of chalcopyrite, pyrrhotite and tetrahedrite; however, inclusions of minor sulphide phases are most common in carbonated dike ores. These ores also contain trace amounts of sphalerite, galena, stibnite, cobaltite, gersdorffite, ullmanite and boulangerite as inclusions in pyrite. In the Prestea ores, some larger grains of sphalerite, chalcopyrite and tetrahedrite occur as separate grains.

The main sulphidation event also produced abundant euhedral, acicular arsenopyrite crystals early in the Stage 3 alteration. Many arsenopyrites are 0.1 mm or less in size, and are often partly or completely enclosed by pyrite porphyroblasts (Plate 6.1B). The arsenopyrite grains are up to 1 mm in length at Bogosu, but coarser crystals up to 5 mm in length are more typical of Prestea ores.

In Bogosu ores pyrite always exceeds arsenopyrite in abundance, whereas in most Prestea ores, arsenopyrite predominates over pyrite. The formation of arsenopyrite occurred during an arsenic-rich phase in the evolution of the hydrothermal fluid which simultaneously crystallizated arsenian pyrite in porphyroblastic grains up to several millimeters in diameter. However, pyrite formation continued over a longer time interval as evidenced by the ophitic-like textures of arsenopyrite contained within pyrite.

Compositional Zoning of Arsenopyrite and Pyrite

The compostions of pyrite and arsenopyrite were determined by electron microprobe analyses using a JEOL JXA 8600 Superprobe at the University of Western Ontario. Variations in compostion were noted from different parts of

Table 6.2: Mineral chemistry of selected arsenopyrite grains (wt%).

Sample	Fe	As	S	Ni	Cu	Co	Sb	Au	Total	Comment
C-11-1	34.5	44.5	19.3	0.04	ND	0.32	0.03	0.00	98.7	
C-11-1	35.1	42.9	21.6	0.38	ND	0.15	0.00	0.02	100.1	
C-11-9	33.9	44.9	19.8	0.17	ND	0.80	0.05	0.00	99.5	
D-10-5	35.0	44.4	20.2	0.15	ND	0.03	0.00	0.00	99.8	
DM-3-4	33.2	45.3	20.9	0.02	0.03	0.01	0.01	0.02	99.4	
DM-11-6b	32.7	44.8	21.1	1.05	0.06	0.03	0.04	0.00	99.8	μ-xtal
DM-11-6c	31.9	45.1	20.9	0.23	0.00	0.01	0.10	0.00	98.2	μ-xtal
DM-11-7b	32.0	45.4	20.5	0.08	0.02	0.00	0.15	0.06	98.3	incl.
DM-11-7c	32.2	44.9	21.0	0.18	0.01	0.60	0.06	0.00	98.8	μ-xtal
DM-11-8	31.9	42.6	22.5	0.00	0.00	0.00	0.00	0.07	97.0	core
DM-11-8	32.9	46.1	20.3	0.07	0.01	0.11	0.02	0.00	99.5	margin
P-2-1	35.4	43.9	20.4	0.06	ND	0.00	0.00	0.00	99.7	
P-2-1	35.8	44.3	20.6	0.02	ND	0.00	0.01	0.04	100.7	
P-2-1	36.2	41.4	22.5	0.02	ND	0.03	0.00	0.02	100.2	
P-2-1	35.1	43.3	20.5	0.10	ND	0.16	ND	0.00	99.1	
P-19-7	34.7	44.7	20.3	0.12	ND	0.13	0.01	0.02	100.0	margin
P-19-7	35.8	41.7	22.5	0.02	ND	0.03	0.02	0.00	100.0	middle
P-19-7	35.5	44.5	20.5	0.00	ND	0.00	0.01	0.00	100.5	core
P-28D-5	33.2	43.8	22.2	0.01	0.02	0.04	0.00	0.05	99.3	
P-28D-5	32.0	47.2	19.6	0.04	0.01	1.08	0.08	0.05	100.1	margin
P-28D-5	35.7	42.1	23.2	0.01	0.00	0.00	0.03	0.00	100.9	
P-30-6a	32.4	43.3	20.8	0.97	0.00	0.02	0.00	0.00	97.5	
P-30-6b	35.8	43.3	22.3	0.01	0.00	0.00	0.00	0.03	101.4	alt. core
P-30-6b	35.1	47.4	19.9	0.12	0.00	0.11	0.00	0.07	102.8	margin

C = Chujah deposit, Bogosu; D, DM = Dumassie deposit, Bogosu; P = Prestea mine
Incl. = inclusion in pyrite; alt. = altered from pyrrhotite, marcasite and pyrite
μ-xtal = recrystallized microcrystal in pyrite

Table 6.3: Mineral chemistry of selected pyrite grains illustrated in the text (wt%).

Plate	#	Fe	As	S	Ni	Co	Au	Total
6.1 A	11	45.5	0.0	53.0	0.00	0.02	0.00	98.6
6.1 A	12	45.6	3.6	50.1	0.00	0.00	0.00	99.3
6.1 A	13	46.6	0.0	53.4	0.02	0.00	0.00	100.1
6.1 F	37	45.6	0.1	52.9	0.00	0.20	0.00	98.9
6.1 F	38	46.1	0.5	53.2	0.03	0.06	0.00	99.9
6.1 F	39	45.5	1.5	52.6	0.50	0.09	0.00	100.2
6.1 F	40	46.0	0.7	52.7	0.01	0.08	0.04	99.6
6.1 F	41	45.4	1.6	52.6	0.60	0.21	0.00	100.4
6.1 F	42	45.9	1.2	52.5	0.03	0.00	0.00	99.6
6.1 F	43	45.9	0.9	53.2	0.01	0.00	0.02	100.0
6.1 F	44	46.2	0.3	52.1	0.08	0.00	0.00	98.6
6.1 F	45	46.1	0.1	53.1	0.01	0.00	0.00	99.3
6.1 F	46	46.5	1.0	52.6	0.00	0.00	0.00	100.0
6.1 F	47	46.3	0.9	52.6	0.00	0.00	0.00	99.7
6.1 F	48	45.3	1.6	52.4	0.71	0.05	0.03	100.1
6.1 F	49	46.2	0.4	52.9	0.00	0.03	0.03	99.5
6.1 F	50	46.0	0.9	52.6	0.01	0.00	0.00	99.5
6.1 F	51	46.2	0.3	52.9	0.01	0.05	0.00	99.5
6.1 F	52	46.1	0.6	53.0	0.07	0.00	0.00	99.8
6.1 F	53	43.0	0.3	49.1	0.08	0.09	0.00	92.6
6.2 A	54	46.4	0.1	53.5	0.04	0.07	0.00	100.0
6.2 A	55	46.5	0.1	53.3	0.02	0.13	0.00	100.0
6.2 A	56	46.0	0.0	53.9	0.04	0.00	0.03	100.1
6.2 A	57	45.9	1.4	52.0	0.56	0.10	0.00	99.9

Plate number refers to illustrations in the text.
C = Chujah deposit, Bogosu; D = Dumassie deposit, Bogosu; P = Prestea mine
# = analysis number

the gold system and the results are listed in Tables 6.2 and 6.3. Arsenopyrite grains were found to be compositionally zoned, with arsenic contents ranging from 42 to 47 wt%. High As contents correlated with low S, and vice-versa. Compostional variations were detected also for minor amounts of Ni, Co and Sb; 0 to 1 wt% for Ni and Co and 0 to 0.4 wt% for Sb. Some typical compositional zoning patterns are illustrated in Figure 6.1.

Arsenic concentrations cluster around specific values, which are different for Bogosu and Prestea arsenopyrites. Furthermore, the range of averaged values is greater for Prestea ores (29.1 to 34.0 at% As) than Bogosu ores (30.7 to 32.7 at% As). The genetic significance of this compositional information will be discussed later in this section. Concentrations as low as 29 at% are found in arsenopyrites from Prestea, including some grains that have formed by alteration from pre-existing sulphides (Figure 6.1D). Simple zoning was detected in some Bogosu grains (Figure 6.1A) with low arsenic cores (30.7 ± 0.2 at% As) that carry gold, and higher arsenic (32.7 ± 0.7 at% As) outer rims that are barren of gold. Complex zoning is common, and some grains illustrate the apparent growth of arsenopyrite needles in response to differential stress. Arsenopyrite grains grew best in the plane of foliation, sub-perpendicular to the principal stress. Rythmic compositional zoning is oriented sub-parallel to the principal stress, such that crystal growth propagates from the grain tip in a direction of minimal stress. In the grain illustrated in Figure 6.1C and Plate 6.1D, growth has incorporated four arsenopyrite microcrystals, and a late outer rim surrounds a rythmically zoned core. This crystal contains 2 gold inclusions, which is an uncommon feature in arsenopyrite from Bogosu.

Compositional banding is more pronounced in pyrite than arsenopyrite from both the Bogosu and Prestea regions. Pyrite that crystalized during Stage 3

Figure 6.1: Compositional and textural zoning of arsenopyrite grains from Bogosu and Prestea ores.

A: Simple zoning of arsenopyrite crystals. The low-As cores of these grains are Au-rich.

B: Complex recrystallization of arsenian pyrite to form arsenopyrite and pyrrhotite microcrystals, and a mosaic of As-poor pyrite. The arsenian pyrite is Au-rich, but the arsenopyrite microcrystals are Au-poor. See also Plate 6.2B.

C: Rythmic growth banding of an acicular arsenopyrite crystal that has included several smaller grains. In this particular grain, Au in solid-solution was concentrated in the As-poor bands. See also Plate 6.1D.

D, E: Rythmic compositional zoning of arsenopyrite. The sieve-textured cores are believed to have altered progressively from pyrrhotite to marcasite to pyrite to arsenopyrite. The sieve-textured cores are Au-poor.

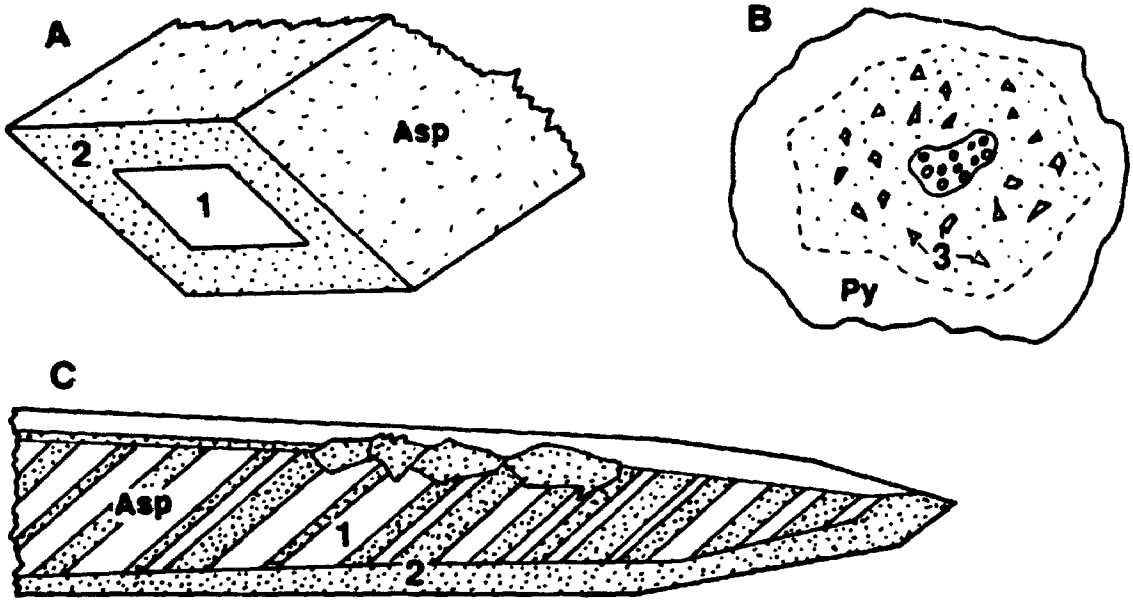

Compositional Zoning of Arsenopyrite from Bogosu (at% As)

1.) 30.7 ± .2, Au-Bearing, n=2
2.) 32.7 ± .7, No Au, n=6
3.) 32.5 ± .4, No Au, n=4, Recrystallized from arsenian pyrite

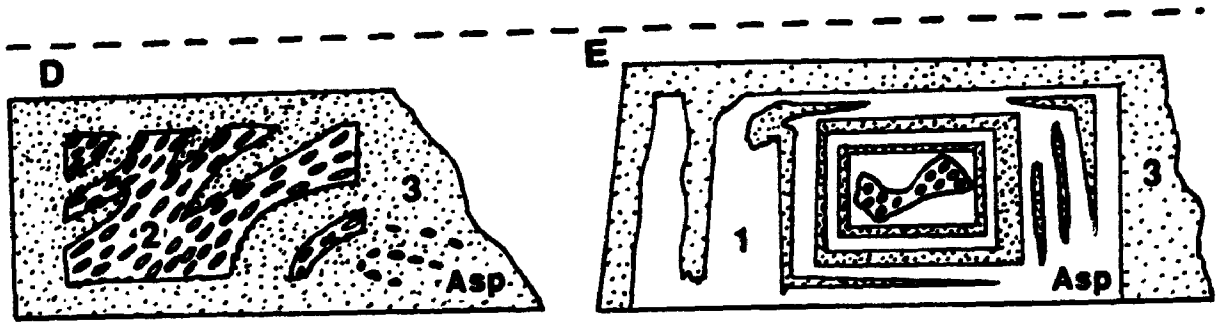

Compositional Zoning of Arsenopyrite from Prestea (at% As)

1.) 29.1 ± .1, Au-Bearing, n= 3
2.) 30.2 (Au-Bearing ?), n=1, Altered from Py-Marc
3.) 31.6 ± .3, Au-Bearing, n=7
34.0 ± .4, (Au-Bearing ?), n=2

alteration, the main gold depostional event, has As-rich growth bands that can contain in excess of 5 wt% As (cf. Fleet et al., 1989, MacLean, 1991). Minor zoning of nickel and cobalt is present also, with some grains containing up to 0.7 wt% and 0.2 wt%, respectively. However, some Prestea grains have bands containing up to 4.8 wt% Ni. These Ni and Co enrichments generally occur together in the same zones, and apparently reflect the mafic parentage of the rocks in which they occur.

Two main types of compositional-zoned microstructures were observed in pyrite grains. At Bogosu, pyrite grains often have a central core barren of arsenic. This is surrounded by a band of arsenian pyrite and then an outer rim of arsenic-poor pyrite (Plate 6.1A). This zoning pattern is similar to compositional variations in pyrites from the Agnico-Eagle and Fairview mines (Fleet et al., 1989). The central arsenic-barren core is often seive-textured, possibly suggesting an origin from pyrrhotite that converted to marcasite and finally pyrite. The core is an early sulphide remnant that pre-dated the main arsenian event and does not contain gold. The record of the arsenian sulphidation event is clearly preserved in the pyrite grain shown in Plate 6.1A as an arsenic-rich band that surrounds the core. On close inspection, this band displays rythmic compositional microzoning, however, the microzoning is too fine-scale to be clearly resolved and generally blends into a single arsenic-rich band. The final stage of pyrite growth was clearly non-arsenian, although minor arsenic values may persist in this zone. Some grains have an arsenic-rich core suggesting that nucleation and early growth of these grains occurred during the arsenian event . However, this may be and artifact of the grain orientation in the plane of the polished section.

At Prestea, rythmic zoning of arsenian pyrites is readily resolved by colour

staining (Fleet et al., 1989; Fleet and Chryssoulis, 1991) and back-scattered electron imaging, and can extend from the core to the rim of individual grains (e.g. Plates 6.1E and 6.1F, Table 6.3). Even aggregates and small veinlets of euhedral to subhedral pyrite crystals and microcrystals show complex zoning throughout (Plate 6.2A), demonstrating their formation entirely during the main arsenian event. At both Bogosu and Prestea, the arsenian event was concluded with the precipitation of rims of normal pyrite, with or without minor arsenic values.

Sulphide Recrystallization

Arsenopyrite and pyrrhotite microcrystals ranging from 1 to about 15 μm in length occur scattered within the most arsenic-rich portions of many arsenian pyrite grains at Bogosu. This feature is well illustrated in Plates 6.2B and 6.2C. A profile of As contents in this grain is illustrated in Figure 6.2. The core region consists of an early generation of As-poor pyrite, which is partly converted from earlier pyrrhotite ± marcasite (Plate 6.2D). This is rimmed and cemented together by pyrite with a high As content, and then overgrown by a large outer zone of arsenian pyrite to form a porphyroblastic grain about 1.5 mm in diameter. The As profile (Figure 6.2) indicates that initially the arsenian event produced pyrites with As contents of up to 5 wt%. This was followed by a gradual waning of the arsenian event until the last pyrite that precipitated formed As-poor rim.

Arsenopyrite microcrystals intermixed with pyrrhotite grains occur in a mosaic with As-poor pyrite within the arsenian zones of some pyrite grains (Plate 6.2C). The arsenic-free pyrite mosaic is distinguished from the core zone of pyrite grains by lack of pyrite crystal morphology and absence of seive-

PLATE 6.2

EMP back-scattered electron images of polished sections from Bogosu and Prestea ores: Asp-arsenopyrite; Po-pyrrhotite; Py-pyrite; Py-(As)-arsenian pyrite; Py-(s.t.)-pyrite seive-textured.

A: Compostional zoning in an aggregate of fine-grained pyrite crystals. Numbers 54 to 57 are the locations of EMP analyses listed in Table 6.3. This sample (P-19) is from a graphitic fissure ore adjacent to the Main Reef quartz vein in the Prestea mine.

B: Complex compositional zoning and recrystallization in a porphyroblastic arsenian pyrite grain. Early As-poor pyrite crystals were cemented together and overgrown by arsenian pyrite. The larger arsenopyrite crystals were included during growth of the pyrite grain. Microcrystals of pyrite, pyrrhotite and arsenopyrite formed during late recrystallization of the arsenian pyrite. Gold concentration by SIMS (ppm) is shown for 5 analyses. This sample (DM-11) is from a carbonated-dike ore from the Dumassie deposit, Bogosu concession.

C: Detail of the recrystallized portion of the arsenian pyrite crystal shown in Plate 6.2B. Arsenopyrite and pyrrhotite microcrystals and a mosaic of As-poor pyrite formed during recrystallization of arsenian pyrite. This sample (DM-11) is from a carbonated-dike ore from the Dumassie deposit, Bogosu concession.

D: Detail of the sieve-textured (s.t.) core of the arsenian pyrite crystal shown in Plate 6.2B. The pyrite core region is As-poor, and is believed to be an alteration from early pyrrhotite and marcasite. This sample (DM-11) is from a carbonated-dike ore from the Dumassie deposit, Bogosu concession.

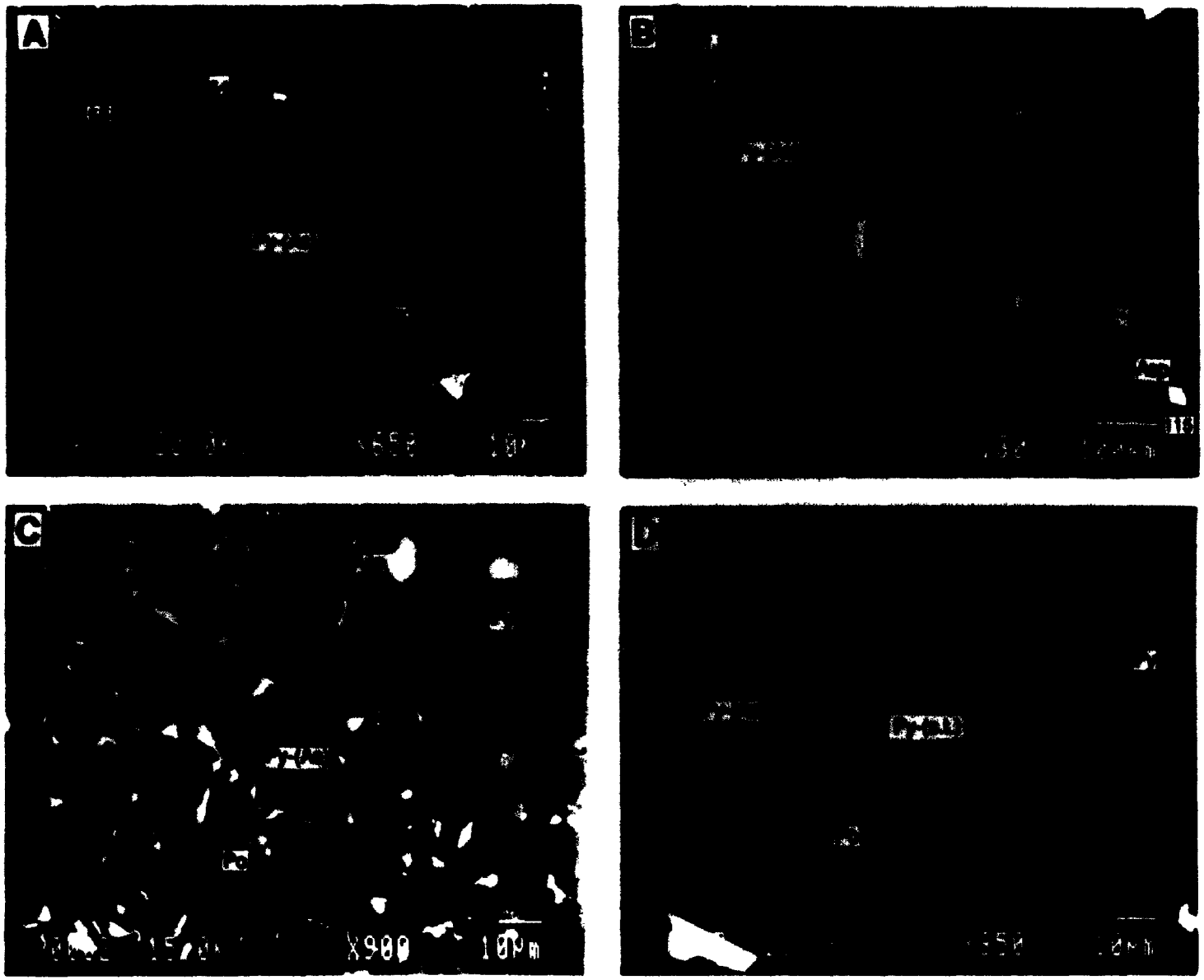
A
B
C
D
X900
10μm

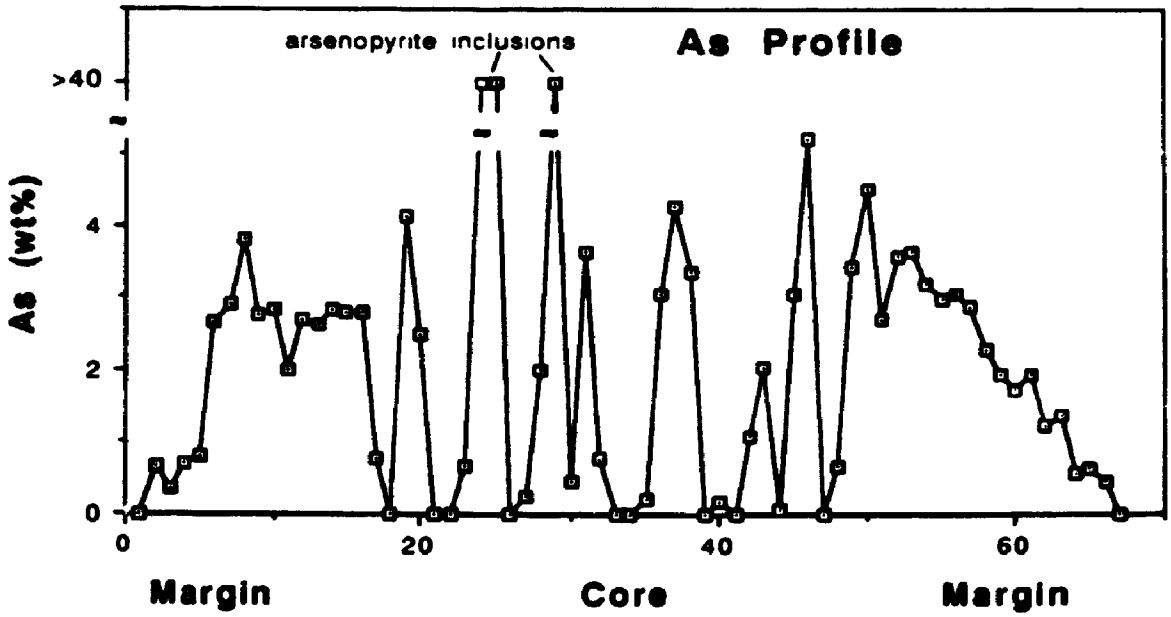

Figure 6.2: Variations in arsenic concentration (wt%) across the arsenian pyrite grain illustrated in Plate 6.2B.

texture. Electron microprobe results show that As substitutes for S in the crystal structure of pyrite (Tables 6.2). The stoichiometry for this recrystallization phenomenon is easily modelled, and a possible equation for the recrystallization of pyrite containing 10 at% substitution of S by As is given below:

$$10\ Fe(S_{0.9}\ As_{0.1})_2 + Fe \text{ --------> } 2FeAsS + 2FeS + 7FeS_2$$

Arsenian Pyrite ----------> Arsenopyrite + Pyrrhotite + Pyrite

This documentation of the crystallization of arsenopyrite and pyrrhotite from arsenian pyrite suggests that a similar phenomenon may take place with respect to some of the other sulphide phases that occur as micron-sized crystals within pyrite. In Bogosu and Prestea ores, these additional phases include tetrahedrite, chalcopyrite, sphalerite, stibnite, cobaltite, gersdorffite and boulangerite. This suggestion is supported by electron microprobe analyses which show that elevated levels of zinc, copper, antimony, cobalt, nickel, and lead do occur within specific growth zones of some pyrite and arsenopyrite grains (Tables 6.2 and 6.3). Consequently, the possibility of diffusion and/or recrystallization from a metastable pyrite or arsenopyrite solid solution exists. However, some of these grains are likely to be poikiloblastic inclusions that pre-date formation of pyrite poikiloblasts.

Arsenopyrite Geothermometry

Fleet et al. (1989) noted that compositional zoning of arsenian pyrite (and arsenopyrite) is indicative of subtle, but important, changes in the evolution of ore-forming systems. The significance of pH, fO_2 and fS_2 of gold and arsenic-

bearing hydrothermal fluids to the mineral chemistry of arsenopyrite is further discussed by Cathelineau et al. (1989). However, both studies were unable to draw specific conclusions on fluid conditions during gold deposition. In this study compositional zoning will be considered in the context of the paragenetic sequence and some experimentally determined parameters to derive information about gold deposition in the Bogosu and Prestea hydrothermal system.

Kretschmar and Scott (1976) demonstrated the temperature dependance of As concentration in arsenopyrite. From this information they developed a sliding scale geothermometer for arsenopyrite crystallization based on the arsenic content (at%) of arsenopyrite. This geothermometer can be used provided the fS_2 of the system is defined, usually by determining the compositions of coexisting sulphide phases. A number of investigators have used this geothermometer, but obtained anomalous results that could not be independantly verified (e.g. Kay and Strong, 1983; Sharp et al., 1985). Sharp et al. (1985) concluded that the arsenopyrite geothermometer is generally valid for ore deposits metamorphosed at greenschist to lower-amphibolite facies conditions, although the range of arsenopyrite compositions encountered even under these conditions leads to less than desirable results.

In this study the question of anomalous results and varying composition is addressed more carefully by analyzing the zoning characteristics and paragenetic relationships of the different types of arsenopyrite in the gold system. As previously demonstrated, apparently different generations of arsenopyrite do exist, even within a single grain and this association must be resolved before attempting to obtain meaningful results from arsenopyrite geothermometry.

In Bogosu ores, three main types of arsenopyrite were detected (Figure 6.1): 1) low-As core and growth bands that contain gold, 2) rims, grains and bands of higher-As content that do not contain gold, and 3) late microcrystals in arsenian pyrite that do not contain gold. At Prestea, arsenopyrite grains include (Figure 6.1): 1) alterations from pre-existing pyrite, marcasite or pyrrhotite, 2) main stage arsenopyrite crystallization with complex compositional zonation that alternates between high and low As concentrations, and 3) anomalously high As bands. Gold was detected by electron microprobe analyses in all types of arsenopyrite at Prestea. However, some of these results may be anomalous or spurious or due to late remobilization of gold, and further analyses are required to satisfactorily resolve this question. The important gold-bearing arsenopyrite varieties are those associated with the main stage of arsenopyrite crystallization.

Arsenopyrite at Bogosu and Prestea coexists with pyrite and in some cases with both pyrite and pyrrhotite. These coexisting phases adequately define the fS_2 in the system (Kretschmar and Scott, 1976; Sharp et al., 1985), permitting temperatures of formation to be determined by plotting As content in arsenopyrite (at%) on the isopleth diagram of Sharp et al. (1985) (Figure 6.3). The fS_2 is approximately fixed within the pyrite field, and precisely defined along the pyrite-pyrrhotite join so that independant temperatures can be read directly.

Gold-bearing arsenopyrite at Prestea has average contents that fall within the range of 29.1 ± 0.1 to 31.6 ± 0.3 at% As. This corresponds to a range of crystallization temperatures from approximately 410°C to less than 300°C. For temperatures below 300°C anomalous and inconsistent results can occur such that the lower limit of mineralization temperatures cannot be independantly determined by this method (Kretschmar and Scott, 1976; Sharp et al., 1985).

THE ARSENOPYRITE GEOTHERMOMETER

(Kretschmar and Scott, 1976; Sharp et al., 1985)

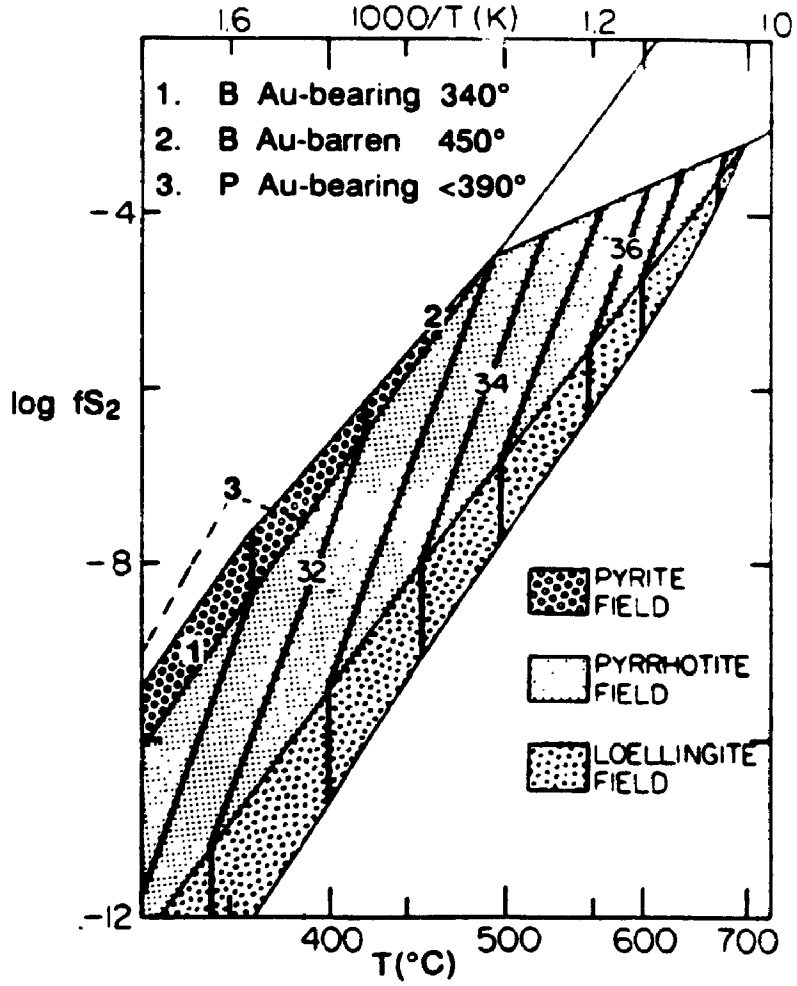

Figure 6.3: Arsenopyrite formation temperatures derived by plotting arsenic contents (at%) for typical Bogosu and Prestea arsenopyrite grains on the arsenopyrite geothermometer of Kretschmar and Scott (1976) and Sharp et al. (1985): B = Bogosu, P = Prestea.

Several EMP analyses show growth bands with high As contents averaging 33.9 at% that yield anomalously high temperatures. The high temperature values may be spurious, but they are consistent with occasional anomalously high temperatures obtained by carbonate geothermometry (Chapter 8).

The temperatures obtained from Bogosu arsenopyrite appear to follow a simple pattern. Analyses from As-poor core and growth bands that are gold-bearing have average As contents of 30.7 ± 0.2 at%, which give a temperature of 340 ± 15°C. As-rich bands that do not contain gold average 32.7 ± 0.7 at% As and give a temperature of 450°C ± 60°C. A slightly lower temperature of about 435 ± 35°C is obtained for the recrystallization of arsenopyrite crystals within arsenian pyrite.

Compositional banding in both pyrite and arsenopyrite is generally better developed in Prestea ores than at Bogosu. This is believed to be the result of hydrothermal fluids entering the system from the deeper portions of the gold system that are now exposed at Prestea. The fluids probably passed through the system in pulses and/or intermittently mixed with a second fluid (cf. Fleet et al., 1989). As the fluids migrated upwards in the system they would tend to diffuse and homogenize such that variations in the compositions of precipitating minerals would be less pronounced. This is evidenced by the characteristic broad zone of arsenian pyrite within pyrite porpyroblasts preserved in the upper levels at Bogosu (Plates 6.1A, 6.2B), while rythmic banding is more distinct in the deeper levels.

Summary of Sulphide Paragenesis

The earliest sulphides occur ubiquitously as minor amounts of finely disseminated anhedral to euhedral pyrite with trace amounts of chalcopyrite in least-altered rocks. The origin of this pyrite may be as early as diagenesis or as late as prograde metamorphism; however, the timing of this event cannot be constrained with the data currently available. The earliest hydrothermal sulphide assemblage related to the onset of mineralization, or Stage 2 alteration, is pyrrhotite that later underwent solution-precipitation conversion to marcasite and pyrite. This points to an increase in both pH and oxidation state, and suggests that temperatures in the system during this phase of alteration were below 200°C to 250°C. The almost complete conversion of pyrrhotite to marcasite and pyrite in Bogosu rocks compared to partial conversion at Prestea is consistent with the carbonate geothermometry (Chapter 8), and indicates lower ambient country rock temperatures at Bogosu than at Prestea during mineralization.

The inversion of pyrrhotite may have been coeval with sulphidation of some siderite ± ankerite to finely disseminated pyrite microcrystals in carbonates during Stage 2 alteration. Trace amounts of arsenopyrite, tetrahedrite, sphalerite and cobalt-nickel arsenides and sulphides formed during later Stage 2 and early Stage 3 alteration. The main hydrothermal gold event, Stage 3, produced abundant coeval arsenopyrite and arsenian pyrite at temperatures ranging from < 300°C to > 450 °C. Gold-bearing arsenopyrites precipitated in the range of < 300°C to 410°C. However, the preferred temperature determination for gold-bearing arsenopyrite is 340 ± 15°C, obtained at Bogosu from the core of some grains with simple zoning. The higher temperatures (± 450°C) are thought to represent pulses of anomalously high-temperature fluid

during mineralization. Arsenian pyrite gradually became less As-rich, and precipitated over a longer time interval than the arsenopyrite. Stage 3 sulphides also include trace amounts of tetrahedrite, sphalerite, chalcopyrite, galena, stibnite, cobaltite, gersdorffite and boulangerite. Late sulphidation of ankerite to pyrite is visible in many veins. Finally, post-mineralization elemental diffusion and recrystallization within metastable arsenian pyrite led to the formation of arsenopyrite, pyrrhotite and possibly other sulphide microcrystal inclusions observed in pyrite at Bogosu.

Chapter 7: Mineral Chemistry of Gold and Paragenesis

Many variations in the mode of occurrence of gold are observed throughout the Bogosu and Prestea area. When considered in the context of the overall hydrothermal system, these variations give clues to and place constraints on some of the mechanisms of gold precipitation and re-distribution within a single large gold system.

Gold is intimately associated with sulphide mineralization throughout the Bogosu and Prestea gold system, although this association is not immediately obvious in all cases. For example, gold produced to date at the Prestea mine has been mainly from free-milling gold in quartz vein lodes, while at Bogosu, past production (1934 to 1954) was entirely from near-surface oxidized ores. However, closer examination reveals a common heritage for all ore types.

Microscopic Gold

Veinlets of native gold occur within Prestea quartz-vein lodes; however, the vast majority of free-milling gold occurs as < 100 μm size grains along fine ribbons of wall-rock within the quartz, and in adjacent fissure ores. These wall-rock partings also are the locus of abundant fine-grained sulphides that are often intimately associated with the gold (e.g., Plates 7.1A, 7.1B, 7.1C and 7.1D). Gold most commonly is associated with pyrite and/or arsenopyrite, or it occurs as free grains in the quartz-albite-ankerite gangue along the wall-rock partings. Occasionally it may be enclosed within, or at and near the margins of chalcopyrite and sphalerite grains. In the mineralized sedimentary rocks and graphitic fissure zones gold occurs as 1 to 50 μm size inclusions within pyrite and/or arsenopyrite, and to a lesser extent within gangue minerals. Generally,

PLATE 7.1

EMP back-scattered electron image of polished sections from Prestea ores: Alb-albite; Asp-arsenopyrite; Cpy-chalcopyrite; Py-pyrite; Qtz-quartz; Sph-sphalerite; Tet-tetrahedrite.

A: Abundant gold with sphalerite and tetrahedrite, included in an irregular grain of chalcopyrite. This sample (P-2) is from the Main Reef quartz vein in the Prestea mine.

B: Gold grains associated with sphalerite. This sample (P-2) is from the Main Reef quartz vein in the Prestea mine.

C: Gold in quartz associated with pyrite, sphalerite, chalcopyrite and tetrahedrite. This sample (P-2) is from the Main Reef quartz vein in the Prestea mine.

D: Gold as inclusions within, and at the grain boundaries of, pyrite and arsenopyrite. This is the most common form of gold-sulphide association in Prestea and Bogosu ores. This sample (P-30) is from carbonaceous fissure-ore adjacent the Main Reef quartz vein in the Prestea mine.

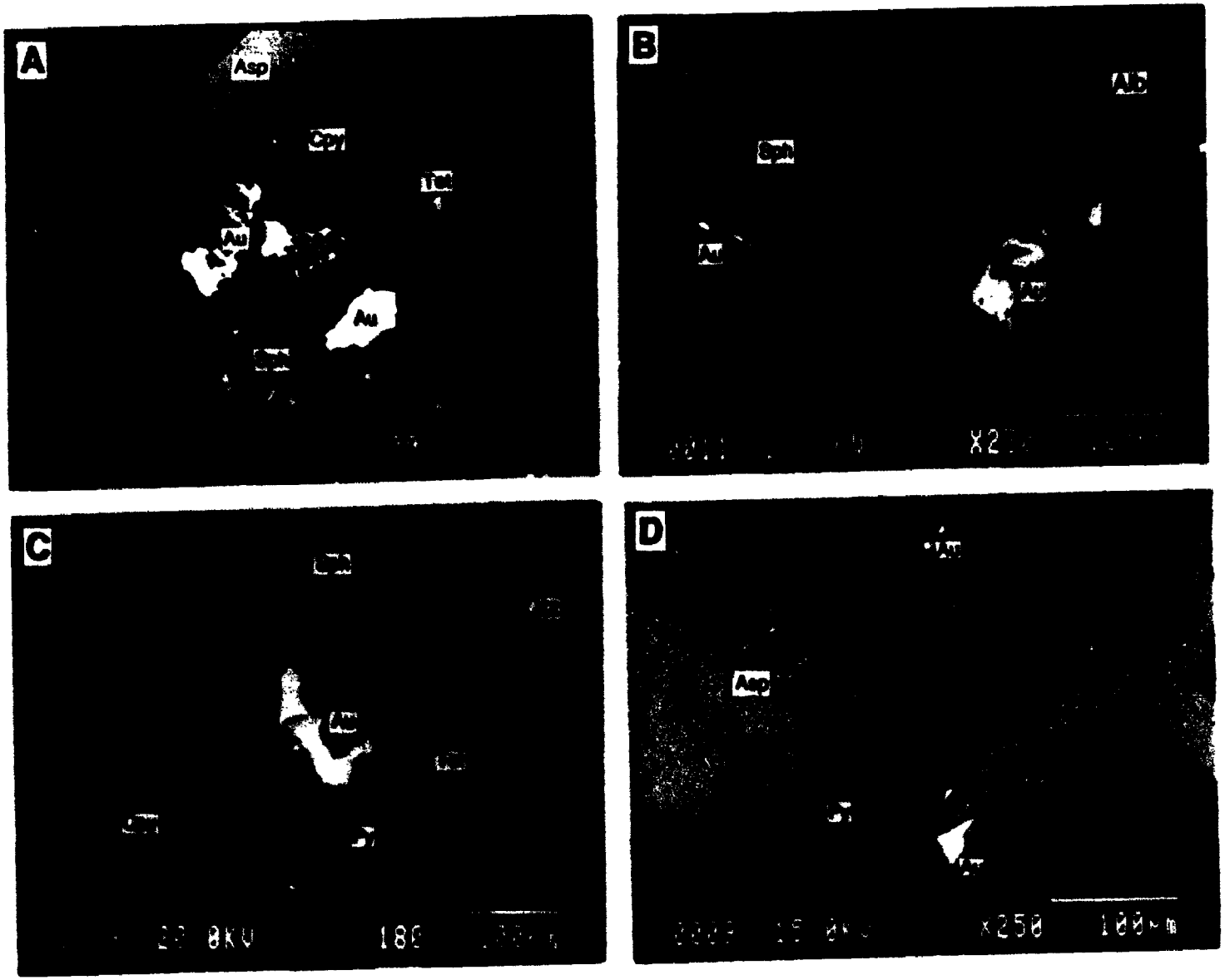
A
Asp
Au
Au
B
Au
X2
C
0KV
D
Asp
x250
100

microscopic inclusions of gold in the sulphides are found within voids and fractures, or along grain boundaries between adjoining sulphide minerals (Plates 7.1D, 7.2A and 7.2B). In mineralized dikes, gold almost exclusively is restricted to inclusions within arsenopyrite and pyrite.

In all types of ores at Bogosu, gold is restricted mostly to microscopic inclusions within pyrite. Individual grains range from < 1 μm to a maximum observed size of 35 μm (Plate 6.1C). Occasionally, small grains are seen within arsenopyrite crystals or in gangue minerals (Plates 6.1D and 7.2C). Consequently, the ores at Bogosu are highly refractory unless oxidized by surface weathering.

Forty-two polished thin sections of representative Bogosu and Prestea ores were systematically scanned visually using reflected light microscopy. Thirty of the 42 slides contained detectable microscopic gold ranging from 0.5 to 92 μm in longest dimension. Individual sections contained from none to 110 grains of identifiable gold for a total of 563 grains that were counted and categorized according to size and distribution. The results are listed in Table 7.1 which shows the approximate distribution of microscopic gold in the ores.

At Bogosu, 90% of the gold is directly associated with pyrite and arsenopyrite, with the remaining 10% interstitial to quartz, albite and carbonate gangue (Table 7.1). Approximately 89% of the sulphide-associated gold occurrs with pyrite (Plates 6.1C and 7.2B). Most of the sulphide-associated gold is enclosed within voids and fractures (95%), while the remainder is found along grain margins. The recorded size range of gold particles at Bogosu was 0.5 to 35 μm, with an average grain size of about 7 μm (longest dimension). Gold is coarser grained in the Prestea ores. The recorded size range of

PLATE 7.2

EMP back-scattered electron image of polished sections from Prestea and Bogosu ores: Alb-albite; Ank-ankerite; Asp-arsenopyrite; Cpy-chalcopyrite; Py-pyrite; Qtz-quartz; Rut-rutile; Sid-siderite; Sph-sphalerite; Stib-stibnite;
(s.t.)-seive-texture; Tet-tetrahedrite.

A: Abundant gold particles within the sieve-texture core of an arsenopyrite grain. Note also the accumulation of gold along fractures. The sieve-textured core is thought to result from the alteration of pyrite and marcasite that originally inverted from primary pyrrhotite. This sample (P-9) is from the Main Reef quartz vein in the Prestea mine.

B: Gold, arsenopyrite, tetrahedrite and stibnite inclusions in arsenian pyrite. This sample (DM-6) is from a carbonated dike ore in the Dumassie deposit, Bogosu concession.

C: Gold grain in albite, ankerite and siderite gangue. This sample (DM-3) is from a graphitic "crush zone" ore in the Dumassie deposit.

D: Gold associated with siderite, quartz and rutile. Minor sphalerite occurs along a fracture in the siderite. This sample (P-35) is from a mineralized carbonaceous phyllite in the Prestea mine.

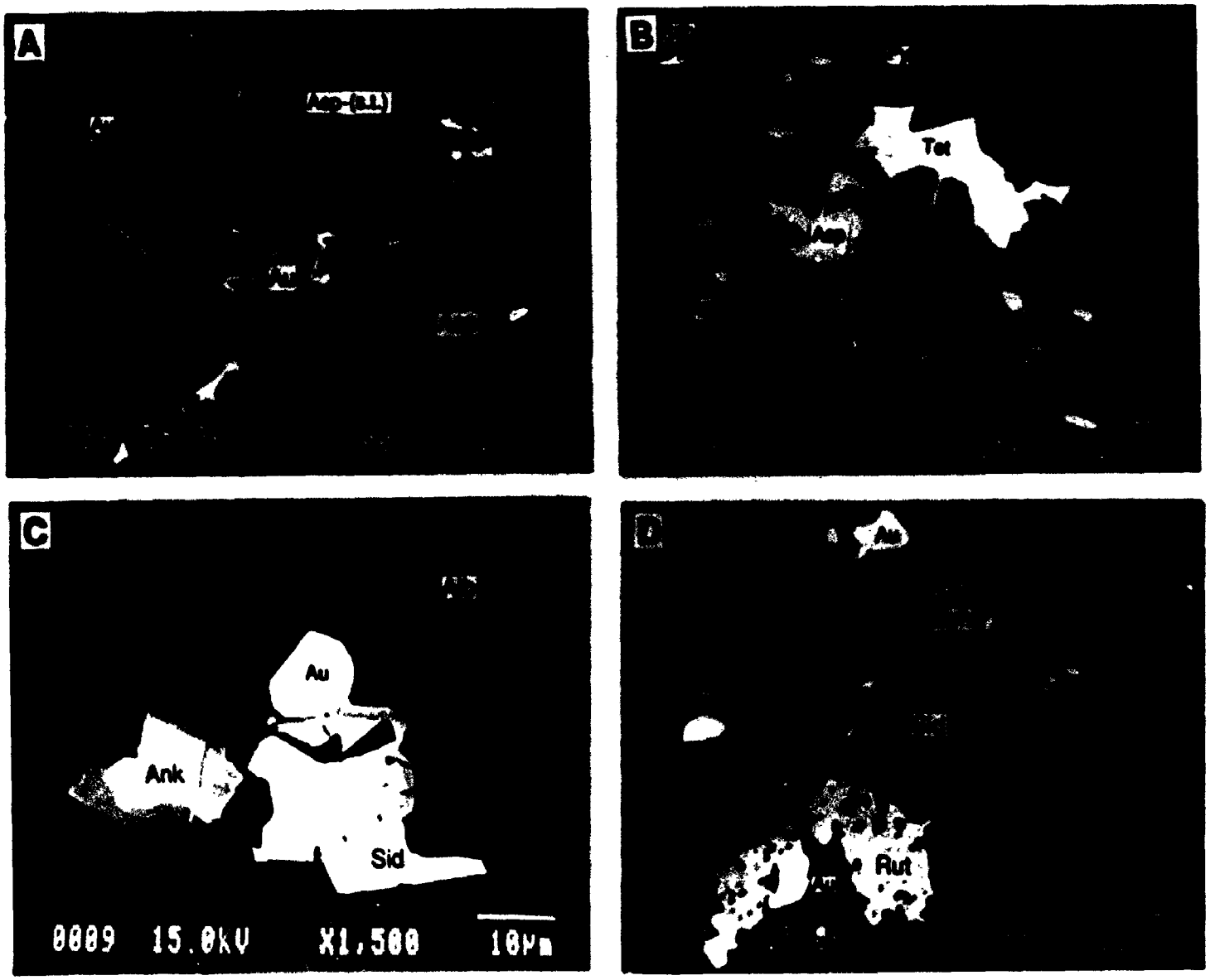
A
B
Tet
C
Au
Ank
Sid
0009 15.0kV X1,500 10µm
D
Au
Rut

Table 7.1: Summary of microscopic gold distribution in Bogosu and Prestea ores.

Polished thin sections surveyed optically for gold distribution = 42
Polished thin sections containing detectable microscopic gold = 30
Size range of gold particles identified = 0.5 to 100 μm (maximum dimension). Total number of microscopic gold grains counted = 563

Total Gold Distribution

In Sulphides	In Gangue	Locality
90%	10%	Bogosu
67%	33%	Prestea

Sulphide-associated Gold Distribution

In Pyrite	In Arsenopyrite	In Cpy, Sph etc.	Locality
89%	11%	0	Bogosu
31%	49%	20%	Prestea

Sulphide-associated Gold Distribution

In Voids and Fractures Within Grains	At Grain Margins	Locality
95%	5%	Bogosu
77.5%	22.5%	Prestea

Gold Size Distribution

Size Range	Average Grain Size	Locality
0.5 to 35 μm	7.0 μm	Bogosu
0.5 to 92 μm	8.0 μm	Prestea

microscopic gold particles less than 100 μm, was from 0.5 to 92 μm, with an average grain size of 8 μm. In the two dimensions of a polished section, only 67% of the Prestea gold is directly in contact with sulphide grains while the remaining 33% is interstitial to quartz, albite and carbonate gangue minerals (Plate 7.2D). Fifty percent of the recorded sulphide-associated gold occurs with arsenopyrite, 31% with pyrite and 19% with other sulphides such as chalcopyrite, sphalerite and, rarely, in tetrahedrite or pyrrhotite (Plates 7.1A, 7.1B, 7.1D and 7.2A). Seventy eight percent of this gold is in voids and fractures within sulphide grains while the remaining 22% occurs at grain margins. Much of the observed arsenopyrite-hosted gold from Prestea occurs as anhedral inclusions in the spongy seive-textured core of grains (Plate 7.2A). These spongy core areas result from conversion and subsequent alteration of earlier sulphides and apparently were good traps for the accumulation of gold particles.

Gold Mineral Chemistry

Microprobe analyses of 27 gold grains from the main ore types at Bogosu and Prestea reveal that gold is silver-bearing. However, Au / Ag ratios vary significantly between ore types and mining districts. Measured Ag concentrations in gold ranged from 1.2 to 7.6 wt% at Bogosu, and 7.6 to 21.3 wt% at Prestea. The average ratio of Au / Ag at Bogosu and Prestea is 23 : 1 and 5 : 1, respectively (Tables 7.1 and 7.2). Highest Ag values were observed in gold from the sedimentary-rock hosted ores and quartz-vein ores, while gold from the mineralized dikes has the lowest Ag content. The average Ag concentration is 3.3 and 6.6 wt% for analysed gold grains in Bogosu dikes ores and graphitic crush zone ores, respectively. At Prestea, gold in dikes average 11.5 wt% Ag, while higher concentrations averaging 18.5 wt% Ag occur in

Table 7.2: Gold mineral chemistry (wt%).

Sample	#	Au	Ag	Hg	Cu	Total	Area	Ore type
C-11	1	91.7	2.9	1.1	0.1	95.8	Bogosu	CDO
C-11	2	94.2	3.7	1.1	0.3	99.2	Bogosu	CDO
C-11	3	91.0	1.2	0.5	0.2	92.9	Bogosu	CDO
C-11	4	93.8	2.9	1.1	0.1	98.0	Bogosu	CDO
DM-3	5	88.1	7.5	0.5	0.1	96.2	Bogosu	GCZ
DM-3	6	91.2	6.4	0.5	0.1	98.1	Bogosu	GCZ
DM-3	7	88.2	7.6	0.6	0.1	96.4	Bogosu	GCZ
DM-11	8	95.4	3.7	0.1	0.0	99.2	Bogosu	CDO
DM-11	9	95.7	2.7	0.2	0.1	98.7	Bogosu	CDO
DM-11	10	89.4	2.6	0.1	0.1	92.2	Bogosu	CDO
DM-11	11	93.6	3.4	0.1	0.0	97.2	Bogosu	CDO
DM-11	12	94.8	3.2	0.1	0.0	98.1	Bogosu	CDO
DM-11	13	94.4	4.3	0.0	0.1	98.7	Bogosu	CDO
D-10	14	93.4	4.8	0.8	0.3	99.3	Bogosu	GCZ
P-28	15	86.3	11.0	0.0	0.0	97.2	Prestea	CDO
P-28	16	87.2	11.8	0.1	0.0	99.1	Prestea	CDO
P-28	17	85.1	11.7	0.0	0.5	97.3	Prestea	CDO
P-2	18	69.9	20.6	0.4	0.1	91.0	Prestea	QVO
P-2	19	73.4	21.1	0.3	0.0	94.8	Prestea	QVO
P-2	20	74.4	19.8	0.5	0.3	95.1	Prestea	QVO
P-2	21	77.4	17.3	0.3	0.0	95.1	Prestea	QVO
P-2	22	77.0	21.3	0.5	0.1	98.8	Prestea	QVO
P-30	23	73.9	18.4	0.4	0.0	92.8	Prestea	GFO
P-30	24	73.8	20.5	0.4	0.0	94.7	Prestea	GFO
P-30	25	76.6	20.3	0.5	0.0	97.5	Prestea	GFO
P-19	26	90.0	7.6	0.5	0.1	98.2	Prestea	GFO

CDO = carbonated dike ore, GCZ = graphitic crush zone ore
GFO = graphitic fissure ore, QVO = quartz vein ore
# = analysis number

gold grains from quartz lodes and sedimentary-rock hosted ores (Figure 7.1). Copper concentrations in gold grains are similar for both areas, averaging about 0.1 wt%. However, the average Hg concentration in gold grains from the Bogosu ores is moderately higher (0.5 wt% Hg) compared to the Prestea ores, which average about 0.3 wt% Hg (Figure 7.2).

Silver-Bearing and Gold-Bearing Tetrahedrite

Trace amounts of tetrahedrite containing Ag and Au were identified in a number of samples of Bogosu and Prestea ores. Most often tetrahedrite occurs as inclusions within pyrite or chalcopyrite, and as previously mentioned some grains may be the result of recrystallization of metals previously held in solid solution (Plates 7.1A and 7.2B). However, tetrahedrite was found also in minor quantities as separate grains interspersed with other sulphides in the ores.

Eighteen grains of tetrahedrite from Bogosu and Prestea ores were analyzed by electron microprobe (Table 7.3). There was no appreciable difference in composition between grains that occurred as inclusions and those that occurred as separate grains. One tetrahedrite grain contained a microscopic inclusion of gold. However, all grains contained minor Au values ranging from 0.1 to 0.5 wt% Au at Prestea, and from 0.0 to 0.3 wt% Au at Bogosu.

Tetrahedrite grains from Prestea are considerably enriched in Ag (up to 17.4 wt% Ag), but also show higher Sb and Au values. The maximum recorded Ag content of Bogosu tetrahedrite was only 0.4 wt%; however, tetrahedrite from Bogosu has notably higher S, As and Cu values. When plotted on an As/(As + Sb) vs Ag/(Ag + Cu) diagram (Figure 7.3), the analyses show a distinct bi-modal compositional distribution. Those grains which originated

Table 7.3: Tetrahedrite mineral chemistry (wt%).

Sample*	#	Au	Ag	S	As	Cu	Zn	Fe	Sb	Pb	Total	Area	Ore type
DM-3	1	0.2	0.2	24.6	3.2	38.3	2.6	5.0	24.6	0.0	98.6	Bogosu	GCZ
DM-3	2	0.1	0.2	23.9	3.1	37.6	2.8	4.0	24.3	0.0	96.0	Bogosu	GCZ
DM-3	3	0.0	0.3	29.2	2.1	29.6	2.6	13.4	19.6	0.0	96.8	Bogosu	GCZ
DM-3	4	0.0	0.0	27.5	0.3	41.2	0.0	2.7	26.4	0.0	98.0	Bogosu	GCZ
DM-3	5	0.1	0.2	23.8	3.6	36.8	3.1	6.3	23.7	0.0	97.5	Bogosu	GCZ
DM-11	6	0.1	0.0	29.1	3.2	41.1	0.1	3.1	21.6	0.1	98.3	Bogosu	CDO
DM-11	6	0.1	0.0	29.1	3.9	42.6	0.0	1.7	21.3	0.1	98.8	Bogosu	CDO
DM-11	7	0.2	0.0	25.0	4.5	38.5	3.8	4.1	22.7	0.0	98.9	Bogosu	CDO
DM-11	8	0.3	0.1	24.5	1.1	38.0	6.8	1.6	27.3	0.0	99.6	Bogosu	CDO
DM-11	9	0.3	0.4	24.0	0.5	36.7	3.1	5.7	27.9	0.0	98.4	Bogosu	CDO
DM-11	9	0.0	0.4	24.1	0.6	36.3	2.9	5.7	27.4	0.0	97.4	Bogosu	CDO
P-2	10	0.3	17.4	21.9	0.3	24.9	4.0	3.2	27.0	0.0	99.0	Prestea	QVO
P-2	11	0.1	9.4	22.5	1.3	30.5	3.2	3.4	26.2	0.0	96.5	Prestea	QVO
P-2	12	0.3	10.5	22.3	0.4	29.3	3.5	4.1	27.5	0.0	97.9	Prestea	QVO
P-2	13	0.5	17.2	21.7	0.4	25.4	2.8	4.9	26.7	0.0	99.6	Prestea	QVO
P-2	14	0.2	8.2	23.2	0.4	30.9	3.0	6.5	25.3	0.0	97.6	Prestea	QVO
P-2	15	0.2	3.1	22.8	0.8	35.1	3.1	3.5	27.7	0.0	96.3	Prestea	QVO
P-2	16	0.3	17.1	21.8	0.8	24.6	2.5	3.9	26.1	0.0	97.1	Prestea	QVO
Tetrahedrite		0.0	0.1	25.1	0.1	42.5	0.0	3.3	29.3	0.0	100.4	NA	standard
Tetrahedrite		0.1	0.1	24.5	0.1	42.5	0.0	3.4	29.2	0.0	99.7	NA	standard

CDO = carbonated dike ore, GCZ = graphitic crush zone ore, QVO = quartz vein ore

= analysis number

* = see appendix 9.2 for sample description

Figure 7.1: Gold and Ag contents of gold grains from Bogosu and Prestea ores. Both graphitic fissure ores and and crack-seal quartz vein ores are associated with sedimentary rocks and have similar geochemical signatures. Note that both host-rock and depth of mineralization influence the Au to Ag ratios, with higher Ag contents in sedimentary rocks and in the deeper ores of Prestea.

Figure 7.2: Mercury content of gold grains from Bogosu and Prestea ores. Increased Hg contents occur in the higher-level ores of the Bogosu concession.

Legend for Figures 7.1 and 7.2

B CDO = Bogosu carbonated dike ore

B GCZ = Bogosu graphitic "crush zone" ore

P CDO = Prestea carbonated dike ore

P QVO = Prestea quartz vein ore

P GFO = Prestea graphitic fissure ore

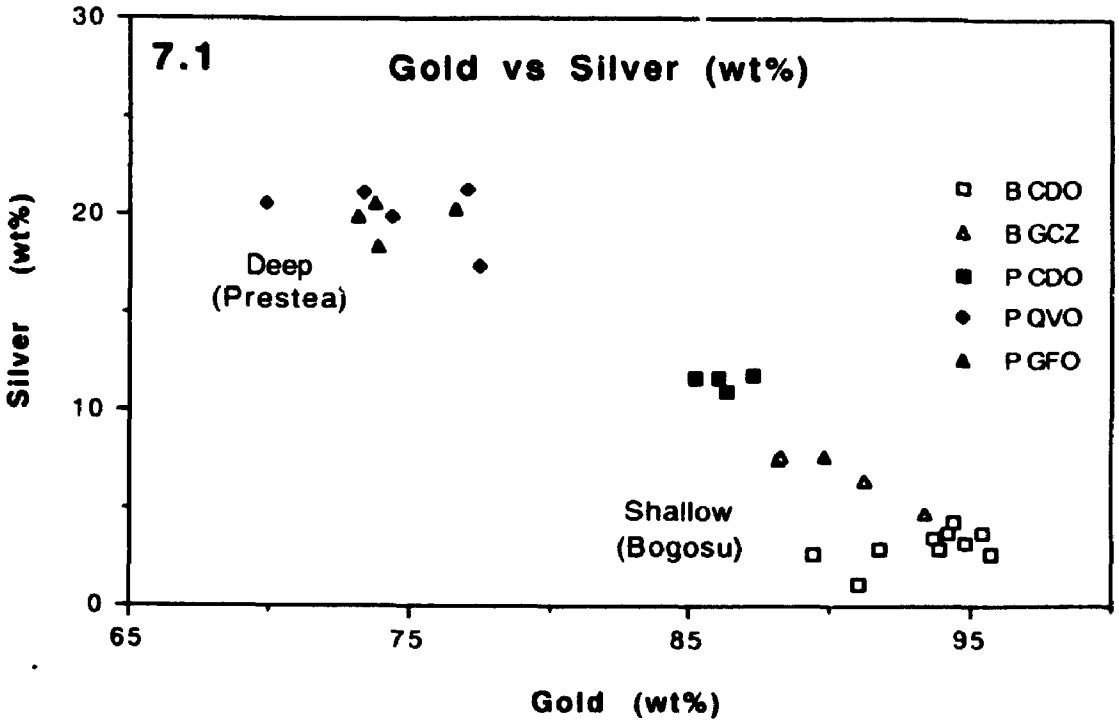
7.1
Gold vs Silver (wt%)
Silver (wt%)
Gold (wt%)
Deep
(Prestea)
Shallow
(Bogosu)
B CDO
B GCZ
P CDO
P QVO
P GFO
30
20
10
0
65
75
85
95

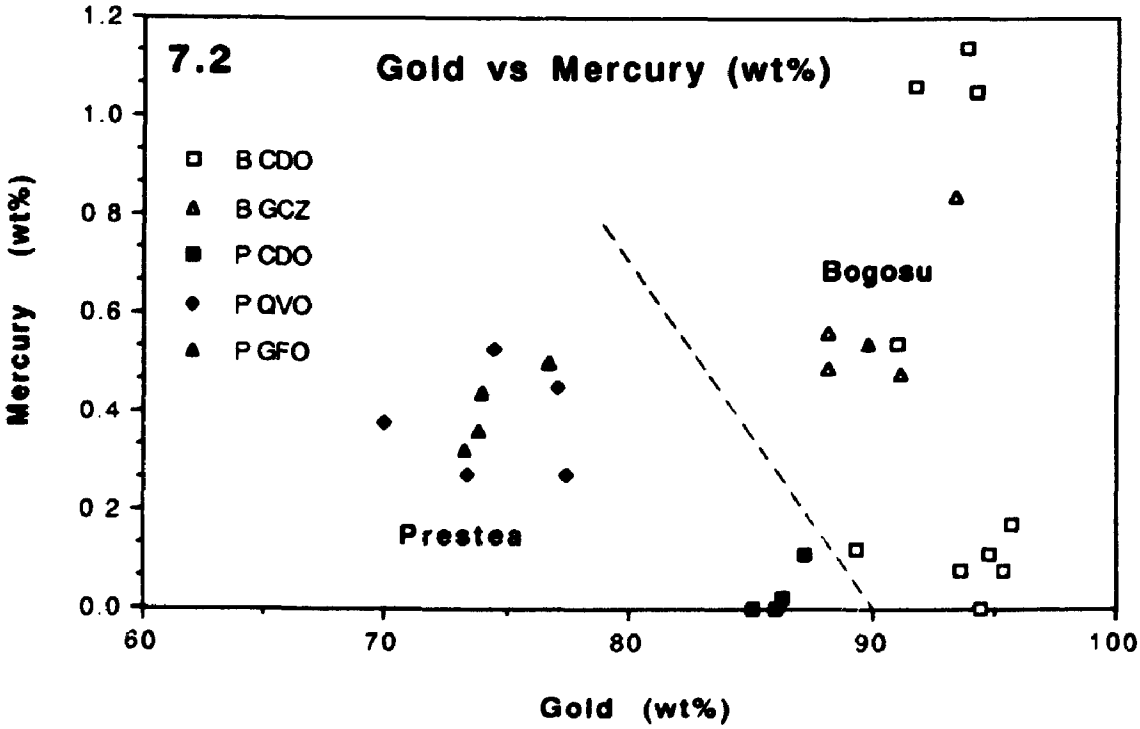
7.2
Gold vs Mercury (wt%)
Mercury (wt%)
Gold (wt%)
B CDO
B GCZ
P CDO
P QVO
P GFO
Bogosu
Prestea
1.2
1.0
0.8
0.6
0.4
0.2
0.0
60
70
80
90
100

Figure 7.3: Bogosu and Prestea ores are distinguished by distinctive tetrahedrite mineral chemistries that plot in the high-Sb tetrahedrite field and in the high-Ag friebergite field, respectively. Tetrahedrite mineral chemistries are believed to reflect compositional changes in the hydrothermal fluid. The higher As and Ag contents in the deeper ores at Prestea are consistent with other observations from the Bogosu and Prestea gold system.

Legend for Figure 7.3

B CDO = Bogosu carbonated dike ore

B GCZ = Bogosu graphitic "crush zone" ore

P CDO = Prestea carbonated dike ore

P QVO = Prestea quartz vein ore

P GFO = Prestea graphitic fissure ore

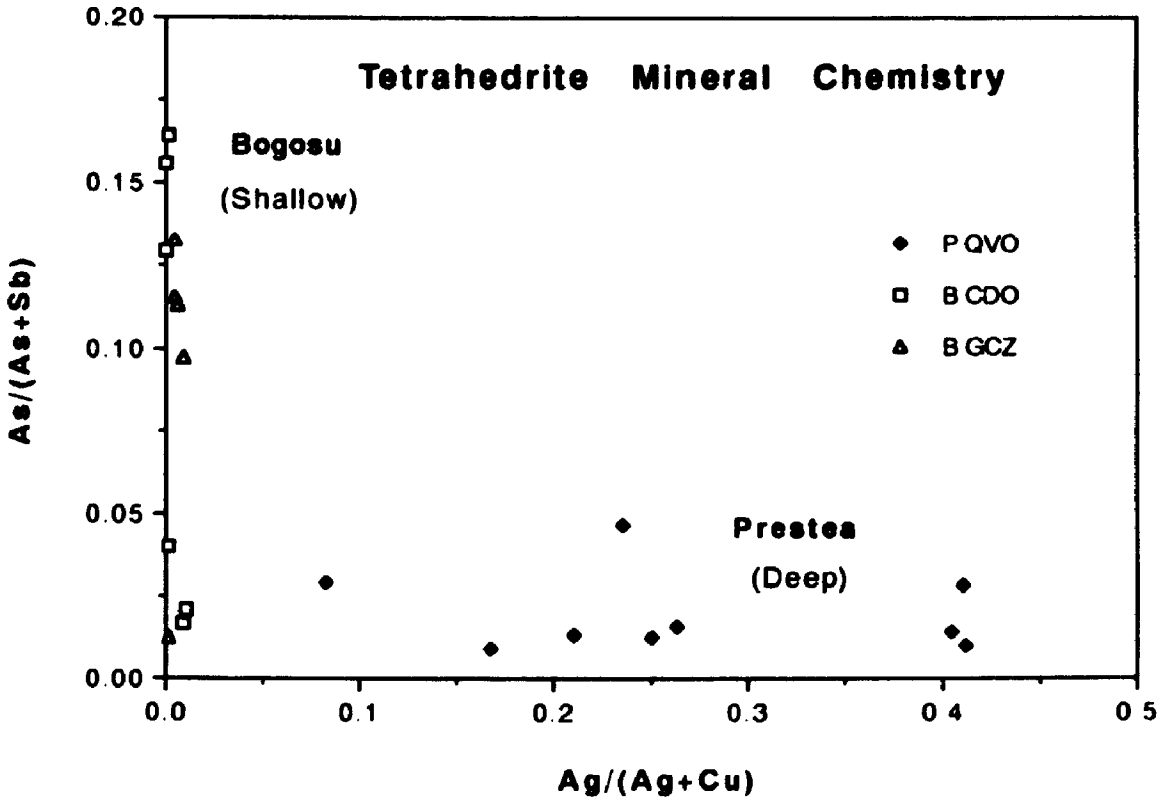
Tetrahedrite Mineral Chemistry
Bogosu
(Shallow)
Prestea
(Deep)
PQVO
BCDO
BGCZ
As/(As+Sb)
Ag/(Ag+Cu)
0.20
0.15
0.10
0.05
0.00
0.0
0.1
0.2
0.3
0.4
0.5

from Bogosu ores plot within the normal tetrahedrite field, while those from Prestea ores plot along the Ag-rich Friebergite trend. The grains exhibit normal substitution patterns, where Ag is exchanging with Cu, and As is occupying Sb sites (Hackbarth and Petersen, 1984; Ebel and Sack, 1989)

This bimodal distribution is similar to that detected by many investigators in both laboratory and natural assemblages from polymetallic base-metal sulphide deposits and bonanza-type precious metal deposits (Wu and Petersen, 1977; Hackbarth and Petersen, 1984; Sack and Loucks, 1985; Ebel and Sack, 1989; Mishra and Mookherjee, 1991). These investigators have demonstrated that tetrahedrite may be an excellent sliding-scale indicator for physico-chemical changes in the environment of ore deposition, particularly for variations in metal and semi-metal element concentrations in the hydrothermal fluid. This is possible since tetrahedrite compostion is relatively insensitive to changes in pH and temperature, and demonstrates near ideal reciprocal exchange reactions for several pairs of elements, including Sb-As, Cu-Ag and Zn-Fe. In the natural assemblages investigated in previous studies, early-formed grains in the centres of the hydrothermal systems were As-rich and Ag-poor, while late, outer zones were Ag-rich and Sb-rich. At the same time, individual grains from the outer zone showed very distinct compositional zoning patterns with the opposite trend. The early-formed core of grains is Ag-rich and Sb-rich, and grains become progressively Ag-poor and As-rich outwards. The Ag content of tetrahedrite is apparently primarily a function of the aAg^+/aCu^+ in the hydrothermal solution, and of the Sb/As ratio of the tetrahedrites. Both must be high in order to produce high-Ag tetrahedrite.

There is little information on tetrahedrite from mesothermal lode gold deposits and direct comparisons to the above noted trends may not be valid.

Nevertheless, some interesting observations can be made. At Bogosu and Prestea, tetrahedrite grains are generally very small (1 μm to 70 μm), and compositional zoning within individual grains was not detected. The trend shown on the As/(As + Sb) vs Ag/(Ag + Cu) plot (Figure 7.3) is very close to that predicted by Sack and Loucks (1985) for tetrahedrite co-precipitating with arsenopyrite, with the data being tightly clustered near the axes. The lack of tennantite is probably due to the excellent sink for As provided by the co-precipitation of arsenopyrite and arsenian pyrite. However, the paragenetic sequence is opposite to that reported in other occurrences, with Ag-rich and As-poor tetrahedrites precipitating in Prestea ores which are believed to be nearer the source. Also, the Hg content of gold grains is highest at Bogosu (Figure 7.2) as expected, but the Ag content is higher at Prestea (Figure 7.1).

The above mentioned characteristics of the Bogosu and Prestea data for tetrahedrite suggest that these occurrences may be treated as being roughly equivalent only to the high Sb (i.e. Ag-rich and As-poor) outer zones recorded and delineated by other investigators (e.g. Wu and Petersen, 1977; Hackbarth and Petersen, 1984). Changes in tetrahedrite composition between Prestea and Bogosu will most likely be the result of changes in metal concentration within the hydrothermal fluid as it migrates upwards through the lode system. In particular, the aAg^+ / aCu^+ must be drastically reduced by the time the upper portions of the system are reached. This correlates very well with a sharp decrease in the Ag content of gold grains toward the upper part of the system (Figure 7.1). The copper content of gold grains remains constant, and it can be concluded that the most likely reason for the observed patterns in tetrahedrite is a decrease in the concentration of Ag in the hydrothermal fluid during ascent.. It is also worth noting that average Au contents in tetrahedrite at Prestea are almost twice the concentration of those in Bogosu ores. This may be an

indication that Au concentration in the hydrothermal fluid was somewhat depleted also by the time ore deposition occurred in the upper levels (i.e. at Bogosu).

Invisible Gold

The presence of invisible gold in sulphides was detected in Bogosu and Prestea ores while examing the compositional zoning of pyrite and arsenopyrite, and the mineral chemistry of tetrahedrite with the electron microprobe (EMP). Individual analyses using a beam diameter of about 2.5 μm yielded sporadic values of up to 0.1 wt% invisible gold in both pyrite and arsenopyrite. Gold was detected also in other sulphides; however, values of up to 0.5 wt% invisible gold in tetrahedrite and over 1.00 wt% gold in boulangerite and stibnite are not as reliable due to the lack of appropriate standards. The presence of invisibl. gold was subsequently confirmed and quantified in pyrite and arsenopyrite using secondary ion mass spectrometry (SIMS) at Surface Science Western in the Universtity of Western Ontario. Quantitative analyses were obtained using the external standardization method as described by Chryssoulis et al. (1989; see also Fleet et al. 1993).

In this study the results from the documentation of the distribution of sub-microscopic gold can be interpreted in the context of the entire gold system for which complementary information is available from various mineralogical, geochemical and geological parameters. This has led to some significant new conclusions regarding the precipitation and evolution of gold in lode deposits.

The presence of invisible gold in pyrite and arsenopyrite crystals has been documented previously for several deposits. Examples include the Elmtree

(N.B., Canada), Agnico Eagle (Canada), Fairview (South Africa), Sheba (Transvaal, South Africa), Red Lake (Canada), Carlin (U.S.A.), and Chatelet and Villeranges (Massif Central, France) mines (Cook and Chryssoulis, 1990; Chryssoulis and Cabri, 1990; Fleet et al. 1993; Cathelineau et al., 1989; Cabri et al., 1989; Bakken et al., 1989). These investigators demonstrated that sub-microscopic gold exists both within the pyrite or arsenopyrite crystal lattice in solid solution and as discrete colloidal particles. They further demonstrated that gold was preferentially concentrated within As-rich portions of pyrite. Cathelineau et al. (1989) provided evidence that gold in arsenopyrite from Le Chatelet and Villeranges is in As-rich and (Sb + Fe)-poor zones. The reported concentration of invisible gold is significant, roughly up to 1,000 ppm in pyrite from Fairview and Goldstrike and up to 15,200 ppm in arsenopyrite from Chatelet and Villeranges (Fleet et al., 1993; Marcoux et al., 1989).

Quantitative Analysis of Invisible Gold

Samples were analyzed using a Cameca IMS-3f ion microscope for ^{197}Au, ^{75}As, ^{56}Fe and ^{34}S. All measurements were made with a cesium primary beam of about 500 nA at 14.1 keV while monitoring negative ions. For ion-probe microanalysis, the area analyzed is defined by a set of apertures in the secondary column. All present analyses were made with an aperture of 60 μm. Iron and S were determined to monitor instrumental conditions during the analysis and for standardization. SIMS has been used routinely to quantify the "invisible" Au content and colloidal-size Au in pyrite and arsenopyrite (Cook and Chryssoulis, 1990; Fleet et al., 1993). The Au concentration in ppm (weight) was read from mineral and element specific calibration curves. Molecular ions were eliminated by voltage offsetting: 200 V, fully open evergy-slits for microprobe analysis (Chrysoulis 1990) and 80 V, one-tenth-open slits

for imaging (Chryssoulis and Weisener 1991). With a 10-s counting time for Au, the limit of detection in pyrite is 0.4 ppm Au, with an accuracy of about 10-15% (Chryssoulis et al., 1987; Fleet et al., 1993). Thirty analyses were obtained by this method from 10 pyrite and 13 arsenopyrite grains selected from two ore samples (Tables 7.4a and 7.4b). Sample DM-11 is a gold-rich sample of carbonated dike ore from the Dumassie deposit in the Bogosu area, and sample P-19 is representative of gold-rich fissure and quartz vein ores from Prestea. In addition to the invisible gold, polished thin sections of the same samples contained 99 (DM-11) and 69 (P-19) discrete grains of microscopic gold ranging in size from 0.5 to 32 μm and 0.5 to 48 μm, respectively.

The concentration of invisible gold within arsenopyrite grains of the Bogosu sample was consistantly high and ranged from 16 to 280 ppm Au. This contrasts with low values obtained from 3 arsenopyrite grains at Prestea which ranged from 0.56 to 1.0 ppm gold (Table 7.4). In spite of low gold values in the Prestea sulphides, discrete colloidal gold particles were detected by imaging these grains (e.g. Plate 7.3). The area covered by this image is approximately 10 times greater (150 μm diameter) than the area probed for quantitative analysis (30 to 50 μm diameter). Consequently, the presence or absence of randomly distributed colloidal particles will have a strong effect on the concentration of invisible gold detected during analysis.

A similar pattern of high invisible gold-contents from 0.16 to 330 ppm was detected in Bogosu pyrite, while 6 Prestea pyrite grains yielded consistently lower values of from 0.14 to 3.1 ppm gold (Table 7.4). At Bogosu, the smaller grains had distinctly lower invisible gold contents with only 0.16 and 0.37 ppm in analyses of grains #6 and #7, respectively (Table 7.4), which measured only about 0.1 mm in diameter. Also, the late outer growth zone of As-poor pyrite

Table 7.4A: "Invisible" Au concentration in sulphide minerals at Bogosu by SIMS (Sample DM-11).

PYRITE		ARSENOPYRITE	
Grain #	Au, ppm	Grain #	Au, ppm
5	15.	1	280.
6	0.37	2	15.
7	0.16	3	93.
9	14.	4	106.
10	78.	8	29.
11	115.	15	80.
12	330.	16	21.
13	115.	17	67.
14	1.5	18	144.
20	5.9	19	83.
21	19.		
n $\hat{x}$ $\pm \lambda$	Max. Min.	n $\hat{x}$ $\pm \lambda$	Max. Min.
11 63 ± 57 ppm	330. 0.16	10 92 ± 46 ppm	280. 21.
Median 75 ppm		Median 82 ppm	

Table 7.4B: "Invisible" Au concentration in sulphide minerals at Prestea by SIMS (Sample P-19).

PYRITE		ARSENOPYRITE	
Grain #	Au, ppm	Grain #	Au, ppm
1	3.1	4	1.0
2	1.0	5	0.60
3	1.8	7	0.56
6	0.16	$\hat{x}$	0.72 ppm
8	0.14		
9	0.74		
$\hat{x}$ $\pm \lambda$ 1.2 ± 0.8 ppm			

PLATE 7.3

Ion-probe microanalysis by SIMS (secondary ion mass spectrometry) of distribution of Au and As in an arsenian pyrite grain from a sample of graphitic fissure ore in the Prestea mine (sample P-19).

A: ^{75}As ion map showing strong zoning in As content along pyrite growth bands.

B: Corresponding ^{197}Au ion map showing an evenly distributed low concentration (0.14 ppm) of gold. There is no correlation between the content of gold in solid solution and the strong As zoning. Note the single colloidal particle of gold.

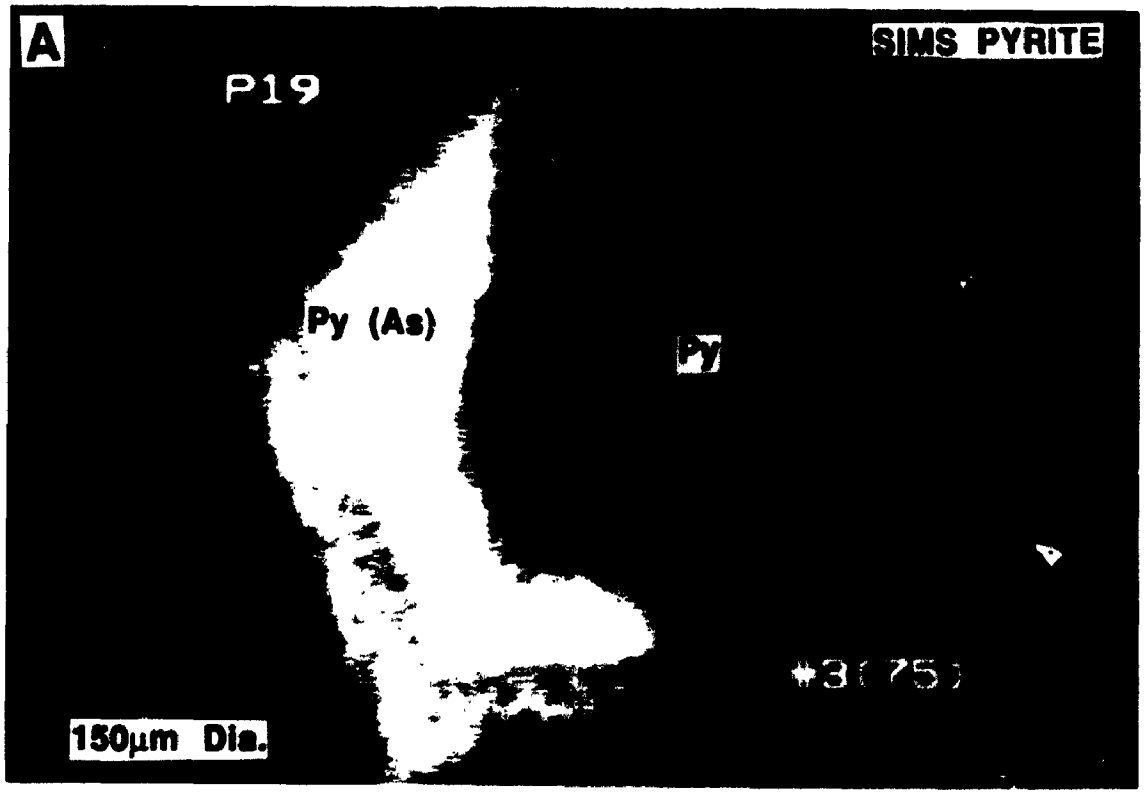
A
SIMS PYRITE
P19
Py (As)
Py
#3(75)
150µm Dia.

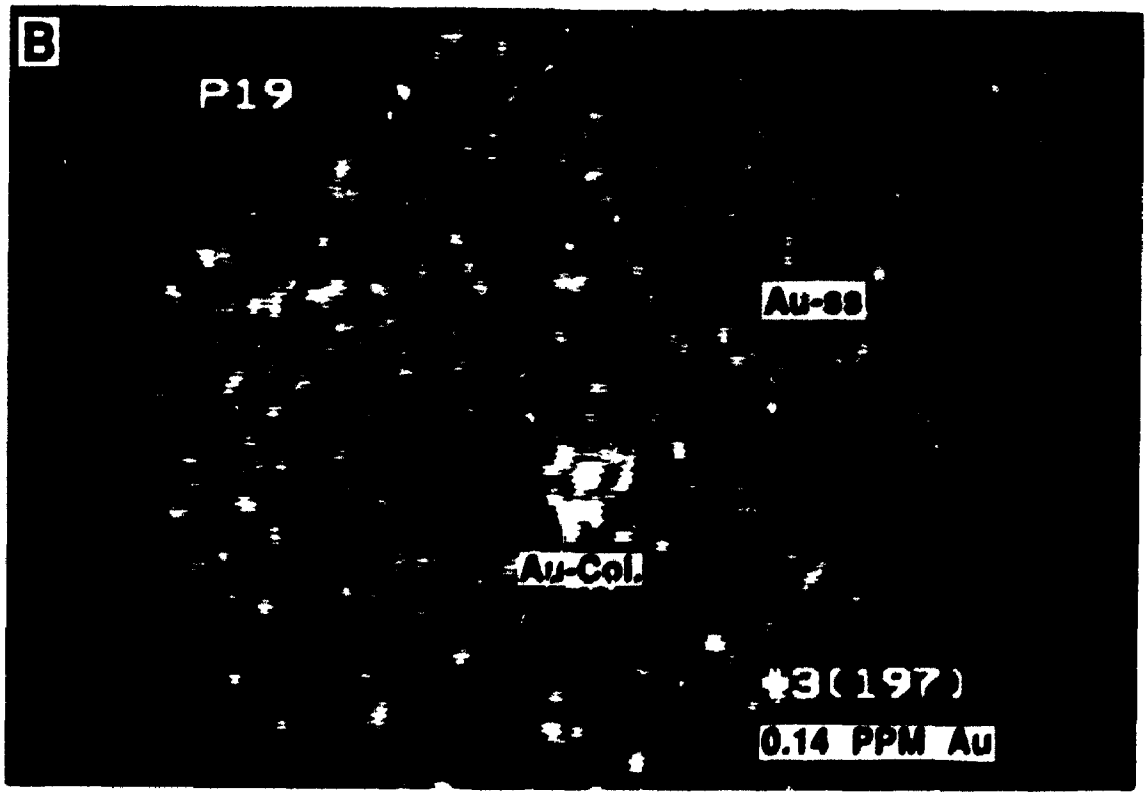
B
P19
Au-ss
Au-Col.
#3(197)
0.14 PPM Au

for the grain shown in Plate (6.2B) had a low concentration at only 1.5 ppm gold (analysis #14, Table 7.4A). In contrast, the highest gold values in pyrite at Bogosu and Prestea were in the larger, As-rich porphyroblastic grains that often exceed 1.0 mm in diameter. Examples include the pyrite grain shown in Plates 6.2B, 7.4 and 7.6, and analyses of grains #5, #9, #14, #20 and #21 at Bogosu and grain #1 at Prestea (Table 7.4).

Distribution of Invisible Gold

To develop an understanding of the distribution of sub-microscopic gold within sulphide / arsenide grains, SIMS was used in the imaging mode to obtain 39 images of S, As and Au distribution patterns from 8 grains of pyrite, arsenopyrite or intergrowths of the two (cf. Fleet et al., 1993). Ion mapping was used to determine the distribution of Au and As within individual grains. Ion imaging was performed by electronically rastering the primary beam over an area of 250 x 250 μm. Images obtained on the dual channel plate were captured by a Cohu solid-state camera and processed by an image-processing system developed at Surface Science Western. The size of the cesium beam at 500 nA is 150 μm, but the effective spatial resolution in the resulting images is about 2 μm. Other details on the present procedure for ion mapping are given in Chryssoulis and Weisener (1991) and Fleet et al. (1993). In the Bogosu ores, Au in solid solution within the pyrite lattice is clearly associated with As-rich zones (Plates 7.4 to 7.7). However, gold occurs also as discrete colloidal size (0.01 to 0.1 μm) particles that may be in either As-rich zones (Plate 7.4) or in As-poor zones (Plate 7.9). The central portion of the pyrite porphyroblast shown in Plates 6.2B, 6.2D and 7.5 is composed of early, As-poor pyrite formed from pre-existing pyrrhotite and marcasite. This core region does not contain Au, with the exception of minor colloidal-size micro-inclusions that

PLATE 7.4

Ion-probe microanalysis by SIMS (secondary ion mass spectrometry) of distribution of Au and As in an arsenian pyrite grain from a sample of carbonated-dike ore from the Dumassie deposit, Bogosu concession (sample DM-11 #2B). The ions maps are from the As-rich band of the arsenian pyrite grain illustrated in Plates 6.2B and 6.2C.

A: ^{75}As ion map showing a mosaic pattern of recrystallization of arsenian pyrite [Py (As)] to As-poor pyrite, pyrrhotite and arsenopyrite (Asp) microcrystals.

B: Corresponding ^{197}Au ion map showing the concentration (78 ppm) of gold in solid solution (Au-ss) in the non-recrystalized, As-rich portions of the pyrite crystal. The recrystalized portions of the pyrite grain are noticeably depleted of gold.

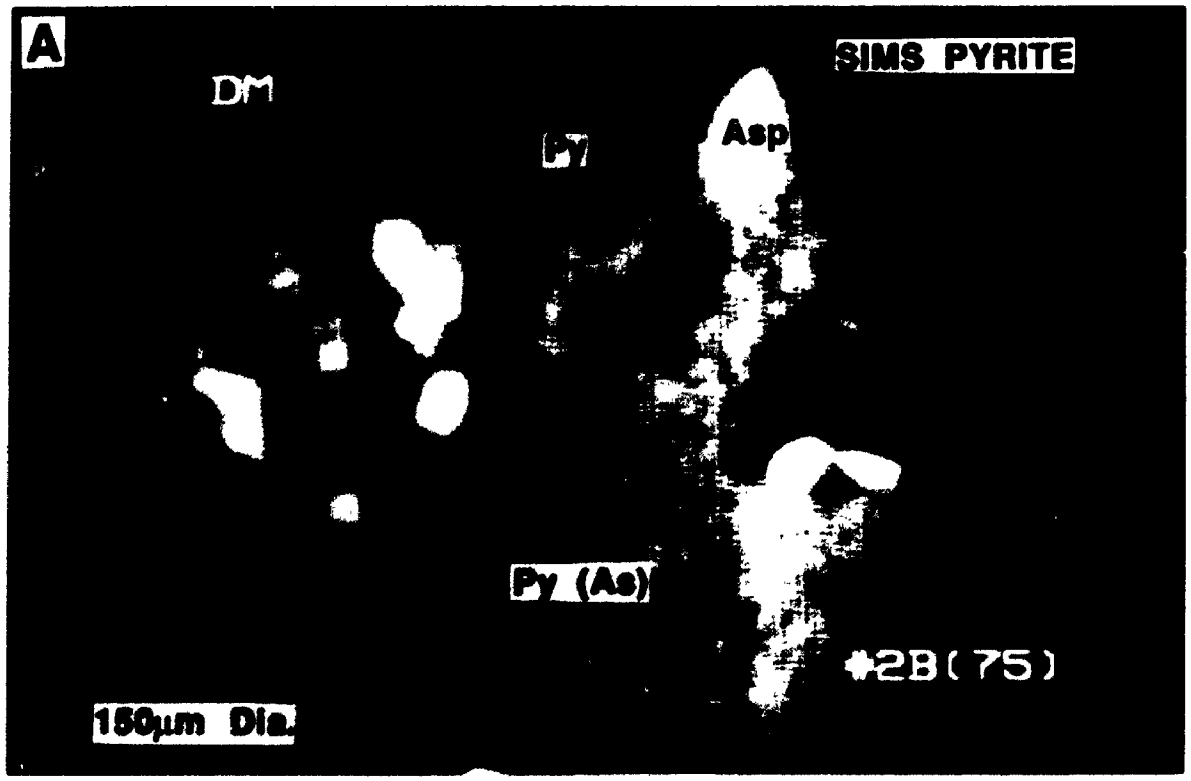
A
SIMS PYRITE
DM
Py
Asp
Py (As)
#2B(75)
150µm Dia.

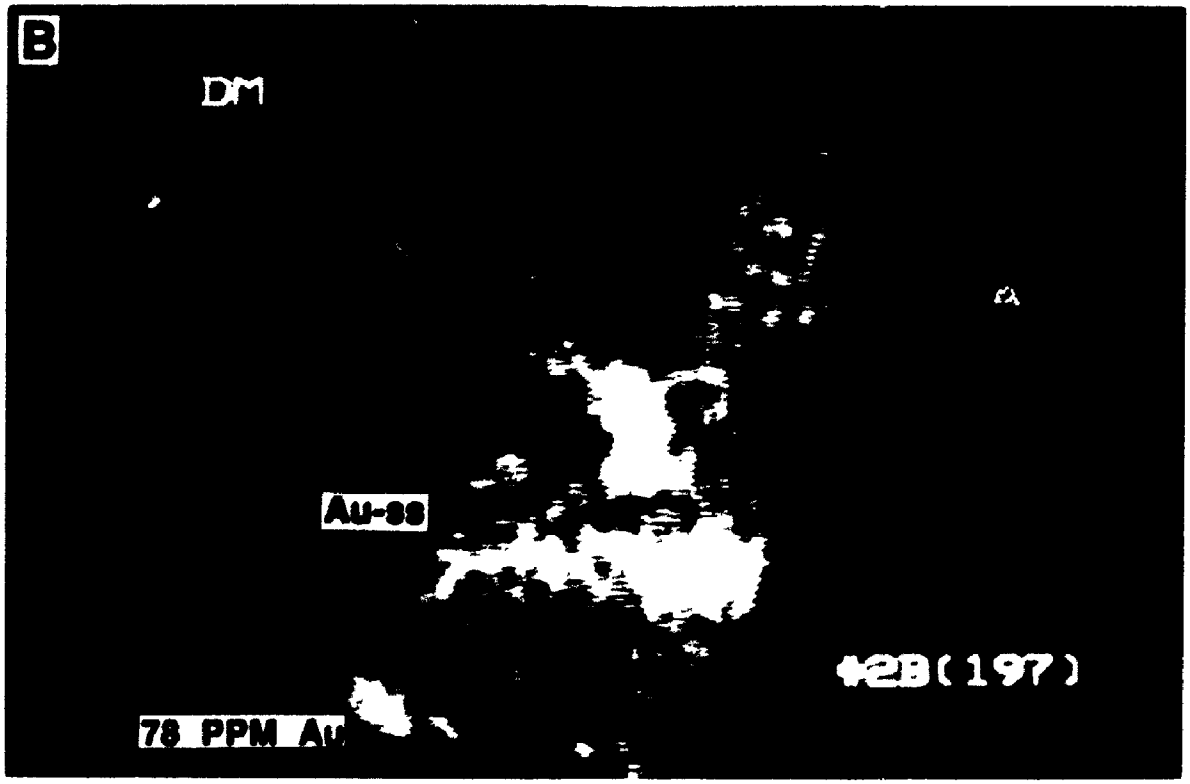
B
DM
Au-ss
#2B(197)
78 PPM Au

PLATE 7.5

Ion-probe microanalysis by SIMS (secondary ion mass spectrometry) of distribution of Au, As and S in an arsenian pyrite grain from a sample of carbonated-dike ore from the Dumassie deposit, Bogosu concession (sample DM-11 #2C). The ions maps are from the As-poor core region of the pyrite grain illustrated in Plates 6.2B and 6.2D.

A: ^{34}S ion map showing distribution of S in the pyrite grain.

B: Corresponding ^{75}As ion map showing two arsenopyrite crystals included during growth of the pyrite grain, but no arsenopyrite microcrystals. Fine As-rich bands in the pyrite are not visible in this map due to contrast with the arsenopyrite crystals; however, they are clearly resolved in Plates 6.2B and 6.2D.

C: Corresponding ^{197}Au ion map showing the concentration of colloidal gold (Au-Col.; most of the Au in this image) and Au in solid solution along fine bands of arsenian pyrite that form a cement around early, As-poor pyrite crystals.

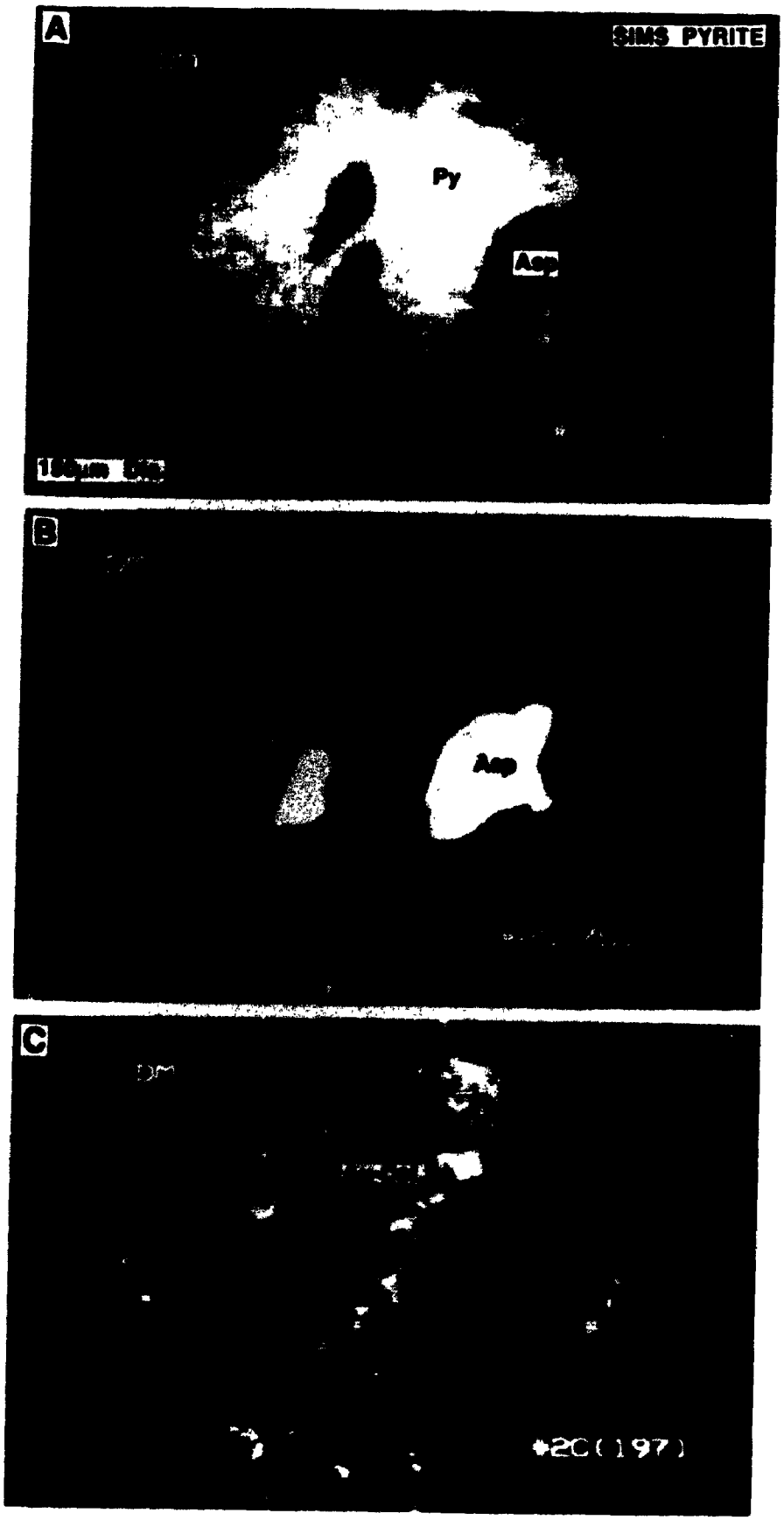
A
SIMS PYRITE
Py
Asp
B
Asp
C
*2C(197)

PLATE 7.6

Ion-probe microanalysis by SIMS (secondary ion mass spectrometry) of distribution of Au and As in an arsenian pyrite grain from a sample of carbonated-dike ore from the Dumassie deposit, Bogosu concession (sample DM-11 #2D). The ions maps are from the As-rich band of the arsenian pyrite grain illustrated in Figures 6.2B and 6.2C.

A: ^{75}As ion map showing distribution of As in the recrystalized portion of the arsenian pyrite. Pyrite, arsenopyrite and pyrrhotite microcrystals are surrounded by the remaining bands of arsenian pyrite.

B: Corresponding ^{197}Au ion map showing Au in solid solution (Au-ss) and colloidal gold (Au-Col.) concentrated (up to 115 ppm) along the remaining As-rich bands. The recrystallized portions of the grain are noticeably Au-poor.

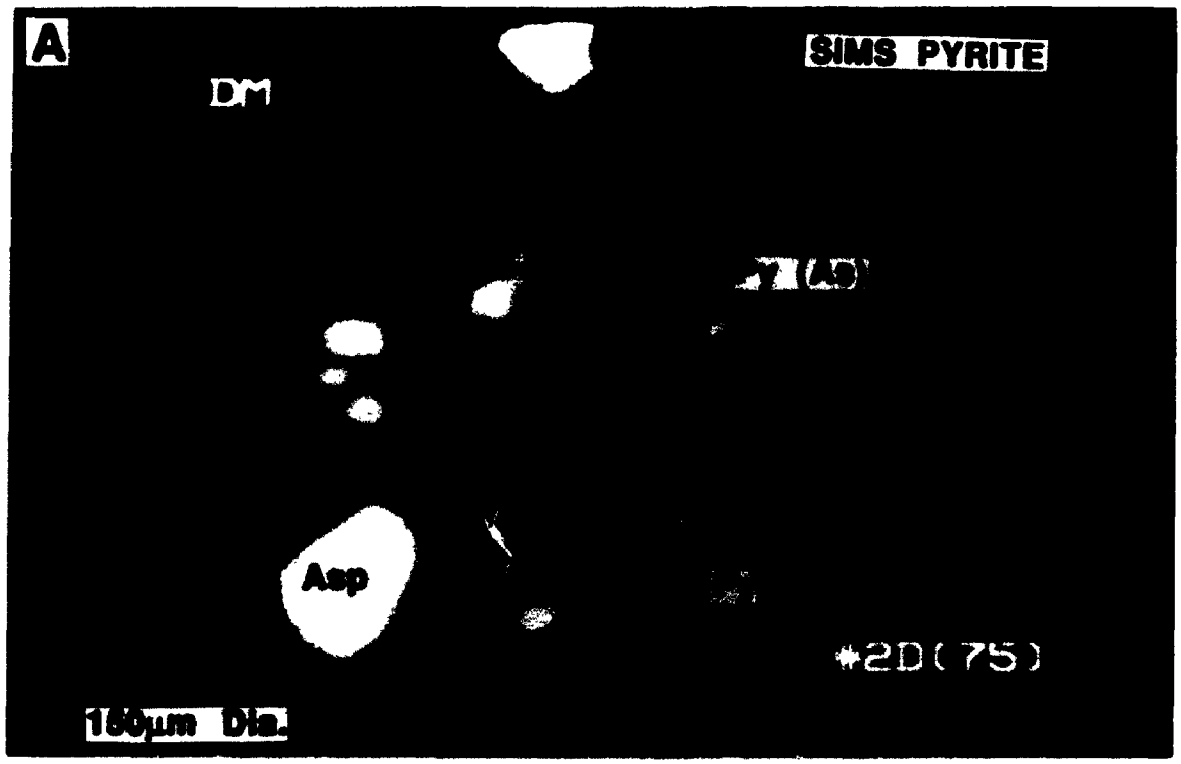
A
SIMS PYRITE
DM
Asp
#2D(75)
160µm Dia.

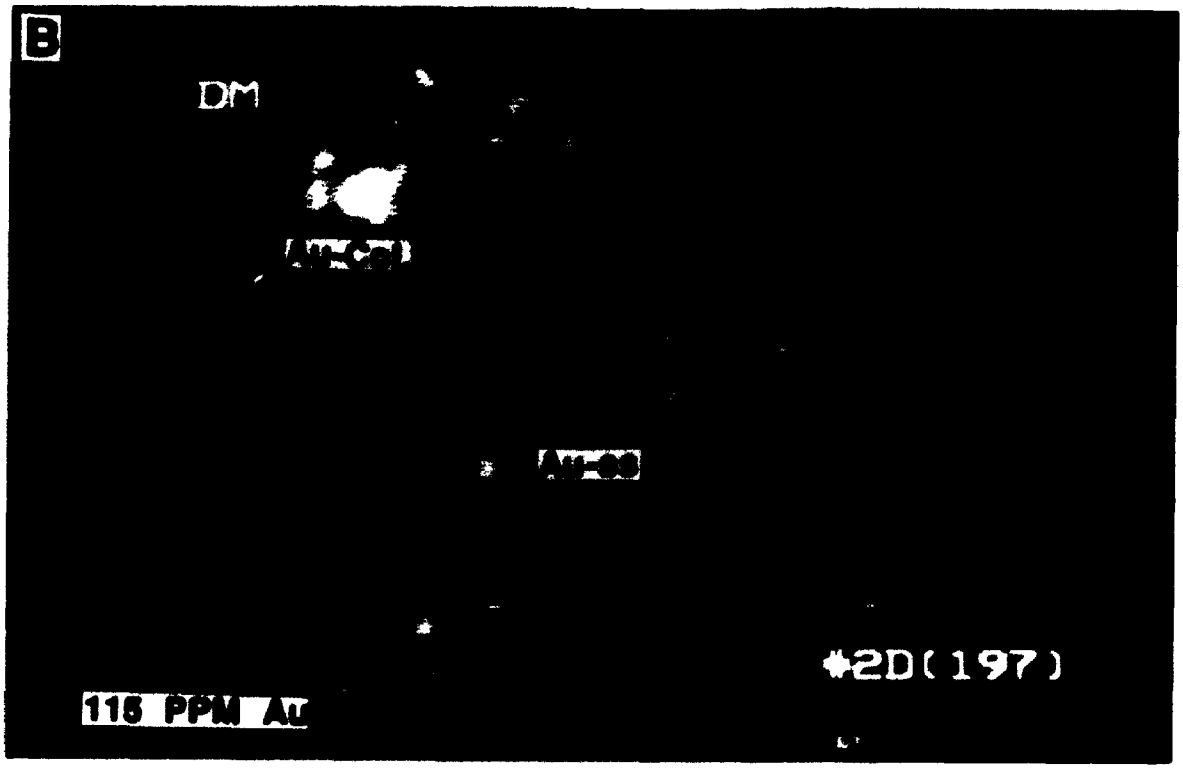
B
DM
#2D(197)
115 PPM Au

PLATE 7.7

Ion-probe microanalysis by SIMS (secondary ion mass spectrometry) of distribution of Au and As in an arsenian pyrite grain from a sample of carbonated-dike ore from the Dumassie deposit, Bogosu concession (sample DM-11 #11B).

A: ^{75}As ion map showing strong zoning of As contents [Py (As)] in the pyrite crystal (Py).

B: Corresponding ^{197}Au ion map showing Au in solid solution (Au-ss) concentrated in the As-rich band of the pyrite grain, and the formation of a particle of colloidal gold (Au-Col.) along a fracture or sub-grain boundary of the pyrite.

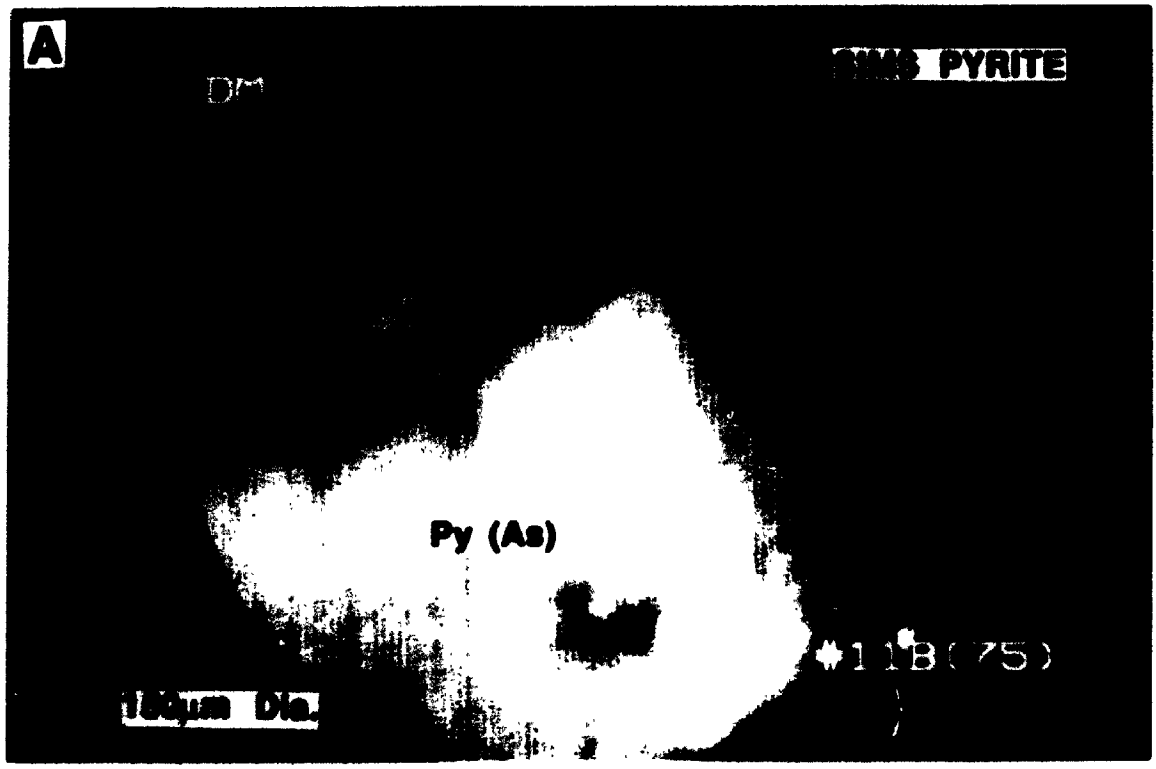
A
DM
PYRITE
Py (As)
#11B(75)

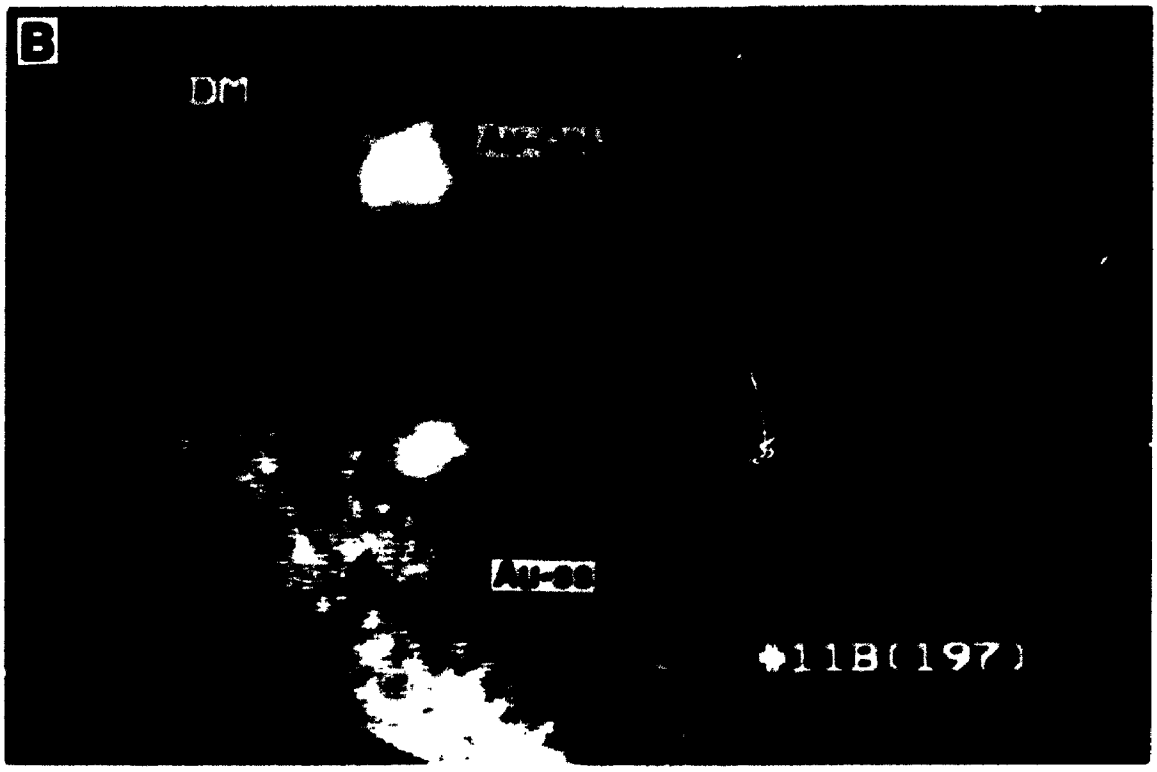
B
DM
#11B(197)

PLATE 7.8

Ion-probe microanalysis by SIMS (secondary ion mass spectrometry) of distribution of Au, As and S in an arsenian pyrite grain that has included a complex arsenopyrite crystal. This sample is from a carbonated-dike ore in the Dumassie deposit, Bogosu concession (sample DM-11 #11).

A: ^{34}S ion map showing distribution of S and the outline of arsenopyrite within the pyrite grain.

B: Corresponding ^{75}As ion map showing distribution of As in the arsenopyrite crystals.

C: Corresponding ^{197}Au ion map showing a strong concentration of Au in solid solution (Au-ss) in the margin of the included arsenopyrite. Minor Au in solid solution occurs in the host pyrite.

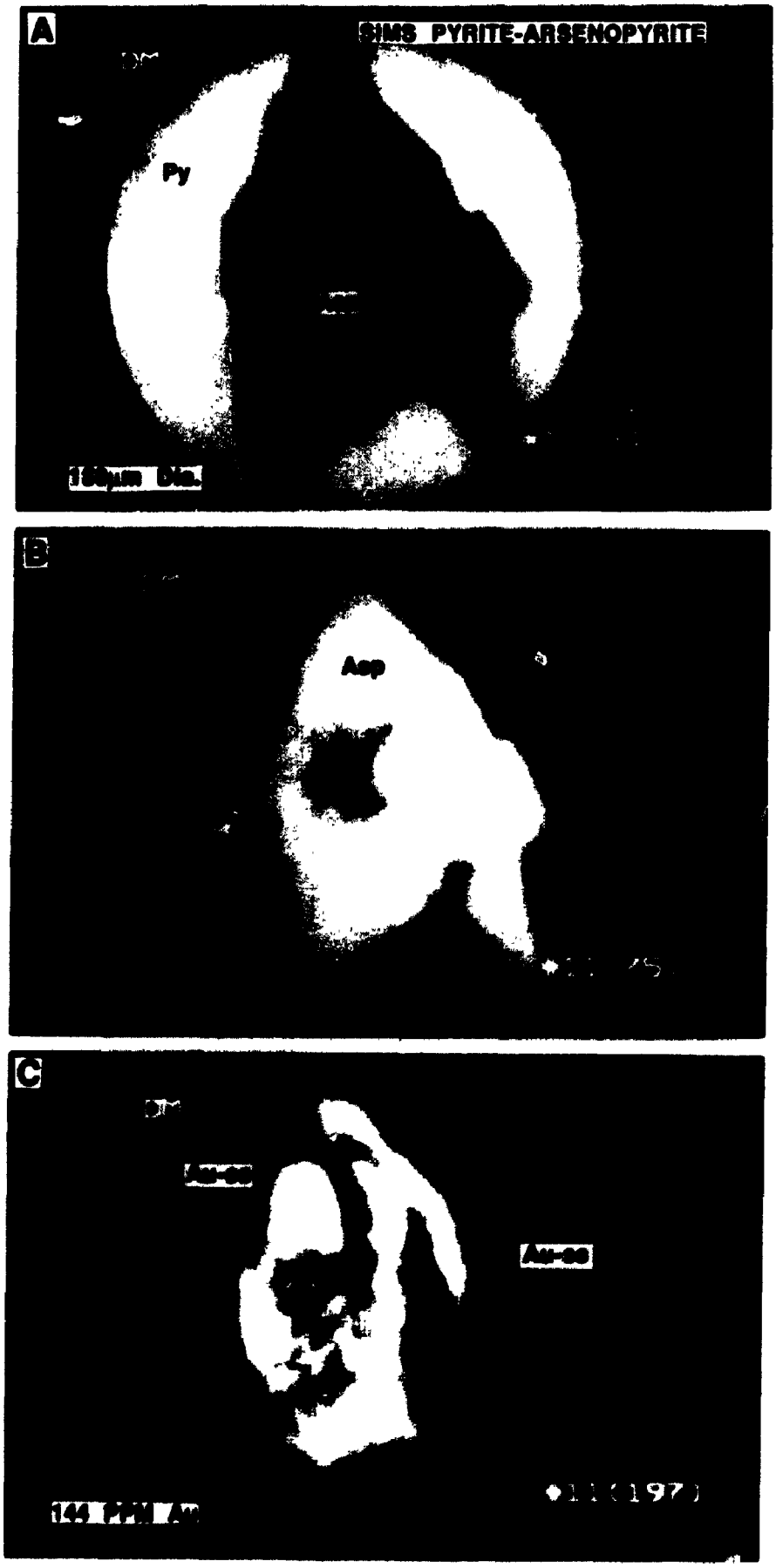
A
SIMS PYRITE-ARSENOPYRITE
Py
B
Asp
C

PLATE 7.9

Ion-probe microanalysis by SIMS (secondary ion mass spectrometry) of distribution of Au and As in an arsenopyrite grain from a sample of carbonated-dike ore from the Dumassie deposit, Bogosu concession (sample DM-11 #6).

A: ^{75}As ion map showing the distribution of As. Note that the EMP BSE images of the same grain demonstrate that the outer growth band of this arsenopyrite crystal is As-rich with-respect-to the core region.

B: Corresponding ^{197}Au ion map showing Au in solid solution concentrated in the As-poor core of the euhedral arsenopyrite crystal.

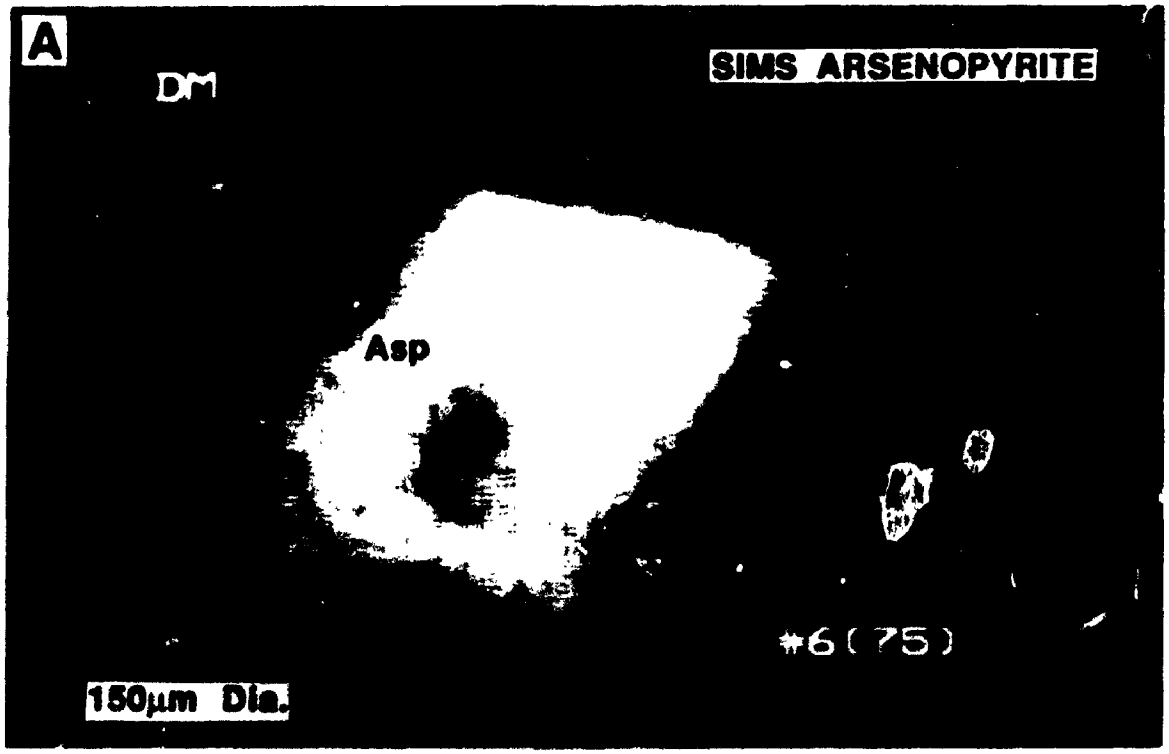
A
DM
SIMS ARSENOPYRITE
Asp
#6(75)
150µm Dia.

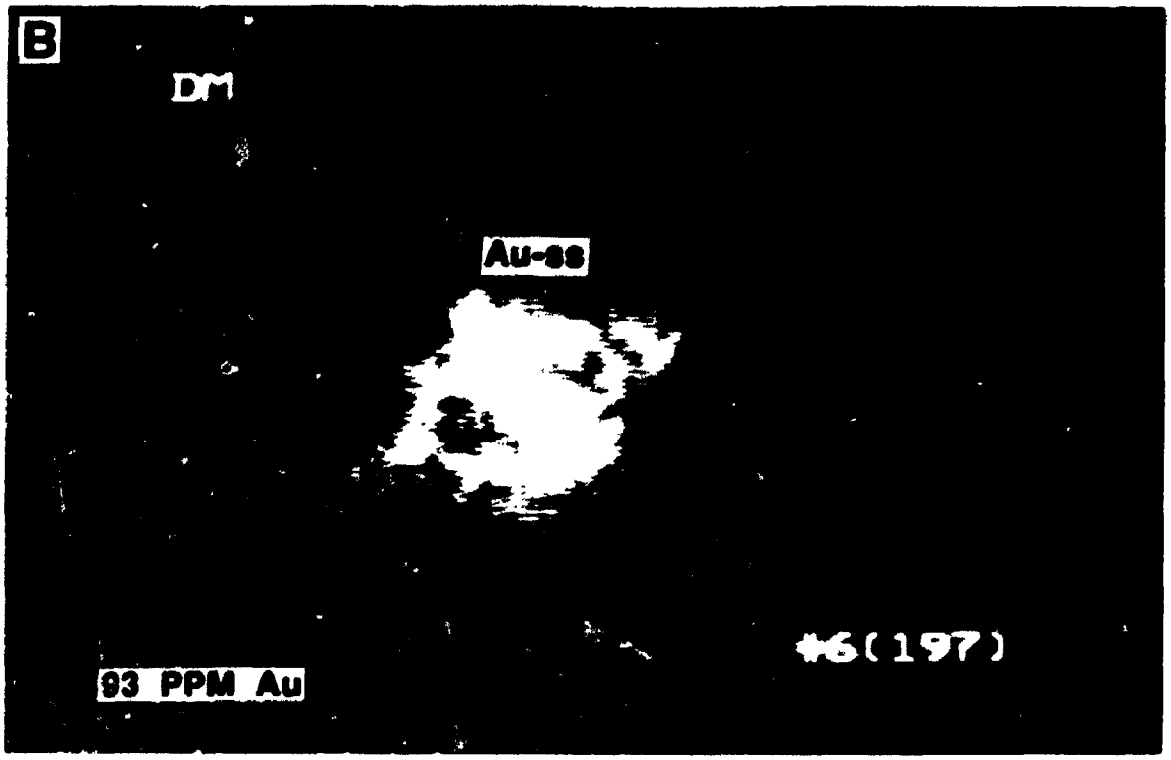
B
DM
Au-ss
#6(197)
93 PPM Au

formed along grain boundaries or micro-fractures. These early grains are cemented together by arsenian pyrite which does contain Au in solid solution. In the Prestea sample, pyrite grains have As-rich zones that are at least as prominent as those in pyrite at Bogosu. However, the distribution of invisible gold clearly does not correlate with As-rich bands in some grains (e.g. Plate 7.3), while in others a correlation is barely discernable, but nevertheless present.

Two generations of arsenopyrite occur as inclusions in pyrite. Euhedral to subhedral arsenopyrite microcrystals are associated with recrystallized As-depleted mosaics in As-rich zones of arsenian pyrite. These arsenopyrite microcrystals are distinctly Au-poor (e.g. Plate 7.4). Pyrite porphyroblasts also contain numerous inclusions of independantly nucleated arsenopyrite grains, and these tend to be Au-rich (e.g. 144 ppm Au from Table 7.4A analysis #15, from the arsenopyrite grain illustrated in Plate 7.8). These early arsenopyrite grains are larger than late recrystallized grains, although some occur also as anhedral to amorphous arsenopyrite microcrystals that carry abundant colloidal and solid solution gold.

The larger arsenopyrite crystals at Bogosu have high invisible Au contents of up to 280 ppm. The Au distribution is strongly zoned in growth bands. In some grains a direct relationship of Au to As and S distribution is not established since subtle compositional variations in S and As are not well resolved in the SIMS images. However, in others, such as the grain illustrated in Plate 7.9, Au is clearly concentrated in the euhedral core region (93 ppm Au), which is surrounded by a Au-poor rim. From back-scattered electron images, the Au-rich core of this grain is As-poor, and contrasts with an As-rich rim which does not contain detectable Au. This clearly demonstrates that

higher Au values in arsenopyrite are not, in all cases, in zones with higher As concentrations. According to the arsenopyrite and carbonate geothermometry (Chapters 6 and 8), formation temperatures indicated by As concentrations in the outer rim of this grain (Plate 7.9) were too high (≈450°C) for gold deposition, whereas, temperatures indicated by the core region do fall within the range for gold precipitation (see Figures 6.1A and 6.3).

More complex zoning is observed in an intergrowth of arsenopyrite crystals entirely enclosed within a pyrite porphyroblast (Plate 7.8). In this particular group, Au (144 ppm) is concentrated along some marginal growth bands, but is noticeably absent from much of the grain at the lower right. Gold is lower in concentration also in the central region of the grain on the left. Optical microscopy reveals that the central, Au-poor region of this arsenopyrite grain is seive-textured. Gold in solid solution is present in the arsenopyrite crystals, and also in small amounts in the surrounding pyrite.

Gold Precipitation and Evolution

It has been demonstrated that gold in the Bogosu-Prestea system is present as: 1) visible gold (> 100 μm) in quartz, albite and carbonate, 2) microscopic gold (> 0.5 μm to < 100 μm) associated with sulphide minerals and interstitial to silicates, and 3) invisible gold (< 0.5 μm). The latter association is comprised of: 1) gold in solid solution within the crystal lattice of sulphide and sulfarsenide minerals, and 2) colloidal-size particles (> atomic size to < 0.5 μm).

The presence of the various types of gold and the occurrence of gold in a variety of modes within a single gold system leads to some interesting

conclusions regarding gold precipitation, distribution and evolution in major lode gold systems. The evidence from Bogosu and Prestea suggests that virtually all gold initially precipitated in solid solution within arsenian pyrite and arsenopyrite, and to a much lesser extent within tetrahedrite, and possibly some of the other sulphides within the system. The paragenetic sequence (Table 6.1) indicates that gold in solid solution precipitated almost entirely during the arsenian event of the Stage 3 hydrothermal alteration, the same event that produced the compositional zoning of pyrite and arsenopyrite described in the previous chapter.

Once precipitated, gold redistribution and crystallization is believed to have commenced almost immediately and proceeded with more or less efficiency depending upon the ambient post-precipitation metamorphic and hydrothermal conditions. Consequently, in a large system such as Bogosu and Prestea, various stages of gold redistribution and concentration are preserved.

Local diffusion of major components and recrystallization of arsenian pyrite is clearly documented with the formation of arsenopyrite and pyrrhotite microcrystals (Plates 6.2B, 6.2C, and 7.4) from As-rich zones, with the creation of As-depleted areas in the pyrite. These arsenian zones are the same areas that contain gold in solid solution. The recrystallized, As-depleted zones in pyrite are also depleted in gold, as are the newly-formed arsenopyrite and pyrrhotite microcrystals. Gold in solid-solution is found only in relict As-rich portions of the pyrite. Most importantly local concentration of gold now occurs, and invisible but discrete colloidal gold particles form in relative abundance along the grain contacts of As-depleted pyrite with or without As-rich pyrite. The process of redistribution and concentration is well illustrated in Plate 7.4. With further evolution of the deposit, invisible gold becomes more concentrated and

some colloidal submicroscopic inclusions grow to the microscopic sizes discussed earlier. The gold in these grains may be redistributed through dissolution and recrystallization processes; however, this does not explain the observations from Prestea. Gold redistribution and concentration is not restricted to areas where recrystallization of pyrite, arsenopyrite and pyrrhotite has occurred, but appears to be ubiquitous in all the pyrite and arsenopyrite grains examined. For example, strong compositional zoning is preserved in Prestea grains as well as in most of the Bogosu sulphides, yet the SIMS images indicate that gold has effectively redistributed and concentrated into discrete colloidal, microscopic and visible particles. This suggests that at least some of the gold is redistributed without recrystallization of arsenian pyrite or arsenopyrite, perhaps through some form of diffusion (infiltration) mechanism. The observed remobilization of gold follows a distinctive pattern. Initially, gold in solid solution migrated towards fractures and voids within the sulphides, then to grain margins and ultimately out of the host sulphide crystals, to be reprecipitated interstitial to gangue minerals, where it appears to have a long residence time. In the more extreme cases illustrated by the Prestea sulphides, most of the gold appears to have migrated out of solid solution with sulphides, leaving behind minor values and only weak remnant correlations to an earlier strong compositional zoning. The small pyrite grains at Bogosu with only minimal invisible gold contents indicate that gold will migrate easily out of small grains, while being trapped as colloidal and microscopic particles in the larger crystals. It seems quite evident that much of the gold initially precipitated with the sulphides. However, subsequent changes in physico-chemical conditions promoted the migration of gold out of the host crystal lattices and its local concentration as microscopic particles.

In some arsenopyrite (and pyrite) grains, gold seems to have preferrentially

migrated to the grain core, particularly to sieve-textured cores (e.g. Plate 7.2A). It is most probable that micro-fractures or grain boundaries within the sulphide grains promoted faster migration and concentration of gold; certainly, this would be a prerequisite for infiltration-dominated diffusion. These microfracture patterns may strongly influence the ultimate gold distribution; whether gold concentrates as inclusions within sulphide grains, or migrates to grain boundaries and interstitial to the surrounding silicate minerals.

It is demonstrated in other Chapters (e.g. 3, 4, 6, 8, 9) that ambient country-rock metamorphic conditions as well as temperatures of mineralization were moderately higher at Prestea during and subsequent to mineralization. Consequently, this is believed to be a major factor in promoting greater recrystallization and redistribution of gold at Prestea following the initial precipitation in sulphide minerals. Most of the gold at Prestea appears to have migrated out of solid solution. It is apparent that higher-grade metamorphic / hydrothermal conditions during and/or after precipitation led to more efficient recrystallization and redistribution of gold and to its eventual migration into gangue. The better preservation of primary gold distribution at Bogosu must be due, at least in part, to the slightly lower grade of metamorphism that affected this district during and after mineralization.

Gold Concentration and Precipitation

As suggested above, gold precipitation from the ore forming fluids in solid solution within sulphides could account for the observed gold distribution patterns and modes of occurrence documented at Bogosu and Prestea. However, it is important to determine whether or not the amounts of

microscopically visible gold observed (e.g. Plates 6.1C and 7.2A) could originate by reconcentration of gold in solid solution within the host grain, or whether gold must be introduced from outside of the host grain. This problem can be addressed with simple calculations. A 1 mm cube of arsenopyrite or pyrite averaging 100 ppm invisible gold will produce the following maximum volume of gold metal:

$$V_{Au} = V_{sulphide\ grain} \times X_{Au} \times (d_{sulphide} / d_{Au})$$

where V = volume in cubic microns, μm^3

X = concentration

d = density ($g.cm^{-3}$)

$$V_{Au} = 10^9\ \mu m^3 \times 10^{-4} \times (5.5 \div 19.3)$$

$$= 28{,}500\ \mu m^3$$

$$\cong 30\ \mu m \text{ diameter particle of gold}$$

This amount of gold could account for the proportion of microscopic gold in Bogosu and Prestea ores, especially since it would be increased somewhat by alloying with silver and other metals. It has been reported that invisible gold contents of some pyrite and arsenopyrite grains locally average as high as 1000 ppm and 4,900 ppm, respectively, (Fleet et al., 1993; Marcoux et al., 1989). This would increase the potential gold metal volume by at least another order of magnitude over the above calculation.

The actual method by which gold is precipitated along with sulphides has not

been addressed in this study. However, many investigators have shown that Au, Ag, As, Sb, Hg and possibly other metals are readily and abundantly carried as bisulphide complexes (e.g. $Au(HS)_2^-$) in hydrothermal solutions similar to those thought to be responsible for the formation of mesothermal gold deposits such as at Bogosu and Prestea (Barnes, 1979; Seward 1989; Seward and Barnes 1989; Hiyashi and Ohmoto, 1991). It was demonstrated above that Fe required for sulphide formation is already present in the gold system as Fe-rich carbonates. Precious metals carried as bisulphide complexes may be incorporated into the crystal lattice of the growing pyrite, arsenopyrite or other sulphide mineral. Fleet et al. (1989) suggested that arsenian pyrite was metastable and that gold was fixed by surface-controlled reactions onto faces of precipitated pyrite crystals. In sedimentary-rock hosted ores, it has been suggested that deposition of gold from bisulphide complexes into the lattice of arsenian pyrite and arsenopyrite may result from coupled redox reactions, where the gold is oxidized and thioarsenide species are reduced (Arehart et al., 1993). However, mineral chemistry, paragenetic and isotopic evidence from Bogosu and Prestea indicate that the hydrothermal fluids were generally oxidizing during gold / sulphide precipitation (Chapters 6 and 9).

This section has focussed on the precipitation of gold in solid-solution within sulphide minerals and its subsequent evolution and concentration into larger particles. However, this does not rule out the possibility that at least some of the microscopic and colloidal gold accumulated directly, as free gold, from the hydrothermal fluid by adsorption (Starling et al., 1989; Knipe et al., 1991) or precipitation (Jean and Bancroft, 1985) onto sulphide mineral surfaces. Alternatively, the microscopic and visible gold may have precipitated separately from the gold in solid solution late in the paragenetic sequence, which is consistent with its presence along sulphide fractures and grain boundaries, but

not with the presence of Au inclusions isolated within sulphide minerals. If gold precipitated at this late stage it would require a separate gold event without simultaneous precipitation of sulphide minerals. Furthermore, it requires late stage permeability in the hydrothermal conduit and the passing of large volumes of hydrothermal fluid through micropores and fractures in pyrite and arsenopyrite. It would also be necessary to explain why this late stage gold only precipitated on arsenian pyrite, and not on ordinary pyrite, marcasite and pyrrhotite which are devoid of gold. The direct accumulation of larger gold particles does not appear to be consistent with observations at Bogosu and Prestea, where sulphide mineral growth occurs before, during and after gold precipitation (Chapter 6, Table 6.1). Also, the weight of evidence from experimental and theoretical calculations shows that gold solubilities in mesothermal hydrothermal systems fall within the stability range of common sulphide minerals such as pyrrhotite, pyrite and arsenopyrite (e.g. Romberger, 1989; Shenberger and Barnes , 1989; Drummond and Ohmoto, 1985). Hence, major episodes of gold precipitation without simultaneous sulphide mineral growth may be rare in natural systems.

Implications for Metallurgy and Exploration

The metallurgical implications of the presence of invisible gold in sulphides are potentially very significant. Ten 10 wt% sulphides averaging 100 ppm of invisible gold will contribute 10 g/t to the overall grade of a gold deposit. It is unclear as to how much of the invisible gold content of gold deposits is routinely and accurately detected by the assay techniques currently in use. Also, this gold is extemely refractory to conventional extraction methods, and to the writer's knowledge has not been metallurgically tested for recovery at Prestea and Bogosu. This gold fraction will not be recovered by conventional

extraction processes. Alternatively, mill recoveries may fluctuate unexpectedly and without apparent reason due to changing proportions of microscopic and visible gold to invisible gold. The sample analysed in this study indicates that the low to moderate grade, bulk-mineable Dumassie deposit (≈ 3 million tonnes at 4 g/t) has a potential invisible gold content of ≈ 77 ppm in sulfarsenide concentrates (DM-11). It is clear that a potential resource is being lost to this mine, since it is wholly or partially non-detectable, and not recoverable by the present extraction techniques.

The potential resource of invisible gold in existing gold mining areas cannot be overstated, particularly where metamorphic, depth and/or hydrothermal gradients can be determined by other geological means. In this way, geologists can document where free-milling gold grades into refractory microscopic gold, and then extrapolate to and predict areas where concentrations of undetected solid-solution gold might exist.

Chapter 8: Carbonate Mineral Chemistry and Paragenesis

Carbonate minerals are common and ubiquitous throughout all rock types in the Bogosu and Prestea districts. Their phase and compositional variations and relationships give valuable information about certain aspects of the physico-chemical conditions of the hydrothermal system, prior to and during mineralization. Calcite, ankerite, siderite, magnesite and dolomite are preserved in both mining districts. Phase appearance primarily is a function of host-rock type and the conditions of hydrothermal or metamorphic alteration (Phillips and Brown, 1987). More important to this study is that many investigators have demonstrated that compositional variations of individual carbonate phases are essentially independent of host-rock and fluid compositional changes, and vary little with pressure. Some co-existing pairs such as calcite and dolomite show compositional variations that are sensitive to a wide range of temperatures which makes them useful as a sliding scale geothermometer (i.e. Harker and Tuttle, 1955; Hutcheon and Moore, 1973; Nesbitt and Essene, 1982; Essene, 1983).

In the Bogosu and Prestea districts, least-altered, lower-greenschist facies dikes with no other evidence of subsequent deformation and alteration, contain calcite disseminated throughout the matrix and in veinlets. Pervasive carbonation of the dikes prior to the onset of sulphidation resulted in an intergrowth of abundant siderite and ankerite in the rock, and complete replacement of calcite (Plate 8.1F). This assemblage is an alteration from, and overprints the pre-existing chlorite-epidote-calcite-quartz assemblage. Typically, carbonates comprise 25 to 60 modal % of these rocks, and siderite constitutes 30 to 50 modal % of the total carbonate. One sample of carbonated dike (C-4) was separated into matrix carbonate, carbonate from vein material

parallel to the general foliation, and carbonate from veins perpendicular to foliation. The highest siderite to ankerite ratios (3:2) occurred in matrix material, whereas vein carbonate parallel to foliation had a siderite:ankerite ratio of 6:7. In vein carbonate perpendicular to foliation this ratio was 1:7, demonstrating the influence of hydrothermal fluids in the precipitation of ankerite carbonates. Finally, during hydrothermal mineralization, only ankerite continued to form, mainly in veins. Also, most siderite and some ankerite was consumed by the sulphidation reactions to produce pyrite, arsenopyrite and other sulphides.

As previously discussed in the section on whole rock geochemistry, FeO remained relatively immobile and MgO, MnO and CaO underwent minor to moderate depletions during alteration. Since there is no addition to the major metal-oxide components of carbonate minerals during hydrothermal processes their abundance and phase-type is primarily controlled by host-rock composition . Primary CO_2 fluid inclusions are abundant in vein quartz from all rock types examined, demonstrating the pervasive influence of a CO_2-rich hydrothermal fluid necessary for carbonation of the rocks.

Mafic dikes appear to have been less permeable to hydrothermal solutions and not as easily sheared and tectonized as the sediments. Consequently, the extent of carbonation was controlled by the degree of fracturing, plus an additional zone of pervasive diffusion of hydrothermal fluids for up to several meters into the matrix of non-tectonized dikes. Carbonation originates from structural conduits in the sediments, and affects adjacent dikes for up to several tens of meters. Some of the larger dikes grade from highly tectonized, altered and mineralized zones adjacent to the structural conduits to least-altered greenschist facies rock in the distal portions. Smaller dikes may be entirely

enclosed within tectonized zones, and in such instances, may be totally carbonated and mineralized (e.g. Figure 3.4).

Samples of least-altered sedimentary rocks devoid of mineralization and preserving primary features such as sedimentary layering (e.g. Plate 4.1B) contain intergrown siderite and ankerite. This mineral assemblage is equivalent to carbonated dikes, suggesting that pervasive carbonation affected all sedimentary rocks within the ± 1 km wide structural zone of the Ashanti Belt. This may be due to greater shearing, fracturing and permeability of the sedimentary units since they are less competent than the dikes. Also, the dikes are late additions to the stratigraphy and may not be as affected by alteration. Sedimentary rock samples were not taken outside of the ± 1 km wide structural zone; therefore it is not possible to determine precisely what the pre-carbonation metamorphic assemblage of these rocks may have been. However, the dikes are a good guide and indicate that a lower-greenschist facies assemblage is most probable.

The proportion of siderite to ankerite is usually greater in the carbonaceous sedimentary rocks than in the dikes, even though dikes have much greater iron contents (see Tables 5.1 and 5.4). Average FeO:MgO ratios in whole-rock analyses are slightly higher in sedimentary rocks than in dikes, being about 3:1 vs 2.5:1, respectively. Abundant chlorite in the pelitic, carbonaceous portions of rythmically banded sedimentary layers may have acted as an MgO sink and further increased the effective FeO:MgO ratio during carbonation, thereby increasing siderite stability. In one sample of typical host-rock turbidite (BS-84 #16), an increasing amount of fine-grained carbonaceous (pelitic) component correlated with an increasing siderite to ankerite ratio in the rock. In this sample, the siderite to ankerite ratio in modal % was 2:5 in the clastic base, 3:2

in moderately carbonaceous portions and 2:1 in finely laminated carbonaceous tops of the turbidite layer.

Mineralization of the sediments produced the same results as in the dikes, with sulphidation of siderite ± ankerite to pyrite and minor sulphide phases. Along with vein precipitation of ankerite, this resulted in a carbonate assemblage dominated by ankerite, with minor or no siderite.

The lone sample of ultramafic intrusion from the Prestea mine footwall (P-34) is pervasively carbonate altered as well. The carbonate in this rock is dominated by porphyroblastic magnesite grains, intergrown with subordinate, slightly ferroan dolomite. This is another example of host-rock control over the carbonate phases present.

Carbonate Mineral Chemistry

Carbonate mineral chemistry was investigated using the JEOL JXA 8600 Superprobe at the University of Western Ontario. One hundred and seventy-nine analyses were obtained from carbonates in all major host-rock and ore types of the Bogosu and Prestea districts. Variations in wt% CaO, MgO, FeO and MnO were determined, and these are listed in Appendices 8.1 and 8.2.

Manganese is a minor component in almost all carbonates. Carbonates in mafic dike rocks contain between 0.3 and 1.2 wt% MnO, while those in sedimentary rocks contain typically less than 1.0 wt% MnO. However, 2 isolated values of up to 4.2 wt%, and several in the range of 2 to 3 wt% MnO occur in carbonates of the sedimentary rocks. Also, one magnesite grain from the ultramafic intrusion returned a value of 12.5 wt% MnO (analysis P-34

#104). Overall, the MnO concentrations in carbonates are not high enough to affect the results of this study in any significant way, and consequently are ignored for the balance of this discussion.

The remaining data for CaO, MgO and FeO have been converted to mol% $CaCO_3$, $MgCO_3$ and $FeCO_3$ and recalculated to 100% to conform with standard methods for the presentation and interpretation of carbonate data. The recalculated data are listed in Tables 8.1 and 8.2, and the entire data set is illustrated in the ternary diagram of Figure 8.1.

There is little variation in the mol% $CaCO_3$ of the various carbonates illustrated. Siderites contain generally less than 1 mol% $CaCO_3$, ankerites cluster around 50 ± 3 mol% $CaCO_3$ and calcites vary in the range of 96 to 98 mol% $CaCO_3$. A few anomalous carbonates plotting between normal siderite and ankerite are most likely metastable compositions.

The most important aspects of the mineral chemistry are large variations in the $FeCO_3$:$MgCO_3$ ratio for all carbonate phases analysed. There is a full range of compositions along the magnesite-siderite join, varying from < 0.1 to 98 mol% $FeCO_3$, although the majority of siderite data fall within the range of 50 to 90 mol% $FeCO_3$. Dolomite-ankerite data fill the range of compositions between ≈ 5 and 28 mol% $FeCO_3$. Calcites contained a maximum of 2.9 mol% $FeCO_3$ and 1.7 mol% $MgCO_3$. The analyses presented here are typical of carbonates for greenschist to sub-greenschist facies conditions, in the range of 400°C or less as demonstrated by Anovitz and Essene (1987).

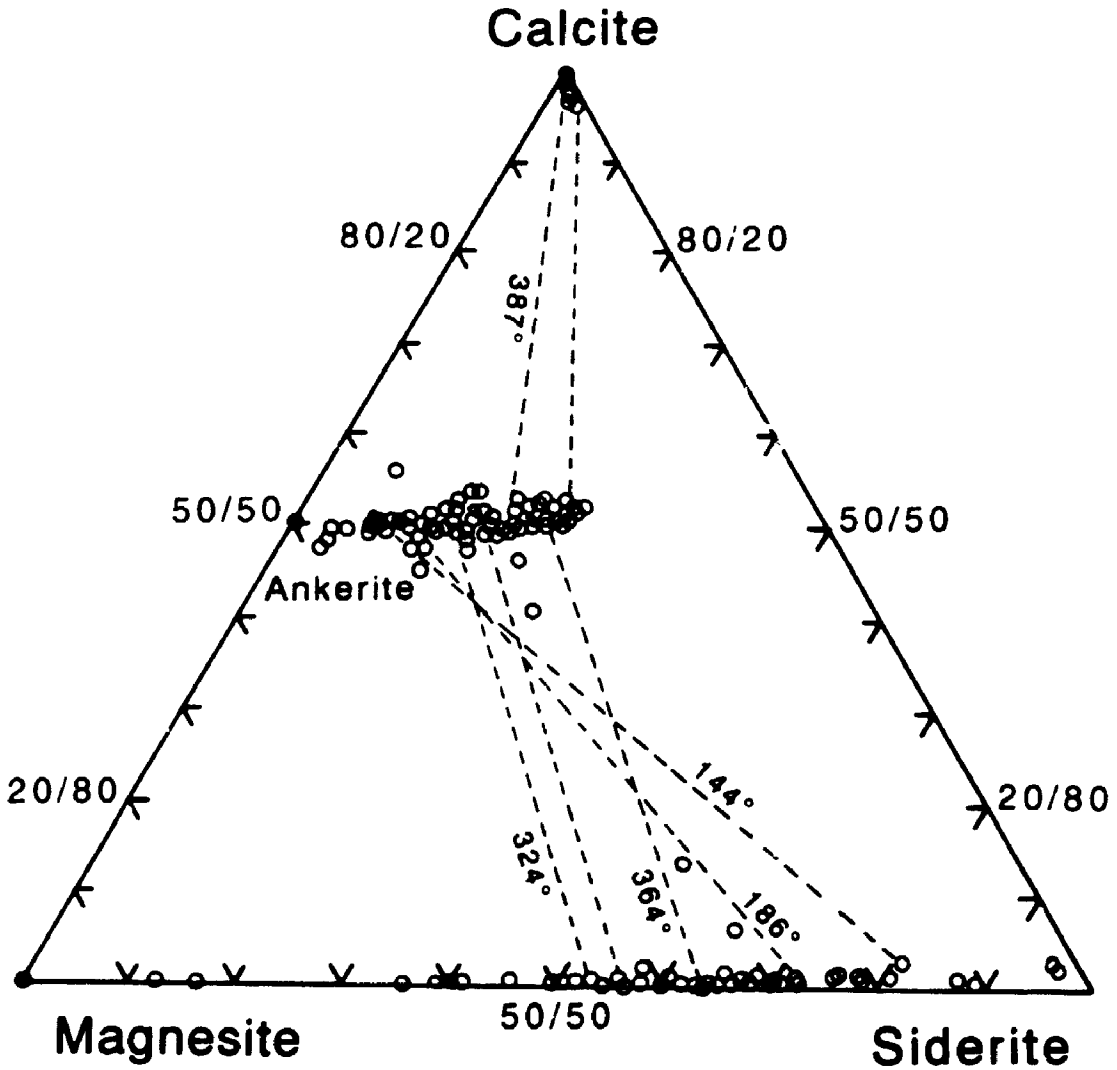

Figure 8.1: Ternary plot of carbonate mineral chemical analyses (mol%). $CaCO_3$ + $MgCO_3$ + $FeCO_3$ recalculated to 100%. All Bogosu and Prestea data are presented. Tie lines are for selected coexisting phases and are steeper for higher formation temperatures (T°C).

Table 8.1: Carbonate mineral chemical analyses and temperature estimates, Bogosu district.

***Sample category	Analysis #	Mol % $CaCO_3$	Mol % $MgCO_3$	Mol % $FeCO_3$	*Total	Temperature **(± 30°C)	Relative timing	Basis for equilibrium
graphitic crush zone ore	1	0.4	42.3	57.3	100	214	E	ss
graphitic crush zone ore	2	1.1	11.9	87.0	100	137	L	ss
graphitic crush zone ore	3	2.5	16.2	81.3	100	**144**	mL	gc
graphitic crush zone ore	4	49.9	41.2	8.9	100	**144**	L	gc
graphitic crush zone ore	5	50.3	40.6	9.2	100	137	L	ss
graphitic crush zone ore	6	13.4	31.4	55.2	100	<393	L	gc
graphitic crush zone ore	7	40.7	32.1	27.2	100	<393	L	gc
graphitic crush zone ore	8	50.4	42.3	7.3	100	**163-216**		gc
graphitic crush zone ore	9	50.3	42.4	7.4	100	**163-216**		gc
graphitic crush zone ore	10	0.6	49.1	50.3	100	**216**	E	gc
graphitic crush zone ore	11	1.6	30.3	68.1	100	**163**	L	gc
graphitic crush zone ore	12	1.3	26.8	71.9	100	**186**	E	gc
graphitic crush zone ore	13	47.8	39.8	12.5	100	**186**	E	gc
graphitic crush zone ore	14	46.3	30.7	23.0	100	**278**	L	gc
graphitic crush zone ore	59	0.2	45.5	54.2	100	**296**	E	gc
graphitic crush zone ore	60	49.5	36.9	13.7	100	**296**	E	gc
graphitic crush zone ore	61	0.3	46.4	53.3	100	**324**	E	gc
graphitic crush zone ore	62	49.2	35.9	14.8	100	**324**	E	gc
carbonated-dike ore	15	53.2	27.2	19.6	100	323	E	est
carbonated-dike ore	16	50.6	40.2	9.2	100	184	mL	est
carbonated-dike ore	17	50.6	42.0	7.4	100	169	L	est
carbonated-dike ore	18	52.8	27.5	19.8	100	322	E	est
graphitic crush zone ore	19	49.9	41.7	8.4	100	217	L	est
graphitic crush zone ore	20	50.3	42.2	7.5	100	206	L	est
graphitic crush zone ore	21	51.7	34.7	13.6	100	310	E	est
graphitic crush zone ore	22	51.7	33.8	14.6	100	328	E	est
graphitic crush zone ore	23	51.1	34.5	14.4	100	323	E	est
phyllitic sedimentary-rock ore	24	0.2	58.7	41.1	100	382		ss

Table 8.1 (continued)

***Sample category	Analysis #	Mol % $CaCO_3$	Mol % $MgCO_3$	Mol % $FeCO_3$	*Total	Temperature **(± 30°C)	Relative timing	Basis for equilibrium
phyllitic sedimentary-rock ore	25	0.3	58.8	40.9	100	384		ss
phyllitic sedimentary-rock ore	26	0.2	59.1	40.7	100	387		ss
phyllitic sedimentary-rock ore	27	0.2	58.6	41.3	100	381		ss
phyllitic sedimentary-rock ore	28	0.2	58.7	41.1	100	382		ss
phyllitic sedimentary-rock ore	29	0.3	59.9	39.8	100	397		ss
phyllitic sedimentary rock ore	30	0.2	54.3	45.4	100	340		ss
phyllitic sedimentary-rock ore	31	50.4	37.4	12.1	100	340-397		ss
carbonated-dike ore	32	52.6	23.0	24.5	100	360		ss
carbonated-dike ore	33	51.3	30.5	18.3	100	288		ss
carbonated-dike ore	34	51.1	25.0	23.9	100	336		ss
carbonated-dike ore	35	51.4	28.0	20.6	100	286		ss
carbonated-dike ore	36	51.3	27.3	21.4	100	297	L	ss
carbonated-dike ore	37	48.5	34.7	16.9	100	257	E	ss
carbonated-dike ore	38	50.0	36.7	13.4	100	222	E	ss
carbonated-dike ore	39	51.9	22.6	25.5	100	374	vL	ss
carbonated-dike ore	40	50.9	23.8	25.3	100	361	vL	ss
carbonated-dike ore	41	50.5	24.7	24.8	100	346		ss
carbonated-dike ore	42	50.1	26.1	23.8	100	**325-364**		gc
carbonated-dike ore	43	6.2	30.1	63.8	100	**364**	L	gc
carbonated-dike ore	44	0.6	28.3	71.1	100	**325**	vL	gc
carbonated-dike ore	45	ND	ND	ND				
carbonated-dike ore	47	51.6	22.8	25.6	100	373		ss
carbonated-dike ore	48	49.9	36.4	13.7	100	225	E-1	est
carbonated-dike ore	49	49.7	44.8	5.6	100	155	M-2	est
carbonated-dike ore	50	49.3	42.1	8.6	100	177	M-3	est
carbonated-dike ore	51	50.1	35.5	14.4	100	234	L-4	est
carbonated-dike ore	52	50.1	32.7	17.2	100	267	L-5	est
carbonated-dike ore	53	0.6	10.5	88.9	100	155	vL	ss
carbonated-dike ore	54	0.3	33.8	65.8	100	**274**	L	gc
carbonated-dike ore	55	50.2	32.6	17.2	100	**263-274**	L	gc

Table 8.1 (continued)

***Sample category	Analysis #	Mol % $CaCO_3$	Mol % $MgCO_3$	Mol % $FeCO_3$	*Total	Temperature **(± 30°C)	Relative timing	Basis for equilibrium
carbonated-dike ore	56	49.8	28.9	21.4	100	511	E	gc
carbonated-dike ore	57	0.5	48.0	51.5	100	511	E	gc
carbonated-dike ore	58	0.7	32.1	67.2	100	263	L	gc
banded turbidite	63	2.6	2.1	95.3	100	131		est
banded turbidite	64	2.0	2.2	95.8	100	131		est
greywacke	65	53.1	25.1	21.8	100	131		est
greywacke	66	47.2	34.9	18.0	100			
greywacke	67	53.1	24.5	22.4	100	131		est
greywacke	68	50.7	25.3	23.9	100	131		est
graphitic crush zone ore	69	0.3	29.9	69.8	100	297		ss
graphitic crush zone ore	70	1.3	23.4	75.3	100	248		ss
graphitic crush zone ore	71	0.3	21.1	78.5	100	231		ss
graphitic crush zone ore	72	49.9	29.0	21.1	100	311		gc
graphitic crush zone ore	73	0.7	31.5	67.9	100	311		gc
carbonated dike	74	51.1	26.3	22.6	100	389-400		gc
carbonated dike	75	0.4	36.3	63.3	100	400		gc
carbonated dike	76	0.5	35.3	64.1	100	389		gc
mineralized veinlet in least-altered dike	77	50.2	29.0	20.8	100	387		gc
mineralized veinlet in least-altered dike	78	96.6	1.7	1.7	100	387		gc
mineralized veinlet in least-altered dike	79	97.4	1.2	1.4	100	342		ss
least-altered mafic dike, carb porphyroblasts	80	95.8	1.2	2.9	100	358		gc
least-altered mafic dike, carb porphyroblasts	81	51.8	22.4	25.8	100	358		gc
least-altered mafic dike, carb porphyroblasts	82	52.5	24.4	23.1	100	350		gc
least-altered mafic dike, carb porphyroblasts	83	96.3	1.1	2.7	100	346		gc
least-altered mafic dike, carb porphyroblasts	84	52.5	26.3	21.2	100	342		ss
least-altered mafic dike	85	98.4	0.7	0.9	100	? 292		est
least-altered mafic dike	86	98.1	0.7	1.2	100	? 296		est
graphitic-phyllite ore	87	49.4	30.7	19.9	100	333	E-1	ss
graphitic-phyllite ore	88	49.3	33.8	16.9	100	290	E-2	ss
graphitic-phyllite ore	89	49.6	32.0	18.4	100	315	E-3	ss

Table 8.1 (continued)

***Sample category	Analysis #	Mol % $CaCO_3$	Mol % $MgCO_3$	Mol % $FeCO_3$	*Total	Temperature **(± 30°C)	Relative timing	Basis for equilibrium
graphitic-phyllite ore	90	49.0	35.2	15.9	100	274	E-4	ss
graphitic-phyllite ore	91	49.2	31.5	19.2	100	328	E-5	ss
graphitic-phyllite ore	92	0.4	41.7	57.9	100	**323**	M	gc
graphitic-phyllite ore	93	0.2	64.1	35.7	100	628	E	ss
graphitic-phyllite ore	94	0.1	34.9	60.0	95	285	L	ss
graphitic-phyllite ore	95	48.4	34.4	17.1	100	**306-406**		ss
graphitic-phyllite ore	96	45.0	40.5	14.5	100			
graphitic-phyllite ore	96R	47.5	38.9	13.6	100			
graphitic-phyllite ore	97	0.1	37.6	62.3	100	290		ss
graphitic-phyllite ore	98	0.3	39.7	60.1	100	**306**	M	gc
graphitic-phyllite ore	99	0.3	50.2	49.5	100	[illegible]	M	gc
graphitic-phyllite ore	100	0.2	61.1	38.8	100	565	E	ss
graphitic-phyllite ore	101	0.1	43.3	56.6	100	**336**	L	gnc
graphitic-phyllite ore	102	0.2	38.1	61.7	100	294	L	ss

* = total recalculated to 100%

** = Maximum uncertainty = ± 30°C for grains with physical contact.

*** = see Appendix 8.3 for sample descriptions

E, M, L=relative timing with respect to co-existing carbonates in same section (E=early, M=middle, L=late).

Basis for equilibrium: direct grain contact (gc), grains in same section but not in physical contact (ss), or estimated from similar carbonates in other sections (est). The most reliable temperatures are shown in bold.

Temperature estimation for Ank-Sid pairs from Kd=($FeCO_3/MgCO_3$)Ank/($FeCO_3/MgCO_3$)Sid (Mol%)=-.691+.00176T (T,K) (Anovitz and Essene,1986)

Temperature estimation for Calc-Ank pairs from graphical procedure of Powell et al., 1984.

Table 8.2: Carbonate mineral chemical analyses and temperature estimates, Prestea district.

***Sample category	Analysis #	Mol % $CaCO_3$	Mol % $MgCO_3$	Mol % $FeCO_3$	*Total	Temperature ** (± 30°C)	Relative timing	Basis for equilibrium
quartz vein ore	105	50.1	37.2	12.7	100	218	E	est
quartz vein ore	106	50.2	29.1	20.7	100	372	L	est
quartz vein ore	107	54.0	30.5	15.5	100	301	mL	est
quartz vein ore	108	56.1	37.2	6.7	100	172	E	est
quartz vein ore	109	53.4	31.4	15.1	100	290	mL	est
quartz vein ore	110	51.8	32.2	16.0	100	296	mL	est
quartz vein ore	111	51.5	33.7	14.8	100	275	mL	est
quartz vein ore	112	51.4	36.4	12.3	100	217	E	est
quartz vein ore	113	49.5	38.5	12.0	100	209	E	est
quartz vein ore	114	49.8	38.5	11.7	100	208	E	est
quartz vein ore	115	50.1	40.2	9.7	100	189	E	est
quartz vein ore	116	49.6	38.6	11.8	100	208	E	est
quartz vein ore	117	50.3	32.9	16.8	100	301	L	est
least-altered mafic dike	118	99.0	0.4	0.6	100			
least-altered mafic dike	119	98.1	0.8	1.1	100			
least-altered mafic dike	120	98.4	0.5	1.1	100			
least-altered mafic dike	120 R	98.6	0.5	0.9	100			
least-altered mafic dike	121	98.3	0.7	1.0	100			
carbonated-dike ore	122	52.2	21.5	26.3	100	554	L	est
carbonated-dike ore	123	50.7	28.1	21.1	100	336	E	est
carbonated-dike ore	124	50.6	28.6	20.9	100	330	L	est
carbonated-dike ore	125	50.5	29.4	20.2	100	318	L	est
carbonated-dike ore	126	49.7	34.7	15.6	100	249	M	est
carbonated-dike ore	127	51.2	24.2	24.7	100	482	E & L	est
carbonated-dike ore	128	49.6	33.6	16.7	100	263	E	est
carbonated-dike ore	129	50.0	30.9	19.1	100	339	L	est
phyllite	130	48.7	31.8	19.5	100	367		ss
phyllite	131	50.1	32.0	18.0	100	346		ss

Table 8.2 (continued) ***Sample category	Analysis #	Mol % $CaCO_3$	Mol % $MgCO_3$	Mol % $FeCO_3$	*Total	Temperature ** (± 30°C)	Relative timing	Basis for equilibrium
phyllite	132	49.6	31.4	19.0	100	363		gc
phyllite	133	1.9	40.7	57.4	100	363	E	gc
phyllite	134	0.7	43.7	55.6	100	390	E	gc
phyllite	135	0.6	32.6	66.9	100	287	L	gc
phyllite	136	0.8	41.6	57.7	100	367	E	ss
phyllite	137	0.3	32.8	66.9	100	288	L	ss
graphitic fissure ore	138	50.0	36.5	13.5	100	250	M	est
graphitic fissure ore	139	48.3	38.8	13.0	100	216	M	est
graphitic fissure ore	140	52.6	33.4	14.1	100	269	E	est
graphitic fissure ore	141	49.4	39.2	11.4	100	203	L	est
graphitic fissure ore	142	49.2	43.3	7.6	100	170	E-1	est
graphitic fissure ore	143	51.7	31.1	17.3	100	317	L-4	est
graphitic fissure ore	144	49.4	39.4	11.2	100	202	M-2	est
graphitic fissure ore	145	49.8	37.8	12.5	100	215	M-3	est
graphitic-phyllite ore	146	50.1	32.6	17.3	100	243-275	L	ss
graphitic-phyllite ore	147	50.7	26.9	22.4	100	461	E	ss
graphitic-phyllite ore	148	1.7	33.4	64.9	100	275-292	L	gc
graphitic-phyllite ore	149	50.2	31.3	18.5	100	257-292	L	gc
graphitic-phyllite ore	150	51.3	23.7	25.0	100	551	E	ss
graphitic-phyllite ore	151	1.0	41.5	57.5	100	551	E	ss
graphitic-phyllite ore	152	1.0	28.8	70.2	100	243-257	L	gc
graphitic-phyllite ore	153	0.6	26.9	72.5	100	244		ss
sedimentary-phyllite ore	154	49.9	29.6	20.5	100	238		gc
sedimentary-phyllite ore	155	49.8	32.0	18.2	100	217		gc
sedimentary-phyllite ore	156-R	1.5	22.8	75.7	100	217-238		gc
sedimentary-phyllite ore	157	1.0	21.0	77.9	100	207-226		ss
ultramafic intrusion	103	49.6	46.5	4.0	100			
ultramafic intrusion	104	0.1	99.9	0.1	100			
ultramafic intrusion	158	50.9	38.7	10.4	100			
ultramafic intrusion	159	48.5	47.4	4.1	100			

Table 8.2 (continued) ***Sample category	Analysis #	Mol % $CaCO_3$	Mol % $MgCO_3$	Mol % $FeCO_3$	*Total	Temperature ** (± 30°C)	Relative timing	Basis for equilibrium
ultramafic intrusion	160	0.1	83.7	16.3	100			
ultramafic intrusion	161	0.1	87.4	12.6	100			
ultramafic intrusion	162-R	47.7	48.4	3.9	100			
ultramafic intrusion	163	51.0	38.5	10.5	100			
ultramafic intrusion	164	0.1	87.4	12.6	100			
ultramafic intrusion	165	0.0	83.5	16.5	100			
Phyllite	166	0.5	34.9	64.6	100	**372**		gc
Phyllite	167	50.0	27.4	22.6	100	**372**		gc
Phyllite	168	51.4	28.3	20.3	100	**329**		gc
Phyllite	169	0.7	33.7	65.6	100	**329**		gc
carbonate-altered dike	170	50.9	28.2	21.0	100	**385**	E	gc
carbonate-altered dike	171	0.5	38.4	61.1	100	**385**	E	gc
carbonate-altered dike	172	0.4	37.8	61.9	100	**360**	E	gc
carbonate-altered dike	173	1.1	18.2	80.7	100			
carbonate-altered dike	174	51.4	28.8	19.9	100	**360**	E	gc
spotted carbonaceous phyllite	175	0.9	38.6	60.5	100	**372**		gc
spotted carbonaceous phyllite	176	49.6	29.7	20.7	100	**372**		gc
spotted carbonaceous phyllite	177	0.3	41.7	58.0	100	320	L	ss
spotted carbonaceous phyllite	178	0.3	45.3	54.4	100	**390**	E	gc
spotted carbonaceous phyllite	179	48.8	32.6	18.6	100	**390**	E	gc

* = total recalculated to 100%

** = Maximum uncertainty = ± 30°C for grains with physical contact.

*** = see Appendix 8.4 for sample descriptions

E, M, L=relative timing with respect to co-existing carbonates in same section (E=early, M=middle, L=late).

Basis for equilibrium: direct grain contact (gc), grains in same section but not in physical contact (ss), or estimated from similar carbonates in other sections (est). The most reliable temperatures are shown in bold.

Temperature estimation for Ank-Sid pairs from Kd=($FeCO_3/MgCO_3$)Ank/($FeCO_3/MgCO_3$)Sid (Mol%)=-.691+.00176T (T,K) (Anovitz and Essene,1986)

Temperature estimation for Calc-Ank pairs from graphical procedure of Powell et al., 1984.

Calcite-Dolomite Geothermometry

It has been demonstrated by several investigators that co-existing calcite-dolomite pairs can be used to derive temperatures of formation. This is possible because compositional variations in individual carbonate phases are caused by changes in formation temperature, and essentially are independant of host-rock and hydrothermal fluid compositional variations and differences in pressure. Examples include Harker and Tuttle (1955), Hutcheon and Moore (1973), Nesbitt and Essene (1982), Essene (1983) and Pan et al. (1992). Because of the high iron contents of the present carbonates, recent studies of the effects of increasing $FeCO_3$ on carbonate geothermometry are most important to this investigation. These studies include Bickle and Powell (1977), Powell et al. (1984), Barron (1974) and Anovitz and Essene (1987).

There are two main approaches to calcite-dolomite geothermometry. Bickle and Powell (1977) experimentally calibrated this geothermometer using equilibrium constants and plotted:

$$K_D, \text{Ank/Cc} = (X^{Fe}/X^{Mg})_{Ank}/(X^{Fe}/X^{Mg})_{Cc} \text{ vs Temperature} \qquad (8\text{-}1)$$

where,

K_D, Ank/Cc = distribution constant for ankerite and calcite

X^{Fe} = mole fraction $FeCO_3$

X^{Mg} = mole fraction $MgCO_3$

A further revision was made by Powell et al. (1984) to better calibrate the correction for iron.

This geothermometer is sensitive to resetting of the compositions of individual phases, and increases in iron content can lead to greater uncertainties. For this reason Anovitz and Essene (1987) proposed a second, empirical thermometer based on the width of the solvus in the ternary system. However, this method yielded temperatures similar to those of the Powell et al. (1984) procedure in the range of 600 to 800°C, and was not calibrated for lower temperatures in the range of the Bogosu and Prestea data. Consequently, the Powell et al. (1984) method is preferred for calcite-ankerite pairs in this study. The degree of uncertainty for carbonate geothermometers is not well constrained. For iron-free calcite-dolomite pairs, Bickle and Powell (1977) estimated accuracy to be ± 20°C, and for iron-bearing varieties, Powell et al. (1984) estimated uncertainties of less than 30°C, but rising for higher iron contents.

In Bogosu and Prestea rocks, calcite-ankerite pairs were found only in least-altered rocks that had been subjected to the earliest stages of carbonate alteration. Six co-existing grains in physical contact from two different samples and two grains from the same sections but not in physical contact are plotted on the Powell et al. (1984) temperature diagram (Figure 8.2). The mol% $FeCO_3$ in ankerite is plotted against the mol% $MgCO_3$ in calcite along with superimposed isotherms for equilibrium between calcite and dolomite.

The calcite-ankerite pairs in physical contact plot in the temperature range of 346 to 387°C. The two carbonate grains that are not in direct contact with their respective co-existing phases and originate from two different deposits both plot at 342°C. The higher temperature results come from a geologically rare situation where a quartz-ankerite vein with an outside selvage of gold-bearing arsenopyrite has invaded a least-altered dike. The result is to place

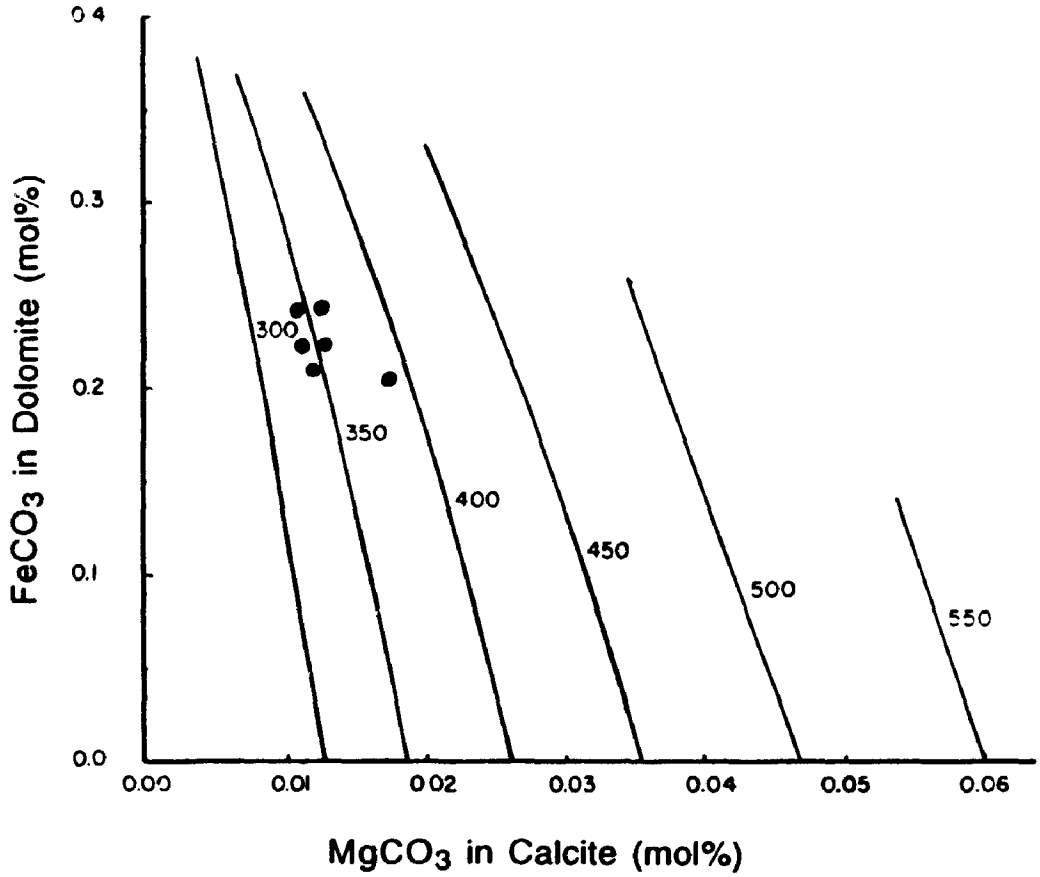

Figure 8.2: The compositions of coexisting calcite and dolomite pairs in least-altered mafic dikes from the Bogosu region plotted on the temperature (°C) diagram of Powell et al. (1984).

ankerites associated with gold deposition in direct contact with matrix calcites (Plate 8.1A). This temperature is near the upper limit for gold-deposition as determined by carbonate geothermometry. The moderately lower temperatures to 342°C are indicative of early phases of carbonate alteration in the least-altered dike assemblage.

Ankerite-Siderite Geothermometry

The vast majority of carbonates in the Bogosu-Prestea region are either: 1) ankerites from ores and veins (e.g., Plates 8.1B and 8.1E), or 2) ankerite-siderite intergrowths that occur in most rock types from least-altered sediments and dikes to their respective mineralized varieties (e.g., Plates 7.2C and 8.1F). Many of these carbonates are compositionally zoned with two types of zoning preserved: 1) oscillatory zoning occurs during carbonate growth in reponse to changes in the hydrothermal fluid (Plate 8.1B), and 2) compositional re-equilibration of rims or portions of pre-existing carbonates due to changes in ambient conditions (Plates 8.1C and 8.1D). Oscillatory zoning is most commonly displayed by ankerites in veins, whereas early-formed siderite-ankerite intergrowths grew during more uniform conditions and often are compositionally homogenous. Many of these latter carbonates have been affected by changes in hydrothermal conditions, resulting in partial or total re-equilibration and compositionally variable rims and patches. These compositional variations have little effect on the $CaCO_3$ content. However, mol% $FeCO_3$:$MgCO_3$ ratios vary from 3.5:1 to 1:1.5 in siderites, and 1.1:1 to 1:8 in ankerites.

The potential use of co-existing ankerite-siderite pairs for carbonate geothermometry was evaluated by Goldsmith et al. (1962), Rosenberg (1967)

PLATE 8.1

EMP back-scattered electron image of polished sections from Bogosu and Prestea ores: Alb-albite; Ank-ankerite; Asp-arsenopyrite; Chl-chlorite; Ep-epidote; Qtz-quartz; Rut-rutile; Sid-siderite

A: Quartz-ankerite veinlet in a least-altered dike that has a Au-bearing arsenopyrite selvage. Numbers 77 and 78 are the locations of EMP analyses listed in Appendix 8.1. This sample (C-15) is from the wallrock of the Chujah deposit, Bogosu.

B: Rythmic compositional banding of ankerite within a quartz-ankerite vein. Numbers 32 to 35 are the locations of EMP analyses listed in Appendix 8.1. This sample, (C-11) is from carbonated-dike ore from the Chujah deposit, Bogosu concession.

C: Compositional zoning of ankerite from the matrix of a mineralized carbonated dike in the Prestea mine (sample P-28D). Numbers 128 and 129 are the locations of EMP analyses listed in Appendix 8.2.

D: Compositional zoning of ankerite from a quartz vein in graphitic-fissure ore adjacent the Main Reef quartz vein in the Prestea mine (sample P-30). Numbers 140 and 141 are the locations of EMP analyses listed in Appendix 8.2.

E: Quartz vein with a selvage of compostionally-zoned ankerite, and arsenopyrite in the matrix adjacent to the vein. This sample, (C-11) is from a carbonated-dike ore from the Chujah deposit, Bogosu concession.

F: Ankerite (Ank) and siderite (Sid) intergrown with quartz (Qtz) and rutile (Rut) in the matrix of carbonate-altered mafic dike from the Prestea mine (sample P-1). Numbers 170 and 171 are the locations of EMP analyses listed in Appendix 8.2; scale bar is 100 μm.

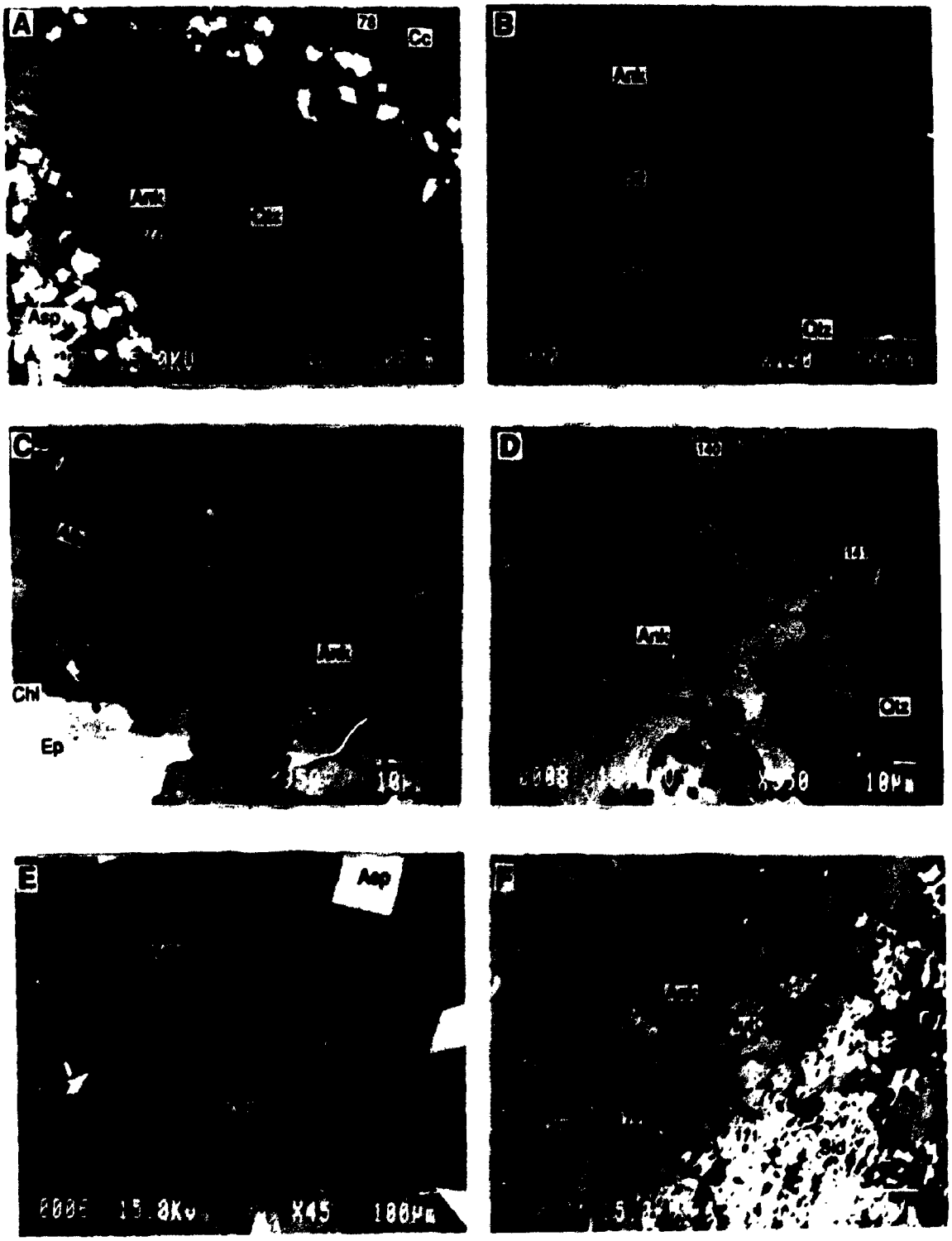
A
Ca
Ank
Ank
Asp
B
Ank
Ch
C
Ank
Chl
Ep
D
Ank
Ch
E
Asp
X45
100µm

and Talantsev and Sazonov (1979) with questionable results. More recently, Anovitz and Essene (1987) used carbonates from natural assemblages and calculated their formation temperatures by using the width of the solvus. Their data show an increase in K_D (distribution constant) with temperature. The resulting composition-based fitted function for averaged K_D values at each temperature provides a linear-sliding scale thermometer that can be applied to the Bogosu-Prestea data:

$$K_D = (X^{FeCO3}/X^{MgCO3})_{Ank} / (X^{FeCO3}/X^{MgCO3})_{Sid} = 0.691+0.00176T\ (K) \quad (8\text{-}2)$$

The accuracy of this geothermometer is not well defined, although the results can be compared to temperatures derived by other techniques available in this study. Nevertheless, the qualitative temperature differences and relationships are probably as revealing about the area being investigated as are a few isolated absolute values.

For the purpose of obtaining temperature estimates the Bogosu and Prestea data have been divided into three categories based on the degree of certainty: 1) co-existing siderite-ankerite pairs where the grains are in physical contact (e.g. Plate 8.1F), 2) ankerites or siderites not in visible physical contact, but where equilibrium with other carbonates from the same section has been inferred on the basis of compositional and textural evidence, and 3) all other grains, where an estimate of possible co-existing compositions has been made on the basis of compositionally and texturally-similar carbonates in comparable samples. For some Prestea ore samples having only ankerite present in the analyzed sections, values for X^{FeCO3}/X^{MgCO3} of possible co-existing siderite were calculated as the average value of siderite co-existing with compositionally similar ankerites in other samples.

The best estimates of actual temperatures must be taken from co-existing pairs with physical grain contact (temperatures in bold type on Tables 8.1 and 8.2). However, all categories can be used to derive qualitative information. This approach is supported by similar temperature estimates from carbonate pairs both in physical contact, and where equilibrium compositions have been inferred. The temperature data are listed in Table 8.1 for the Bogosu samples, and in Table 8.2 for the Prestea samples. All temperature estimates are illustrated on temperature vs mol% $FeCO_3$ plots in Figures 8.3 and 8.4 for Bogosu, and Figures 8.5 and 8.6 for Prestea.

The Prestea data show well defined trends of increasing temperature with: 1) increasing mol% $FeCO_3$ in ankerite, and 2) decreasing mol% $FeCO_3$ in siderite. The Bogosu samples show a similar pattern, and averaged temperature trends defined by both sample sets are nearly identical, despite the increased scatter of the Bogosu data. Ideally, the temperature vs mol% $FeCO_3$ plot should follow the temperature solvus for co-existing ankerite and siderite in equilibrium.

The majority of temperature estimates cut off sharply at about 400°C for both the Bogosu and Prestea data, with some isolated high temperature spikes between 460 and 628°C. These high temperature data may be due to anomolous or metastable compositions, or poorly estimated equilibrium phases. However, it is quite probable that at least some of these anomalously high temperatures represent true high-temperature pulses in the hydrothermal fluid. This is supported by some temperature estimates from co-existing phases in physical contact (e.g. Bogosu analyses #56 and #57, T = 511°C). The lower temperatures below 200°C fall outside the limits of calibration for the ankerite-

Figure 8.3: Ankerite, siderite and calcite formation temperatures for coexisting grains plotted against the $FeCO_3$ content of the carbonates. All data from the Bogosu district are plotted. The estimate of the temperature of peak metamorphism was derived from carbonates in non-mineralized country-rocks: Cc = calcite.

Figure 8.4: Ankerite, siderite and calcite formation temperatures for coexisting grains plotted against the $FeCO_3$ content of the carbonates. Only the most ideal data, from grains in mutal physical contact, from the Bogosu district are plotted. The estimate of the ambient country-rock temperature at the time of mineral deposition was given by the lowest formation temperature of carbonates associated with mineralization: Cc = calcite.

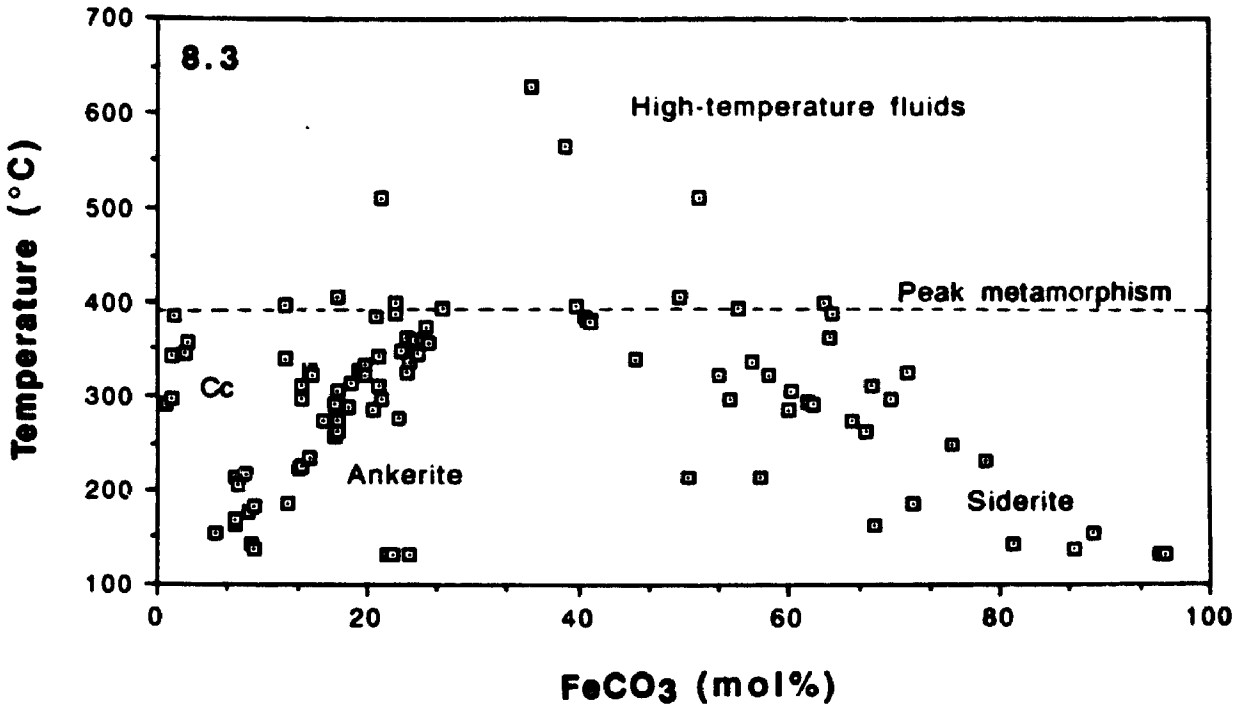
8.3
High-temperature fluids
Peak metamorphism
Cc
Ankerite
Siderite
Temperature (°C)
FeCO3 (mol%)
700
600
500
400
300
200
100
0
20
40
60
80
100

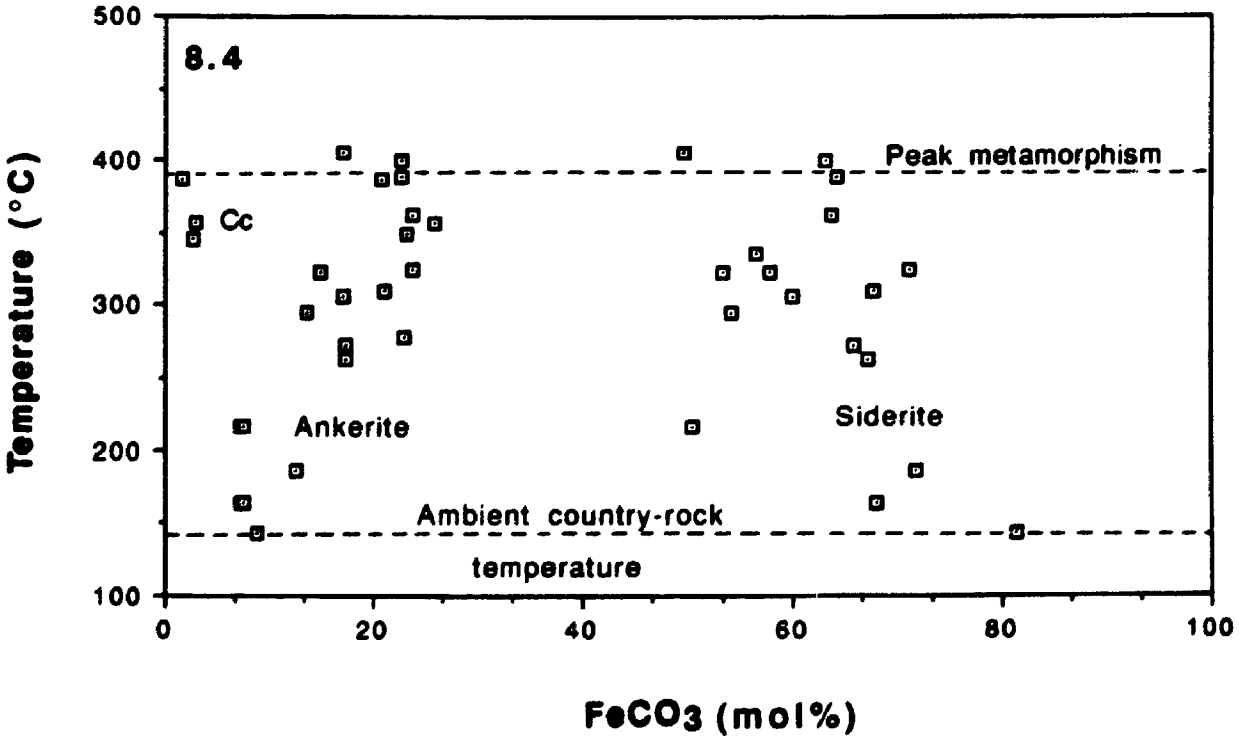
8.4
Peak metamorphism
Cc
Ankerite
Siderite
Ambient country-rock
temperature
Temperature (°C)
FeCO3 (mol%)
500
400
300
200
100
0
20
40
60
80
100

Figure 8.5: Ankerite and siderite formation temperatures for coexisting grains plotted against the $FeCO_3$ content of the carbonates. All data from the Prestea district are plotted. The estimate of the temperature of peak metamorphism was derived from carbonates in non-mineralized country-rocks.

Figure 8.6: Ankerite and siderite formation temperatures for coexisting grains plotted against the $FeCO_3$ content of the carbonates. Only the most ideal data, from grains in mutual physical contact, from the Prestea district are plotted. An estimate of the ambient country-rock temperature at the time of mineral deposition was given by the lowest formation temperature of carbonates associated with mineralization.

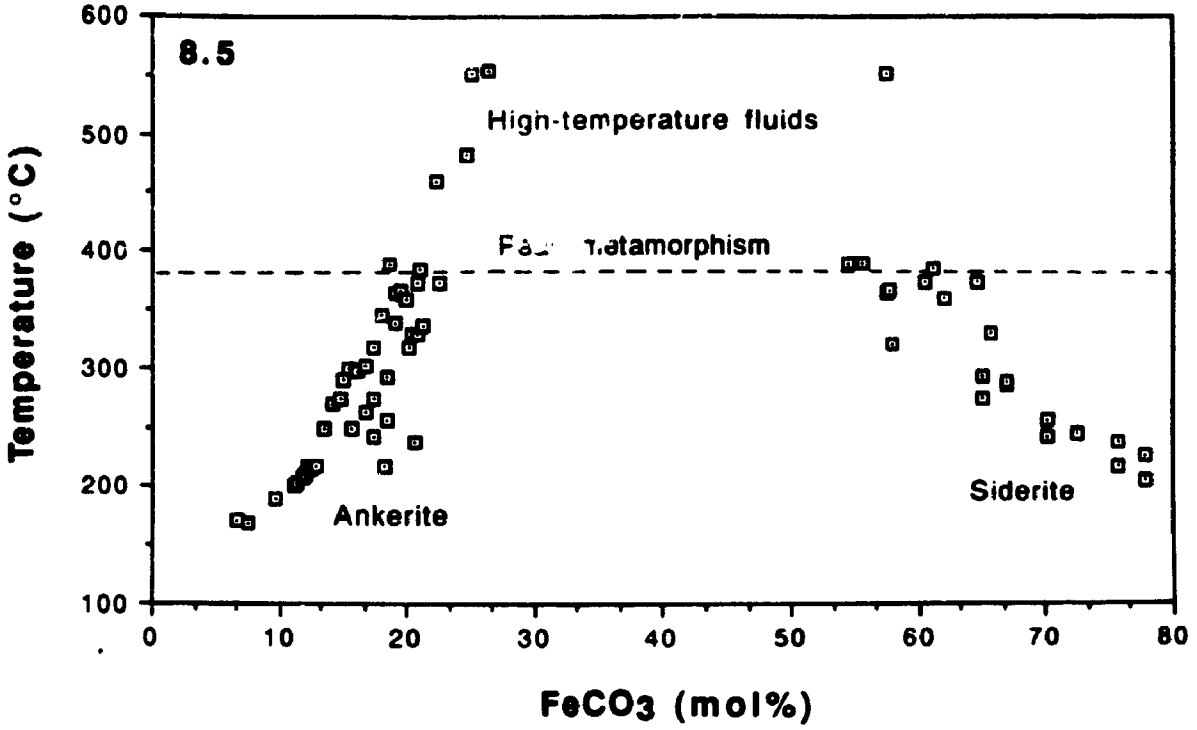
8.5
High-temperature fluids
Peak metamorphism
Ankerite
Siderite
Temperature (°C)
FeCO3 (mol%)
600
500
400
300
200
100
0
10
20
30
40
50
60
70
80

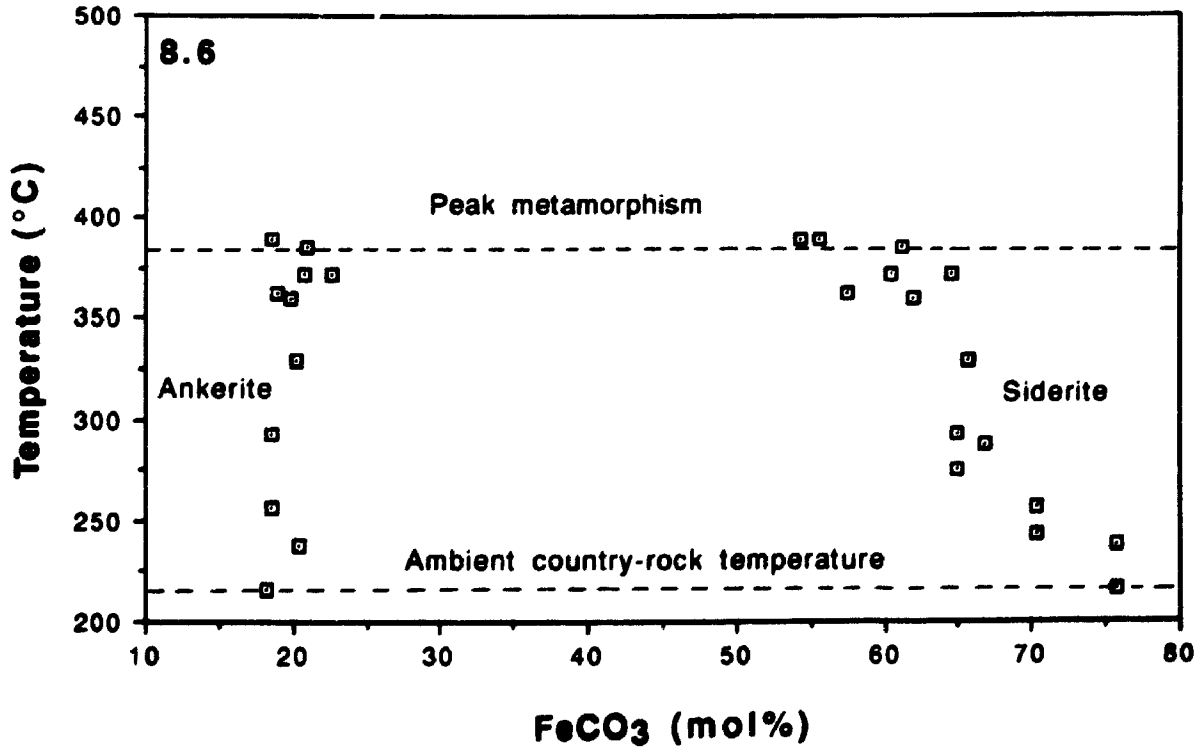
8.6
Peak metamorphism
Ankerite
Siderite
Ambient country-rock temperature
Temperature (°C)
FeCO3 (mol%)
500
450
400
350
300
250
200
10
20
30
40
50
60
70
80

siderite K_D thermometer of Anovitz and Essene (1987) (i.e. 200 - 600°C). Nevertheless, the data follow the general trend although it must be assumed that the degree of uncertainty increases in the lower temperature range.

There is little overall change in the mol% $CaCO_3$ with increasing temperature, although some minor trends can be detected (Figure 8.7). Siderites show an increase of up to 3 mol% $CaCO_3$ in the lower temperature range from 130 to 200°C. Calcites also show a tendency toward increasing mol% $CaCO_3$ with decreasing temperature; however, the calcite data available for this study are limited in number.

There is considerable scatter in the plot of mol% $MgCO_3$ vs temperature for Bogosu carbonates (Figure 8.8). Even so, within these data a very distinct linear trend is detectable for ankerites from all categories of mafic dikes. The temperature relationship for the ankerites are defined approximately by the equation:

$$T(°C) = -10.4(\text{mol\% } MgCO_3) + 600, \quad 150°C \leq T \leq 400°C \qquad (8\text{-}3)$$

Such a relationship may be useful for carbonates in similar rock types where equilibrium pairs are difficult to determine, but would have to be checked under a variety of geological conditions to estimate its reliability in other circumstances.

The most interesting information is obtained when the carbonate temperature data are segregated according to rock-type. Figure 8.9 shows the Bogosu data for sedimentary rocks only, and demonstrate that analyses from carbonates in sedimentary ores or sedimentary host-rocks are the source of the

Figure 8.7: Ankerite, siderite and calcite formation temperatures for coexisting grains plotted against the $CaCO_3$ content of the carbonates. All data from the Bogosu district are plotted.

Figure 8.8: Ankerite, siderite and calcite formation temperatures for coexisting grains plotted against the $MgCO_3$ content of the carbonates. All data from the Bogosu district are plotted.

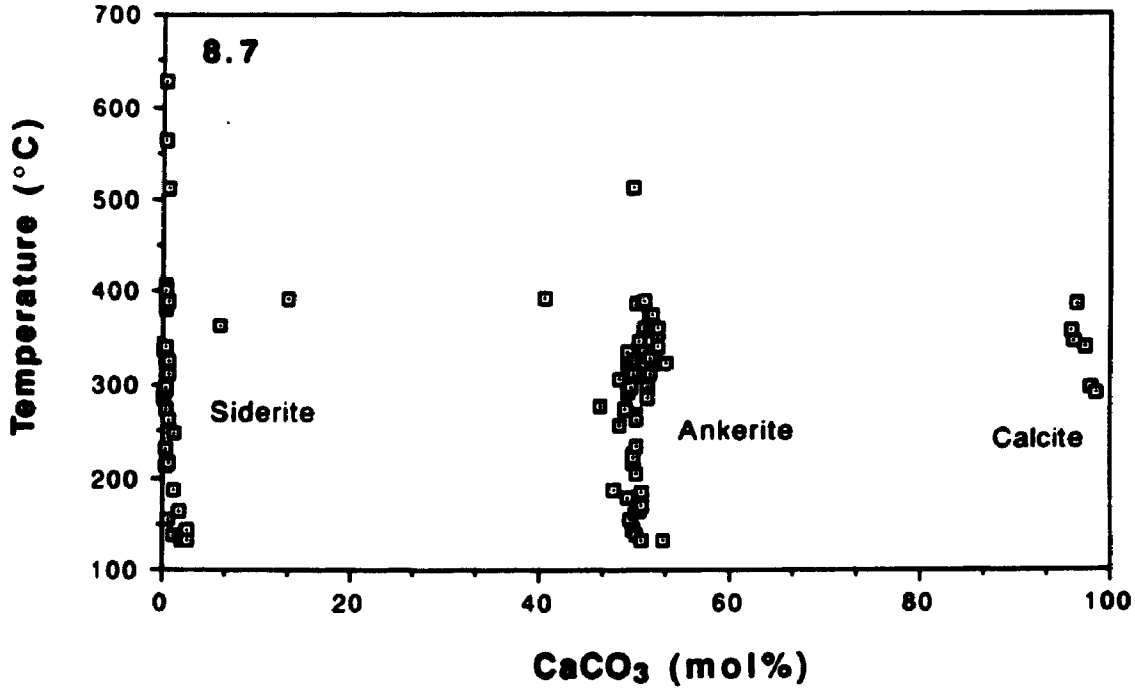
8.7
Temperature (°C)
700
600
500
400
300
200
100
Siderite
Ankerite
Calcite
0
20
40
60
80
100
CaCO3 (mol%)

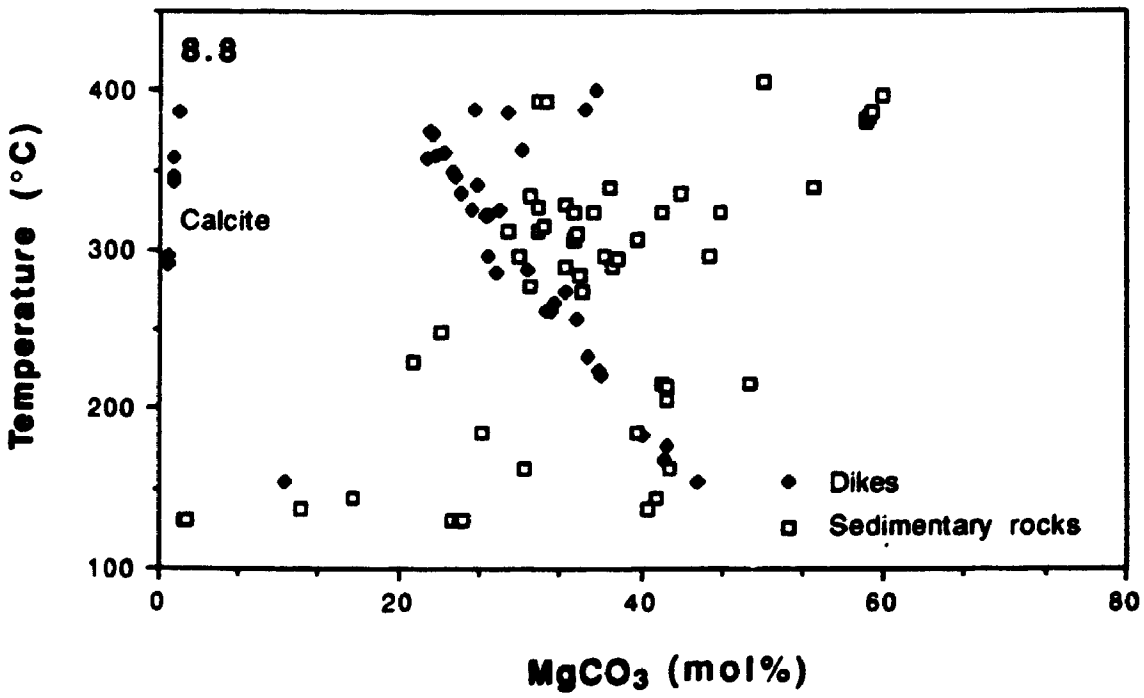
8.8
Temperature (°C)
400
300
200
100
Calcite
Dikes
Sedimentary rocks
0
20
40
60
80
MgCO3 (mol%)

Figure 8.9: Ankerite and siderite formation temperatures for coexisting grains plotted against the $FeCO_3$ content of the carbonates. Only data from sedimentary rocks of the Bogosu district are plotted.

Figure 8.10: Ankerite and siderite formation temperatures for coexisting grains plotted against the $FeCO_3$ content of the carbonates. Only data from sedimentary rocks of the Prestea district are plotted. Carbonates from the host-rocks have the highest formation temperatures. In mineralized samples there is no obvious distinction between the formation temperature of carbonates from either vein or matrix material.

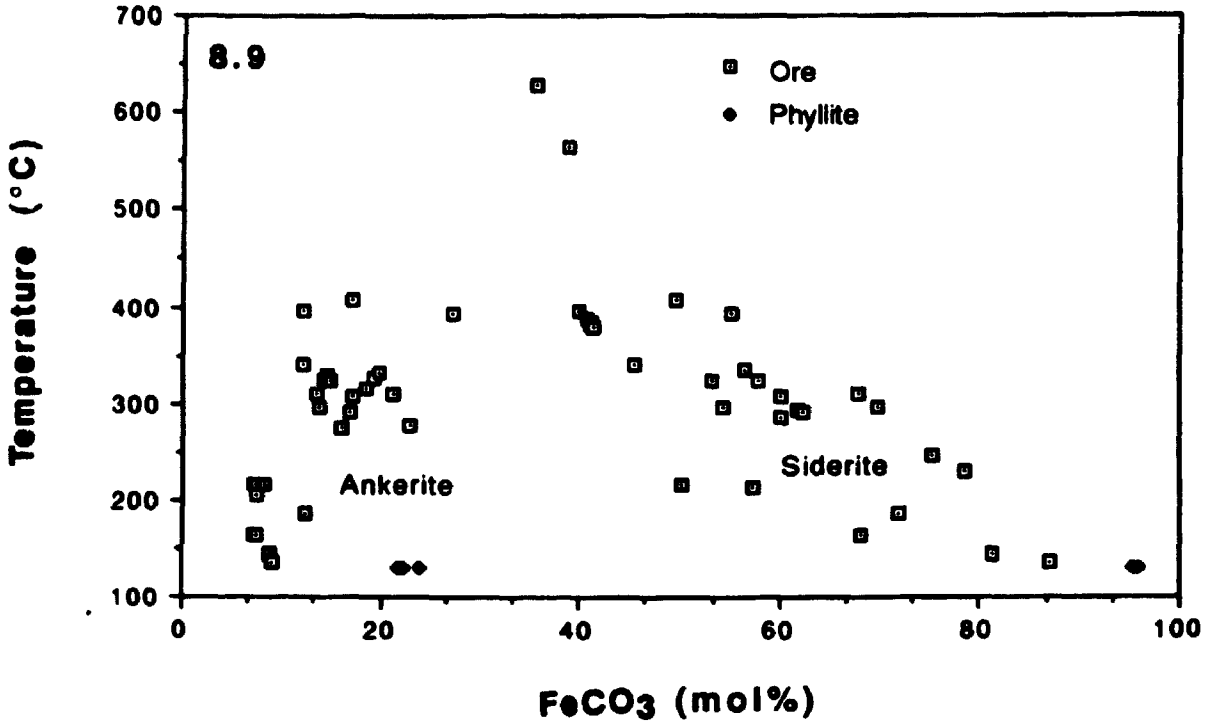
8.9
Ore
Phyllite
Ankerite
Siderite
Temperature (°C)
FeCO3 (mol%)
700
600
500
400
300
200
100
0
20
40
60
80
100

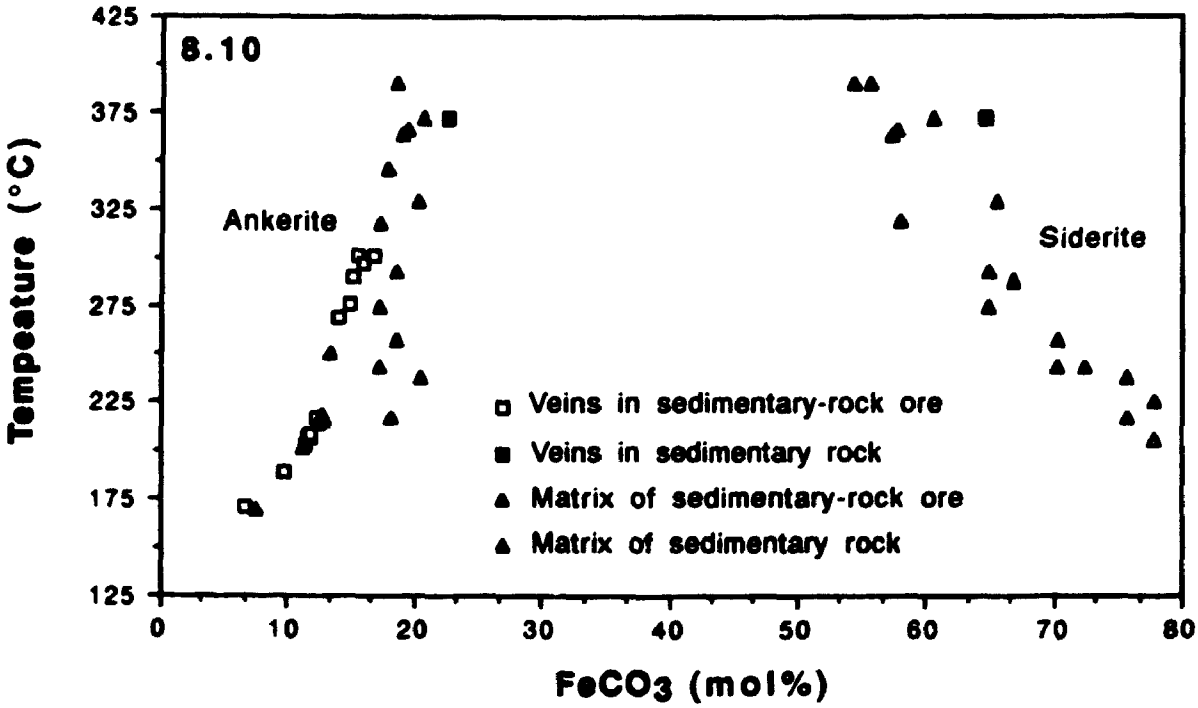
8.10
Ankerite
Siderite
Veins in sedimentary-rock ore
Veins in sedimentary rock
Matrix of sedimentary-rock ore
Matrix of sedimentary rock
Tempeature (°C)
FeCO3 (mol%)
425
375
325
275
225
175
125
0
10
20
30
40
50
60
70
80

wide scatter in the Bogosu data. The reason for greater scatter of the data in Bogosu sedimentary rocks compared to Prestea results is not clearly understood, but may be related, at least in part, to variable host rock compositions and textures within the sedimentary rocks, greater distance from the hydrothermal source, and/or poorer permeability of the host rocks and resultant lack of equilibration of the carbonate phases.

By contrast, a clearly defined temperature trend is revealed when data from Bogosu dikes only are considered. Prestea dike samples fit this trend also (Figure 8.11) and several important points are revealed from this analysis. Temperatures derived from calcite-ankerite pairs are comparable to those from ankerite-siderite pairs in similar rock types. This gives necessary credibility to the magnitude of values obtained from the ankerite-siderite K_D geothermometer of Anovitz and Essene (1987). The highest temperatures (≈ 350 to 400°C) originate from non-mineralized rocks, both carbonate-altered dikes and chlorite-epidote-calcite greenschist facies dikes. With the exception of the high-temperature spikes mentioned earlier, calcite, ankerite and siderite temperatures from both Bogosu and Prestea peak abruptly at about 400°C.

The ankerite data follow a well-defined trend of increasing temperature with increasing mol% $FeCO_3$. This is particularly true for the lower temperature data in the range of 150 to 300°C. It is possible that lower temperature carbonates (<300°C) had longer resident times in contact with hydrothermal fluids, thereby achieving good equilibration and less scatter in their compositions. More abrupt and larger fluctuations at higher temperatures could result in incomplete equilibration and greater scatter of data.

Figure 8.11: Ankerite, siderite and calcite formation temperatures for coexisting grains plotted against the $FeCO_3$ content of the carbonates. Only data from mafic dikes of the Bogosu and Prestea districts are plotted. Most of the high-temperature values are derived from carbonates in non-mineralized samples. Formation temperatures of carbonates in mineralized rocks span a wide range from about 375 to 150°C: Cc = calcite.

Figure 8.12: Ankerite and calcite formation temperatures plotted against the $FeCO_3$ content of the carbonates. Only data from mafic dikes of the Bogosu and Prestea districts are plotted. Most of the high-temperature values are derived from carbonates in non-mineralized samples. Formation temperatures of carbonates in mineralized rocks span a wide range from about 375 to 150°C. There is no obvious difference in the formation temperature of carbonates from vein or matrix material:

CD carbonated dike

CDO carbonated-dike ore

B Bogosu district

P Prestea district

mtx matrix

vn vein

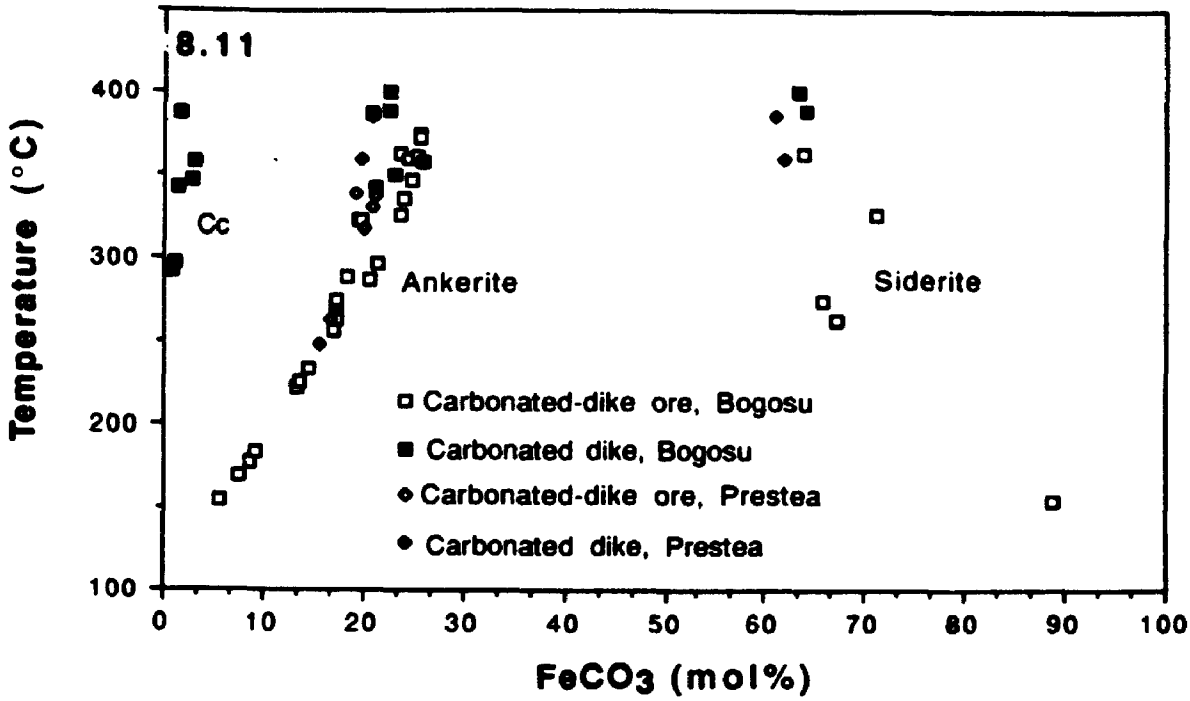
8.11
Temperature (°C)
400
300
200
100
Cc
Ankerite
Siderite
Carbonated-dike ore, Bogosu
Carbonated dike, Bogosu
Carbonated-dike ore, Prestea
Carbonated dike, Prestea
0
10
20
30
40
50
60
70
80
90
100
FeCO3 (mol%)

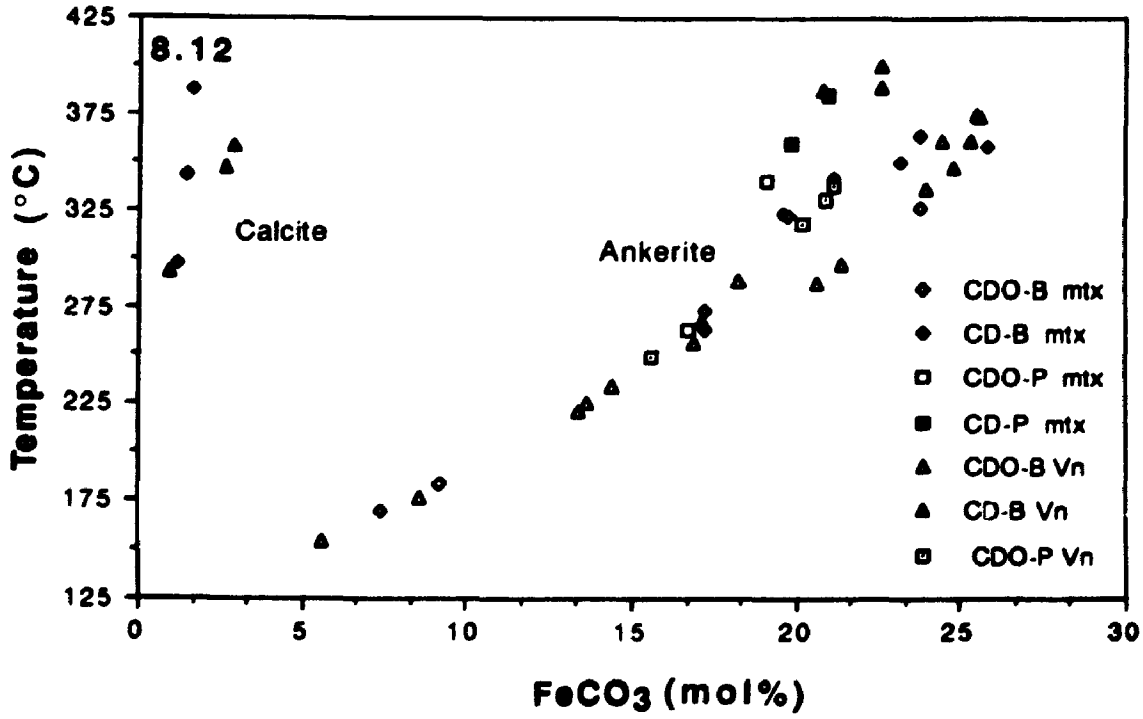
8.12
Temperature (°C)
425
375
325
275
225
175
125
Calcite
Ankerite
CDO-B mtx
CD-B mtx
CDO-P mtx
CD-P mtx
CDO-B Vn
CD-B Vn
CDO-P Vn
0
5
10
15
20
25
30
FeCO3 (mol%)

Ankerite temperatures for mineralized dikes are defined by the equation:

$$T(°C) = 0.163(\text{mol\% } FeCO_3)^2_{Ank} + 5.951(\text{ol\% } FeCO_3)_{Ank} + 114 \qquad (8\text{-}4)$$

This expression may be applied to ankerites formed in mafic rocks under similar conditions, and within the temperature range of data from which this function is derived (150 to 400°C).

Siderite data are too few to define a distinct trend, although temperatures follow the expected tendency toward higher values with lower mol% $FeCO_3$. The highest values are from carbonates formed in least-altered mafic dikes and in carbonated dikes, temperatures decrease in mineralized samples. As noted earlier, calcites show a trend of slightly increasing mol% $FeCO_3$ with increasing formation temperature.

Carbonates considered in this study originate from vein and matrix material. It is an important and interesting point that both vein and matrix carbonates plot along the same trend, even though they have different origins and siderites are found only in the matrix of rocks affected by pervasive carbonation (Figure 8.12). This suggests that at least some of the vein ankerite precipitated in equilibrium with siderites found throughout the matrix of adjacent rocks. Vein ankerites are in direct physical contact with matrix siderite in some samples (e.g. analyses #74, #75 and #76, T = 389 - 400°C), providing an opportunity to obtain reasonable estimates of formation temperatures. Assuming equilibrium or near-equilibrium was attained in at least some vein carbonates, it can be seen that temperatures fluctuated considerably, by 100°C or more during formation of some oscillatory zoned grains (e.g. Bogosu analyses #32 - #35 of the ankerite grain illustrated in Plate

8.1B, T = 286 - 360°C).

Figure 8.10 illustrates the range of temperature data obtained from carbonates in Prestea sedimentary rocks only. These sedimentary rocks include least-altered varieties, graphitic crush zone ores, phyllite ores, fissure ores and quartz-vein ores. As with mafic dikes, siderites occur in matrix material only, and define the expected trend of higher temperature with lower mol% $FeCO_3$. Ankerite data for vein and matrix material define a temperature trend very similar to ankerites in dikes. However, data from carbonates in direct physical contact (Figure 8.6) suggest less variation with temperature than the remainder of the data base. The greater temperature dependancy of the remaining data may reflest bias in the estimation of equilibrium phases. Carbonates in least-altered sediments have the highest formation temperatures, peaking at about 400°C, while carbonates in ores range in temperature from a maximum of 317°C to a minimum of 170°C (Figure 8.10).

Some ankerites and siderites from matrix material of both sediments and dikes that escaped sulphidation and/or complete re-equilibration during mineralization have compositional zoning as discussed earlier (e.g. Plate 8.1D). The core of some of these grains is remnant from pervasive carbonation of the host rock, while their rim represents compositional re-equilibration with later hydrothermal fluids during mineralization. Cores of co-existing grains give higher temperatures, while rims indicate the lower temperatures associated with gold deposition. Examples of co-existing ankerite-siderite pairs with core-rim zoning include Prestea analyses #136 and #137 ($T=367_{core}$ and $288°C_{rim}$), and #151 and #152 ($T=551_{core}$ and $257°C_{rim}$).

Depth of Mineralization

Minimum carbonate temperatures from various categories of Bogosu and Prestea ores are compared in Table 8.3. In all cases Bogosu temperatures are lower than those for Prestea, and sedimentary rocks have moderately lower values than dikes. The reason for lower sedimentary rock temperatures is not fully understood but, at least in part, reflects the smaller number of dike analyses. Compositional or textural factors may also affect the results. Considering the best data from carbonate grains in direct physical contact only, minimum temperatures are 144 and 217°C for Bogosu and Prestea, respectively. These lowest temperatures from ankerite-siderite pairs in ores are thought to represent a good estimate of ambient country-rock conditions at the time of mineralization. This assumption appears justified because in any hydrothermal system where hot ore-bearing fluids are interacting with cooler country-rocks, the lower-bound temperatures recorded would approach that of the country-rocks.

These estimates of ambient temperatures can be used to calculate depths of formation during mineralization. This is accomplished by applying a suitable temperature gradient to the geological environment of formation, which is thought (see Chapters 2 and 10) to be a sediment-dominated accretionary prism. The exact temperature gradient for this section of the Earth's crust during the Early Proterozoic is unknown; however, comparison with modern analogues suggests that 20°C per kilometer depth is a reasonable estimate (cf. Sample and Moore, 1987, southwest Alaska). This gradient indicates mineralization depths of about 7 and 11 km for Bogosu and Prestea, respectively. The difference of 73°C in ambient temperature indicates that Prestea ores, on average, formed about 3.5 km deeper in the crust than Bogosu ores, and are closer to the roots

Table 8.3: Comparison of lowest ankerite-siderite temperatures from Bogosu and Prestea ores. Temperature in °C, uncertainty ± 30°C.

Carbonates from	Bogosu	Prestea
Sedimentary rocks only	137	170
Dikes only	155	*249
Grains in contact	144	217

* Anomalously high temperature due to very few analyses in this category.

of this large gold-bearing hydrothermal system.

Prestea samples were taken at about 1 km vertical depth in the mine, implying that the erosional level at Prestea is about 2.5 km deeper than at Bogosu. This difference in depth exposure between the two regions occurs over a lateral distance of about 20 km. It would be a very interesting test of the usefulness of lower-bound carbonate temperature estimates if suites of carbonates from some of the many deposits occurring between the two mining districts were analyzed. In theory, their lowest temperatures should reflect ambient conditions intermediate between those presented here for Bogosu and Prestea.

Discussion

In summary, there is a sharp cut-off in carbonate formation temperatures at a maximum of about 400°C. Least-altered rocks have temperatures in the range of 325 to 390°C, carbonated dikes have temperatures from about 400°C down to 340°C, and ore temperatures range from 406°C down to as low as 144°C. However, the lowest temperature estimates must be considered to have the highest degree of uncertainty. The maximum temperature of least-altered country rocks of about 390°C is thought to represent peak metamorphic conditions in the Bogosu-Prestea region. High-temperature spikes above 400°C may arise from anomalous metastable mineral compositions, or represent pulses of higher temperature fluids originating from deeper in the structural conduit. The ascent of these fluids would have to be rapid to minimize cooling toward ambient conditions. Minimum temperatures of 144 and 217°C for Bogosu and Prestea, respectively, represent ambient host-rock temperatures at the time of mineralization. These temperatures also suggest that mineralization took place

at depths of about 7 to 11 km for Bogosu and Prestea ores, respectively.

The large spread of estimated temperatures for mineralized samples (144 to 406°C) is believed to result from: 1) contact of hot ascending fluids with host-rocks at relatively low ambient temperatures, and 2) possible mixing of the hot ascending fluids with cooler, entrained or trapped country-rock fluids at ambient temperatures.

The good correlation between calcite-dolomite temperatures and ankerite-siderite temperatures suggest that the latter method provides reasonable temperature estimates. Even though the degree of uncertainty is higher than ideal, the data nevertheless provide some excellent qualitative information on spatial and temporal temperature fluctations in the system.

Carbonate temperatures are difficult to compare directly to estimates obtained by arsenopyrite geothermometry. It is not possible to identify carbonate and arsenopyrite grains that formed exactly at the same time in a system where temperatures appear to be fluctuating considerably. However, gold-bearing arsenopyrite temperatures of <390°C correlate very well with ankerite-siderite temperatures of <406°C from ores. Also, the occasional high-temperature spikes that occur when using the carbonate geothermometer are mirrored by anomalous peaks in the arsenopyrite temperatures. However, numerous carbonate temperatures below 300°C from mineralized samples cannot be verified by the arsenopyrite method, since the latter geothermometer is known to be invalid in the lower temperature range. Over all, these three methods of temperature estimation give very similar results.

In the following chapter on stable isotope geochemistry, three additional

methods of temperature estimation will be discussed. The evidence corroborates the findings presented in this chapter, and documents a significant part of the evolution of the hydrothermal fluid.

Chapter 9: Stable Isotope Geochemistry

The ratios of ^{13}C to ^{12}C and ^{18}O to ^{16}O in hydrothermal minerals are known to be sensitive to, and vary systematically with, a number of physico-chemical parameters in the hydrothermal system, including: 1) temperature, 2) fluid composition, 3) mineral-fluid fractionation characteristics, 4) pH and 5) other processes such as phase separation, boiling and pressure changes that in turn affect fluid compositions, pH and oxidation states (Ohmoto, 1986; Kerrich, 1987a and 1987b; Taylor, 1987). In the Bogosu and Prestea districts, hydrothermal carbonate minerals are ubiquitous in all rock types and have been documented in Chapter 8. Carbon and oxygen isotopic ratios of carbonates have been measured and are used to document part of the evolution of hydrothermal processes in this gold system. In addition, $\delta^{18}O$ and $\delta^{13}C$ values for several quartz and graphite-bearing samples have been measured also.

Sixty-nine samples, originating mostly from ore and host rocks of the Bogosu and Prestea districts were analyzed (Appendix 9.2). The selected samples included 7 from the Ashanti Goldfields Corporation mines in the Obuasi district, approximately 100 km northeast of Bogosu-Prestea along the Ashanti Gold Belt. For each sample, co-existing carbonate minerals ± quartz and graphite were analyzed separately. In total, including duplicates, this yielded the 90 $\delta^{13}C$ and 94 $\delta^{18}O$ measurements reported below. In addition, about 40 measurements were rejected because of various forms of contamination and experimental error, which were particularly evident when testing for optimum analytical techniques.

All sample preparations and isotopic analyses were performed at the Laboratory for Stable Isotope Studies, University of Western Ontario.

Analytical Procedures

Carbonates

The selected samples contained fine-grained mixtures of intergrown, co-existing carbonate minerals comprising typically from about 7 to 50% of the total rock mass. The various assemblages and intergrowths are documented and illustrated in chapters 4 and 8, and include: 1) ankerite-siderite (most common), 2) calcite-ankerite, 3) ankerite-magnesite, 4) calcite-ankerite-siderite, and 5) samples with only one of ankerite, calcite or siderite. For many samples crushed material was hand-sorted under a stereoscopic microscope in order to separate vein and matrix material. For some samples, micro-drilling techniques were used to extract vein materials. All hand-sorted and bulk materials were subsequently pulverized to approximately -200 mesh and analysed by powder X-ray diffraction (PXRD) using a Rigaku RTP 300 RC rotating anode X-ray diffractometer at the Laboratory for Stable Isotope Studies, University of Western Ontario. Identification and proportion (where greater than about 1%) of mineral species present were determined in this manner and are listed in Appendix 9.1.

Carbonate grain sizes typically were too small and their intergrowths with other minerals too complex for physical mineral separation to be a viable option. Even larger porphyroblastic grains were intergrowths of more than one carbonate mineral with inclusions of several other gangue minerals (e.g., Plate 3.1C). Consequently, an adaption of the chemical separation / extraction techniques developed by Al-Aasm et al. (1990), Rosenbaum and Sheppard (1986) and McCrea (1950) were used.

The CO_2 gases from different carbonate species were liberated separately using the discrimination afforded by the diverse time and temperature reaction rates of the carbonate in 100% anhydrous orthophosphoric acid. The optimum times and temperatures for extractions were determined by a series of trial runs and comparison with standards and duplicates. Pulverized samples were placed in reaction vessels with a separate arm for the phosphoric acid. These vessels were evacuated under high vacuum, sealed and brought to the appropriate temperature before the acid reaction was initiated. The sample weight reacted was determined as the equivalent of a minimum 10 mg of contained carbonate. Hence, sample weights varied from a minimum of 15 mg (i.e. ≈ 67 wt% carbonate in the sample) to a maximum of 1 gm (i.e. ≈ 1 wt% carbonate in the sample). In most cases, an excess sample weight of up to 50 wt% was used to ensure adequate carbonate was available for reaction. Phosphoric acid amounts varied from 3 ml to 10 ml, with larger amounts used to ensure that the larger sample sizes were completely reacted with the acid.

Samples containing calcite only were reacted at 25°C for 4 hours using the standard method of McCrea (1950). Those with calcite and ankerite were reacted for about 1 hour at 25°C. The CO_2 thus liberated was essentially all from calcite and was removed for analysis. The reaction vessel with sample was then allowed to react for an additional 3 hours at room temperature under vacuum to remove any remaining calcite CO_2. The vessel was then sealed and reacted overnight (17-22 hours) at 50°C to release CO_2 from ankerite.

Ankerite-siderite-bearing samples were reacted at 50°C overnight. The CO_2 thus liberated from ankerite was extracted and analysed. The reaction vessel with remaining sample was evacuated under high vacuum, sealed and placed in

an oven at 150°C for 2 hours to liberate CO_2 from the siderite. This gas was then extracted and analysed.

Samples with ankerite only were reacted at 50°C for 17-22 hours, and samples with siderite only were reacted at 150°C for 2 hours. Magnesite was reacted in the same manner as ankerite.

After acid extraction, some of the most carbonaceous (graphite-bearing) samples were found to be contaminated with SO_2 gas liberated during the acid digestion. The source of the SO_2 was not identified, but was suspected to originate from extremely fine-grained sulphides, or less likely from very fine-grained and undetected sulphates. Samples containing SO_2 were cleaned by freezing liberated CO_2 and SO_2 into a reaction vessel containing a few grams of silver phosphate (Ag_3PO_4). The silver phosphate was previously de-gassed thoroughly for at least 24 hours at room temperature and a minimum of 2 hours at approximately 200°C, and was checked every usage by standards to ensure that no contamination occurred. After freezing into the silver phosphate vessel, SO_2 contaminated gases were warmed to room temperature and allowed to react with silver phosphate for about 5 minutes. Gases were scanned before and after silver phosphate treatment using the VG Optima mass spectrometer to test for contaminant gases and ensure the CO_2 had been purified.

All extractions were performed on a high vacuum extraction line modified after McCrea (1950) to handle multiple (up to 4) extractions simultaneously. The extracted CO_2 gas volumes from samples with multiple carbonate species were measured to ensure sufficient quantities of CO_2 were obtained from each carbonate for reliable measurements, and to check that gas volumes correlated with the ratio of carbonate species in the sample.

The $\delta^{18}O$ and $\delta^{13}C$ measurements of extracted CO_2 gases were made on a VG Optima mass spectrometer. Standards for each carbonate species as well as calcite standards were analysed with each run to monitor accuracy of analysis. The standards used included: WS 1 (calcite), DOLO 368 (dolomite) and 82-21 (siderite). Numerous duplicates were analysed to check the precision of the results. For samples with two or more duplicates, the average value is reported. Maximum deviation from the average of duplicates is ± 0.18‰ $\delta^{18}O$ and ± 0.27‰ $\delta^{13}C$ for calcite and ± 0.33‰ $\delta^{18}O$ and ± 0.11‰ $\delta^{13}C$ for ankerite. Only sample number 15 had a greater deviation in duplicates of ± 1.1‰ $\delta^{18}O$ and ± 0.56‰ $\delta^{13}C$. Results for samples that were suspect because of contamination or procedural difficulties are not reported.

Graphite

The maximum carbon content of graphite shears from ore zones is estimated at 5 wt% C, and for carbonaceous sediments at 1 wt% C. The samples were prepared through cleaning and preconcentration of C in pulverized rock samples by reacting about 1 gm of material with warm aqua-regia for 24 hours. This removed all carbonate minerals and phyllosilicates. The residue was washed and decanted several times with distilled water, then filtered and dried. Sufficient sample to provide an equivalent of 2 mg C was mixed with CuO, placed in the reaction chamber, evacuated, then reacted under vacuum at 825°C to convert all carbon in the sample to CO_2. The CO_2 was subsequently purified by freezing twice with liquid nitrogen and evacuating to remove any noncondensible gases. The clean CO_2 was then extracted and analysed. The procedure for graphite was tested against 4 internal carbon standards with precision better than ± 0.05‰ $\delta^{13}C$. The results were also monitored using

international standards NBS-18 (carbonatite), NBS-19 (limestone), NBS-20 (limestone), NBS-21 (graphite) and WS 1 to ensure accuracy of the results. Sample #10 was duplicated with no detectable difference between the runs (i.e., precision of better than ± 0.01‰).

Quartz

Pure quartz separates for 10 samples and 1 duplicate were obtained in the following manner. Samples were crushed to -3/8 inch and then hand-sorted under a stereoscopic microscope, except sample #69 which was drilled to obtain pure smokey quartz from a small vein. These separates were pulverized to -200 mesh and analysed by PXRD to determine the phases present. Sample numbers 1, 12 and 69 yielded clean quartz separates after the hand-picking and drilling. Sample numbers 3, 8 and 24 were digested in warm aqua regia for 24 hours to remove carbonate and phyllosilicate impurities, after which sample number 24 required gravity separation to remove a few flakes of graphite. Sample numbers 8 and 51 were treated with fluorosilicic acid at room temperature for 8 and 4 days, respectively, to remove albite. The remaining quartz separates were digested in warm HCl for 24 hours to remove carbonate impurities. All samples were finally tested again by PXRD to ensure that only pure quartz remained. A duplicate of number 51 was prepared only by hand-sorting under the stereoscopic microscope to test reproducibility of results. Results for the duplicates varied by 0.21‰ $\delta^{18}O$.

The pure quartz separates were reacted using the standard BrF_5 procedure modified from the original methods of Clayton and Mayeda (1963) and Friedman and Gleason (1973). The extraction line performance was monitored by running one NBS-28 quartz standard with the samples. Liberated oxygen (as

CO_2) was analysed on the VG Optima mass spectrometer using the WS 1 calcite standard to monitor machine analytical performance.

Results

All results are reported in standard δ notation with respect to SMOW for $\delta^{18}O$ values (Craig, 1961) and PDB for $\delta^{13}C$ values (Craig, 1957). Calcite, siderite, ankerite, graphite and quartz isotope ratios are listed in Tables 9.1 through 9.5, respectively, along with corresponding $\delta^{18}O$ and $\delta^{13}C$ calculations for co-existing fluids.

Calculations of fluid isotopic composition were made using temperatures derived from the carbonate mineral chemistries reported in the previous chapter. However, such carbonate temperatures are grain specific, and even zone specific in the many instances where compositional zoning occurs. By contrast, isotopic analyses are values derived from the average of all the materials that comprise any particular sample, which may have weighed originally up to several hundred grams. Consequently, average temperatures derived for carbonates of the different categories of host, altered and mineralized rocks were used to calculate fluid $\delta^{13}C$ and $\delta^{18}O$ compositions. Average carbonate temperatures ranged from 247°C in some ore samples to 375°C for some host-rocks.

Fluid $\delta^{13}C$ and $\delta^{18}O$ calculations were mostly of the form 1000 ln α (mineral-fluid) = $AT^{-2} + B$, where α is the factor for isotopic fractionation between the mineral and fluid and T is temperature in K. Values for A and B were taken from the best available information in existing literature, or recalculated on the basis of new and/or existing information. For all

Table 9.1: Calculated fluid $\delta^{18}O$ and $\delta^{13}C$ for calcite.

Sample category	#	n	Carbonate avg T(°C)	$\delta^{13}C$ Calcite	$\delta^{18}O$ Calcite	$\delta^{18}O$ H_2O	$\delta^{13}C$ CO_2
Prestea least-altered dike	2	1	369	-10.2	13.9	10.0	-9.4
Prestea least-altered dike	3	1	369	-10.4	13.8	10.0	-9.7
Bogosu least-altered dike	19	1	369	-9.1	14.1	10.3	-8.3
Bogosu least-altered dike	20	1	369	-6.9	14.1	10.2	-6.2
Bogosu least-altered dike	36	2	369	-5.0	17.5	13.6	-4.3
Bogosu least-altered dike	38	2	369	-8.3	16.1	12.2	-7.6
Bogosu least-altered dike	42	3	369	-5.6	14.5	10.6	-4.8
Bogosu least-altered dike	50	1	369	-9.5	13.9	10.1	-8.8
Bogosu least-altered dike	58	2	369	-7.8	14.7	10.8	-7.0

1000 ln α (Cc-H_2O) = 2.78×10^6 T^{-2}-2.89, ($\delta^{18}O$), Friedman and O'Neil, 1977.
1000 ln α (Cc-CO_2) = 1.194×10^6 T^{-2}-3.63, ($\delta^{13}C$), Deines et al., 1974.
see Appendix 9.2 for sample descriptions.

Table 9.2: Calculated fluid $\delta^{18}O$ and $\delta^{13}C$ for siderite.

Sample category	#	n	Carbonate Avg T(°C)	$\delta^{13}C$ Siderite	$\delta^{18}O$ Siderite	$\delta^{18}O$ H_2O	$\delta^{13}C$ CO_2
Bogosu sedimentary rock	21	1	339	-12.6	17.4	12.5	-13.0
Bogosu sedimentary rock	22	1	339	-12.9	16.6	11.8	-13.3
Bogosu sedimentary rock	23	1	339	-12.6	16.7	11.9	-13.1
Bogosu sedimentary rock	26	1	131	-16.7	29.2	13.5	-22.9
Bogosu sedimentary rock	57	1	339	-11.1	17.2	12.3	-11.5
Bogosu sedimentary rock	34	1	339	-11.4	17.7	12.8	-11.8
Bogosu sedimentary rock	41	1	339	-12.2	16.4	11.6	-12.6
Bogosu sedimentary-rock ore	40	1	270	-13.2	16.7	9.5	-14.5
Bogosu least-altered dike	42	1	369	-6.4	16.9	12.8	-6.7
Bogosu carbonated dike	46	1	373	-7.8	16.8	12.8	-8.0
Bogosu carbonated dike	63	1	373	-10.3	17.1	13.1	-10.5
Bogosu carbonated dike	48	1	373	-9.0	17.0	13.0	-9.2
Bogosu carbonated dike	35	1	373	-10.3	17.4	13.4	-10.5
Bogosu carbonated dike	44	1	373	-9.0	17.5	13.5	-9.2
Bogosu carbonated dike	15	1	373	-11.5	17.3	13.3	-11.7
Bogosu carbonated-dike ore	43	1	330	-10.1	17.9	12.7	-10.6
Ashanti sedimentary rock	49	1	339	-13.6	15.4	10.6	-14.1
Ashanti sedimentary rock	52	1	288	-12.1	15.7	9.2	-13.1
Ashanti sedimentary rock	55	1	339	-12.4	16.8	11.9	-12.8
Ashanti sedimentary-rock ore	64	1	288	-12.2	16.6	10.1	-13.2
Prestea sedimentary rock	66	1	351	-12.4	16.6	12.0	-12.7
Prestea sedimentary rock	54	1	375	-10.9	16.5	12.6	-11.1
Prestea sedimentary rock	59	1	339	-12.6	16.4	11.6	-13.0
Prestea carbonated dike	29	1	373	-12.0	16.5	12.5	-12.1
Prestea carbonated dike	45	1	373	-12.8	16.2	12.2	-13.0
Prestea carbonated-dike ore	47	1	330	-13.3	16.0	10.9	-13.8

$1000 \ln \alpha$ (Sid-H_2O) = $3.13 \times 10^6 T^{-2} - 3.50$, ($\delta^{18}O$), Carothers et al., 1988.
$1000 \ln \alpha$ (Sid-CO_2) = $4.34 \times 10^6 T^{-2} - 11000 + T + 6.82$, ($\delta^{13}C$), calculated from theoretical values of Golyshev et al. (1981) for temperatures of 127, 227 and 327°C.
see Appendix 9.2 for sample descriptions.

Table 9.3: Calculated fluid $\delta^{18}O$ and $\delta^{13}C$ for ankerite.

Sample category	#	n	Carbonate Avg T(°C)	$\delta^{13}C$ Ankerite	$\delta^{18}O$ Ankerite	$\delta^{18}O$ *H_2O	$\delta^{18}O$ **H_2O	$\delta^{13}C$ CO_2
Bogosu least-altered dike	36	1	369	-5.1	17 1	12.5	15.0	-5.3
Bogosu least-altered dike	38	1	369	-8 8	14.7	10.2	12.6	-9.0
Bogosu least-altered dike	58	1	369	-7.8	14.5	10.0	12.4	-8.0
Bogosu least-altered dike	42	1	369	-3.4	14.0	9.4	11.8	-3.6
Bogosu carbonated dike	15	4	373	10.9	14.9	10.5	12.9	10.7
Bogosu carbonated dike	35	1	373	-10.0	15.1	10.7	13.1	-10.1
Bogosu carbonated dike	44	1	373	-8.9	15.6	11.1	13.5	-9.1
Bogosu carbonated dike	46	1	373	-8.4	15.0	10.5	12.9	-8.6
Bogosu carbonated dike	48	2	373	-8.3	14.2	9.8	12.2	-8.5
Bogosu carbonated dike	63	1	373	-10.2	15.4	10.9	13.4	-10.4
Bogosu carbonated-dike ore	67	1	330	-11.1	14.6	9.0	11.4	-11.6
Bogosu carbonated-dike ore	43	1	330	-10.0	15.0	9.4	11.8	-10.5
Bogosu carbonated-dike ore	13	1	261	-14.0	13.5	5.4	7.8	-15.4
Bogosu carbonated-dike ore	14A	1	261	-13.5	13.9	5.8	8.2	-15.0
Bogosu carbonated-dike ore #	31	1	346	-11.1	13.8	8.7	11.1	-11.5
Bogosu sedimentary rock	34	2	339	-12.2	15.2	9.9	12.3	-12.6
Bogosu sedimentary rock	41	1	339	-12.0	14.7	9.4	11.8	-12.5
Bogosu sedimentary rock	21	1	339	-12.5	15.3	10.0	12.4	-12.9
Bogosu sedimentary rock	22	4	339	-13.0	14.4	9.1	11.5	-13.4
Bogosu sedimentary rock	23	1	339	-13.0	14.8	9.5	11.9	-13.4
Bogosu sedimentary rock	57	1	339	-11.2	16.2	10.9	13.3	-11.7
Bogosu sedimentary rock	61	2	339	-13.1	13.8	8.4	10.8	-13.5
Bogosu sedimentary-rock ore	11	1	287	-13.3	14.0	7.0	9 4	-14.3
Bogosu sedimentary-rock ore	40	1	270	-13.1	14.6	7.0	9.4	-14.3
Bogosu sedimentary-rock ore	28	1	287	-12.6	14.2	7.2	9.6	-13.6
Bogosu sedimentary-rock ore	30	1	270	-12.4	15.3	7.6	10.0	-13.6
Bogosu sedimentary-rock ore	62	1	264	-13.5	14.3	6.4	8.8	-14.9
Bogosu sedimentary-rock ore QV	51	1	270	-12.6	14.9	7.2	9.6	-13.9
Prestea carbonated dike	45	1	373	-14.5	15.3	10.8	13.2	-14.7
Prestea carbonated dike	29	1	373	-12.2	14.3	9.8	12.3	-12.4
Prestea carbonated dike	68	1	373	-11.5	15.4	10.9	13.3	-11.7
Prestea carbonated dike	27	1	373	-11.9	14.1	9.7	12.1	-12.1
Prestea carbonated-dike ore	6	1	306	-13.1	13.9	7.5	10.0	-13.9
Prestea carbonated-dike ore	8	1	306	-13.0	14.0	7.6	10.0	-13.7
Prestea carbonated-dike ore	47	3	330	-13.1	13.7	8.1	10.5	-13.6
Prestea carbonated-dike ore	37	2	306	-12.9	14.0	7.6	10.0	-13.7
Prestea sedimentary rock	39	1	339	-13.8	14.2	8.9	11.3	-14.3
Prestea sedimentary rock	54	1	375	-10.9	14.4	10.0	12.4	-11.1
Prestea sedimentary rock	59	1	339	-12.8	14.2	8.9	11.3	-13.2
Prestea sedimentary rock	66	1	351	-12.5	13.8	8.8	11.2	-12.8
Prestea sedimentary-rock ore	4	1	247	-14.2	13.8	5.2	7.6	-16.0
Prestea sedimentary-rock ore QV	10	1	288	-13.5	14.2	7.2	9.6	-14.5
Prestea sedimentary-rock ore QV	9	1	288	-13.9	13.9	6.9	9.3	-14.9

Table 9.3 continued: Calculated fluid $\delta^{18}O$ and $\delta^{13}C$ for ankerite.

Sample category	#	n	Carbonate Avg T(°C)	$\delta^{13}C$ Ankerite	$\delta^{18}O$ Ankerite	$\delta^{18}O$ *H_2O	$\delta^{18}O$ **H_2O	$\delta^{13}C$ CO_2
Ashanti carbonated-dike ore	65	1	330	-13 7	14 2	8.6	11.0	-14 2
Ashanti carbonated-dike ore	33	2	330	-13 1	14.1	8.5	10.9	-13 6
Ashanti sedimentary rock	55	1	339	-13 1	15 4	10 0	12 5	-13 6
Ashanti sedimentary rock	53	1	339	-12.9	14 2	8 9	11 3	-13 3
Ashanti sedimentary rock	49	1	339	-13 6	14 3	9.0	11 4	-14 0
Ashanti sedimentary-rock ore	52	1	288	-12 3	13 4	6 4	8.8	-13 3
Ashanti sedimentary-rock ore	64	1	288	-12.8	13 7	6 7	9 1	-13.8

* 1000 ln α (Dol-H_2O) = 3.23×10^6 T^{-2}-3.29, ($\delta^{18}O$), Land (1983) after Sheppard and Schwarcz (1970).

** 1000 ln α (Ank-H_2O) = 3.23×10^6 T^{-2}-0.88, ($\delta^{18}O$), (this study).

1000 ln α (Ank-CO_2) ~ 1000 ln α (Sid-CO_2) = 4.34×10^6 T^{-2}-11000+T+6.82, ($\delta^{13}C$), calculated from theoretical values of Golyshev et al. (1981) for temperatures of 127, 227 and 327°C.

see Appendix 9.2 for sample descriptions.

QV = crack-seal quartz vein

Table 9.4: Calculated fluid $\delta^{13}C$ for graphite.

Sample category	#	n	Carbonate Avg T(°C)	$\delta^{13}C$ Graphite	$\delta^{13}C$ CO_2
Prestea sedimentary-rock ore	5	1	247	-27.8	-10.2
Prestea sedimentary-rock ore QV	10	2	288	-28.1	-12.9
Bogosu sedimentary-rock ore	11	1	287	-30.4	-15.2
Bogosu sedimentary rock	23	1	339	-27.7	-14.7
Bogosu sedimentary rock	26	1	339	-29.8	-16.8

1000 ln α (Cc-CO_2)-1000 ln α (Gr-CO_2) = 1000 ln α (Cc-Gr).
1000 ln α (Cc-CO_2) = 1.194×10^6 T^{-2}-3.63, ($\delta^{13}C$), Deines et al., 1974.
1000 ln α (Cc-Gr) = 5.6×10^6 T^{-2}-2.4, ($\delta^{13}C$), Wada and Suzuki, 1983.
1000 ln α (Gr-CO_2) ~ -4.41×10^6 T^{-2}-1.23, ($\delta^{13}C$), (T, K).
# see Appendix 9.2 for sample descriptions.
QV = crack-seal quartz vein

Table 9.5: Calculated fluid $\delta^{18}O$ for quartz.

Sample category	#	n	Carbonate Avg T(°C)	$\delta^{18}O$ Quartz	$\delta^{18}O$ H_2O
Prestea least-altered dike	3	1	369	15.6	10.8
Prestea carbonated-dike ore	69	1	330	14.4	8.5
Prestea sedimentary-rock ore QV	1	1	288	15.1	7.8
Prestea sedimentary-rock ore QV	9	1	288	17.4	10.1
Bogosu carbonated-dike ore	14A	1	261	14.8	6.4
Bogosu carbonated-dike ore #	31	1	346	16.3	10.9
Bogosu sedimentary rock	24	1	339	15.8	10.2
Bogosu sedimentary-rock ore	12	1	287	15.0	7.6
Bogosu sedimentary-rock ore QV	51	2	270	16.0	7.9

1000 ln α (Qtz-H_2O) = 3.34×10^6 T^{-2}-3.31, ($\delta^{18}O$), Matsuhisa et al., 1979.
# see Appendix 9.2 for sample descriptions.
QV = crack-seal quartz vein

calculations, 1000 ln α (mineral-fluid) is approximated as δ mineral - δ fluid (Longstaffe, 1989) since the difference in the two methods of calculation is negligible relative to experimental and analytical error for the values reported in this study.

At temperatures below 600°C, the dominant carbon species in natural hydrothermal solutions are CO_2(aq), H_2CO_3, HCO_3^-, CO_3^{-2}, and CH_4(aq) (Seward, 1989; Faure, 1986). The abundance of the carbonate species and their oxidation states are strongly affected by the pH and fugacity of oxygen. This in turn could have a dramatic effect upon the $\delta^{13}C$ of the residual fluid if organic species like CH_4, which is strongly enriched in ^{12}C, are partitioned out of the fluid. At oxygen fugacities above 10^{-38} bar most carbon is oxidized, CH_4(aq) is negligible and the $\delta^{13}C$ of the fluid will be relatively low. If the fluid is more reducing, CH_4(aq) will increase in abundance, and if subsequently removed the residual hydrothermal fluid will be strongly enriched in ^{13}C (Faure, 1986). However, this possibility is not likely; sulphide mineral assemblages discussed in Chapter 6 (pyrite-arsenopyrite), carbonate mineral precipitation in the ore zone, the carbonate mineral buffer in the country rocks and isotope data are not consistent with a strongly reducing ore fluid. Primary fluid inclusions in 10 ore samples that were examined contained CO_2 as the dominant or only phase present. This high concentration of CO_2 in the ore fluid is consistent with fluids documented from other areas where the host-rocks are carbonaceous sediments. Because of its predominace over other carbon species, only CO_2 was considered in calculating the $\delta^{13}C$ of fluids associated with mineral precipitation.

Fluid $\delta^{18}O$ and $\delta^{13}C$ values were calculated for calcite using formulae derived by Friedman and O'Neil (1977) and Deines et al. (1974), respectively

(i.e., 1000 ln α (Cc - H_2O) = 2.78 x 10^6T^{-2} - 2.89, and 1000 ln α (Cc - CO_2) = 1.194 x 10^6T^{-2} - 3.63, see Table 9.1). Fluid $\delta^{18}O$ values for siderite were calculated using the formula derived by Carothers et al. (1988); 1000 ln α (Sid - H_2O) = 3.13 x 10^6T^{-2} - 3.50. Although the experimental work of Carothers et al. (1988) was conducted only to temperatures of 197°C, the theoretical results of Golyshev et al. (1981) and Becker and Clayton (1976) justify extrapolation of these results to the higher temperatures required in this study. In the absence of an appropriate equation, in the literature, for the calculation of $\delta^{13}C$ in the hydrothermal fluid for equilibrium with siderite, the formula 1000 ln α (Sid - CO_2) = 4.34 x 10^6T^{-2} - 11000T^{-1} + 6.82 was derived from the theoretical results of Golyshev et al. (1981), using values of 1000 ln α calculated by Carothers et al. (1988) for temperatures of 127, 227 and 327°C (i.e., 6.38, 2.20 and 0.56, respectively). At temperatures above 300°C (applicable to most siderites in this study), the $\delta^{13}C$ fractionation between siderite and fluid is less than 1‰, decreases with increasing temperature and is negligible at about 400°C (Table 9.2).

Textural and paragenetic evidence presented in Chapter 8 demonstrates that in the study area most siderite formed simultaneously with ankerite in carbonate-altered rocks, prior to mineralization. Ankerite yielded a measured $\delta^{18}O$ mineral-water fractionation averaging 1.9‰ lower than coexisting siderite (n = 19). Nevertheless, both carbonate phases should yield similar fluid $\delta^{18}O$ values, particularly from non-mineralized samples where equilibrium textures are preserved. However, the fluid $\delta^{18}O$ values calculated from ankerite data using the equation of Fisher and Land (1986), 1000 ln α (Ank - H_2O) = 2.78 x 10^6T^{-2} + 0.11, yielded values that averaged about 4.8‰ lower than corresponding values from siderite. The equation of Fisher and Land (1986) is based on the calcite-H_2O equation of Friedman and O'Neil (1977) with

estimated dolomite-calcite and dolomite-ankerite fractionations of 3‰ and 0‰, respectively. However, the siderite-H_2O equation used here has good experimental and theoretical corroboration from several investigators, and is therefore considered to be more reliable. In the absence of a rigorously determined equation, fluid $\delta^{18}O$ values are presently derived from ankerite data using the following reasoning.

The structure of ankerite is closer to that of dolomite than to calcite. Several dolomite - H_2O equations (Land 1983) were tried with results closest to the siderite calculations using the equation of Land (1983) after Sheppard and Schwarcz (1970); $1000 \ln \alpha (Dol - H_2O) = 3.23 \times 10^6 T^{-2} - 3.29$. Fluid values calculated from this equation are listed in Table 9.3, and are illustrated in Figure 9.1 along with fluid $\delta^{18}O$ values calculated from co-existing siderites. These calculated values are still lower on average by 2.4‰ $\delta^{18}O$ than fluid values calculated from data for co-existing siderite. Mineral paragenetic and textural evidence (Chapter 8) does not support the possibility that ankerite and siderite formed at different times from isotopically different fluids, with the exception of ankerite that formed during mineralization. Consequently, contemporaneous siderite and ankerite should yield similar isotopic values for their common fluid. Therefore, the dolomite equation for ankerite has been modified to:

$$1000 \ln \alpha (Ank - H_2O) = 3.23 \times 10^6 T^{-2} - 0.88$$

(Table 9.3), which is equivalent to simply adjusting the fluid $\delta^{18}O$ values from ankerite by + 2.4‰ This arbitrary adjustment does not alter the direction or magnitude of isotopic variations between samples. Only the absolute values are affected. Throughout the remainder of this thesis, only the adjusted $\delta^{18}O$

Figure 9.1: Calculated fluid $\delta^{18}O$ values for syngenetic (co-existing) siderite and ankerite using the equations of Carothers et al. (1988) for siderite, and Land (1983) after Sheppard and Schwarcz (1970) for ankerite (see Tables 9.2 and 9.3 for calculations). Fluid values calculated from ankerite are on average 2.4‰ lower than corresponding fluid values calculated from siderite.

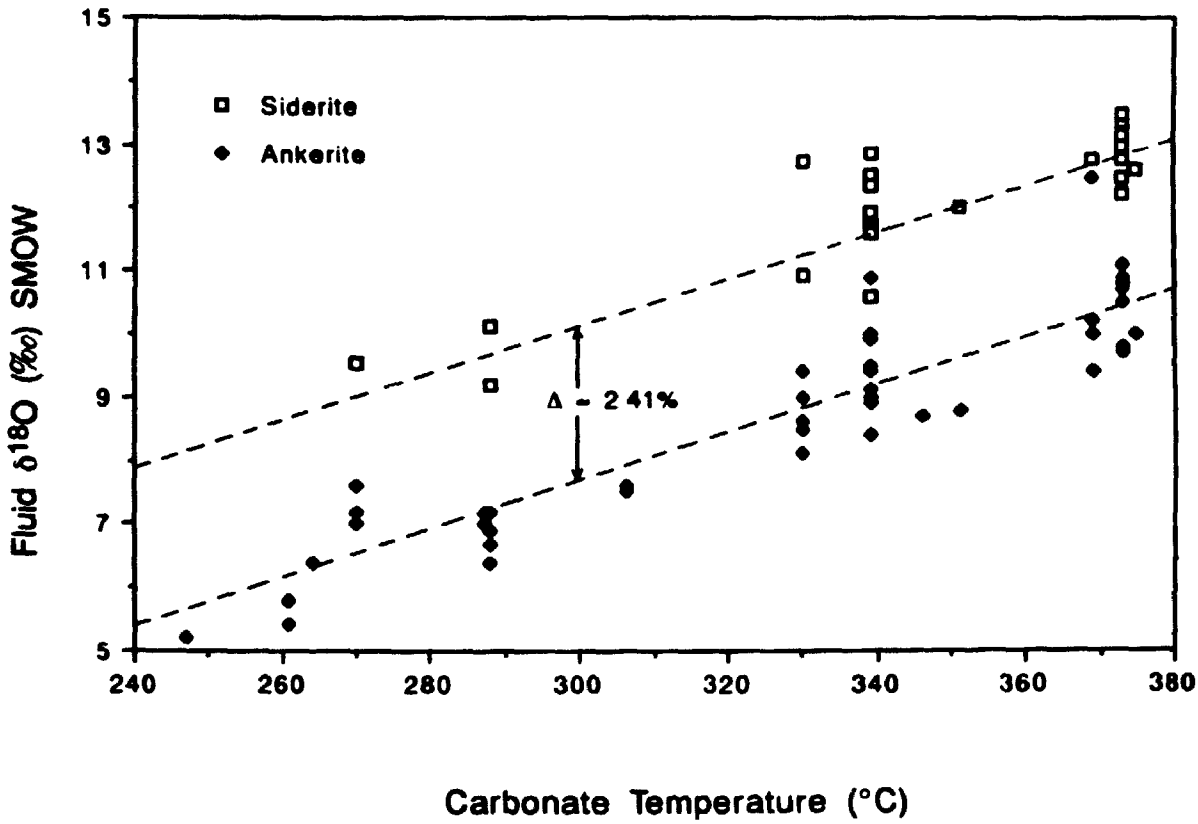
Siderite
Ankerite
Δ = 2.41‰
Fluid δ18O (‰) SMOW
Carbonate Temperature (°C)
15
13
11
9
7
5
240
260
280
300
320
340
360
380

values of fluids calculated from ankerite data are used.

The average difference between 25 co-existing ankerite and siderite $\delta^{13}C$ values is less than 0.02‰ (Tables 2 and 3). Calculated $\delta^{13}C$ values of CO_2 in the hydrothermal fluid should be the same assuming both carbonates formed together, and as previously mentioned approach those of siderite for temperatures above 300°C. Hence, the siderite equation (above) for the calculation of $\delta^{13}C$ fluid values has been used to approximate fluid values calculated from ankerite data.

Graphite in the Bogosu and Prestea rocks is believed to be residual material from diagenesis and metamorphism of organic matter in the Birimian carbonaceous sediments. The presence of this material in least-altered rocks throughout the Birimian suggests graphite formation pre-dated the hydrothermal event, and requires the formation of the hydrothermal fluid in the presence of the graphitic material. This enables a further estimate of the carbon isotope composition of the hydrothermal fluid from graphite $\delta^{13}C$ values. The equations of Deines et al. (1974), $1000 \ln \alpha (Cc - CO_2) = 1.194 \times 10^6 T^{-2} - 3.63$, and Wada and Suzuki (1983), $1000 \ln \alpha (Cc - Gr) = 5.6 \times 10^6 T^{-2} - 2.4$, were combined to derive the equation used here for graphite - CO_2 fractionation; $1000 \ln \alpha (Gr - CO_2) \approx -4.41 \times 10^6 T^{-2} - 1.23$. The results are listed in Table 9.4.

Fluid $\delta^{18}O$ estimates were also made from the $\delta^{18}O$ of quartz samples using the equation of Matsuhisa et al. (1979), $1000 \ln \alpha (Qtz - H_2O) = 3.34 \times 10^6 T^{-2} - 3.31$. These results are listed in Table 9.5.

Discussion of Results

Isotope Geothermometry

Isotope geothermometers have been developed for a number of mineral-mineral pairs, based upon differing mineral-H_2O oxygen-isotope fractionations between co-existing phases. The mineral pairs with the largest fractionation, including quartz-magnetite, quartz-hematite, calcite-magnetite, plagioclase-magnetite, pyroxene-magnetite and quartz-scheelite, have been widely employed in isotope geothermometry. However, quartz-calcite, quartz-muscovite and quartz-chlorite are commonly used because of their presence in hydrothermal deposits (O'Neil, 1986; Ohmoto, 1986; Kyser, 1987). In this study, potential isotopic thermometers are restricted to the quartz-calcite oxygen-isotope fractionation and the ankerite-graphite carbon-isotope fractionation. For these pairs, the fractionations are small, making these thermometers less sensitive than desired. Nevertheless, they still provide an interesting comparison to temperatures derived by mineral-chemistry geothermometers.

Quartz-calcite pairs only co-exist in least-altered dikes. One pair yielded a formation temperature of 303°C using the formula calculated from the mineral-water fractionations of Friedman and O'Neil (1977). This temperature is about 50°C below the range of temperatures derived by carbonate geothermometry for similar rocks (i.e., 350 - 387°C).

With the exception of the dikes, the host rocks of the Bogosu and Prestea district are carbonaceous sedimentary rocks, and as previously discussed, these sedimentary rocks are the main host-rock for the entire Birimian sequence of southwestern Ghana. All carbonates in these rocks formed in the presence of

graphite, so that the graphite-dolomite $\delta^{13}C$ relationship of Wada and Suzuki (1983) may be used to estimate formation temperatures [i.e., 1000 ln α (Dolo - Gr) = $5.9 \times 10^6 T^{-2} - 1.9$, (K) can be rewritten as $T°C_{Ank - Gr} = SQRT(5.9 \times 10^6 + (\delta Ank - \delta Gr + 1.9)) - 273.15$].

All graphite $\delta^{13}C$ values fall within a narrow range of -30.4 to -27.6‰. These values are within the range of reduced carbon in sedimentary and metamorphic rocks, and most likely had a biogenic origin (Ohmoto and Rye, 1979). Because of this narrow range, ankerite-graphite carbon-isotope temperatures were calculated using an average $\delta^{13}C$ graphite value of -28.7‰, except for those samples where the graphite was analysed, in which case, actual values were used.

The calculated ankerite-graphite isotopic temperatures are listed in Table 9.6 along with the full range of temperatures for various rock and ore types as calculated from carbonate mineral compositions. As stated above, carbonate temperatures are grain and mineral specific, while isotope temperatures are based on average isotopic compositions of samples up to several hundred grams in weight. It follows that the isotopic temperatures should be an average of the range of temperatures preserved by the carbonate data. The average carbonate temperatures vary from 247 to 375°C, compared with ankerite-graphite carbon-isotope temperatures of 275 to 346°C for the same sample set (Table 9.6). On an individual sample basis, most isotopic temperatures fall within the range of carbonate temperatures, although some exceptions do exist. These may result from sampling or analytical errors. It is evident from Figure 9.2 that unlike the carbonate chemistry geothermometers, the isotope temperatures are not sensitive to differences between ore and host-rocks, and that a one-to-one correlation between carbonate and isotope temperatures does not exist on an

Table 9.6: Calculated temperatures for quartz-calcite and graphite-ankerite isotopic fractionations.

Sample category	#	Carbonate T(°C) minimum	Carbonate T(°C) maximum	$\delta^{13}C$ T(°C) Gr-Ank	$\delta^{13}C$ Ankerite	$\delta^{13}C$ Graphite
Bogosu sedimentary rock	21	287	390	316	-12.5	**-27.6**
Bogosu sedimentary rock	22	287	390	324	-13.0	**-27.6**
Bogosu sedimentary rock	23	287	390	325	-13.0	**-27.6**
Bogosu sedimentary rock	34	287	390	293	-12.2	-28.7
Bogosu sedimentary rock	41	287	390	291	-12.0	-28.7
Bogosu sedimentary rock	57	287	390	279	-11.2	-28.7
Bogosu sedimentary rock	61	287	390	308	-13.1	-28.7
Bogosu sedimentary-rock ore	62	144	324	314	-13.5	-28.7
Bogosu sedimentary-rock ore	40	163	324	307	-13.1	-28.7
Bogosu sedimentary-rock ore	11	206	328	284	-13.3	**-30.4**
Bogosu sedimentary-rock ore	28	206	328	299	-12.6	-28.7
Bogosu sedimentary-rock ore	30	163	324	296	-12.4	-28.7
Bogosu sedimentary-rock ore QV	51	163	324	299	-12.6	-28.7
Prestea sedimentary rock	54	360	390	275	-10.9	-28.7
Prestea sedimentary rock	59	287	390	302	-12.8	-28.7
Prestea sedimentary rock	39	287	390	320	-13.8	-28.7
Prestea sedimentary rock	66	329	372	298	-12.5	-28.7
Prestea sedimentary-rock ore	4	202	269	346	-14.2	**-27.7**
Prestea sedimentary-rock ore QV	9	217	324	333	-13.9	**-28.1**
Prestea sedimentary-rock ore QV	10	217	324	326	-13.5	**-28.1**
Ashanti sedimentary rock	53	287	390	304	-12.9	-28.7
Ashanti sedimentary rock	55	287	390	308	-13.1	-28.7
Ashanti sedimentary rock	49	287	390	316	-13.6	-28.7
Ashanti sedimentary-rock ore	52	217	324	294	-12.3	-28.7
Ashanti sedimentary-rock ore	64	217	324	302	-12.8	-28.7
				$\delta^{18}O$ T(°C) Qtz-Calc	$\delta^{18}O$ Calcite	$\delta^{18}O$ Quartz
Prestea least-altered dike	3	350	387	303	13.8	15.6

Qtz-Cc $\delta^{18}O$ T(°C) = SQRT($6x10^5$+(δQtz-δCc+0.01))-273.15, calculated from mineral-water fractionations of Friedman and O'Neil, 1977.
Ank-Gr $\delta^{13}C$ T(°C) = SQRT($5.9x10^6$+(δAnk-δGr+1.9))-273.15, Wada and Suzuki, 1983. Graphite carbon-isotope values in bold are from actual measurements; all other values are the average of measured values.
# see Appendix 9.2 for sample descriptions.
QV = crack-seal quartz vein

Figure 9.2: Comparison of calculated ankerite-graphite carbon-isotope ($\delta^{13}C$) temperatures with temperature estimates from carbonate mineral chemistries (Chapter 8). Carbon-isotope temperatures do not discriminate between ore and host-rocks in the present application.

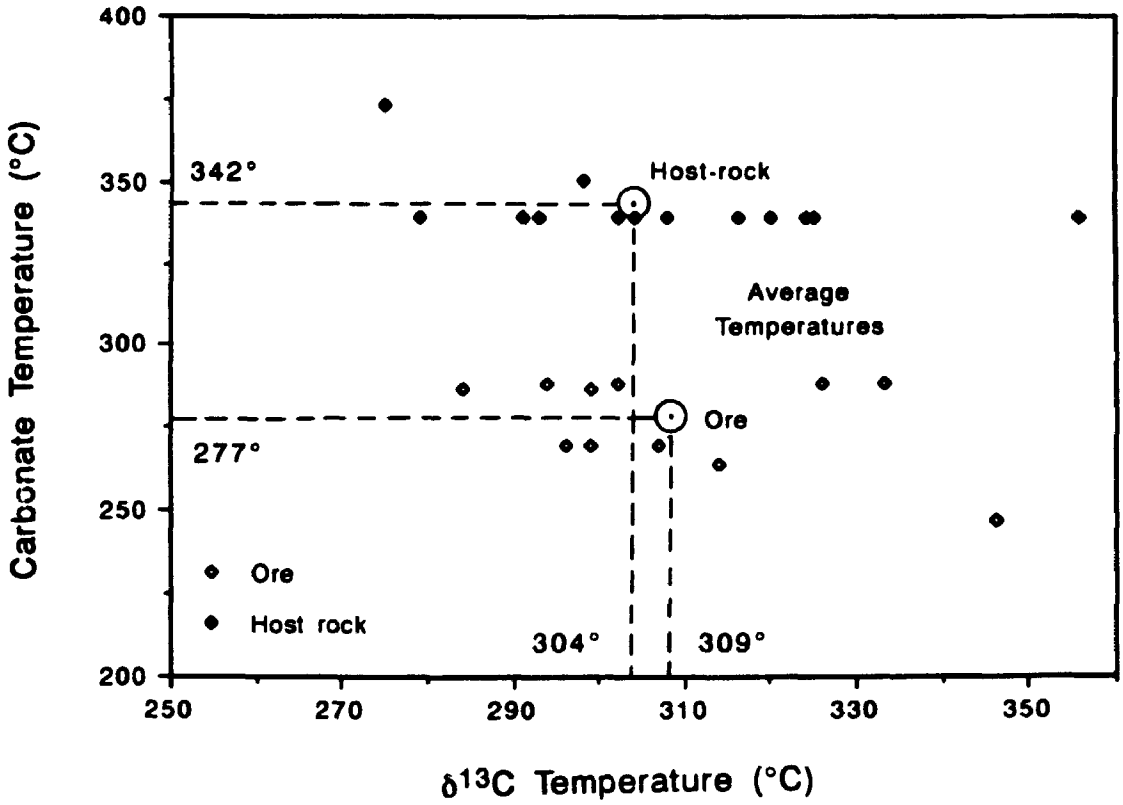
400
350
300
250
200
Carbonate Temperature (°C)
342°
Host-rock
Average
Temperatures
Ore
277°
Ore
Host rock
304°
309°
250
270
290
310
330
350
δ13C Temperature (°C)

individual sample basis. For the same data set shown in Figure 9.2, host-rock temperatures average 342 and 304°C and ore temperatures average 277 and 309°C for carbonate mineral chemistry and carbon-isotope data, respectively. Overall, however, carbonate and isotope temperatures average 314 and 306°C, respectively, which is remarkably close considering the large difference in the methods used, and limited experimental and theoretical evidence to support both sets of geothermometers.

The carbon-isotope temperature estimates are compared with calculated fluid $\delta^{18}O$ values (from ankerite ± siderite data) in Figure 9.3. Temperatures for ore and host-rocks are similar. Much of the range in temperature and sensitivity to change in temperature achieved using the carbonate mineral chemistry geothermometers is lost in the present application of isotopic geothermometry. However, it is interesting to note that ore temperatures from Prestea are higher by about 35°C on average than from Bogosu, which is consistent with earlier findings from mineral chemistry. When the calculated $\delta^{18}O$ of the fluid is plotted versus average carbonate temperatures, the sharp distinction between ore and host rocks is preserved, with higher temperatures of 330 to 375°C almost entirely from host rocks (Figure 9.4). Ores give average temperatures in the range from 247 to 345°C (Figures 9.2 and 9.4). Regardless of which temperature method is used, the fluid $\delta^{18}O$ values are distributed distinctly bimodally between ore and host rocks, averaging about 9.7 and 12.3‰, respectively, as shown in Figures 9.3 and 9.4.

While clustering of carbon-isotope temperature estimates around 306°C is attributable in large part to the averaging of carbonate materials that crystallized over a range of temperatures, this does not fully explain the lack of preservation of lower temperatures from ore samples (e.g., Figures 9.2 and

Figure 9.3: Calculated fluid $\delta^{18}O$ values compared with carbon-isotope temperatures. The $\delta^{18}O$ of the fluid is distributed distinctly bimodally between ore and host-rocks.

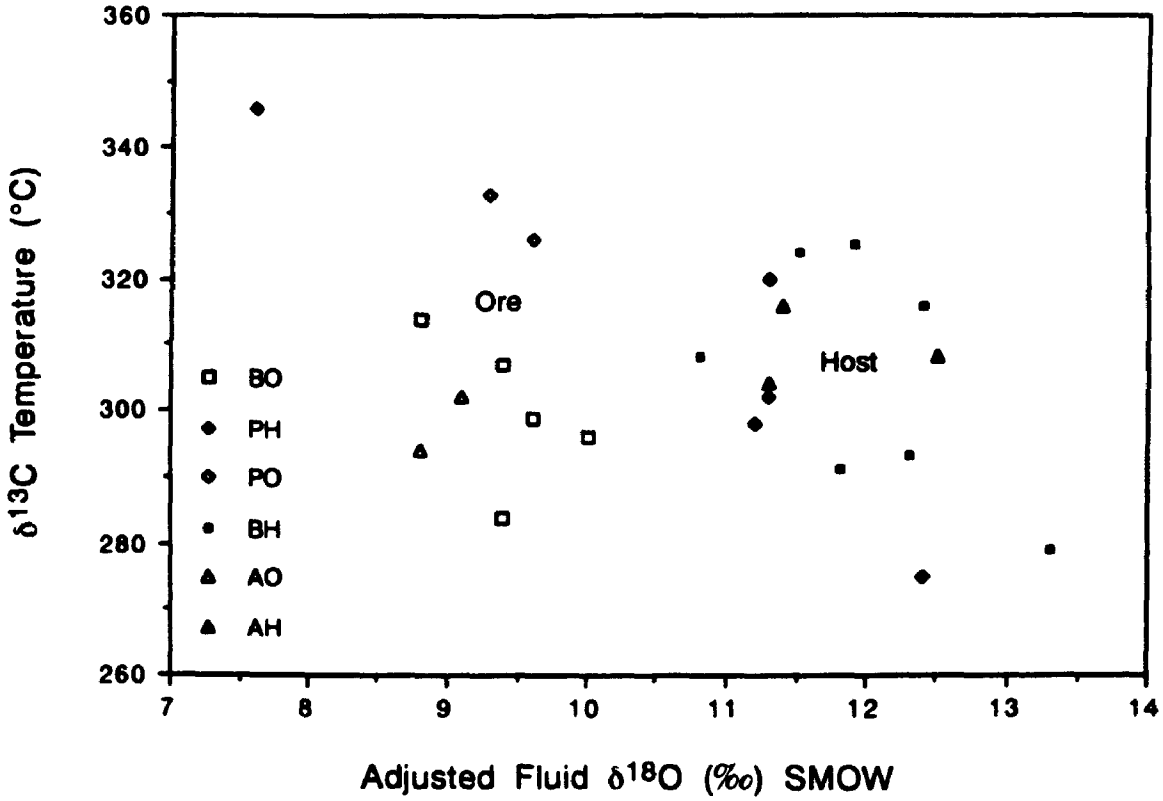
360
340
320
300
280
260
7
8
9
10
11
12
13
14
δ13C Temperature (°C)
Adjusted Fluid δ18O (‰) SMOW
Ore
Host
BO
PH
PO
BH
AO
AH

Figure 9.4: Average temperature estimates from carbonate mineral chemistries (Chapter 8) compared with calculated fluid $\delta^{18}O$ values from ankerite data. Ore and host-rocks are distinguished on the basis of estimated formation temperatures and the $\delta^{18}O$ value of associated fluids: a) data categorized according to rock type, and b) data categorized according to locality.

Legend:

D	= least-altered dike
CD	= carbonate-altered dike
CDO	= carbonated-dike ore
S	= sedimentary rock
SO	= sedimentary-rock ore
BO	= Bogosu ore
BH	= Bogosu host rock
PO	= Prestea ore
PH	= Prestea host rock
AO	= Ashanti ore
AH	= Ashanti host rock

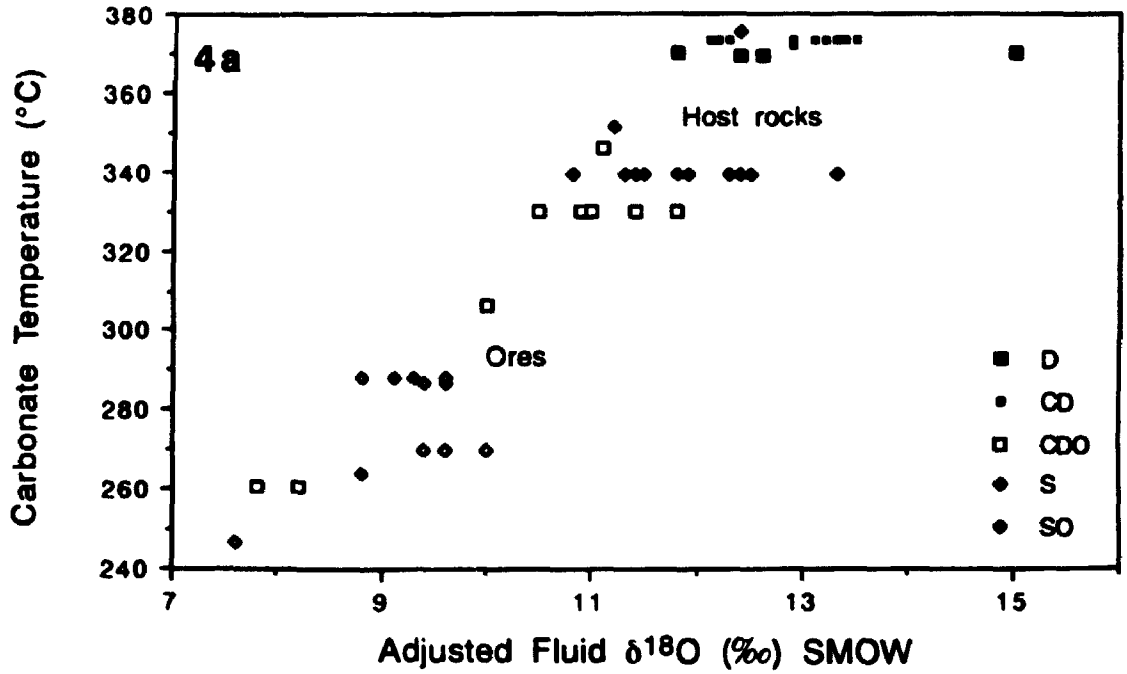
4a
Host rocks
Ores
D
CD
CDO
S
SO
Carbonate Temperature (°C)
Adjusted Fluid δ18O (‰) SMOW
380
360
340
320
300
280
260
240
7
9
11
13
15

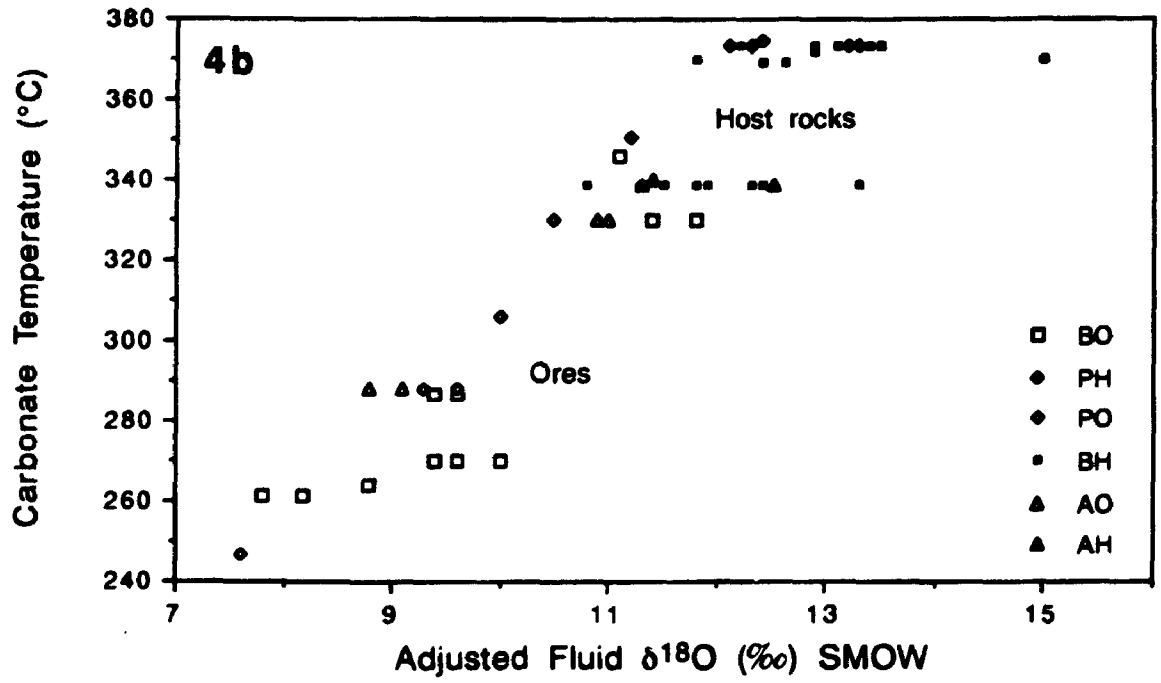
4b
Host rocks
Ores
BO
PH
PO
BH
AO
AH
Carbonate Temperature (°C)
Adjusted Fluid δ18O (‰) SMOW
380
360
340
320
300
280
260
240
7
9
11
13
15

9.3). Valley and O'Neil (1981) and Wada and Suzuki (1983) presented evidence indicating $\delta^{13}C$ exchange between graphite and carbonate minerals is sluggish at temperatures below 300 to 400°C in metamorphic systems. This is consistent with the current findings which suggest that the decreased sensitivity to lower temperatures may be attributable in part to locking in of the carbon-isotope ratios in graphite and/or ankerite at about 300°C. At lower temperatures, isotopic exchange rates may be too slow for re-equilibration between the hydrothermal fluid and carbon-bearing minerals. This may be particularly pertinent to hydrothermal systems in which fluid activity is restricted to short-lived pulses. Thus, time and temperature factors may have contributed to fixing of the $\delta^{13}C$ fractionation between graphite and ankerite, while cationic exchange of Fe, Mg, Mn and/or Ca continued to lower temperatures (Chapter 8).

Ten ore samples were examined to obtain an estimate of the temperatures of fluid trapping in fluid inclusions. Measurements were made on a LINKAM TH 600 programmable heating-cooling stage by standard methods as outlined by Shepherd (1981) and MacDonald and Spooner (1981). Only two of the samples examined (P-12 and DM-7) contained identifiable primary H_2O liquid-vapour inclusions, although all samples contained an abundance of primary CO_2 inclusions. Homogenization temperatures obtained from ten separate H_2O liquid-vapour primary inclusions in sample P-12 clustered around 296 ± 16°C, 332 ± 5°C and 382 ± 10°C. Although these values are uncorrected for pressure, they indicate trapping temperatures well within the range of measurements recorded by other means for the Prestea mine. For example, carbon-isotope temperature estimates for sample P-12 are 326 and 333°C, and the range of carbonate mineral chemistry temperatures from similar samples is 217 to 324°C.

Fluid Evolution

Variations in the calculated $\delta^{13}C$ and $\delta^{18}O$ ratios of the co-existing fluid, categorized according to rock-type and locality are illustrated in Figures 9.5, 9.6 and 9.7 for calcite, siderite and ankerite, respectively. The paragenetic relationships of the carbonate minerals are crucial to understanding the evolution of the isotopic composition of the fluid. Calcite in least-altered dikes is easily recognized as being an early carbonate that originated during greenschist facies metamorphism. Early deformation and alteration of these dikes is preserved in some samples where early-formed ankerite ± siderite co-exist with calcite (Figure 9.5, Table 9.1). The main carbonation event prior to mineralization produced pervasive intergrown siderite and ankerite. However, only ankerite was formed during mineralization, while much of the previously formed siderite altered to iron sulphides, or recrystallized in contact with the mineralizing fluid (Chapter 8).

Least-altered dikes have average $\delta^{18}O$ fluid values of 10.1 ± 0.2‰ (Table 9.1, Figure 9.5). For samples of least-altered dikes showing slight to moderate deformation and alteration, $\delta^{18}O$ values increase to a maximum of 13.6‰. Early formed ankerite and siderite from the same samples also yielded fluid $\delta^{18}O$ values of 12 to 15‰. Fluids associated with siderite and ankerite from pervasively carbonate-altered but unmineralized dike rocks have average $\delta^{18}O$ values of 13.0 ± 0.9‰. These values decrease to an average of 10.2 ± 2.2‰ (range = 7.8 to 11.8‰) for fluids associated with carbonates in mineralized dikes (Tables 9.2 and 9.3, Figures 9.6 and 9.7).

The isotopic values for carbonate minerals associated with the ores reflect

Figure 9.5: Calculated fluid $\delta^{18}O$ values compared with calculated fluid $\delta^{13}C$ values associated with calcite in least-altered dikes (see Table 9.1 for calculations). The data for least-altered dikes are believed to reflect the influence of early greenschist facies metamorphism and metasomatism upon the original magmatic signatures of the dikes. The higher isotopic values calculated from calcite in slightly-altered dikes may have been caused by interaction with a gaseous fluid during phase separation of the ore fluid.

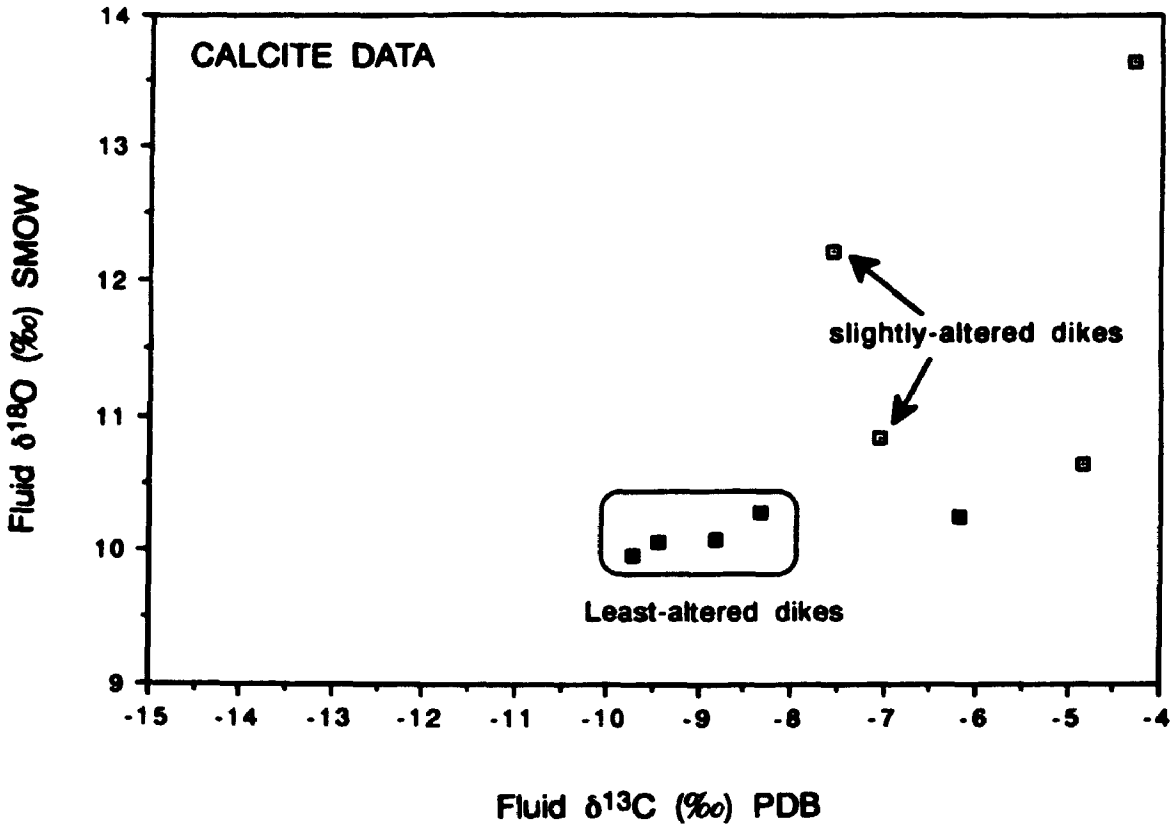
CALCITE DATA
slightly-altered dikes
Least-altered dikes
Fluid δ18O (‰) SMOW
Fluid δ13C (‰) PDB
14
13
12
11
10
9
-15
-14
-13
-12
-11
-10
-9
-8
-7
-6
-5
-4

Figure 9.6: Calculated fluid $\delta^{18}O$ values compared with calculated fluid $\delta^{13}C$ values associated with siderite (see Table 9.2 for calculations): a) data categorized according to rock type, and b) data categorized according to locality.

Legend:

D	= least-altered dike
CD	= carbonate-altered dike
CDO	= carbonated-dike ore
S	= sedimentary rock
SO	= sedimentary-rock ore
BO	= Bogosu ore
BH	= Bogosu host rock
PO	= Prestea ore
PH	= Prestea host rock
AO	= Ashanti ore
AH	= Ashanti host rock

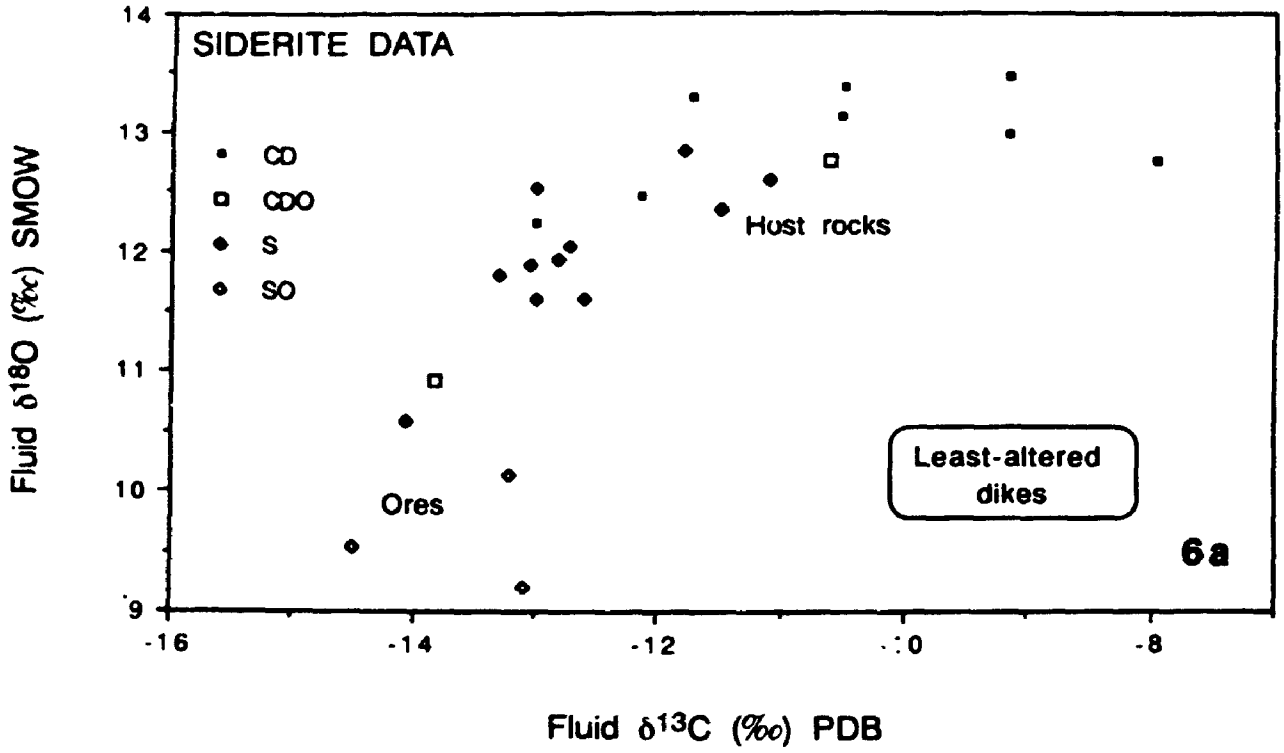
SIDERITE DATA
CD
CDO
S
SO
Host rocks
Ores
Least-altered dikes
6a
Fluid δ18O (‰) SMOW
Fluid δ13C (‰) PDB
14
13
12
11
10
9
-16
-14
-12
-10
-8

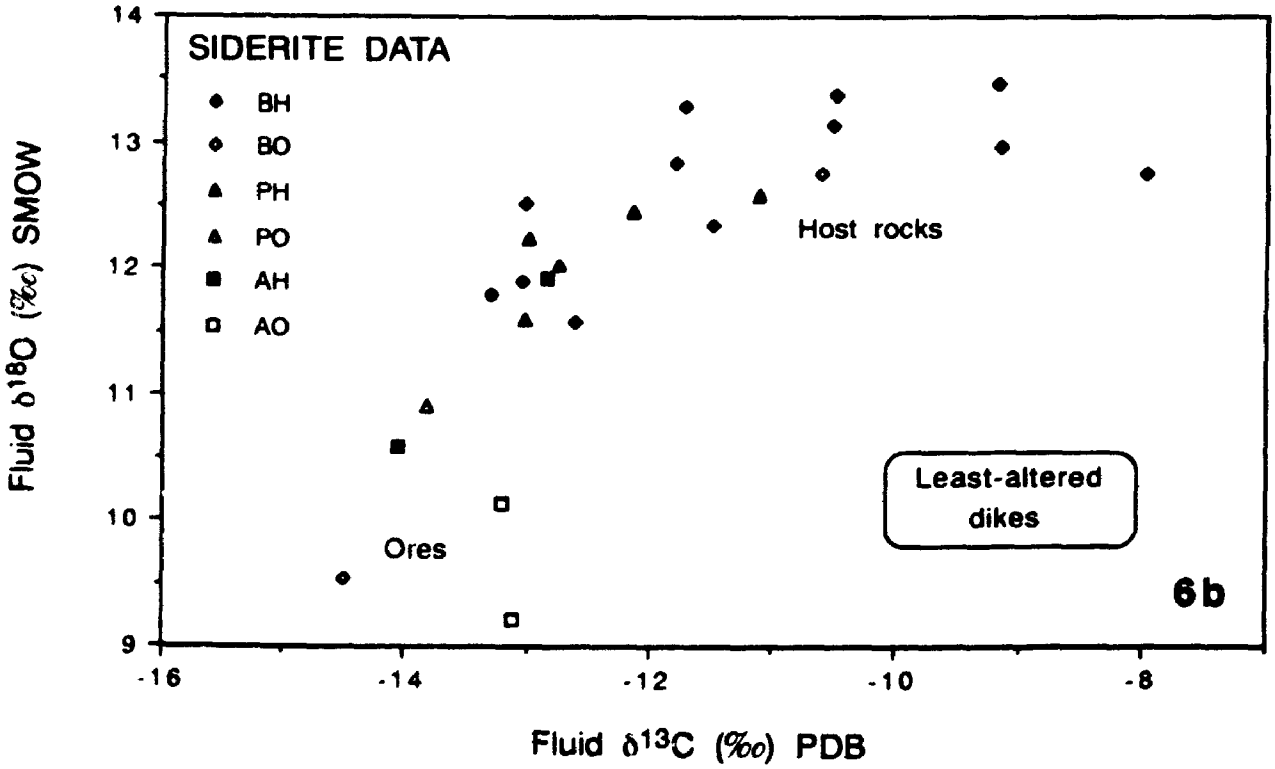
SIDERITE DATA
BH
BO
PH
PO
AH
AO
Host rocks
Ores
Least-altered dikes
6b
Fluid δ18O (‰) SMOW
Fluid δ13C (‰) PDB
14
13
12
11
10
9
-16
-14
-12
-10
-8

Figure 9.7: Calculated fluid $\delta^{18}O$ values compared with calculated fluid $\delta^{13}C$ values for fluids associated with ankerite (see Table 9.3 for calculations): a) data categorized according to rock type. and b) data categorized according to locality.

Legend:

D	= least-altered dike
CD	= carbonate-altered dike
CDO	= carbonated-dike ore
S	= sedimentary rock
SO	= sedimentary-rock ore
BO	= Bogosu ore
BH	= Bogosu host rock
PO	= Prestea ore
PH	= Prestea host rock
AO	= Ashanti ore
AH	= Ashanti host rock

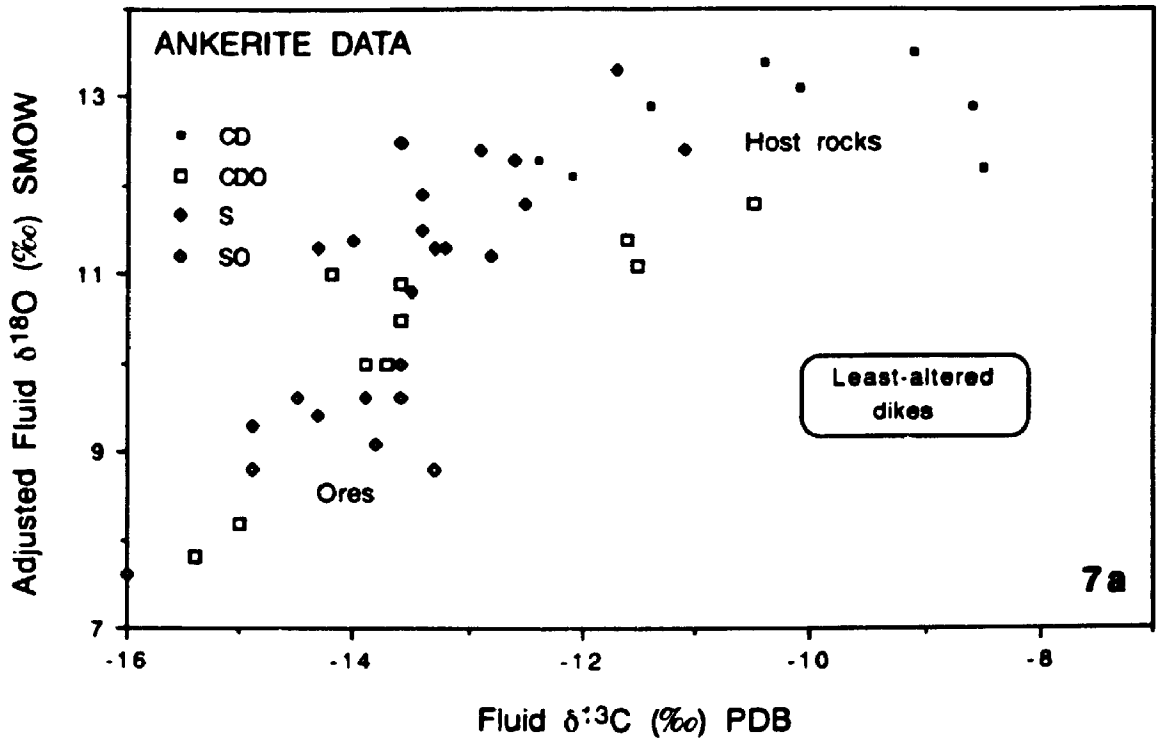
ANKERITE DATA
CD
CDO
S
SO
Host rocks
Least-altered dikes
Ores
7a
Adjusted Fluid δ18O (‰) SMOW
Fluid δ13C (‰) PDB
13
11
9
7
-16
-14
-12
-10
-8

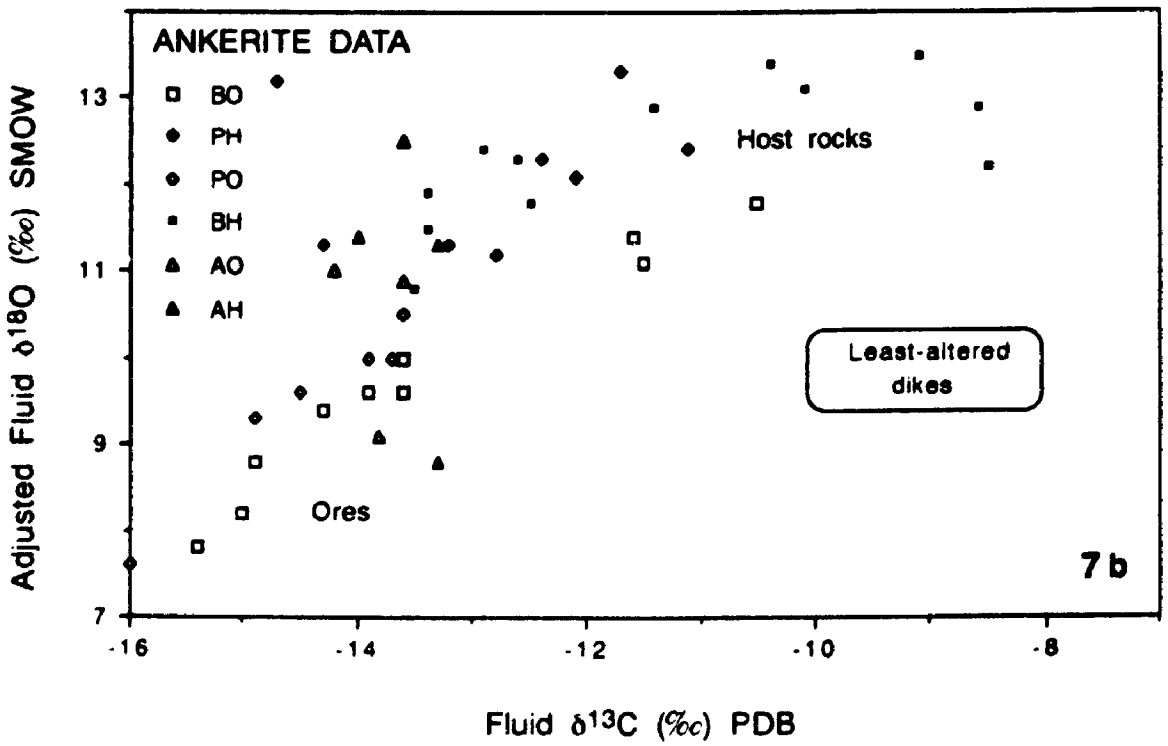
ANKERITE DATA
BO
PH
PO
BH
AO
AH
Host rocks
Least-altered dikes
Ores
7b
Adjusted Fluid δ18O (‰) SMOW
Fluid δ13C (‰) PDB
13
11
9
7
-16
-14
-12
-10
-8

the protracted hydrothermal alteration history of the gold system. Ankerite and siderite formed early and were later overprinted by the gold mineralizing event. This aspect of carbonate mineral paragenesis was discussed in detail in Chapter 8, where it was demonstrated that in many cases the elemental compositions of pre-existing carbonates did not achieve complete equilibration with the mineralizing fluid. This will be true also for isotopic compositions whose equilibration rates may be slower than those of Fe, Mg and Ca, as discussed above. Hence, the actual $\delta^{18}O$ values of the ore fluids may be lower than those indicated by most of the carbonate data.

Results for sedimentary rocks suggest a slightly different story. Calcite does not occur in the sedimentary rocks, nor are there obvious examples of pervasive ankerite-siderite alteration adjacent to ores, as is common in the dike rocks. Rather, all host sediments, including those that show no signs of deformation related to mineralization, contain moderate to abundant ankerite and siderite in the rock matrix, regardless of direct association with mineralization.

Fluid $\delta^{18}O$ values calculated for least-altered, greenschist facies sedimentary rocks average about 11.8 ± 1.5‰. One sample of deformed, but non-mineralized sedimentary rock yielded a slightly heavier fluid value of 12.3‰. The trend toward fluids with lower $\delta^{18}O$ values, averaging 9.2 ± 1.5‰ (siderite and ankerite data), in mineralized sediments is the same as for dike rocks (Figures 9.6 and 9.7).

The $\delta^{13}C$ values of fluids calculated for least-altered dikes (calcite data) averages -9.1 ± 0.8‰, with one value of -6.2‰ from a quartz-calcite veinlet. These values increase to a high of -3.6‰ (Table 9.2, sample # 42) in slightly altered and deformed dikes (calcite, ankerite and siderite data). Pervasive

carbonate alteration of the dikes produced siderite and ankerite from fluids that contained CO_2 with an average $\delta^{13}C$ value of -10.7 ± 3.8‰. Even lower values have been calculated using carbonates from ore samples (to -13.3 ± 2.8‰).

In contrast to the dikes, the variation in calculated $\delta^{13}C$ values of fluids associated with sediments is small. Fluid $\delta^{13}C$ values calculated from least-altered sedimentary rocks average -12.3 ± 1.4 and -13.1 ± 1.8‰ from siderite and ankerite data, respectively. Fluids associated with mineralized sedimentary rocks have moderately lower $\delta^{13}C$ values, -13.6 ± 0.9 and -14.3 ± 1.7‰ (as calculated from siderite and ankerite results, respectively).

Fluid evolution patterns follow common trends for both the Bogosu and Prestea regions. However, similar trends are reflected in samples taken from the Ashanti Goldfields Corporation mines in the Obuasi district. These data suggest that fluid evolution patterns found in the Bogosu and Prestea district may be representative of patterns common to the whole of the Ashanti Gold Belt (Table 9.7, Figures 9.5, 9.6b and 9.7b). In spite of similar trends, moderately lower fluid $\delta^{13}C$ values were obtained for the Prestea locality for both host and mineralized rocks. The corresponding fluid $\delta^{18}O$ values are only slightly lower at Prestea than Bogosu.

Graphite

Fluid $\delta^{13}C$ values calculated using graphite from three ore samples range from -15.2 to -10.2‰, similar to that obtained using ankerite and siderite data. One sample of host-rock for which reasonable carbonate temperatures were obtained yielded a $\delta^{13}C$ value for the fluid of -14.7‰. This value compares

reasonably with fluid $\delta^{13}C$ estimates by other means.

Quartz

Fluid $\delta^{18}O$ values calculated using quartz isotopic ratios show a similar temperature vs $\delta^{18}O$ trend to that for the carbonate data (Table 9.5). Both quartz and calcite from the host-rock sample P-7 (analyses # 2 and 3) give similar fluid $\delta^{18}O$ values of 10.8 and 10.0‰, respectively. Quartz $\delta^{18}O$ values were not obtained from pervasively carbonate-altered dike rocks.

A few direct comparisons are possible for oxygen-isotope compositions calculated for the ore-fluid using both quartz and carbonate data. Sample P-12 (analyses # 9 and 10) yielded similar results for both data sets, while samples DM-5, DM-7, DM-11 and Prestea 27 (analyses # 11 to 14A, 28, 47, and 51) gave average fluid $\delta^{18}O$ values of 7.6 and 9.4‰ from quartz and carbonate data, respectively. This discrepancy may result from incomplete re-equilibration of early-formed carbonates during mineralization, whereas most of the quartz in veins formed during the mineralization event. The implication is that the data for quartz may provide the most reliable estimate of the true $\delta^{18}O$ value of the ore fluid. Some of the most intensely mineralized samples have fluid $\delta^{18}O$ values calculated from ankerites that are similar to average fluid $\delta^{18}O$ values obtained using quartz data. Examples include samples DM-11, fluid $\delta^{18}O$ (ankerite data) = 7.8 and 8.2‰ (analyses # 13 and 14A), and P-30, fluid $\delta^{18}O$ (ankerite data) = 7.6‰ (analysis # 4). By comparison, calculated $\delta^{18}O$ values (from ankerite) for weakly mineralized samples such as P-28 and Prestea 27 are higher, 10.0 and 10.5‰ (analyses # 6, 8 and 47), respectively, demonstrating the effect of incomplete isotopic re-equilibration of pre-existing carbonates.

Discussssion and Conclusions

The fluid $\delta^{13}C$ and $\delta^{18}O$ values calculated using carbonate, quartz and graphite demonstrate that hydrothermal minerals at Bogosu and Prestea precipitated from, or altered in response to, fluids with distinctly different isotopic compositions (Tables 9.7a and 9.7b).

The predominant sedimentary rocks forming in southwestern Ghana during the Birimian period were carbonate-bearing and carbonaceous greywackes and turbidites. Evolution of an ore fluid must have involved equilibration with these rocks. It has been demonstrated by investigators such as Bottinga (1968), Ohmoto and Kerrick (1977) and Valley and O'Neil (1981) that, if a metamorphic fluid were buffered by graphite ($\delta^{13}C_{Gr}$ = -25% = $\delta^{13}C_{\Sigma C}$) at 300 to 500°C, the $\delta^{13}C_{CO2}$ would be ≈ -13 ± 2‰. This value is entirely consistent with the calculated ore fluid (from ankerite and siderite) and graphite $\delta^{13}C$ values of -13.3 to -14.3 ± 2.8‰ and -30.4 to -27.7‰, respectively, for the Bogosu and Prestea districts (Tables 9.7 and 9.4). A magmatic source for carbon ($\delta^{13}C_{CO2}$ ≈ -3.0 to -5.5‰, Taylor, 1979, 1987) does not fit the isotopic data. Nevertheless, intrusive bodies may have played a minor role in non-gold related alteration long before the mineralizing event took place, and an igneous component may have been added to the fluids in the system at that time.

The calculated carbon and oxygen-isotope fluid values for the study area fall within the broad range of values for fluids with a metamorphic origin, especially those originating in carbonaceous sedimentary rocks (Taylor, 1986, 1979; Ohmoto and Kerrick, 1977; Kerrich, 1987). It has been demonstrated in

Table 9.7a: Calculated fluid $\delta^{18}O$ and $\delta^{13}C$ compositions for the main alteration zones of mafic dikes.

	Greenschist Metamorphism	Pervasive Carbonation	Mineralization
$\delta^{18}O$ ‰	10.1 ± 0.2	13.0 ± 0.9	10.2 ± 2.1 (Ank) 7.5 ± 1.1 (Qtz)
$\delta^{13}C$ ‰	-9.1 ± 0.8	-10.7 ±3.8	-13.3 ±2.8

Calculated from carbonate isotopic compositions unless otherwise indicated.

Table 9.7b: Calculated fluid $\delta^{18}O$ and $\delta^{13}C$ compositions for the main alteration zones of sedimentary rocks.

	Greenschist Metamorphism	Pervasive Carbonation	Mineralization
$\delta^{18}O$ ‰	11.8.0 ± 1.5	NA	9.2 ± 1.5 (Ank) 8.4 ± 1.7 (Qtz)
$\delta^{13}C$ ‰	-12.7 ± 2.2	NA	-14.3 ± 1.7

Calculated from carbonate isotopic compositions unless otherwise indicated.

Chapters 3, 4 and 5 that calcite and quartz in least-altered dikes are part of the greenschist facies metamorphic / metasomatic assemblage that has affected all rocks examined in the Ashanti structural zone of the Bogosu and Prestea concessions. Hence, fluid compositions ($\delta^{18}O = 10.1 \pm 0.2‰$, $\delta^{13}C = -9.1 \pm 0.8‰$) calculated using these minerals are believed to reflect the influence of pre-mineralization, greenschist facies metamorphic conditions upon the original magmatic isotope signature of the dike rocks (i.e., lower $\delta^{18}O$ and higher $\delta^{13}C$ values for magmatic fluids, Figure 9.8). These values contrast with calculated fluid $\delta^{18}O$ and $\delta^{13}C$ values of 11.8 ± 1.5 and $-12.7 \pm 2.2‰$, respectively, obtained for the least-altered sedimentary country-rocks. Mineral assemblages and temperature estimates (Chapters 3, 4 and 8) indicate that both the dikes and carbonaceous country-rocks were contemporaneously metamorphosed. However, the above data suggest incomplete equilibration of the dikes with a metamorphic fluid that appears to have been buffered by the host-sedimentary rocks. During peak metamorphic conditions it is probable that these dikes were in a zone of low-permeability, and hence would have been subjected to low water-rock ratios which may account for the observed incomplete isotopic equilibration with the sedimentary country-rocks.

Carbonate-altered dikes yielded fluid $\delta^{18}O$ values of $13.0 \pm 0.9‰$ and $\delta^{13}C$ values of $-10.7 \pm 3.8‰$. By contrast, ores associated with both dike and sedimentary rocks indicate mineralizing fluids had lower $\delta^{18}O$ values averaging 10.5, 9.7 and 8.1‰ based on analysis of siderite, ankerite and quartz, respectively. Paragenetic, compositional and textural evidence presented in Chapters 4, 6 and 8 demonstrate that: 1) siderite formed prior to mineralization, 2) ankerite formed before and during mineralization, 3) most quartz in the ore zone precipitated contemporaneous with gold deposition, and 4) ankerite and siderite did not completely re-equilibrate with the ore fluid

Figure 9.8: Fluid evolution diagram showing calculated $\delta^{18}O$ and $\delta^{13}C$ values of fluids associated with gold mineralization in the Bogosu, Prestea and Obuasi (Ashanti) mining districts of the Ashanti Gold Belt. The primary ore fluid is believed to be a metamorphic fluid buffered by the carbonaceous country-rocks.

Stages in the isotopic evolution of fluids associated with mafic dikes and carbonaceous sedimentary rocks:

1) Range of possible isotopic compositions for magmatic fluids (1) associated with the mafic dikes.
2) Superposition of country-rock isotopic signatures (3) (proposed ore fluid) on the dikes (2) at greenschist facies temperatures and low water-rock ratios. A low water-rock ratio during metamorphism is believed to be the reason for incomplete isotopic equilibration of the dikes with the country-rocks.
3) Alternative 1: Carbonation of the mafic dikes (4) by the proposed ore fluid at the high water-rock ratio and lower-temperatures found in the zone of mineral deposition.
4) Alternative 2: Separation from the proposed ore fluid of a CO_2 gas phase that has higher $\delta^{18}O$ and $\delta^{13}C$ values. This less viscous gas phase could permeate the wall-rocks adjacent to the structural conduits and cause carbonation of the mafic dikes (4).
5) Mineral precipitation from a residual ore fluid after phase separation (5). The residual fluid will be isotopically lower than the original (unseparated) proposed ore fluid. During mineralization the lower isotopic signature (of the residual fluid) will be superimposed upon the previously-carbonated rocks. Average isotope values for the residual ore fluid calculated from siderite, ankerite and quartz are shown separately. The change from higher $\delta^{18}O$ fluid values associated with siderite to lower $\delta^{18}O$ fluid values associated with quartz follows a trend toward increasing equilibration of these minerals with the residual ore fluid. Calculated $\delta^{13}C$ fluid values suggest a similar, but less obvious trend toward lighter values with increased equilibration of hydrothermal minerals and the residual ore fluid.

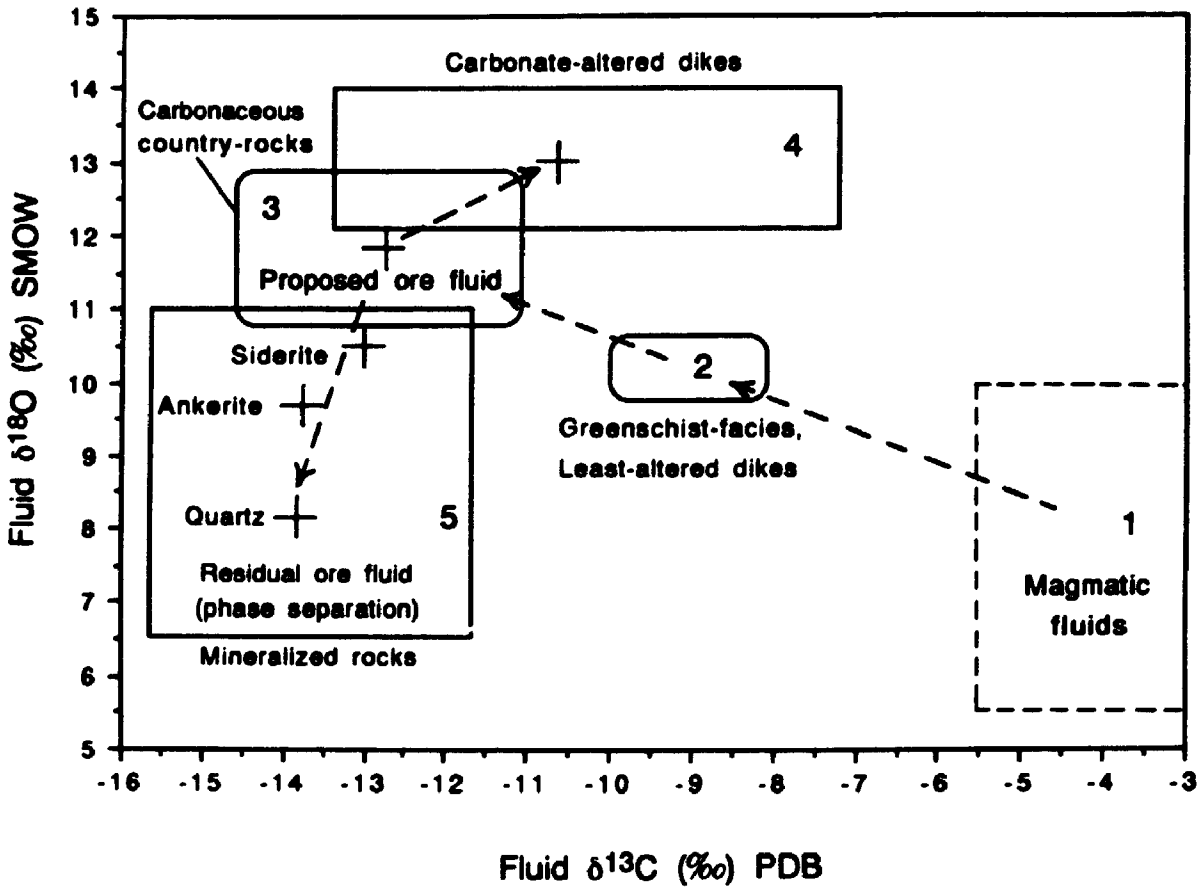
Carbonate-altered dikes
Carbonaceous country-rocks
4
3
Proposed ore fluid
Siderite
Ankerite
Quartz
5
Residual ore fluid (phase separation)
Mineralized rocks
2
Greenschist-facies, Least-altered dikes
1
Magmatic fluids
Fluid δ18O (‰) SMOW
Fluid δ13C (‰) PDB
15
14
13
12
11
10
9
8
7
6
5
-16
-15
-14
-13
-12
-11
-10
-9
-8
-7
-6
-5
-4
-3

during mineralization. Consequently, the change from higher $\delta^{18}O$ fluid values associated with siderite to lower $\delta^{18}O$ fluid values associated with quartz is believed to be the result of increasing equilibration of these minerals with the ore fluid during mineralization (Figure 9.8). Hence, quartz associated with mineralization yields the best $\delta^{18}O$ estimate of the associated fluid. Corresponding fluid $\delta^{13}C$ values associated with mineralization decrease to -13.3 ± 2.8 and -14.3 ± 1.7‰ as calculated for dike and sedimentary-rock ores, respectively. These values are are up to 1 to 2‰ lower than obtained for the host sedimentary rocks.

The zone of pervasive carbonate alteration that is present in mafic dikes is not detected in sedimentary rocks, even though the two mineralized rock types (dike and sedimentary) are always found adjacent to each other and most mineralization is sediment-hosted. Both host sedimentary rocks and their mineralized zones contain pervasive, disseminated ankerite and siderite. The isotopic evidence presented here affords the best explanation for this ubiquitous association of ankerite and siderite, in showing that the ore fluids were equilibrated with the host sediments. Hence, even though the sediments were affected by the same fluids causing pervasive carbonation of the dikes, these fluids had a minimal, further affect on the sedimentary rocks.

The carbonate relationships discussed above might suggest that the ore fluids originated in sedimentary country-rocks adjacent to the ores, and migrated laterally into the structural zones. However, the foregoing analysis in Chapter 8 demonstrated that ambient country-rock temperatures at the time of mineralization were much lower than the peak metamorphic temperatures recorded in the same host-rocks, and were lower than temperatures associated with the bulk of gold deposition. Consequently, the adjacent country-rocks

could not have been the source of mineralizing fluids for the Bogosu and Prestea ores. Rather, the ore fluids are believed to originate from similar rocks at a deeper level in the crust beneath the mineralized zones where higher rock-temperatures occur.

It is necessary to account for the isotopic difference between the proposed ore fluid ($\delta^{18}O \approx 11.8 \pm 1.5‰$ and $\delta^{13}C \approx -12.7 \pm 2.2‰$), and actual isotopic fluid values calculated from: 1) rocks with pervasive carbonate alteration that preceeded gold mineralization ($\delta^{18}O \approx 13.0 \pm 0.9‰$ and $\delta^{13}C \approx -10.7 \pm 3.8‰$), and 2) gold mineralized rocks ($\delta^{18}O \approx 8.1 \pm 1.7‰$ (quartz) and $\delta^{13}C \approx -13.8 \pm 2.8‰$ (ankerite)). Phase separation in the ore fluid provides an explanation for the observed increase of isotopic ratios in fluids associated with carbonate-altered rocks as well as the lower fluid isotope ratios calculated from ore samples (Table 9.7). Phase separation can also explain the presence of two distinct primary fluid inclusion types. Fluid immiscibility can occur in response to a number of parameters affecting the ore fluid including: pressure release resulting from tensional fracturing, lowering of hydrostatic pressures during fluid ascent, temperature decrease, and other mechanisms that would promote formation of a secondary gaseous fluid phase into which CO_2 and other volatiles partition. According to the theoretical calculations of Bowers (1991), temperature decrease has the most dramatic influence on inducing fluid immiscibility, with pressure decline being most important below about 2000 bars for a temperature of 250°C. Both mechanisms may have played an important role at Bogosu and Prestea. Phase separation with removal of gaseous CO_2 causes depletion of ^{18}O and ^{13}C in the residual fluid, particularly if decarbonation of the fluid occurs by Rayleigh (continuous) distillation in an open system (Bowers,1991; Lattanzi et al., 1980; Bowman et al., 1985). The amount of the ^{18}O depletion varies significantly with temperature, pressure and

the proportion of CO_2 in the original fluid (Bowers, 1991), and can account for the observed depletions (1-2‰ $\delta^{13}C$ and 2-5‰ $\delta^{18}O$) at Bogosu and Prestea. For example, it has been calculated by Higgins and Kerrich (1982), that separation of 20 mol% CO_2 at 300°C would cause a 3 per mil depletion in ^{18}O of the residual fluid assuming a $CO_{2(gas)}$-$H_2O_{(liquid)}$ fractionation of 14 per mil at 300°C (Bottinga, 1968; Kerrich, 1987).

During the process of phase separation it is unlikely that a unique isotopic composition for the residual ore fluid will result. It is more probable that a range of values will occur, to a maximum end-member composition largely constrained by the content of CO_2 (± other volatiles) in the original fluid and the temperature at which phase separation occurred. Consequently, the range of residual ore fluid values shown in Figure 9.8 may represent an evolution of the fluid, as well as the effects of increasing equilibration with associated mineral phases (discussed above).

Ellis and Mahon (1977) and Spooner et al., (1987) suggest that when phase separation occurs, the volatile phase is significantly less viscous than the residual fluid. Consequently, it can penetrate to greater distances in the wall-rock, and can permeate the host-rock faster, thereby altering the host prior to contact with the residual ore fluid. Such behaviour may have important implications at Bogosu and Prestea. It can explain the presence of the zone of pervasive carbonate alteration in dikes, which preceeded gold mineralization and permeated the wall-rocks adjacent to ore zones for up to several tens of metres, even where fracturing is minimal. Fractionation of the heavier isotopes, ^{13}C and ^{18}O, to a CO_2 gaseous phase can also account for higher fluid values calculated for the carbonated dikes (13.0 ± 0.9‰ $\delta^{18}O$ and -10.7 ± 3.8‰ $\delta^{13}C$), which could have reacted with this gas phase prior to, or in lieu of,

contact with the residual ore fluid.

If the gaseous phase was produced by boiling of an H_2O fluid as opposed to phase separation, the lighter isotopes (^{16}O and ^{12}C) would partition into the H_2O vapour phase, producing an isotopically heavier residual fluid. However, CO_2 gas is enriched in ^{18}O and ^{13}C relative to liquid H_2O, and its removal leaves the residual fluid depleted in ^{18}O and ^{13}C. The CO_2 contents of ore fluids in many lode gold systems are in the range of 1 to 12%, which generally restricts ^{18}O depletion to <2% (Smith and Kesler, 1985). However, deposits hosted by carbonaceous sedimentary rocks commonly have much higher CO_2 contents in the associated fluids, consistent with the larger depletions calculated for the Bogosu and Prestea fluids.

Alternatively, carbonation of the dikes prior to mineralization may have been caused by reaction with the ore fluid prior to phase separation. High water-rock ratios in the structural conduit, and lower rock-temperatures may have caused the ankerite-siderite-sericite (+K, +Ba, -Ca) alteration halo prior to mineralization. This contrasts with the chlorite-calcite-epidote (-K, -Ba, +Ca) alteration of similar mafic rocks caused by the same fluids at higher temperatures and low water-rock ratios during greenschist facies metamorphism (Chapters 3, 4, and 5). Most importantly, the isotopic fractionation between the proposed ore fluid (11.8‰ $\delta^{18}O$ and -12.7‰ $\delta^{13}C$) and measured isotopic values in carbonate-altered dikes is consistent with experimentally and theoretically determined fractionations (e.g., Carothers et al., 1988; Land 1983; Golyshev et al., 1981, Tables 9.2 and 9.3). Subsequent phase separation in the ore zone could then have produced a residual ore fluid that could account for the lower isotopic fluid values calculated from mineralized samples.

The carbon and oxygen-isotopic evidence presented and discussed in this Chapter is most consistent with the evolution of an ore fluid that equilibrated with the carbonaceous sedimentary rocks of the Birimian. These fluids migrated in focussed flow along the dilatant major structural failures of the Ashanti Structural Belt. The isotopic evidence further suggests that phase separation into CO_2 gas and a residual fluid occurred and was probably responsible for gold precipitation, and the patterns of hydrothermal alteration documented in the ore zones.

Chapter 10: Evolution of the Bogosu and Prestea Ore System

The Ashanti Structural Belt is a crustal thrust belt in the Proterozoic Birimian rocks of Ghana, West Africa. The Birimian consists largely of greywackes and turbidites that are characteristically carbonaceous (both carbonates and graphite) within the Ashanti Structural Belt, and are believed to be carbonaceous also on a more regional scale. The structural belt is intruded by numerous dikes of variable, but mainly mafic, composition that were interpreted previously to be extrusive volcanic rocks.

The gold ores of the Bogosu and Prestea concession are mesothermal, and closer to Cordilleran mesothermal deposits (Leitch et al., 1991; Nesbitt et al., 1989; Goldfarb et al., 1986) than to Archean lode gold deposits (Colvine, 1989; Groves et al., 1989). Gold mineralization occurs in large crack-seal quartz-vein lodes and narrow carbonaceous shear zones at the Prestea concession, that are interpreted to be deeper ores within the gold system (Figure 3.3, Plate 4.4A), and in wide zones of tectonically-disrupted sediments and carbonate-altered dikes (Figure 3.4, Plates 4.3 and 4.4B) at the Bogosu concession (Figure 10.3), that are interpreted to be higher-level ores.

Mineralization occurred during episodic relaxation of the tectonic environment, when the Ashanti Structural Belt became a dilatant structural failure of regional extent. Upward surging ore fluids were focussed along permeable pathways, and mineralization occurred preferentially in dilatant structures. Ores and wallrocks were repeatedly and complexely overprinted by later pulses of ore fluids. On a broader scale, the Birimian sedimentary rocks are interpreted to represent a sediment-dominated accretionary prism that formed together with the later Ashanti Structural Belt in a tectonic setting

similar to that of the southwest coast of Alaska. The evidence supporting these interpretations is reviewed below.

All host-rocks within the Bogosu and Prestea districts of the Ashanti Structural Belt were overprinted by an early greenschist facies metamorphism, at fairly low water / rock ratios. The characteristic mineral assemblages are obscured by the later hydrothermal alteration in the mafic dikes and the slight mineralogical changes that this alteration would have caused to the iron-carbonate rich sedimentary rocks. However, in the least-altered mafic dikes the mineral assemblage is dominated by chlorite, calcite, quartz and epidote typical of greenschist facies metamorphism (Table 5.2). The subsequent hydrothemal alteration of the mafic rocks resulted in a mineral assemblage quite similar to that of the enclosing sediments; i.e. dominated by ankerite, siderite, sericite, quartz, albite, chlorite and rutile (Table 3.1). Evidently, this phase of alteration was associated with a very high fluid / rock ratio, and therefore could only have taken place when the fluids were focussed within the dilatant structures. Deposition of sulphide and arsenide minerals and gold followed immediately after the hydrothermal alteration; the latter therefore being an intrinsic part of the gold mineralizing event.

The geochemical, mineral chemical and isotopic evidence for the late alteration and gold deposition, presented in Chapters 5, 8, and 9, respectively, point to the generation of a metamorphogenic fluid at depth below the ore deposits, and in equilibrium with the Birimian sedimentary rocks (cf. Powell et al., 1991). Formation temperatures calculated from mineral-chemical geothermometers peak at about 390°C for metamorphic minerals and 406°C for hydrothermal minerals (Tables 8.1 and 8.2). The anomalously high calculated temperatures of 400 to 600°C indicated by some ankerite-siderite and

arsenopyrite (Figure 6.3) geothermometers may be attributable to pulses of higher-temperature fluids, and are temperatures at which decarbonation and dehydration reactions occur.

The metamorphogenic fluids were focussed along the Ashanti Structural Belt during periods of dilatancy, (Figures 10.2 and 10.3) and reacted with the sedimentary and intrusive igneous host-rocks during their ascent. Mass-balance calculations (Table 5.3) from whole-rock geochemical analyses for sedimentary and mafic igneous host-rocks within the structural belt show large increases in volatile contents during the greenschist facies metamorphism / metasomatism. The chlorite-dominated mineralogy of mafic dikes, and abundance of sericite and chlorite in sedimentary rocks suggest that hydration of the country rocks created a sink for H_2O from the hydrothermal fluid during its migration through the approximately 1 km wide structural zone of the Ashanti Belt. Although the sedimentary rocks contain an abundance of carbonate minerals, it cannot be determined whether or not these rocks also removed CO_2 from the hydrothermal fluid, since the Birimian sedimentary rocks are believed to have been carbonate-rich since the time of their deposition.

The partial removal of volatiles would have had several important effects upon the hydrothermal fluid prior to reaching the zone of gold-sulphide deposition, including: 1) increasing the concentration of dissolved metals in the residual fluid, 2) preferential removal of H_2O, thereby increasing the proportion of CO_2 in the residual fluid, and 3) reaction with the wall-rocks that apparently contributed several elements such as K and Ba to the hydrothermal fluid (Table 5.3). Three stages in the evolution of the hydrothermal fluid suggested by the current investigation are illustrated in Figure 10.2: 1) metamorphic fluid generation by decarbonation and dehydration reactions, 2)

reaction of the metamorphic fluids with the country-rocks at decreasing temperatures during upward migration along the structural conduit, and 3) phase separation at relatively high crustal levels and low ambient pressure and temperature conditions (Chapter 9).

Phase separation has been documented, primarily by fluid inclusion analyses, in many lode gold systems including: Doyon and Sigma mines in Quebec, Hollinger-McIntyre and Pamour #1 in Ontario, and Hunt, Morning Star, Mount Charlotte and other metasedimentary-rock-hosted deposits in Western Australia (Guha et al., 1982; Robert and Kelly, 1987; Wood et al., 1986; Groves et al., 1984; Ho et al., 1985). Phase separation is an excellent method for inducing ore precipitation; its effects on mineral solubility have been discussed by many investigators (e.g. Arnorsson, 1978; Drummond and Ohmoto, 1985; Spooner et al., 1987). During phase separation, volatile species progressively partition into the secondary gaseous fluid according to their gas/liquid partition coefficients (H_2>CH_4>CO_2>H_2S>SO_2). This affects the residual ore fluid by causing: rapid oxidation, loss of metal complexing ligands (mainly HS^-), temperature decrea e and pH fluctuations. At Bogosu and Prestea, the documented transformation of early pyrrhotite to marcasite and pyrite (Table 6.1) indicates increasing pH and fO_2 of the ore fluid to the range of values that would promote dramatic increases in the solubility of gold (Romberger, 1989; Murowchick, 1992) and inhibit gold precipitation. However, the combined physico-chemical changes associated with phase separation are sufficient to supercede other factors and cause rapid precipitation of sulphide and arsenide minerals and gold. The solubility of metals in the residual ore fluid can readily decrease by several orders of magnitude (Drummond, 1981; Spooner et al., 1987; Shenberger and Barnes, 1989; Brown, 1989; Seward, 1989).

The critical changes to the ore fluid chemistry that occur during phase separation are most likely responsible for the rapid precipitation of arsenian pyrite, arsenopyrite and gold, in solid-solution within the sulphide and arsenide minerals. As discussed in Chapter 7, the evolution of the gold deposit did not stop with mineral precipitation. Important changes occurred as gold in solid-solution within arsenian pyrite and arsenopyrite recrystalized, redistributed and concentrated to form colloidal and microscopic gold particles within cavities, microfractures and at internal grain boundaries. It appears that under higher-temperature late alteration overprinting, as in the Prestea ores, some of this gold migrated out of the host sulphide grains and reprecipitated in fractures and cavities interstitial to silicate minerals.

The Bogosu and Prestea ore system can be reconstructed on the basis of the many documented differences between the relatively deep and higher-level ores. These differences are schematically summarized in Figure 10.1, and result from a gradual change in three main physico-chemical parameters, namely temperature, confining pressure and chemical compostion of the hydrothermal fluid. It has been demonstrated that Prestea ores formed in the deeper part of the gold system (Chapters 3, 4, 6, 7, 8 and 9). Also, the carbonate mineral geothermometry (Chapter 8, Table 8.3) suggests average temperature and depth differences of 73°C and 3.5 km between Bogosu and Prestea ores.

The difference in the depth of mineralization is sufficient to span a range of structural styles from brittle-ductile at Prestea to brittle deformation at Bogosu (Chapters 3 and 4). This also resulted in many significant mineralogical and geochemical differences which are summarized in Figure 10.1 and discussed throughout the thesis. These differences are believed to be gradual changes that

Figure 10.1: Schematic section through the Bogosu-Prestea ore system. Gold depostits exposed on the Bogosu concession represent higher levels of mineralization, whereas deeper-level ores are exposed within the Prestea mine:

Ag = silver, Asp = arsenopyrite, Au ↓ = gold precipitation, Cpy = chalcopyrite, Gg = gangue, P = pressure Po = pyrrhotite, Py = pyrite, S_2 = sulphide minerals, Sph = sphalerite, T = temperature.

Figure 10.1: Schematic section through the Bogosu-Prestea ore system.

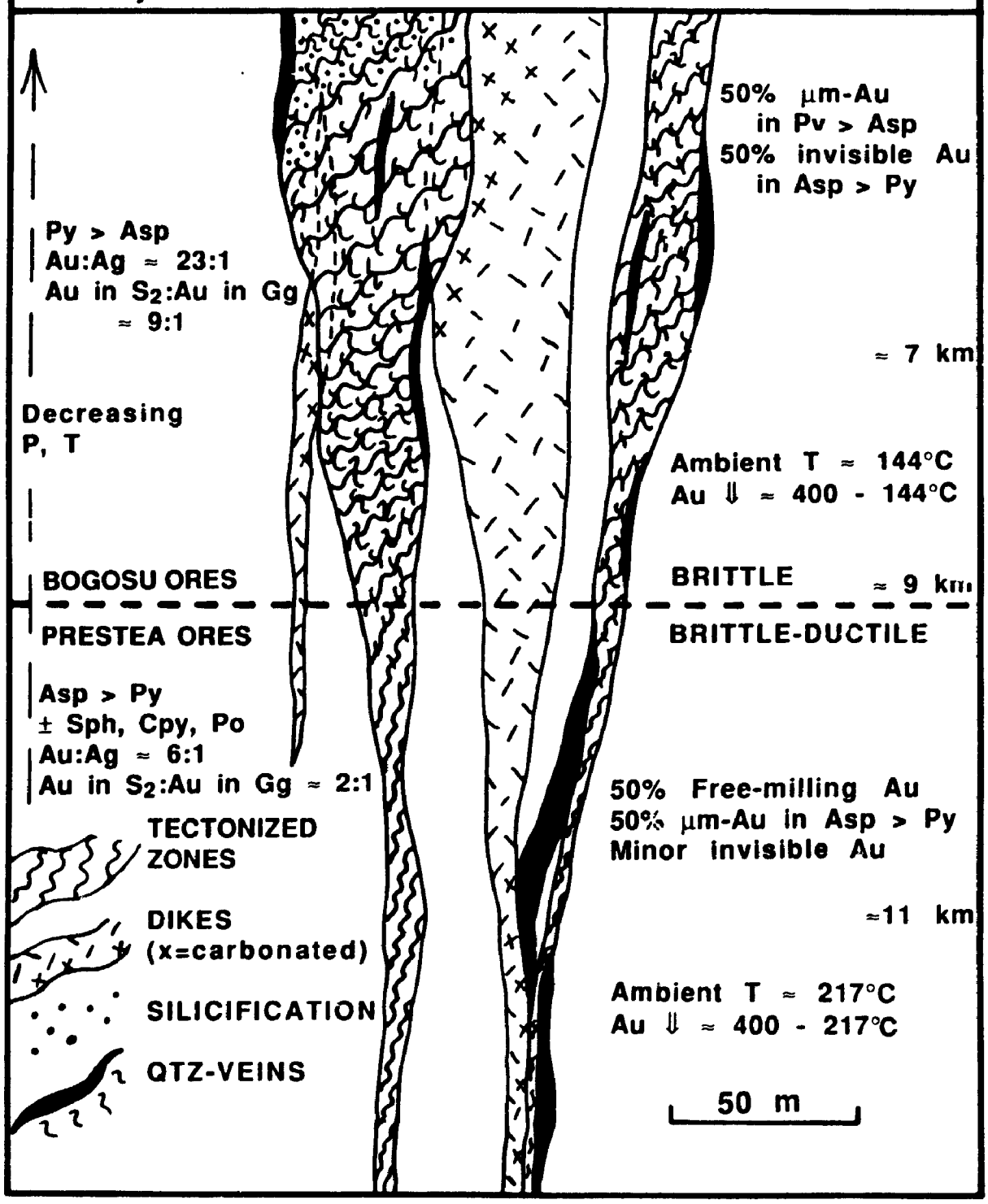

Figure 10.2: Evolution of the ore-forming fluids of the Bogosu and Prestea gold system.

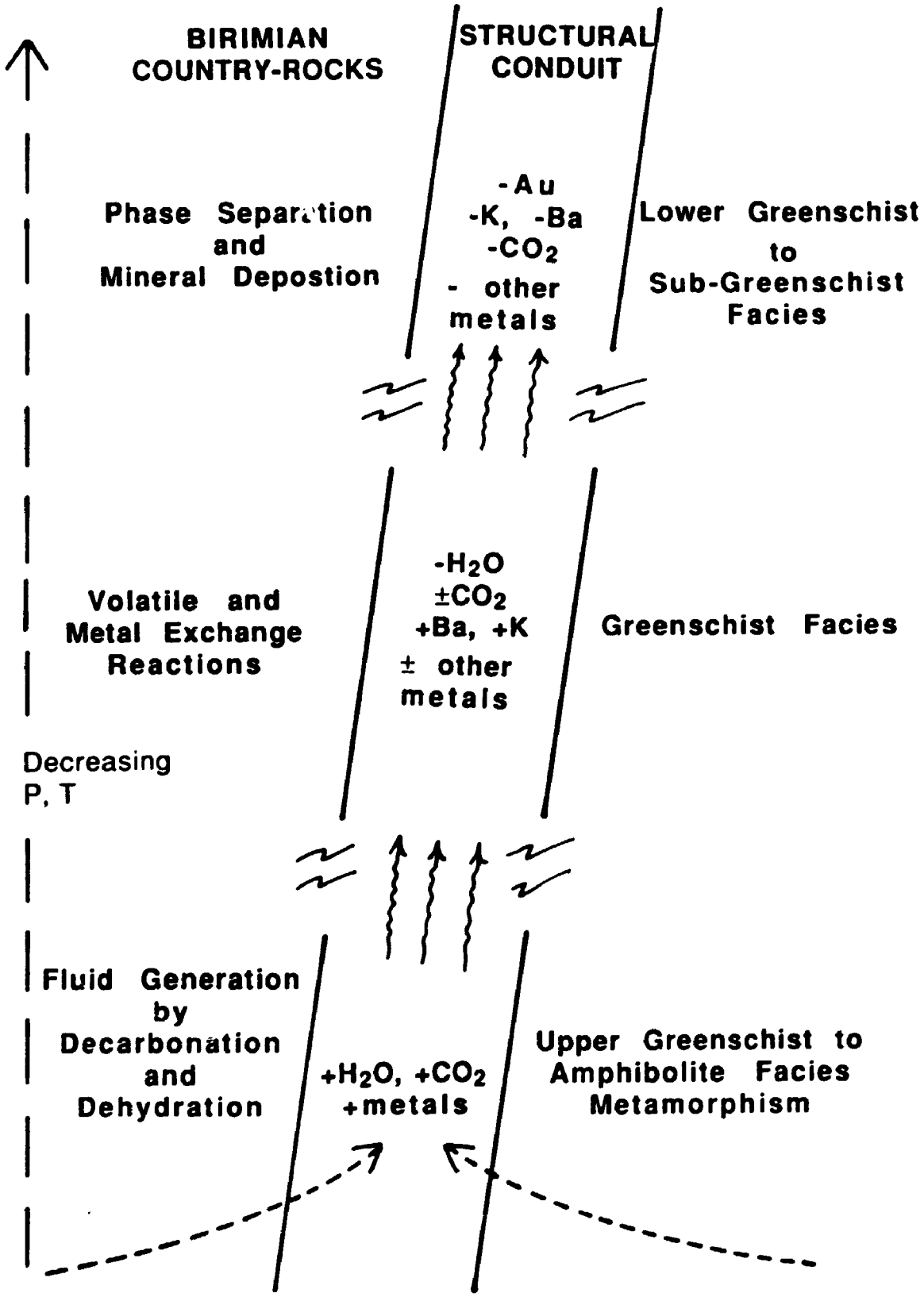

Figure 10.3: Model for the evolution of Ashanti Gold Belt mineralization in a sediment-dominated accretionary prism.

MODEL FOR ASHANTI-TYPE GOLD MINERALIZATION IN A SEDIMENT-DOMINATED ACCRETIONARY PRISM

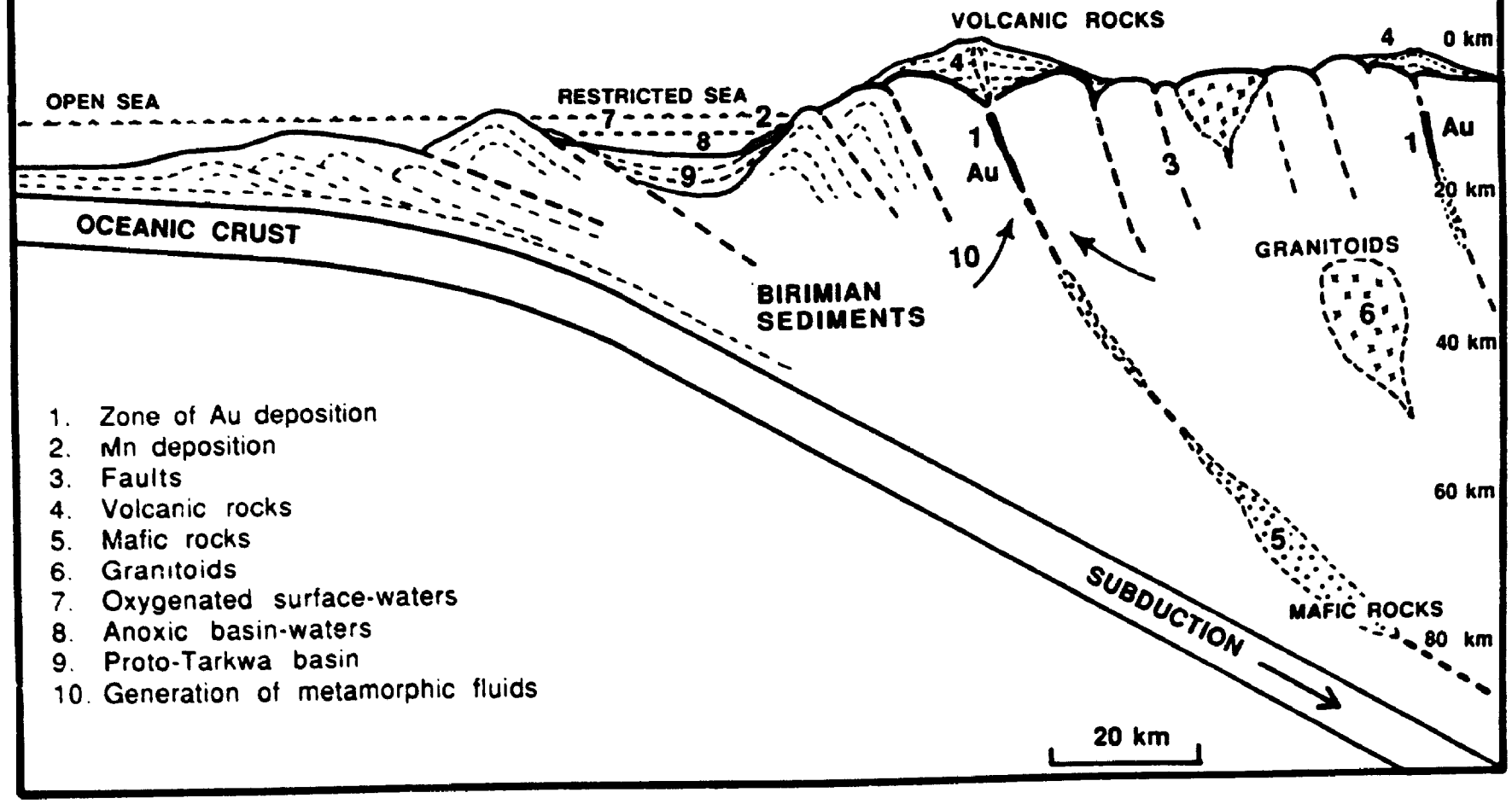

took place during fluid migration to higher levels in the system. However, sudden changes may be induced by dynamic effects such as new pulses of higher-temperature ore fluids, intermittent phase separation, seismic fault failure (Sibson et al., 1988) and differences in rock chemistry and texture. Consequently, on a local scale many diverse features may be superimposed. Nevertheless, regionally the distinction between deep and high-level ores is well preserved between the Prestea and Bogosu districts (cf. Colvine, 1989; Colvine et al., 1988).

In respect to the oxygen and carbon-isotope characteristics of quartz and carbonate minerals, the Bogosu and Prestea deposits are closer to Cordilleran mesothermal deposits (Leitch et al., 1991; Nesbitt et al., 1989), than to the geologically and structurally similar Archean lode gold deposits (Golding et al., 1989; Kerrich, 1987). Of particular interest are the mesothermal gold deposits of the Valdez Group near Juneau, Alaska (Goldfarb et al, 1991, 1989, 1988) which have many characteristics in common with the gold ores of the Bogosu and Prestea concessions including: 1) a variety of mineralization styles hosted by tectonically-disrupted sediments and intrusive rocks, 2) location in second-order structures of a major crustal lineament, caused by the competency contrast of juxtaposed intrusive and sedimentary rocks, 3) moderate to low-grade, disseminated-sulphide-hosted deposits as well as higher-grade quartz vein deposits, and 4) similar compositions of the ore fluids. On a regional scale, the geological features of southwestern Ghana have many similarities with some areas of active subduction including the southern coast of Alaska (cf. Sample and Moore, 1987). Consequently, it is proposed that the Ashanti gold deposits developed in a sediment-dominated accretionary prism in a tectonic setting analogous to that of the gold deposits of the Juneau district. The major features of the present model are illustrated in Figure 10.3.

It has been demonstrated above that there is no direct genetic link between major gold and manganese deposition in the Birimian of southwestern Ghana (Chapter 5, Table 5.3). Nevertheless, the geological model shown in Figure 10.3 is a plausible setting for the development of black-shale basin type manganese deposits (Force and Cannon, 1988; Frakes and Bolton, 1992, 1984), and thus can account for the presence of abundant stratiform manganese deposits aligned in belts parallel to the major tectonic features of the Birimian (Figure 2.5).

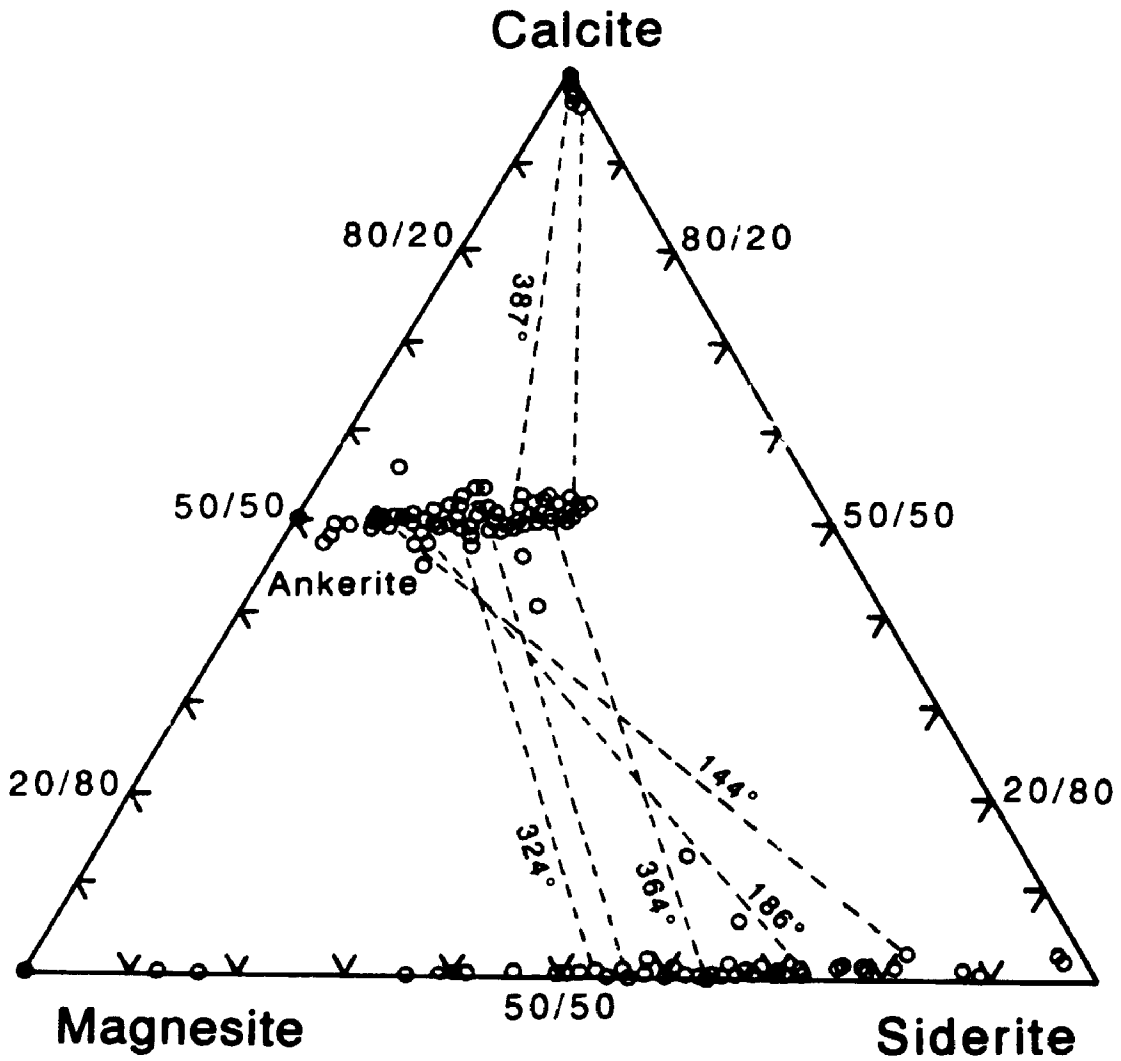

Figure 8.1: Ternary plot of carbonate mineral chemical analyses (mol%). $CaCO_3$ + $MgCO_3$ + $FeCO_3$ recalculated to 100%. All Bogosu and Prestea data are presented. Tie lines are for selected coexisting phases and are steeper for higher formation temperatures (T°C).

Chapter 11: Conclusions

The Ashanti Gold Belt of southwestern Ghana is hosted by Birimian (2.1 Ga) carbonaceous and carbonate-rich sedimentary rocks. The sedimentary rocks are categorized into phyllites, greywackes, turbidites and tectonized rocks on the basis of graphite content, thickness of bedding, grain size and the degree of metamorphic and structural alteration and deformation. The mesothermal gold ores of the Bogosu and Prestea districts occupy dilatant structures within the thrust-related Ashanti Structural Belt, and formed during periods of relaxation of tectonic stresses. Mineralization is post-peak metamorphism, and follows hydrothermal alteration of sedimentary and mafic lithologies to an assemblage containing abundant ankerite, siderite and sericite.

Economic gold deposits exposed along the 33 km strike length of the Bogosu and Prestea concessions are believed to have been deposited by the same hydrothermal system. Subsequent erosion has exposed deeper portions of the gold system on the Prestea concession, and higher-level ores on the Bogosu concession. Crack-seal quartz veins and narrow, carbonaceous shear-zones (graphitic fissures) are the common ore types in the brittle-ductile rocks at Prestea. Zones of tectonically-disrupted sediments (graphitic crush zones) up to 50 m wide with sheared quartz stockwork veining, and smaller zones of carbonate-altered mafic dikes are the common ore types at Bogosu. However, variations of all ore styles occur in both the higher-level (brittle-zone) and deeper (brittle-ductile) ores. Deeper-level ores similar to those of the Prestea concession may be located at depth below the Bogosu gold deposits.

Whole-rock geochemistry indicates that mafic rocks within the Ashanti Structural Zone are altered, intrusive equivalents of Birimian tholeiitic lavas.

During greenschist facies metamorphism and metasomatism, the least-altered dikes were depleted in K, Ba and possibly other metals that are typically enriched in the mineralized rocks.

Pyrrhotite was the first sulphide to precipitate in the hydrothermal system, however, increasing pH and fO_2 caused alteration of early pyrrhotite to marcasite and pyrite. This was followed by precipitation of arsenian pyrite and arsenopyrite. In-situ analysis and ion mapping by SIMS suggest that most of the gold may have precipitated initially in solid-solution with the arsenian pyrite and arsenopyrite. However, gold was subsequently redistributed, concentrated and crystallized as colloidal and microscopic particles within voids, microfractures and at grain boundaries of the arsenian pyrite, arsenopyrite and trace amounts of sphalerite, chalcopyrite, tetrahedrite and possibly other sulphides. The higher metamorphic grade conditions at Prestea, both during and subsequent to gold deposition, apparently caused a greater degree of redistribution and concentration of gold, including the migration of gold into the gangue assemblage. This reconstruction of the history of gold deposition may be a useful guide for identifying areas of the ore bodies where a significant proportion of the gold content is "invisible"; that is, occurring in solid-solution or as colloidal particles.

Ankerite-siderite and arsenopyrite geothermometers indicate that mineral deposition took place over a wide range of temperature, from 406 to 144°C. The highest temperatures are constrained by pulses of hot ore fluids. Some anomalously high temperatures of up to 600°C may reflect rare pulses of higher-temperature fluid. The lower limit of formation temperatures derived from carbonate mineral-chemical geothermometers suggest that the ambient country-rock temperatures at the time of mineralization were about 144 and

217°C for Bogosu and Prestea ores, respectively. An estimate of the temperature for peak metamorphism of ≈ 390°C is derived from ankerite-siderite geothermometry of co-existing grains in least-altered country-rocks.

Calculated oxygen-isotope and carbon-isotope values for the hydrothermal fluid ($\delta^{18}O \approx 11.8 \pm 1.5‰$, $\delta^{13}C \approx -12.7 \pm 2.2‰$) are consistent with the generation of a metamorphic ore fluid in equilibrium with the Birimian carbonaceous sediments. The isotopic signature of this fluid was superimposed on the intrusive dikes within the structural zone during all stages of their alteration and mineralization. However, lower calculated fluid $\delta^{18}O$ and $\delta^{13}C$ values of 8.1 ± 2.0‰ and -13.8 ± 3.3‰ respectively, for quartz and carbonates in mineralized samples suggest that phase separation of the ore fluid to a CO_2-rich gas phase and a residual ore fluid occurred prior to mineralization. Phase separation and concomitant increase of fO_2 and decrease in fluid temperature are believed to have been the principal mechanisms for inducing gold-sulphide deposition in the zone of mineralization.

The Ashanti Gold Belt and associated carbonaceous sedimentary rocks are believed to have formed in a sediment-dominated accretionary prism similar to the tectonic setting of the southern coast of Alaska. In this environment, the indicated ambient country-rock temperatures of 144 and 217°C suggest average burial depths at the time of mineralization of approximately 7 and 11 km for Bogosu and Prestea ores, respectively. The ore deposits of the Bogosu and Prestea districts also show similarities with the Alaska-Juneau and related Au deposits in structural style, host-rock associations, mineralogy, gold distribution and the composition of ore fluids.

Appendix 8.1: Carbonate mineral chemical analyses (EMP), Bogosu district.

*Sample category	Analysis #	Wt % CaO	Wt % MgO	Wt % FeO	Wt % MnO	Wt % C	Wt % Total
graphitic crush zone ore	1	0.21	16.23	39.23	1.00	13.03	69.70
graphitic crush zone ore	2	0.54	4.30	56.14	0.46	13.03	74.47
graphitic crush zone ore	3	1.26	5.82	52.08	0.46	13.03	72.64
graphitic crush zone ore	4	28.84	17.11	6.57	0.62	13.03	66.17
graphitic crush zone ore	5	28.56	16.57	6.68	0.58	13.03	65.43
graphitic crush zone ore	6	6.63	11.17	34.98	0.80	13.03	66.61
graphitic crush zone ore	7	14.35	8.14	12.28	0.39	13.03	48.18
graphitic crush zone ore	8	29.53	17.83	5.48	0.55	13.03	66.42
graphitic crush zone ore	9	29.23	17.72	5.50	0.57	13.03	66.05
graphitic crush zone ore	10	0.33	18.82	34.34	1.16	13.03	67.68
graphitic crush zone ore	11	0.81	11.05	44.26	0.73	13.03	69.89
graphitic crush zone ore	12	0.63	9.33	44.52	0.57	13.03	68.08
graphitic crush zone ore	13	27.09	16.22	9.07	0.68	13.03	66.09
graphitic crush zone ore	14	24.86	11.85	15.80	0.51	13.03	66.06
graphitic crush zone ore	59	0.12	17.67	37.51	1.19	13.03	69.51
graphitic crush zone ore	60	28.48	15.28	10.07	0.51	13.03	67.36
graphitic crush zone ore	61	0.17	17.94	36.72	1.09	13.03	68.95
graphitic crush zone ore	62	28.17	14.78	10.88	0.54	13.03	67.40
carbonated dike ore	15	29.30	10.75	13.83	0.36	13.03	67.26
carbonated dike ore	16	29.08	16.60	6.80	0.45	13.03	65.95
carbonated dike ore	17	29.13	17.39	5.45	0.49	13.03	65.49
carbonated dike ore	18	29.64	11.09	14.24	0.31	13.03	68.31
graphitic crush zone ore	19	28.49	17.12	6.11	0.51	13.03	65.25
graphitic crush zone ore	20	28.70	17.31	5.51	0.53	13.03	65.08
graphitic crush zone ore	21	28.96	13.96	9.77	0.46	13.03	66.19
graphitic crush zone ore	22	27.39	12.88	9.88	0.40	13.03	63.58
graphitic crush zone ore	23	28.95	14.04	10.48	0.41	13.03	66.90
phyllitic sedimentary-rock ore	24	0.09	20.77	25.95	0.51	13.03	60.35

*Sample category	Analysis #	Wt % CaO	Wt % MgO	Wt % FeO	Wt % MnO	Wt % C	Wt % Total
phyllitic sedimentary-rock ore	25	0.13	21.64	26.85	0.43	13.03	62.08
phyllitic sedimentary-rock ore	26	0.09	16.84	20.64	0.40	13.03	51.00
phyllitic sedimentary-rock ore	27	0.08	18.99	23.85	0.39	13.03	56.34
phyllitic sedimentary-rock ore	28	0.10	21.44	26.80	0.52	13.03	61.89
phyllitic sedimentary-rock ore	29	0.08	12.70	15.04	0.22	13.03	41.07
phyllitic sedimentary-rock ore	30	0.12	20.14	30.01	0.40	13.03	63.69
phyllitic sedimentary-rock ore	31	28.69	15.30	8.85	0.15	13.03	66.02
carbonated dike ore	32	28.52	8.95	16.99	0.41	13.03	67.91
carbonated dike ore	33	28.40	12.12	12.95	0.59	13.03	67.10
carbonated dike ore	34	27.93	9.81	16.74	0.44	13.03	67.96
carbonated dike ore	35	27.90	10.90	14.33	0.45	13.03	66.62
carbonated dike ore	36	27.59	10.59	14.75	0.41	13.03	66.35
carbonated dike ore	37	28.12	14.46	12.55	0.55	13.03	68.71
carbonated dike ore	38	28.01	14.77	9.59	0.51	13.03	65.93
carbonated dike ore	39	28.17	8.82	17.73	0.46	13.03	68.20
carbonated dike ore	40	27.67	9.28	17.65	0.43	13.03	68.06
carbonated dike ore	41	27.70	9.73	17.39	0.44	13.03	68.29
carbonated dike ore	42	27.70	10.36	16.83	0.38	13.03	68.29
carbonated dike ore	43	3.08	10.81	40.87	0.64	13.03	68.42
carbonated dike ore	44	0.28	10.22	45.76	0.73	13.03	70.03
carbonated dike ore	45	ND	ND	ND	ND	ND	ND
carbonated dike ore	47	28.36	9.00	18.00	0.52	13.03	68.91
carbonated dike ore	48	28.24	14.80	9.89	0.47	13.03	66.42
carbonated dike ore	49	28.52	18.48	4.12	0.83	13.03	64.98
carbonated dike ore	50	28.38	17.42	6.34	0.73	13.03	65.91
carbonated dike ore	51	28.29	14.43	10.46	0.55	13.03	66.76
carbonated dike ore	52	28.15	13.21	12.35	0.51	13.03	67.25
carbonated dike ore	53	0.26	3.57	53.83	0.62	13.03	71.31
carbonated dike ore	54	0.17	12.41	43.05	1.09	13.03	69.75
carbonated dike ore	55	28.20	13.18	12.41	0.52	13.03	67.34

*Sample category	Analysis #	Wt % CaO	Wt % MgO	Wt % FeO	Wt % MnO	Wt % C	Wt % Total
carbonated dike ore	56	26.41	11.02	14.53	0.42	13.03	65.41
carbonated dike ore	57	0.28	18.27	34.96	1.16	13.03	67.10
carbonated dike ore	58	0.35	11.55	43.13	1.15	13.03	69.21
banded turbidite	63	1.16	0.66	54.02	4.21	13.03	73.09
banded turbidite	64	0.90	0.69	54.35	3.99	13.03	72.97
greywacke	65	28.26	9.58	14.87	2.24	13.03	67.99
greywacke	66	17.46	9.28	8.52	0.43	13.03	48.73
greywacke	67	28.58	9.46	15.46	0.79	13.03	67.32
greywacke	68	27.99	10.05	16.90	0.63	13.03	68.60
graphitic crush zone ore	69	0.16	11.07	46.02	0.70	13.03	70.98
graphitic crush zone ore	70	0.66	8.75	50.22	0.75	13.03	73.40
graphitic crush zone ore	71	0.17	7.61	50.43	0.70	13.03	71.90
graphitic crush zone ore	72	27.73	11.58	15.01	0.30	13.03	67.35
graphitic crush zone ore	73	0.35	11.98	46.02	0.68	13.03	72.10
carbonated dike	74	28.37	10.47	16.07	0.37	13.03	68.31
carbonated dike	75	0.21	13.61	42.28	0.55	13.03	69.68
carbonated dike	76	0.28	13.16	42.60	0.52	13 03	69.59
mineralized veinlet in least-altered dike	77	28.06	11.67	14.89	0.31	13.03	67.96
mineralized veinlet in least-altered dike	78	53.15	0.67	1.17	0.39	13.03	68.41
mineralized veinlet in least-altered dike	79	53.65	0.46	1.00	0.37	13.03	68.51
least-altered mafic dike, carb porphyroblasts	80	52.29	0.48	2.05	0.46	13.03	68.31
least-altered mafic dike, carb porphyroblasts	81	28.40	8.64	18.14	0.52	13.03	68.94
least-altered mafic dike, carb porphyroblasts	82	28.94	9.67	16.35	0.52	13.03	68.52
least-altered mafic dike, carb porphyroblasts	83	52.85	0.43	1.87	0.41	13.03	68.59
least-altered mafic dike, carb porphyroblasts	84	28.99	10.45	14.96	1.20	13.03	68.63
least-altered mafic dike	85	53.18	0.26	0.63	0.79	13.03	67.89
least-altered mafic dike	86	53.57	0.28	0.83	0.77	13.03	68.48
graphitic phyllite ore	87	28.01	12.52	14.46	0.38	13.03	68.40
graphitic phyllite ore	88	27.99	13.82	12.31	0.37	13.03	67.52
graphitic phyllite ore	89	28.08	13.02	13.33	0.46	13.03	67.91

*Sample category	Analysis #	Wt % CaO	Wt % MgO	Wt % FeO	Wt % MnO	Wt % C	Wt % Total
graphitic phyllite ore	90	28.44	14.68	11.82	0.38	13.03	68.35
graphitic phyllite ore	91	28.15	12.96	14.09	0.42	13.03	68.65
graphitic phyllite ore	92	0.19	15.99	39.56	0.72	13.03	69.50
graphitic phyllite ore	93	0.12	26.28	26.06	1.07	13.03	66.55
graphitic phyllite ore	94	0.05	14.83	39.69	0.67	13.03	68.26
graphitic phyllite ore	95	27.58	14.09	12.50	0.27	13.03	67.48
graphitic phyllite ore	96	18.84	12.17	7.78	0.19	13.03	52.01
graphitic phyllite ore	96R	21.75	12.79	7.98	0.20	13.03	55.76
graphitic phyllite ore	97	0.06	14.14	41.78	0.84	13.03	69.85
graphitic phyllite ore	98	0.15	15.40	41.59	0.63	13.03	70.80
graphitic phyllite ore	99	0.18	19.81	34.85	0.89	13.03	68.75
graphitic phyllite ore	100	0.10	25.32	28.66	1.08	13.03	68.19
graphitic phyllite ore	101	0.05	15.59	36.26	0.69	13.03	65.62
graphitic phyllite ore	102	0.12	14.58	42.06	0.79	13.03	70.58

* see Appendix 8.3 for sample descriptions.

Appendix 8.2: Carbonate mineral chemical analyses (EMP), Prestea district.

*Sample category	Analysis #	Wt % CaO	Wt % MgO	Wt % FeO	Wt % MnO	Wt % C	Wt % Total
quartz vein ore	105	28.90	15.43	9.40	0.80	13.03	67.56
quartz vein ore	106	28.35	11.83	15.01	0.52	13.03	68.74
quartz vein ore	107	30.04	12.20	11.08	0.71	13.03	67.86
quartz vein ore	108	31.75	15.16	4.87	0.76	13.03	65.57
quartz vein ore	109	30.08	12.72	10.90	0.66	13.03	67.40
quartz vein ore	110	29.56	13.20	11.72	0.78	13.03	67.28
quartz vein ore	111	29.12	13.71	10.73	0.66	13.03	67.25
quartz vein ore	112	30.31	15.42	9.26	0.49	13.03	68.51
quartz vein ore	113	28.51	15.94	8.81	0.66	13.03	66.96
quartz vein ore	114	28.98	16.12	8.76	0.75	13.03	67.63
quartz vein ore	115	29.26	16.85	7.28	0.82	13.03	67.25
quartz vein ore	116	28.94	16.21	8.86	0.79	13.03	67.83
quartz vein ore	117	28.51	13.42	12.21	0.60	13.03	67.77
least-altered mafic dike	118	53.22	0.15	0.44	0.49	13.03	67.33
least-altered mafic dike	119	53.01	0.32	0.73	0.63	13.03	67.72
least-altered mafic dike	120	57.88	0.22	0.80	0.77	13.03	72.69
least-altered mafic dike	120 R	54.28	0.21	0.60	0.79	13.03	68.91
least-altered mafic dike	121	52.67	0.28	0.67	0.67	13.03	67.31
carbonated-dike ore	122	29.10	8.62	18.80	0.30	13.03	69.85
carbonated-dike ore	123	28.41	11.32	15.17	0.79	13.03	68.72
carbonated-dike ore	124	28.44	11.55	15.03	0.85	13.03	68.90
carbonated-dike ore	125	28.39	11.88	14.55	0.76	13.03	68.60
carbonated-dike ore	126	28.76	14.42	11.53	0.67	13.03	68.41
carbonated-dike ore	127	28.46	9.67	17.59	0.31	13.03	69.06
carbonated-dike ore	128	28.27	13.77	12.20	0.68	13.03	67.95
carbonated-dike ore	129	28.39	12.61	13.92	0.73	13.03	68.68
phyllite	130	27.17	12.76	13.93	0.55	13.03	67.45
phyllite	131	28.11	12.90	12.93	0.34	13.03	67.30

*Sample category	Analysis #	Wt % CaO	Wt % MgO	Wt % FeO	Wt % MnO	Wt % C	Wt % Total
phyllite	132	27.06	12.32	13.29	0.47	13.03	66.70
phyllite	133	0.98	15.44	38.80	0.59	13.03	68.85
phyllite	134	0.37	16.70	37.81	0.68	13.03	68.59
phyllite	135	0.29	11.81	43.21	0.77	13.03	69.11
phyllite	136	0.40	15.91	39.38	0.63	13.03	69.35
phyllite	137	0.15	11.94	43.47	0.82	13.03	69.41
graphitic fissure ore	138	28.09	14.75	9.68	0.57	13.03	66.12
graphitic fissure ore	139	28.76	16.59	9.90	0.43	13.03	68.71
graphitic fissure ore	140	28.64	13.05	9.80	1.98	13.03	66.50
graphitic fissure ore	141	28.08	16.02	8.30	0.98	13.03	66.40
graphitic fissure ore	142	28.20	17.85	5.56	1.02	13.03	65.65
graphitic fissure ore	143	28.06	12.12	12.01	2.10	13.03	67.32
graphitic fissure ore	144	28.25	16.22	8.24	0.42	13.03	66.16
graphitic fissure ore	145	28.20	15.38	9.04	0.57	13.03	66.22
graphitic-phyllite ore	146	26.70	12.49	11.83	2.19	13.03	66.24
graphitic-phyllite ore	147	26.87	10.86	15.21	1.60	13.03	66.97
graphitic-phyllite ore	148	0.82	11.57	40.09	1.55	13.03	67.06
graphitic-phyllite ore	149	27.03	12.12	12.77	2.44	13.03	67.40
graphitic-phyllite ore	150	27.26	9.07	17.02	1.42	13.03	67.80
graphitic-phyllite ore	151	0.48	14.73	36.36	3.51	13.03	68.11
graphitic-phyllite ore	152	0.41	8.82	38.35	2.78	13.03	63.39
graphitic-phyllite ore	153	0.30	9.07	43.65	2.99	13.03	69.04
sedimentary-phyllite ore	154	27.47	11.71	14.45	0.66	13.03	67.33
sedimentary-phyllite ore	155	27.92	12.90	13.06	0.60	13.03	67.51
sedimentary-phyllite ore	156-R	0.68	7.40	43.70	0.62	13.03	65.44
sedimentary-phyllite ore	157	0.49	7.14	47.15	0.68	13.03	68.48
ultramafic intrusion	103	29.67	20.01	3.03	0.05	13.03	65.80
ultramafic intrusion	104	0.04	38.41	0.04	12.49	13.03	64.01
ultramafic intrusion	158	28.08	15.35	7.36	1.40	13.03	65.22
ultramafic intrusion	159	29.25	20.56	3.17	0.17	13.03	66.18

*Sample category	Analysis #	Wt % CaO	Wt % MgO	Wt % FeO	Wt % MnO	Wt % C	Wt % Total
ultramafic intrusion	160	0.03	38.17	13.24	0.19	13.03	64.66
ultramafic intrusion	161	0.03	40.61	10.41	0.02	13.03	64.10
ultramafic intrusion	162-R	28.24	20.63	2.96	0.07	13.03	64.93
ultramafic intrusion	163	28.46	15.45	7.48	1.08	13.03	65.50
ultramafic intrusion	164	0.05	40.22	10.32	0.02	13.03	63.65
ultramafic intrusion	165	0.02	38.07	13.40	0.16	13.03	64.67
Phyllite	166	0.26	12.88	42.53	0.48	13.03	69.18
Phyllite	167	27.45	10.80	15.87	0.36	13.03	67.52
Phyllite	168	27.92	11.04	14.13	0.60	13.03	66.73
Phyllite	169	0.33	12.03	41.77	0.32	13.03	67.48
carbonate-altered dike	170	27.74	11.04	14.67	0.56	13.03	67.05
carbonate-altered dike	171	0.27	14.53	41.25	0.16	13.03	69.24
carbonate-altered dike	172	0.18	14.14	41.28	0.35	13.03	68.98
carbonate-altered dike	173	0.54	6.44	50.78	0.27	13.03	71.06
carbonate-altered dike	174	28.08	11.30	13.93	0.77	13.03	67.12
spotted carbonaceous phyllite	175	0.48	14.47	40.42	0.10	13.03	68.50
spotted carbonaceous phyllite	176	27.27	11.73	14.59	0.56	13.03	67.18
spotted carbonaceous phyllite	177	0.16	15.78	39.14	0.69	13.03	68.79
spotted carbonaceous phyllite	178	0.16	17.42	37.27	0.08	13.03	67.95
spotted carbonaceous phyllite	179	27.33	13.12	13.35	0.13	13.03	66.96

* see Appendix 8.4 for sample descriptions.

Appendix 8.3: Sample descriptions for carbonate mineral chemical analyses, Bogosu district.

Analysis #	Sample #	Sample category	Occurrence & Grain #	Relative timing	*Basis for equilibrium	*Coexisting grains
1	DM-3	graphitic crush zone ore	mtx 1a	E	ss	5
2	DM-3	graphitic crush zone ore	mtx 1b	L	ss	5
3	DM-3	graphitic crush zone ore	mtx 1c x	mL	gc	4
4	DM-3	graphitic crush zone ore	mtx 1d x	L	gc	3
5	DM-3	graphitic crush zone ore	mtx 1e	L	ss	2
6	DM-3	graphitic crush zone ore	mtx-vn 2	L	gc	7
7	DM-3	graphitic crush zone ore	mtx-vn 2	L	gc	6
8	DM-3	graphitic crush zone ore	mtx-vn 2 x		gc	10&11
9	DM-3	graphitic crush zone ore	mtx-vn 2 x		gc	10&11
10	DM-3	graphitic crush zone ore	mtx-vn 2 x	E	gc	8&9
11	DM-3	graphitic crush zone ore	mtx-vn 2 x	L	gc	8&9
12	DM-3	graphitic crush zone ore	mtx-vn 3 y	E	gc	13
13	DM-3	graphitic crush zone ore	mtx-vn 3 y	E	gc	12
14	DM-3	graphitic crush zone ore	mtx-vn 3	L	gc	12
59	DM-3	graphitic crush zone ore	mtx 4a x	E	gc	60
60	DM-3	graphitic crush zone ore	mtx 4a x	E	gc	59
61	DM-3	graphitic crush zone ore	mtx 4b y	E	gc	62
62	DM-3	graphitic crush zone ore	mtx 4b y	E	gc	61
15	DM-4	carbonated dike ore	mtx 1	E	est	54&58
16	DM-4	carbonated dike ore	mtx 1	mL	est	54&58
17	DM-4	carbonated dike ore	mtx 1	L	est	54&58
18	DM-4	carbonated dike ore	mtx 1	E	est	54&58
19	DM-7	graphitic crush zone ore	mtx 1	L	est	54&58
20	DM-7	graphitic crush zone ore	mtx 1	L	est	54&58
21	DM-7	graphitic crush zone ore	mtx 1	E	est	54&58
22	DM-7	graphitic crush zone ore	mtx 1	E	est	54&58
23	DM-7	graphitic crush zone ore	mtx 1	E	est	54&58
24	DM-9	phyllitic sedimentary-rock ore	mtx 1		ss	31

Analysis #	Sample #	Sample category	Occurrence & Grain #	Relative timing	*Basis for equilibrium	*Coexisting grains
25	DM-9	phyllitic sedimentary-rock ore	mtx 1		ss	31
26	DM-9	phyllitic sedimentary-rock ore	mtx 1		ss	31
27	DM-9	phyllitic sedimentary-rock ore	mtx 1		ss	31
28	DM-9	phyllitic sedimentary-rock ore	mtx 1		ss	31
29	DM-9	phyllitic sedimentary-rock ore	mtx 1		ss	31
30	DM-9	phyllitic sedimentary-rock ore	mtx 1		ss	31
31	DM-9	phyllitic sedimentary-rock ore	mtx 1 b		ss	24-30
32	C-11	carbonated dike ore	vn 1a		ss	44
33	C-11	carbonated dike ore	vn 1a		ss	43
34	C-11	carbonated dike ore	vn 1a		ss	44
35	C-11	carbonated dike ore	vn 1a		ss	44
36	C-11	carbonated dike ore	vn 2a	L	ss	44
37	C-11	carbonated dike ore	vn 2a-Co	E	ss	43
38	C-11	carbonated dike ore	vn 2a-Co	E	ss	43
39	C-11	carbonated dike ore	vn 2a	vL	ss	44
40	C-11	carbonated dike ore	vn 2a	vL	ss	44
41	C-11	carbonated dike ore	vn 1a		ss	44
42	C-11	carbonated dike ore	mtx 3a xy		gc	43&44
43	C-11	carbonated dike ore	mtx 3b x	L	gc	42
44	C-11	carbonated dike ore	mtx 3c y	vL	gc	42
45	C-11	carbonated dike ore				
47	C-11	carbonated dike ore	vn 4		ss	44
48	DM-11	carbonated dike ore	vn 2	E-1	est	54&58
49	DM-11	carbonated dike ore	vn 2	M-2	est	54&58
50	DM-11	carbonated dike ore	vn 2	M-3	est	54&58
51	DM-11	carbonated dike ore	vn 2	L-4	est	54&58
52	DM-11	carbonated dike ore	vn 2	L-5	est	54&58
53	DM-11	carbonated dike ore	mtx1a	vL	ss	55
54	DM-11	carbonated dike ore	mtx1a x	L	gc	55
55	DM-11	carbonated dike ore	mtx1b x	L	gc	54&58

Analysis #	Sample #	Sample category	Occurrence & Grain #	Relative timing	*Basis for equilibrium	*Coexisting grains
56	DM-11	carbonated dike ore	mtx1c-Co	E	gc	57
57	DM-11	carbonated dike ore	mtx1d-Co	E	gc	56
58	DM-11	carbonated dike ore	mtx1d x	L	gc	55
63	BS-1	banded turbidite	mtx P 1		est	67
64	BS-1	banded turbidite	mtx P 2		est	67
65	BS-4	greywacke	mtx P 1		est	63&64
66	BS-4	greywacke	mtx P 1			
67	BS-4	greywacke	mtx P 2		est	63&64
68	BS-4	greywacke	mtx P 2		est	63&64
69	C-18	graphitic crush zone ore	mtx 1		ss	72
70	C-18	graphitic crush zone ore	mtx 1		ss	72
71	C-18	graphitic crush zone ore	mtx 1		ss	72
72	C-18	graphitic crush zone ore	mtx 2		gc	73
73	C-18	graphitic crush zone ore	mtx 2		gc	72
74	C-18	carbonated dike	vn 3a		gc	75&76
75	C-18	carbonated dike	mtx 3b		gc	75
76	C-18	carbonated dike	mtx 3c		gc	75
77	C-15	mineralized veinlet in least-altered dike	vn 1 x		gc	78
78	C-15	mineralized veinlet in least-altered dike	mtx 1 x		gc	77
79	C-15	mineralized veinlet in least-altered dike	mtx 2		ss	77
80	CH-13	least-altered mafic dike, carbonate porphyroblasts	vn 1a		gc	81&82
81	CH-13	least-altered mafic dike, carbonate porphyroblasts	mtx1b		gc	80&83
82	CH-13	least-altered mafic dike, carbonate porphyroblasts	mtx 1b		gc	80&83
83	CH-13	least-altered mafic dike, carbonate porphyroblasts	vn 1a		gc	81&82
84	CH-13	least-altered mafic dike, carbonate porphyroblasts	mtx P 2		ss	80&83
85	CH-15	least-altered mafic dike	vn 1		est	81&82
86	CH-15	least-altered mafic dike	mtx 2		est	81&82
87	D-10	graphitic phyllite ore	vn 1a	E-1	ss	94&102
88	D-10	graphitic phyllite ore	vn 1a	E-2	ss	94&102
89	D-10	graphitic phyllite ore	vn 1a	E-3	ss	94&102

Analysis #	Sample #	Sample category	Occurrence & Grain #	Relative timing	*Basis for equilibrium	*Coexisting grains
90	D-10	graphitic phyllite ore	vn 1a	E-4	ss	94&102
91	D-10	graphitic phyllite ore	vn 1a	E-5	ss	94&102
92	D-10	graphitic phyllite ore	mtx2a x	M	gc	95
93	D-10	graphitic phyllite ore	mtx2a	E	ss	95
94	D-10	graphitic phyllite ore	mtx2a	L	ss	95
95	D-10	graphitic phyllite ore	mtx 2b x		ss	92
96	D-10	graphitic phyllite ore	vn 1a			
96R	D-10	graphitic phyllite ore	vn 1a			
97	D-10	graphitic phyllite ore	mtx 2c		ss	95
98	D-10	graphitic phyllite ore	mtx 2c x	M	gc	95
99	D-10	graphitic phyllite ore	mtx 2c x	M	gc	95
100	D-10	graphitic phyllite ore	mtx 2c	E	ss	95
101	D-10	graphitic phyllite ore	mtx 2c x	L	gnc	95
102	D-10	graphitic phyllite ore	mtx 2c	L	ss	95

* = basis for selection of coexisting grains for temperature calculations: gc = grain contact, ss = same section, est = best estimate
E, M, L=relative timing with respect to co-existing carbonates in same section (E=early, M=middle, L=late).
vn =vein, x & y=selected co-existing phases
BS = Bogosu South area, C & CH = Chujah deposit, D & DM = Dumassie deposit,
Co = core, mtx = matrix, P = porphyroblast, vn = vein, x & y = selected coexisting grains.

Appendix 8.4: Sample descriptions for carbonate mineral chemical analyses, Prestea district.

Analysis #	Sample #	Sample category	Occurrence & Grain #	Relative timing	*Basis for equilibrium	*Coexisting grain# or average analysis
105	P-2	quartz vein ore	core 5	E	est	1.97
106	P-2	quartz vein ore	rim 5	L	est	1.60
107	P-2	quartz vein ore	Cb-V 6	mL	est	1.60
108	P-2	quartz vein ore	Cb-V 6	E	est	1.97
109	P-2	quartz vein ore	Cb-V 6	mL	est	1.60
110	P-2	quartz vein ore	Cb-V xc 7a	mL	est	1.60
111	P-2	quartz vein ore	Cb-V xc 7a	mL	est	1.60
112	P-2	quartz vein ore	Cb-V xc 7a	E	est	1.97
113	P-2	quartz vein ore	Cb-V 7b	E	est	1.97
114	P-2	quartz vein ore	Cb-V 7b	E	est	1.97
115	P-2	quartz vein ore	Cb-V 7b	E	est	1.97
116	P-2	quartz vein ore	Cb-V 7b	E	est	1.97
117	P-2	quartz vein ore	Cb-V 7b	L	est	1.60
118	P-7	least-altered mafic dike	Cb-V xc 1			
119	P-7	least-altered mafic dike	Cb-QV 1			
120	P-7	least-altered mafic dike	mtx 2			
120 R	P-7	least-altered mafic dike	mtx 2			
121	P-7	least-altered mafic dike	mtx 2			
122	P-28D	carbonated-dike ore	QV-selv 1	L	est	1.60
123	P-28D	carbonated-dike ore	QV-selv 1	E	est	1.97
124	P-28D	carbonated-dike ore	QV-selv 1	L	est	1.97
125	P-28D	carbonated-dike ore	QV-selv 1	L	est	1.97
126	P-28D	carbonated-dike ore	QV-selv 2	M	est	1.97
127	P-28D	carbonated-dike ore	QV-selv 2	E & L	est	1.60
128	P-28D	carbonated-dike ore	mtx 3	E	est	1.97
129	P-28D	carbonated-dike ore	mtx 3	L	est	1.60
130	P-36	phyllite	mtx Gbn 1		ss	#133
131	P-36	phyllite	mtx Gbn 2		ss	#133

Analysis #	Sample #	Sample category	Occurrence & Grain #	Relative timing	*Basis for equilibrium	*Coexisting grain# or average analysis
132	P-36	phyllite	mtx Cbn 3		gc	#133
133	P-36	phyllite	mtx Cbn 3	E	gc	#132
134	P-36	phyllite	mtx Cbn 3	E	gc	#132
135	P-36	phyllite	mtx Cbn 3 r	L	gc	#132
136	P-36	phyllite	mtx Gbn 4a c	E	ss	#132
137	P-36	phyllite	mtx Gbn 4a r	L	ss	#132
138	P-30	graphitic fissure ore	mtx 5a	M	est	1.60
139	P-30	graphitic fissure ore	mtx 5a	M	est	1.97
140	P-30	graphitic fissure ore	QV 4a-c	E	est	1.60
141	P-30	graphitic fissure ore	QV 4a-r	L	est	1.97
142	P-30	graphitic fissure ore	mtx 2	E-1	est	1.97
143	P-30	graphitic fissure ore	mtx 2	L-4	est	1.60
144	P-30	graphitic fissure ore	mtx 2	M-2	est	1.97
145	P-30	graphitic fissure ore	mtx 2	M-3	est	1.97
146	P-35	graphitic-phyllite ore	mtx 3a	L	ss	#148&152
147	P-35	graphitic-phyllite ore	mtx 3a	E	ss	#151
148	P-35	graphitic-phyllite ore	mtx 4a y	L	gc	#146&149
149	P-35	graphitic-phyllite ore	mtx 4b xy	L	gc	#148&152
150	P-35	graphitic-phyllite ore	mtx 4b	E	ss	#151
151	P-35	graphitic-phyllite ore	mtx 4c c	E	ss	#150
152	P-35	graphitic-phyllite ore	mtx 4c r x	L	gc	#146&149
153	P-35	graphitic-phyllite ore	Au-bearing		ss	#149
154	P-70	sedimentary-phyllite ore	mtx 5		gc	#156R
155	P-70	sedimentary-phyllite ore	mtx 5		gc	#156R
156-R	P-70	sedimentary-phyllite ore	mtx 5		gc	#154&155
157	P-70	sedimentary-phyllite ore	mtx 6		ss	#154&155
103	P-34	ultramafic intrusion	mtx-p 1			
104	p-34	ultramafic intrusion	mtx-p 1			
158	P-34	ultramafic intrusion	mtx-p 3a r			
159	P-34	ultramafic intrusion	mtx-p 3a c			

Analysis #	Sample #	Sample category	Occurrence & Grain #	Relative timing	*Basis for equilibrium	*Coexisting grain# or estimated analysis
160	P-34	ultramafic intrusion	mtx-p 3b r			
161	P-34	ultramafic intrusion	mtx-p 3b c			
162-R	P-34	ultramafic intrusion	mtx-p 4a			
163	P-34	ultramafic intrusion	mtx-p 4b			
164	P-34	ultramafic intrusion	mtx-p 4c			
165	P-34	ultramafic intrusion	mtx-p 4d			
166	P-1	Phyllite	QV-selv 1a		gc	#167
167	P-1	Phyllite	QV-selv 1b		gc	#166
168	P-1	Phyllite	mtx 2a		gc	#169
169	P-1	Phyllite	mtx 2b		gc	#168
170	P-1	carbonate-altered dike	mtx 3a x	E	gc	#171
171	P-1	carbonate-altered dike	mtx 3b x	E	gc	#170
172	P-1	carbonate-altered dike	mtx 4a x	E	gc	#174
173	P-1	carbonate-altered dike	mtx 4a			
174	P-1	carbonate-altered dike	mtx 4b x	E	gc	#172
175	52-A	spotted carbonaceous phyllite	p 1a		gc	#176
176	52-A	spotted carbonaceous phyllite	p 1b		gc	#175
177	52-A	spotted carbonaceous phyllite	p 2a y	L	ss	1.97
178	52-A	spotted carbonaceous phyllite	p 2b x	E	gc	#179
179	52-A	spotted carbonaceous phyllite	p 2c xy	E	gc	#178

* = basis for selection of coexisting grains for temperature calculations: gc = grain contact, ss = grains in same section, est = best estimate from similar carbonates in other sections.
E, M, L=relative timing with respect to co-existing carbonates in same section (E=early, M=middle, L=late).
c=core, Cbn=clastic band, Cb-V=carbonate vein, Gbn=graphitic band, mtx=matrix, p=porphyroblast, QV=quartz vein, r=rim, selv=selvage vn =vein, x & y=selected co-existing phases

Appendix 9.1: Relative mineral abundances from PXRD analysis.

Analysis #	1	2	3	4	6	8	9	10	11	12	13
Quartz	100 0	52 9	33.6	55 2	35.7	9.7	76.5	37.4	15.2	91.2	4.7
Albite	0.0	19.1	0.0	22.3	19 2	38.6	0.0	25.1	67.4	7.2	49.4
Ankerite	0 0	0 0	0.0	10.9	40.6	22.1	22.1	10.7	9.0	1.7	28.7
Siderite	0.0	0.0	0.0	0.8	0 0	0.0	0.0	3.3	0 3	0.0	1.0
Calcite	0.0	9.5	64.5	0.0	0.0	0 0	0.0	0.0	0.0	0.0	0.0
Chlorite	0 0	18.5	1.8	0.0	3.7	23.0	0 0	5.9	0.0	0.0	0.0
Muscovite	0.0	0.0	0 0	2.3	0 8	1.7	0.0	8.0	1.3	0.0	3.4
Pyrite	0.0	0.0	0.0	5.9	0.0	3.9	1.4	2.7	6.5	0.0	12.0
Arsenopyrite	0.0	0.0	0.0	0.0	0.0	1.0	0.0	3.4	0.3	0.0	0.7
Graphite	0.0	0.0	0.0	2.6	0 0	0.0	0.0	3.5	0.0	0.0	0.0
Other	0.0	0 0	0.0	0.0	0.0	0.0	0.0	0.0	0.0	0.0	0.0

Analysis #	14A	14B	15	16	17	19	20	21	22	23	24
Quartz	98 2	77.1	53.1	80.5	85.0	46.5	16.2	72.1	58.9	49.6	91.0
Albite	0.0	22.8	1.2	0 0	0.0	10.0	0.0	13.5	14.3	10.4	0.7
Ankerite	1.8	0.0	16.0	9.5	13.2	0.0	0.0	5.2	3.3	2.4	0.0
Siderite	0.0	0.0	23.1	7.8	1.8	0.0	0.0	2.2	5.6	5.7	3.5
Calcite	0.0	0.0	0.0	0.0	0.0	12.2	83.8	0.0	0.0	0.0	0.0
Chlorite	0.0	0.0	0.0	0.0	0.0	31.4	0.0	3.5	8.9	18.6	3.3
Muscovite	0.0	0.1	6.6	2.2	0.0	0.0	0.0	3.6	7.4	12.0	1.5
Pyrite	0.0	0.0	0.0	0.0	0.0	0.0	0.0	0.0	0.0	0.0	0.0
Arsenopyrite	0.0	0.0	0.0	0.0	0.0	0.0	0.0	0.0	0.0	0.0	0.0
Graphite	0.0	0.0	0.0	0.0	0 0	0.0	0.0	0.0	0.0	0.0	0.0
Other	0.0	0.0	0.0	0.0	0.0	0.0	0.0	0.0	1.6	1.3	0.0

Analysis #	26	27	28	29	30	31	32	33	34	35
Quartz	55.0	54.1	55.0	51.3	60.5	97.2	0.0	42.5	60.8	40.3
Albite	8.7	0.0	26.1	1.2	17.3	0.0	0.0	1.1	2.3	4.5
Ankerite	0.0	37.7	12.6	25.0	14.4	2.8	51.8	28.4	18.7	23 5
Siderite	3.7	0.7	0.0	17.5	0.9	0.0	1.5	2.3	9.5	16.8
Calcite	0.0	0.0	0.0	0.0	0.0	0.0	0.0	0.0	0.0	0 0
Chlorite	23.0	0.0	0.0	0.0	0.0	0.0	0.0	0.9	0.0	6.3
Muscovite	9.6	7 5	0.8	5.0	5 3	0.0	7.6	14.8	8.6	8.6
Pyrite	0 0	0 0	4.7	0.0	0.5	0.0	1.7	4.8	0.0	0.0
Arsenopyrite	0.0	0 0	0.7	0.0	1.2	0.0	0.0	5.1	0.0	0.0
Graphite	0.0	0.0	0.0	0.0	0.0	0.0	0.0	0.0	0.0	0.0
Other	0 0	0 0	0 0	0.0	0.0	0.0	37.4	0.0	0.0	0.0

Appendix 9.1 continued: Relative mineral abundances from PXRD analysis.

Analysis #	36	37	38	39	40	41	42	43	44	45	46
Quartz	35.6	16.4	45.6	83 0	6 6	63.0	50.0	42.2	0 0	43 9	55 7
Albite	1.6	32.7	12 5	7 2	18 4	6 5	3.5	1 3	0.0	1 8	1 7
Ankerite	28.4	24.3	17 1	3.2	36.1	12 4	1 6	35 9	41 3	20 3	18 5
Siderite	0.5	0.0	0.0	0.9	3 0	8 6	1.8	12 1	39 7	19 8	19 5
Calcite	23.8	0 0	1.2	0.0	0 0	0 0	14.4	0.0	0.0	0.0	0 0
Chlorite	5.8	18.6	22.9	1.1	0.0	0.0	28.7	0 0	0 9	0 9	0 0
Muscovite	4.3	2.2	0.0	4.6	26 9	8.5	0.0	8.1	18.1	13.3	4.6
Pyrite	0.0	4.5	0.5	0.0	6.2	0.0	0.0	0.5	0.0	0 0	0 0
Arsenopyrite	0.0	1.3	0.0	0.0	2 7	1 0	0.0	0.0	0.0	0 0	0 0
Graphite	0.0	0.0	0.0	0.0	0.0	0.0	0 0	0.0	0.0	0 0	0.0
Other	0.0	0.0	0 0	0 0	0.0	0 0	0.0	0.0	0.0	0 0	0 0

Analysis #	47	48	49	50	51	52	53	54	55	56	57
Quartz	23.6	45.2	58.5	40.3	93.0	17.0	76.9	64.8	37.6	63.8	53 6
Albite	32.2	1.4	0.0	6.6	5.9	1.2	7.2	9.8	8.9	2 5	4 6
Ankerite	29.8	34.0	6.1	0 0	0.9	64.2	8.7	8.5	14.5	9.9	1 8
Siderite	6.3	10.6	23.1	0.0	0.2	2.9	0 0	9 9	25.2	13.7	25 9
Calcite	0.0	0.0	0.0	15 6	0.0	0.0	0.0	0.0	0 0	0.0	0.0
Chlorite	0.6	0.0	0.0	37.5	0.0	1.6	3.1	0.7	3.1	0 0	0 0
Muscovite	4.6	5.9	11.4	0 0	0.0	13.1	4 1	6.3	7.2	10.1	13 0
Pyrite	0.9	1.2	0.0	0.0	0.0	0.0	0.0	0.0	0.0	0.0	1 1
Arsenopyrite	2.0	1.7	0.9	0.0	0 0	0.0	0.0	0.0	1.1	0 0	0 0
Graphite	0.0	0.0	0.0	0 0	0.0	0.0	0.0	0 0	0 0	0 0	0 0
Other	0.0	0.0	0.0	0.0	0 0	0.0	0.0	0.0	2 6	0 0	0 0

Analysis #	58	59	60	61	62	63	64	65	66	67	68
Quartz	51.1	39.5	60.6	70.5	32.1	55.5	44.6	48.0	42.0	59.5	59.3
Albite	1.8	15.6	0.0	5.9	51.4	1 3	0.9	0.0	1 2	0.9	0.0
Ankerite	5.7	16.6	26.7	1.9	13 9	27.5	24.5	29.4	32.6	27.9	5.1
Siderite	0.0	8.8	1.8	1.9	1.4	12.5	14.3	1.7	14.7	0.0	0.0
Calcite	11.2	0.0	0.0	0.0	0.0	0 0	0.0	0.0	0.0	0.0	0.0
Chlorite	30.2	6.2	0.0	11.0	0 0	0.0	4 1	0.0	0.0	0 0	2 8
Muscovite	0.0	11.9	9.3	8.8	1.2	3.2	9.1	14.1	9.5	5.3	0 0
Pyrite	0.0	0.0	1.6	0.0	0.0	0.0	0.5	3.2	0 0	3 9	0 0
Arsenopyrite	0.0	1.3	0.0	0 0	0.0	0 0	2 0	3 5	0 0	2 5	0 0
Graphite	0 0	0 0	0.0	0.0	0 0	0 0	0 0	0 0	0.0	0 0	0.0
Other	0.0	0.0	0.0	0 0	0 0	0.0	0.0	0 0	0 0	0 0	32 8

Appendix 9 2· Sample descriptions

Analysis #	Location number	District	Sample description
1	P-29	Prestea	crack-seal quartz-vein ore
2	P-7	Prestea	least-altered mafic dike, matrix material
3	P-7	Prestea	least-altered mafic dike, quartz-carbonate vein
4	P-30	Prestea	graphitic fissure zone ore
5	P-30	Prestea	graphitic fissure zone ore, graphitic material
6	P-28	Prestea	carbonated dike ore, 80% vein material
8	P-28	Prestea	carbonated dike ore, matrix material
9	P-12	Prestea	crack-seal quartz-vein ore
10	P-12	Prestea	crack-seal quartz-vein ore, carbonaceous partings
11	DM-7	Bogosu	graphitic crush zone ore, matrix material
12	DM-7	Bogosu	graphitic crush zone ore, quartz vein material
13	DM-11	Bogosu	carbonated dike ore, matrix material
14A	DM-11	Bogosu	carbonated dike ore, quartz-vein material
15	C-4	Bogosu	carbonated dike, matrix
19	C-17	Bogosu	least-altered mafic dike, matrix material
20	C-17	Bogosu	least-altered mafic dike, carbonate vein
21	BS-84#16	Bogosu	greywacke-turbidite bed, clastic base
22	BS-84#16	Bogosu	greywacke-turbidite bed, moderately graphitic
23	BS-84#16	Bogosu	greywacke-turbidite bed, graphitic top of bed
24	BS-2	Bogosu	turbidite, moderately sheared, quartz-carbonate vein material
26	BS-2	Bogosu	turbidite, moderately sheared, matrix material
27	P-37	Prestea	carbonated dike
28	DM-7	Bogosu	graphitic crush zone ore
29	P-82	Prestea	carbonated dike
30	CH-162-113	Bogosu	greywacke-turbidite, finely laminated ore
31	C-15C	Bogosu	gold-bearing quartz-carbonate veinlet in least-altered dike
33	AGC 16350	Ashanti	carbonated dike ore
34	CH-178-167.5	Bogosu	graphitic crush zone, moderately sheared
35	C3-208-66.5	Bogosu	carbonated dike, sheared
36	C-16	Bogosu	least-altered mafic dike, sheared, foliated, pyritic
37	P-28	Prestea	carbonated dike ore
38	CH-192-71	Bogosu	least-altered mafic dike with carbonate porphyroblasts
39	P-20	Prestea	greywacke-turbidite with 2% pyrite
40	CH-178-147	Bogosu	greywacke-graphitic crush zone ore
41	DM-10	Bogosu	greywacke-turbide, laminated
42	CH-192-101	Bogosu	least-altered mafic dike with very fine carbonate fractures
43	CH-180-164	Bogosu	carbonated-dike ore
44	CH-180-192	Bogosu	carbonated dike
45	P-1A	Prestea	carbonated dike
46	CH-192-66 5	Bogosu	carbonated dike
47	Prestea 27	Prestea	carbonated dike ore
48	C3-208-99	Bogosu	carbonated dike
49	AGC 16092	Ashanti	greywacke turbidite, sheared
50	C-15A	Bogosu	least-altered dike near gold-bearing quartz-carbonate veinlet

Appendix 9.2 (continued). Sample descriptons

Analysis #	Location number	District	Sample description
51	DM-5	Bogosu	crack-seal quartz-vein ore
52	AGC 16349	Ashanti	phyllite ore
53	AGC 16355	Ashanti	turbidite, laminated
54	P-52	Prestea	spotted phyllite, carbonate porphyroblasts
55	AGC 16093	Ashanti	greywacke-turbidite, laminated
57	CH-174-95	Bogosu	phyllite, carbonaceous and laminated
58	C3-208#18	Bogosu	least-altered mafic dike, slightly carbonated
59	P-60	Prestea	turbidite, carbonaceous and laminated
61	BS-3	Bogosu	turbidite
62	DM-3	Bogosu	graphitic crush zone ore near contact with carbonated dike
63	CH-11	Bogosu	carbonated dike, sheared
64	AGC 16094	Ashanti	turbidite ore
65	AGC 16348	Ashanti	carbonated dike ore
66	P-1B	Prestea	greywacke near contact with carbonated dike
67	C3-224-DO	Bogosu	carbonated dike ore
68	P-34	Prestea	carbonated ultramafic intrusion
69	Prestea 27	Prestea	carbonate-altered dike ore, quartz-vein material
70	BS-84-90.5	Bogosu	carbonaceous greywacke-turbidite
71	CH-176-92	Bogosu	carbonaceous turbidite, sheared
72	DE-200-10	Bogosu	graphitic crush zone ore, 5% py + asp
73	DE-200-28	Bogosu	graphitic crush zone, < 1% py
74	NK-204-20	Bogosu	graphitic crush zone ore, 1-2% py + asp
75	NK-204-9	Bogosu	graphitic crush zone ore, silicified, 2-3% py + asp

References

Abouchami, W., Boher, M., Michard, A. and Albarede, F., 1990. A major 2.1 Ga event of mafic magmatism in West Africa: An early stage of crustal accretion. Journal of Geophysical Research, 95: 17,605-17,629.

Adjimah, C. L., 1988. Petrological studies on the genesis of the gold deposits of Prestea, Ghana. Bundesanstalt fur Geowissenschaften und Rohstoffe, Hanover, (unpub.) thesis, 274 pgs.

Agyei, E. K. and Manu, J., 1989. Conventional potassium-argon age of the Shai Hills, Southeastern Ghana. Journal of African Earth Sciences, 9: 665-667.

Agyei, E. K., van Landewijk, J. E. J. M., Armstrong, R. E., Harakal, J. E. and Scott, K. L., 1987. Rb-Sr and K-Ar geochronometry of southeastern Ghana. Journal of African Earth Sciences, 6: 153-161.

Al-Aasm, I. S., Taylor, B. E. and South, B., 1990. Stable isotope analysis of multiple carbonate samples using selective acid extraction. Chemical Geology (Isot. Geosci. Sect.), 80: 119-125.

Angoran, Y. and Kadio, E., 1983. Apercu de precambrien de Cote d"Ivoire: geologie-metallogenie. Journal of African Earth Sciences, 1: 167-176.

Anovitz, L. M. and Essene, E. J., 1987. Phase equilibria in the system $CaCO_3$-$MgCO_3$-$FeCO_3$. Journal of Petrology, 28: 389-414.

Arehart, G. B., Chryssoulis, S. L. and Kesler, S. E., 1993. Gold and arsenic in iron sulfides from sediment-hosted disseminated gold deposits: Implications for depositional processes. Economic Geology, 88: 171-185.

Arnorsson, S., 1978. Precipitation of calcite from flashed geothermal waters in Iceland. Contributions to Mineralogy and Petrology, 66: 21-28.

Bakken, B. M., Hochella, M. F., Jr., Marshall, A. F. and Turner, A. M., 1989. High resolution microscopy of gold in unoxidized ore from the Carlin mine, Nevada. Economic Geology, 84: 171-179.

Barnes, H. L., 1979. Solubilities of ore minerals. In Barnes, H. L. (ed.), Geochemistry of Hydrothermal Ore Deposits (2nd Edition), Wiley Interscience, pp. 404-508.

Barron, B. J., 1974. The use of coexisting calcite-ankerite solid solutions as a

geothermometer. Contr. Miner. Petrol., 36: 147-154.

Becker, R. H. and Clayton, R. N., 1976. Oxygen isotope study of a precambrian banded iron-formation, Hamersley Range, Western Australia. Geochimica et Cosmochimica Acta 40: 1153-1165.

Bickle, M. J. and Powell, R., 1977. Calcite-dolomite geothermometry for iron-bearing carbonates. Contrib. Mineral. Petrol., 59: 281-292.

Bonhomme, M. G. and Bertrand-Sarfati, J., 1982. Correlation of Proterozoic sedimentary rocks of Western and Central Africa and South America based upon radiochronological and palaeontological data. Precambrian Research, 18: 171-194.

Bottinga, Y., 1969. Calculated fractionation factors for carbon and hydrogen isotope exchange in the system calcite-carbon dioxide-graphite-methane-hydrogen-water vapor. Geochim. et Cosmochim. Acta 33, pp. 49-64.

Bottinga, Y., 1968. Calculation of fractionation factors for carbon and oxygen isotopic exchange in the system calcite-carbon dioxide-water. J. Phys. Chem., 72: 800-808.

Bowers, T. S., 1991. The deposition of gold and other metals: Pressure-induced fluid immiscibility and associated isotopic signatures. Geochimica et Cosmochimica Acta 55: 2417-2434.

Bowman, J. R., Covert, J. J., Clark, A. H. and Mathieson, G. A., 1985. The CanTung E zone scheelite skarn orebody, Tungsten, Northwest Territories: Oxygen, hydrogen and carbon isotope studies. Economic Geology 80: 1872-1895.

Brown, K. L., 1989. Kinetics of gold precipitation from experimental hydrothermal sulfide solutions. Economic Geology Monograph 6: 320-327.

Cabri, L. J., Chryssoulis, S. L., De Villiers, J. P. R., Laflamme, J. H. G. and Buseck, P. R., 1989. The nature of "invisible" gold in arsenopyrite. The Canadian Mineralogist, 27: 353-362.

Caen-Vachete, M., 1988. Le craton ouest-africain et le bouclier guyanais: un seul craton au Proterozoique inferieur? Journal of African Earth Sciences, 7-2: 479-488.

Caen-Vachete, M., 1988. A review of new geochronological data for Archean

and Proterozoic times from Eastern Senegal to Gabon in Africa, with possible correlations with the north of South America. (Abstr.), Journal of African Earth Sciences, 7-2: pg 515.

Caen-Vachete, M., Tempier, P. and Camil, J., 1984. Age Rb/Sr de 1670 M.a. pour les mylonites de l'accident du Sassandra (Cote d'Ivoire) consequence pour la datation des mouvements fini-eburneens dans le craton ouest-africain. Journal of African Earth Sciences, 2-4: 359-364.

Cahen, L., Snelling, N. J., Delhal, J. and Vail, J. R., 1984. The geochronology and evolution of Africa. Clarendon Press, Oxford: 512 pgs.

Carothers, W. W., Adami, L. H. and Rosenbauer, R. J., 1988. Experimental oxygen isotope fractionation between siderite-water and phosphoric acid liberated CO_2-siderite. Geochimica et Cosmochimica Acta 52: 2445-2450.

Cathelineau, M., Boiron, M. C., Hollinger, P., Marion, P. and Denis, M., 1989. Gold in arsenopyrites: crystal chemistry, location and state, physical and chemical conditions of deposition. Economic Geology Monograph 6: 328-341.

Chryssoulis, S. L., 1990. Quantitative trace precious metal analysis of sulphide and sulpharsenide minerals by SIMS. In Secondary Ion Mass Spectrometry SIMS VII (A. Binninghoven, C. A. Evans, K. D, McKeegan, H. A. Storms and H. W. Werner, eds.). John Wiley and Sons, New York, pp. 405-408.

Chryssoulis, S. L. and Cabri, L. J., 1990. Significance of gold mineralogical balances in mineral processing. Trans. Inst. Min. Metall., 99: C1-C10.

Chryssoulis, S. L. and Fleet, M. E., 1990. Paragenesis of gold minerals and of submicroscopic gold within pyrite and arsenopyrite. 8th IAGOD Symposium, Ottawa, Canada, Program with Absracts, pp. A140-A141.

Chryssoulis, S. L. and Weisener, C. G., 1991. Quantification and imaging of submicroscopic Au in ore minerals by SIMS. In Secondary Ion Mass Spectrometry SIMS VIII (A. Benninghoven, K. T. F. Janssen, J. Tumpner and H. W. Werner, (eds.), John Wiley and Sons, Chichester, U. K. pp. 517-520.

Chryssoulis, S. L., Cabri, L. J. and Lennard, W., 1989. Calibration of the ion microprobe for quantitative trace precious metal analyses of ore minerals. Economic Geology, 84.

Clauer, N., Caby, R., Jeannette, D. and Trompette, R., 1982. Geochronology of sedimentary and metasedimentary Precambrian rocks of the West African Craton. Precambrian Research, 18: 53-81.

Clayton, R. N. and Mayeda, T. K., 1963. The use of bromine pentaflouride in the extraction of oxygen from oxides and silicates for isotopic analysis. Geochim. et Cosmochim. Acta 27: 43-52.

Colvine, A.C., 1989. An empirical model for the formation of Archean gold deposits: Products of cratonization of the Superior Province, Canada. Economic Geology Monograph 6: 37-53.

Colvine, A. C., Andrews, A. J., Cherry, M. E., Durocher, M. E., Fyon, A. J., Lavingne, M. J., Macdonald, A. J., Poulsen, K. H., Springer, J. S. and Troop, D. G., 1984. An integrated model for the origin of Archean lode gold deposits. Ontario Geological Survey, Open File Report 5524, 98 pgs.

Colvine, A. C., Fyon, J. A., Heather, K. B., Marmont, S., Smith, P. M. and Troop, D. G., 1988. Archean lode gold deposits in Ontario. Mines and Minerals Division, Ontario Geol. Survey, Misc. Paper 139.

Cook, N. J. and Chryssoulis, L., 1990. Concentrations of "invisible gold" in the common sulfides. Canadian Mineralogist, 28: 1-16.

Craig, H., 1957. Isotopic standards for carbon and oxygen and correction factors for mass-spectrometric analysis of carbon dioxide. Geochimica et Cosmochimica Acta, 12: 133-149.

Craig, H., 1961. Standards for reporting concentrations of deuterium and oxygen-18 in natural waters. Science 133: 1833-1834.

Deines, P., 1980. The isotopic composition of reduced organic carbon. Chp. 9 in Fritz and Fontes (eds.), Handbook of Environmental Isotope Geochemistry, Vol. 1, The Terrestrial Environment, A. Elsevier, New York, pp. 329-406.

Deines, P., Langmuir, D. and Harmon, R. S., 1974. Stable carbon isotope ratios and the existence of a gas phase in the evolution of carbonate ground water. Geochimica et Cosmochimica Acta 38: 1147-1164.

De Kun, N., 1963. The mineralogenetic provinces of Africa. Economic Geology, 58: 774-782.

Drummond, S. E., 1981. Boiling and mixing of hydrothermal fluids: Chemical

effects on mineral precipitation. Ph.D. dissertation, Pennsylvania State University.

Drummond, S. E. and Ohmoto, H., 1985. Chemical evolution and mineral deposition in boiling hydrothermal systems. Economic Geology, 80: 126-147.

Ebel, D. S. and Sack, R. O., 1989. Ag-Cu and As-Sb exchange energies in tetrahedrite-tennantite fahlores. Geochim. et Cosmochim. Acta, 53: 2301-2309.

Eisenlohr, B. N., 1992. Conflicting evidence on the timing of mesothermal and paleoplacer gold mineralization in Early Proterozoic rocks from southwest Ghana, West Africa. Mineralium Deposita, 27: 23-29.

Ellis, A. J. and Mahon, W. A. J., 1977. Chemistry and geothermal systems. Academic Press, New York, 392 pgs.

Essene, E. J., 1983. Solid solutions and solvi among metamorphic carbonates with applications to geologic thermometry. In R. J. Reeder (ed.), Carbonates: Mineralogy and Chemistry. MSA Reviews in Mineralogy, 11: 77-96.

Faure, G., 1986. Principles of isotopic geology. Second Edition, John Wiley and Sons, New York, Chichester, Brisbane, Toronto, Singapore, 589 pgs.

Fisher, R. S. and Land, L. S., 1986. Diagenetic history of Eocene Wilcox sandstones, south-central Texas. Geochimica et Cosmochimica Acta 50: 551-561.

Fleet, M. E., Chryssoulis, S. L., MacLean, P. J., Davidson, R. and Weisener, C. G., 1993. Arsenian pyrite from gold deposits: Au and As distribution investigated by SIMS and EMP, and color staining and surface oxidation by XPS and LIMS. Canadian Mineralogist, 31: 1-17.

Fleet, M. E. and Chryssoulis, S. L., 1991. Arsenian pyrite from gold deposits: Au and As distribution and surface oxidation studied by EMP, SIMS, XPS and LIMS. Proceedings of Toronto 1991, GAC/AGA : MAC/AMC : SEG, Programme with Abstracts, vol. 16, pp. A37.

Fleet, M. E., MacLean, P. J. and Barbier, J., 1989. Oscillatory-zoned As-bearing pyrite from strata-bound and stratiform gold deposits: An indicator of ore fluid evolution. Economic Geology Monograph 6: 356-362.

Force, E. R. and Cannon, W. F., 1988. Depositional model for shallow-marine manganese deposits around black shale basins. Economic Geology, 81: 93-117.

Foster, R. P., 1989. Archean gold mineralization in Zimbabwe: Implications for metallogenesis and exploration. Economic Geology Monograph 6: 54-70.

Frakes, L. A. and Bolton, B. R., 1984. Origin of manganese giants: Sea level change and anoxic-oxic history. Geology, 12: 83-86.

Frakes, L. A. and Bolton, B. R., 1992. Effects of ocean chemistry, sea level, and climate on the formation of primary sedimentary manganese ore deposits. Economic Geology, 87: 1207-1217.

Friedman, I. and O'Neil, J. R., 1977. Compilation of stable isotope fractionation factors of geochemical interest. In: Data of Geochemistry, sixth edtition. M. Fleisher ed., United States Geological Survey Professional Paper 440-KK.

Ghana Geological Survey, 1969. Mineral Deposits Map.

Goldfarb, R. J., Leach, D. L., Rose, S.C. and Landis, G. P., 1989. Fluid inclusion geochemistry of gold-bearing quartz veins of the Juneau gold belt, southwestern Alaska. Economic Geology Monograph 6: 363-375.

Goldfarb, R. J., Newberry, R. J., Pickthorn, W. J. and Gent, C. A., 1991. Oxygen, hydrogen, and sulfur isotope studies in the Juneau Gold Belt, south-eastern Alaska: Constraints on the origin of hydrothermal fluids. Economic Geology, 86: 66-80.

Golding, S. D., McNaughton, N. J., Barley, M. E., Groves, D. I., Ho, S. E., Rock, N. M. S. and Turner, J. V., 1989. Archean carbon and oxygen reservoirs: Their significance for fluid sources and circulation paths for Archean mesothermal gold deposits of the Norseman-Wiluna Belt, Western Australia. Economic Geology Monograph 6: 376-388.

Goldsmith, J. R., Witters, J. and Northrup, D. A., 1962. Studies in the system $CaCO_3$-$MgCO_3$-$FeCO_3$: A method for major-element spectrochemical analysis; 3. Composition of some ferroan dolomites. Journal of Geology, 70: 659-687.

Golyshev, S. I., Padalko, N. L. and Pechenkin, S. A., 1981. Fractionation of stable oxygen and carbon isotopes in carbonate systems. Trans. from Geokhimiya, no. 10: 1427-1441.

Grant, J. A., 1986. The isocon diagram-a simple solution to Gresens' equation for metasomatic alteration. Economic Geology, 81: 1976-1982.

Greer, I. R., Netherway, D. G. and Pertzel, B. A., 1988. The geology and exploration of the Detchikrom and Mpeasem concessions, Tarkwa Basin, Ghana. International Conference and Workshop on the Geology of Ghana with Special Emphasis on Gold, Program with Abstracts, Accra, Ghana.

Gresens, R. L., 1967. Composition-volume relationships of metasomatism. Chemical Geology, 2: 47-55.

Grindley, G. W., 1965. The geology structure and exploitation of the Wairakei geothermal field, Taupo, New Zealand. New Zealand Geol. Survey Bull. 75, 131 pgs.

Groves, D. I. and Phillips, G. N., 1987. The genesis and tectonic control on Archean gold deposits of the Western Australian Shield: A metamorphic-replacement model. Ore Geology Reviews, 2: 287-322.

Groves, D. I., Barley, M. E. and Ho, S.E., 1989. Nature, genesis, and tectonic setting of mesothermal gold mineralization in the Yilgarn Block, Western Australia. Economic Geology Monograph 6: 71-85.

Groves, D. I., Phillips, G. N., Ho, S. E. and Standing, C. A., 1987. Craton-scale distribution of Archean greenstone gold deposits: Predictive capacity of the metamorphic model. Economic Geology, 82: 2045-2058.

Groves, D. I., Phillips, G. N., Ho, S. E., Henderson, C. A., Clark, M. E. and Woad, G. M., 1984. Controls on distribution of Archean hydrothermal gold deposits in Western Australia. In: Foster, R. P. (ed.), Gold '82: Rotterdam, A. A. Balkema Pub.: 669-712.

Guha, J., Gauthier, A., Vallee, M., Descarreaux, J. and Lange-Brard, F., 1982. Gold mineralization at the Doyon Mine (Silverstack), Bousquet, Quebec. In: Geology of Canadian Gold Deposits, Hodder, R. W. and Petruk, W. (eds.). CIM Spec. Vol. 24, pp. 50-66.

Hackbarth, C. J. and Petersen, U., 1984. Systematic compositional variations in argentian tetrahedrite. Economic Geology, 79: 448-460.

Harker, R. I. and Tuttle, O. F., 1955. Studies in the system CaO-MgO-CO_2. Part 2. Limits of the solid solution along the binary join $CaCO_3$-$MgCO_3$. American Journal of Science, 253: 274-282.

Hastings, D. A. 1982: On the tectonics and metallogenesis of West Africa: A model incorporating new geophysical data. Geoexploration, 20: 295-327.

Hastings, D. A., 1988. On the Precambrian tectonic fabric of southern West Africa and its influence on metallogenesis and subsequent tectonic events. (Abstr.), Journal of African Earth Sciences, 7-2: pg 516.

Hawkes, D. D., 1972. The geology of Sierra Leone. In Conference on African Geology, Proceedings, Ibadan, Nigeria, pp. 471-482.

Hayashi, K.-I. and Ohmoto, H., 1991. Solubility of gold in NaCl and H_2S-bearing aqueous solutions at 250-350°C. Geochim. et Cosmochim. Acta, 55: 2111-2126.

Higgins, N. and Kerrich, R., 1982. Progressive ^{18}O depletion during CO_2 separation from a carbon dioxide rich hydrothermal fluid: Evidence for the Gray River tungsten deposit. Can. J. Earth Sci. 19: 2247-2257.

Hirdes, W., Davis, D. W. and Eisenlohr, B. N., 1992. Reassessment of Proterozoic granitoid ages in Ghana on the basis of U/Pb zircon and monazite dating. Precambrian Research, 56: 89-96.

Hirdes, W. and Leube, A., 1989. On gold mineralization of the Proterozoic Birimian Supergroup in Ghana, West Africa. Ghanaian-German Mineral Prospecting Project, BGR Hanover, 179 pgs.

Ho, S. E., Groves, D. I. and Phillips, G. N., 1985. Fluid inclusion as indicators of the nature and source of ore fluids and ore depositional conditions for Archean gold deposits of the Yilgarn block, Western Australia. Geol. Soc. South Africa Trans., 88: 149-158.

Hooper, P. J. M., 1989. Prestea Goldfields Limited: Brief description of operations. Unpublished company report.

Hubbard, F., 1986. The diamond-source kimberlite paradox of Sierra Leone: an alternative kimberlite emplacement model. Journal of African Earth Sciences, 5-6: 599-605.

Hutcheon, I. and Moore, J. M., 1973. The tremolite isograd near Marble Lake, Ontario. Canadian Journal of Earth Science, 10: 936-947.

Javoy, M. L., Pineau, F. and Iiyama, I., 1978. Experimental determination of the isotopic fractionation between gaseous CO_2 and carbon dissolved in theoleiitic magma. Contrib. Mineral. Petrol. 67: 35-39.

Jean, G. E. and Bancroft, G. M., 1985. An XPS and SEM study of gold deposition at low temperatures on sulphide mineral surfaces: concentration of gold by adsorption/reduction. Geochim. et Cosmochim. Acta, 49: 979-987.

Jenson, L. S., 1976. A new cation plot for classifying subalkalic volcanic rocks. Ontario Division of Mines, Toronto, Misc. pap. 66.

Junner, N. R., 1946. Progress in geological and mineral investigations in the Gold Coast. Bulletin No. 16, Geological Survey of the Gold Coast.

Junner, N. R., 1935. Gold in the Gold Coast. Memoir No. 4, Geological Survey of the Gold Coast.

Junner, N. R., 1932. The geology of the Obuasi Goldfields. Memoir No. 2, Geological Survey of the Gold Coast.

Kay, A. and Strong, D. F., 1983. Geologic and fluid controls on As-Sb-Au mineralization in the Moretons Harbour area, Newfoundland. Economic Geology, 78: 1590-1604.

Kerrich, R., 1987. The stable isotope geochemistry of Au-Ag vein deposits in metamorphic rocks. In: Short Course in Stable Isotope Geochemistry of Low Temperature Fluids, T. K. Kyser, editor, Mineral. Assoc. Canada, Short Course Handbook, 13: 287-336.

Kerrich, R., 1987b. Stable isotope studies of fluids in the crust. In: Short Course in Stable Isotope Geochemistry of Low Temperature Fluids, T. K. Kyser, (ed.), Mineral. Assoc. of Canada, Short Course Handbook, 13: 258-286.

Kerrich, R., 1989. Lithophile element systematics of gold vein deposits in Archean greenstone belts: Implications for source processes. Economic Geology Monograph 6: 508-519.

Kesse, G. O., 1985. The Mineral and Rock Resources of Ghana. A. A. Balkema, Rotterdam. 610 pgs.

Knipe, S. W. and Foster, R. P., 1991. Hydrothermal precipitation of precious metals on sulfide substrates. In Brazil Gold 91, The Economics, Geology, Geochemistry and Genesis of Gold Deposits, E. A. Ladeira

(ed.), pp. 431-435.

Knopf, D. J., 1988. Gold in West Africa and the Ivory Coast. Mining Magazine, May 1988: 392-396.

Kone, M., Caen-Vachete, M., et Tempier, P., 1988. Age eburneen du leucogranite de Morifingso intrusif dans les mylonites de la faille de Sassandra (Cote d'Ivoire). Journal of African Earth Sciences, 7: 783-787.

Kretschmar, U. and Scott, S. D., 1976. Phase relations involving arsenopyrite in the system Fe-As-S and their application. Canadian Mineralogist, 14: 364-386.

Kyser, T. K., 1987. Equilibrium fractionation factors for stable isotopes. In: Short Course in Stable Isotope Geochemistry of Low Temperature Fluids, T. K. Kyser, editor, Mineral Assoc. of Canada, Short Course Series, 13: 1-84.

Land, L. S., 1983. The application of stable isotopes to studies of the origin of dolomite and to problems of diagenesis of clastic sediments. In: Stable Isotopes in Sedimentary Geology. Society of Economic Paleontologists and Mineralogists, Short Course 10: 4.1-4.22.

Lattanzi, P., Rye, D. M. and Rice, J. M., 1980. Behavior of ^{13}C and ^{18}O in carbonates during contact metamorphism at Marysville, Montana: Implications for isotope systematics in pure dolomite limestones. Am. Jour. Sci., 280: 890-906.

Ledru, P., Milesi, J-P., Vinchon, C., Ankrah, P. T., Johan, V. and Marcoux, E., 1988. Geology of the Birimian series of Ghana. International Conference and Workshop on the Geology of Ghana with Special Emphasis on Gold, Programme with Abstracts, Accra, Ghana.

Leitch, C. H. B . 1990. Bralorne: a mesothermal, shield-type vein gold deposit of Cretaceous age in southwestern British Columbia. CIM Bulletin, September, 1990.

Leitch, C. H. B., Godwin, C. I., Brown, T. H. and Taylor, B. E., 1991. Geochemistry of mineralizing fluids in the Bralorne-Pioneer mesothermal gold vein deposit, British Columbia, Canada. Economic Geology, 86: 318-353.

Leube, A., Hirdes, W., Mauer, R. and Kesse, G. O., 1990. The Early Proterozoic Birimian Supergroup of Ghana and some aspects of its

associated gold mineralization. Precambrian Research, 46: 139-165.

Leube, A., Hirdes, W. and Mauer, R., 1986. The Birrimian Supergroup of Ghana. G.G.M.P.P. Technical cooperation project No. 80.2040.6, Bundesanstalt fur Geowissenschaften und Rohstoffe, Hannover, 259 pgs.

Longstaffe, F. J., 1989. Stable isotopes as tracers in clastic diagenesis. In: Short Course in Burial Diagenesis, edited by I. E. Hutcheon, Mineral. Assoc. of Canada short Course Series, 15: 201-277.

MacDonald, A. J and Spooner, E. T. C., 1981. Calibration of a Linkam TH600 programmable heating-cooling stage for microthermometric examination of fluid inclusions. Economic Geology 76: 1248-1258.

MacLean, P. J., 1991. Characterization of pyrite from gold deposits. Ph.D. thesis, University of Western Ontario, London Ontario.

Marcoux, E., Bonnemaison, M., Braux, C. and Johan, Z., 1989. Distribution de Au, Sb, As, et Fe dans l'arsenopyrite aurifere du Chatelet et de Villeranges. (Creuse, Massif Central Francais). C. R. Acad. Sci. 308, Ser. II, pp. 293-300.

Matsuhisa, Y., Goldsmith, J. R. and Clayton, R. N., 1979. Oxygen isotopic fractionation in the system quartz-albite-anorthite-water. Geochimica et Cosmochimica Acta 43: 1131-1140.

McCrea, J. M., 1950. On the isotopic chemistry of carbonates and a paleotemperature scale. Journal of Chemical Physics, 18-6: 849-857.

Minter, W. E. L., Hill, W. C. N., Kidger, R. J., Kingsley, C. S. and Snowden, P. A., 1986. The Welkom Goldfield. In: Mineral Deposits of Southern Africa, C. A. Anhauser and C. R. Maske (eds.): 497-540.

Mishra, B. and Mookherjee, A., 1991. Tetrahedrite mineral chemistry and metal zoning: a thermodynamic assessment from the Rajpura-Dariba polymetallic deposit, India. Economic Geology, 86: 1529-1538.

Molina, P., 1988. Correlation geologique Afrique-Amerique du Sud et provinces uraniferes. Journal of African Earth Sciences, 7: 489-497.

Mumin, A. H., 1991. Geology of a gold-bearing "crush zone" in the Ashanti Gold Belt, Ghana, West Africa. (Abstr.) Central Canada Geological Conference, Hamilton.

Mumin, A. H., Clarke, G. A., Flach, G. and Badu, F., 1988. Geology and

mineralogy of gold mineralization at the Bogosu concession, Western Region, Ghana. International Conference and Workshop on the Geology of Ghana with Special Emphasis on Gold, Program with Abstracts, Accra, Ghana.

Murowchick, J. B., 1992. Marcasite inversion and the petrographic determination of pyrite ancestry. Economic Geology, 87: 1141-1152.

Murowchick, J. B., 1990. Iron monosulfide precursors in low-temperature pyrite and marcasite formation. Geol. Soc. America, Program with abstracts.

Murowchick, J. B. and Barnes, H. L., 1986. Marcasite precipitation from hydrothermal solutions. Geochim. et Cosmochim. Acta, 50: 2615-2629.

Naumov, G. B., Ryzhenko, B. N. and Khodakovsky, I. L., 1974. Handbook of thermodynamic data: U. S. Geol. Survey Rept. USGS-WRD-74-001, 328 pgs.

Nesbitt, B. E. and Essene, E. J., 1982. Metamorphic thermometry and barometry of a portion of the southern Blue Ridge province. American Journal of Science, 282: 701-729.

Nesbitt, B. E., Muehlenbachs, K. and Murowchick, J. B., 1989. Genetic implications of stable isotope characteristics of mesothermal Au deposits and related Sb and Hg deposits in the Canadian Cordillera. Economic Geology, 84: 1489-1506.

Nesbitt, B. E., Murowchick, J. B. and Muehlenbachs, K., 1986. Dual origins of lode gold deposits in the Canadian Cordillera: Geology 14: 506-509.

Ntiamoah-Agyakwa, Y., 1979. Relationship between gold and manganese mineralization in the Birimian of Ghana, West Africa. Geology Magazine, 116-5: 345-352.

Ohmoto, H., 1986. Stable isotope geochemistry of ore deposits: in Valley, J. W., Taylor, H. P. and O'Neil, J. R. (eds) Reviews in Mineralogy Vol. 16
Stable Isotopes in High Temperature Geological Processes, pp. 491-559.

Ohmoto, H. and Kerrick, D. M., 1977. Devolatilization equilibria systems. Amer. J. Sci., 277: 1013-1044.

Ohmoto; H. and Rye, R. O., 1979. Isotopes of sulfur and carbon: in Barnes, H. L. (ed.), Geochemistry of Hydrothermal Ore Deposits, 2nd Ed. John

Wiley and Sons, New York, pp. 509-567.

Olade, M. A., 1980. Precambrian metallogeny in West Africa. Geol. Rdsch, 69: 411-428.

O'Neil, J. R., 1986. Theoretical and experimental aspects of isotopic fractionation: In: Valley, J. W., Taylor, H. P., Jr. and O'Neil, J. R. (eds.), Reviews in Mineralogy Vol. 16, Stable Isotopes in High Temperature Geological Processes, pp. 1-37.

Onstott, T. C. and Dorbor, J., 1987. Ar-40/Ar-39 and paleomagnetic results from Liberia and the Precambrian APW data base for the West African Shield. Journal of African Earth Sciences, 6: 537-552.

Pearce, J. A., 1982. Trace element characteristics of lavas from destructive plate boundaries. In: R. S. Thorpe (ed.), Andesites. Wiley, Chichester, pp. 525-548.

Phillips, G. N. and Brown, I. J., 1987. Host rock and fluid control on carbonate assemblages in the Golden Mile dolerite, Kalgoorlie gold deposit, Australia. Canadian Mineralogist, 25: 265-273.

Powell, R., Condliffe, D. M. and Condliffe, E., 1984. Calcite-dolomite geothermometry in the system $CaCO_3$-$MgCO_3$-$FeCO_3$: an experimental study. Journal of Metamorphic Geology, 2: 33-41.

Powell, R., Will, T. M. and Phillips, G. N., 1991. Metamorphism in Archean greenstone belts: calculated fluid compostions and implications for gold mineralization. Journal of Metamorphic Petrology, 9: 141-150.

Pretorius, D. A., 1964. Gold and uranium in quartz-pebble conglomerates. Economic Geology, 75th Anniversary Volume.

Ramsay, J. G., 1980. Shear zone geometry: a review. Journal of Structural Geology, 2: 83-99.

Robert, F. and Kelly, W. C., 1987. Ore-forming fluids in Archean gold-bearing quartz veins at the Sigma mine, Abitibi greenstone belt, Quebec, Canada. Economic Geology 82:1464-1482.

Romberger, S. B., 1989. Transport and deposition of precious metals in epithermal deposits. In: Mechanisms of Gold Transport and Deposition in Low Temperature Hydrothermal Systems: given by S. Romberger of Colorado School of Mines, at the National Centre for Management

Research, Univer. of Western Ontario, London, Ontario, Nov. 3, 1989.

Rosenbaum, J. and Sheppard, S. M. F., 1986. An isotopic study of siderites, dolomites and ankerites at high temperatures. Geochimica et Cosmochimica Acta 50: 1147-1150.

Rosenberg, P. E., 1967. Subsolidus relations in the system $CaCO_3$-$MgCO_3$-$FeCO_3$ between 350 and 550°C. American Mineralogist, 52: 787-797.

Sack, R. O. and Loucks, R. R., 1985. Thermodynamic properties of tetrahedrite-tennantites: constraints on the interdependence of the Ag-Cu, Fe-Zn, Cu-Fe, and As-Sb exchange reactions. American Mineralogist, 70: 1270-1289.

Sample, J. C. and Moore, J. C., 1987. Structural style and kinematics of an underplated slate belt, Kodiak and adjacent islands, Alaska. GSA Bulletin, 99: 7-20.

Schoonen, M. A. A. and Barnes, H. L., 1991a. Reactions forming pyrite and marcasite from solution: I. Nucleation of FeS_2 below 100°C. Geochim. et Cosmochim. Acta, 55: 1495-1504.

--------1991b. Reactions forming pyrite and marcasite from solution: II. Via FeS precursors below 100°C. Geochim. et Cosmochim. Acta, 55: 1505-1514.

Sestini, G., 1973. Sedimentology of a paleoplacer: the gold-bearing Tarkwaian of Ghana. In: Sedimentary Ores, G. C. Amstutz and A. J. Bernard (eds.), Springer Verlag, Berlin, pp. 275-305.

Seward, T. M., 1989. The hydrothermal chemistry of gold and its implications for ore formation: Boiling and conductive cooling as examples. Economic Geology Monograph 6: 398-404.

Seward, T. M. and Barnes, H. L., 1989. Metal transport and deposition by hydrothermal ore fluids: An introduction. In: Barnes, H. L., and Ohmoto, H., (eds.), Hydrothermal Processes-Application to Ore Genesis, Dordrecht, Reidel.

Sharp, Z. D., Essene, E. J. and Kelly, W. C., 1985. A re-examination of the arsenopyrite geothermometer: Pressure considerations and applications to natural assemblages. Canadian Mineralogist, 23: 517-534.

Shenberger, D. M. and Barnes, H. L., 1989. Solubility of gold in aqueous sulfide solutions from 150 to 350° C. Geochim. et Cosmochim. Acta, 53: 269-278.

Shepherd, T., 1981. Temperature-programmable, heating-freezing stage for microthermometric analysis of fluid inclusions: Economic Geology, 76: 1244-1247.

Sheppard, S. M. F., 1986. Characterization and isotopic variations in natural waters, Chp. 6. In: Valley, J. W., Taylor, H. P., Jr. and O'Neil, J. R. (eds.),
Stable isotopes in High Temperature Geological Processes. Reviews in Mineralogy, 16: 165-184.

Sheppard, S. M. F. and Schwartz, H. P., 1970. Fractionation of carbon and oxygen isotopes and magnesium between coexisting metamorphic calcite and dolomite. Contr. Mineral. and Petrol. 26: 161-198.

Sibson, R. H., 1977. Faults and fault rock mechanisms. Journal of the Geological Society of London, 133: 191-213.

Sibson, R. H., 1983. Continental fault structures and the shallow earthquake source. Journal of the Geological Society of London, 140: 741-767.

Sibson, R. H., Robert, F. and Poulsen, K. H., 1988. High-angle reverse faults, fluid pressure cycling, and mesothermal gold-quartz deposits. Geology, 16: 551-555.

Simpson, C., 1986. Determination of movement sense in mylonites. Journal of Geological Education, 34: 246-260.

Smith, T. J. and Kesler, S. E., 1985. Relation of fluid inclusion geochemistry to wallrock alteration and lithogeochemical zonation at the Hollonger-McIntyre gold deposits, Timmins, Ontario, Canada. CIM Bulletin, 78: 35-46.

Spooner, E. T. C., Bray, C. J., Wood, P. C., Burrows, D. R. and Callan, N. J., 1987. Au-quartz vein and Cu-Au-Ag-Mo-anhydrite mineralization, Hollinger-McIntyre Mines, Timmins, Ontario: $\partial^{13}C$ values (McIntyre), fluid inclusion gas chemistry, pressure (depth) estimation, and H_2O-CO_2 phase separation as a precipitation and dilation mechanism. In: Geosci. Research Grant Prog. Summary of Research 1986-1987, OGS Misc. P. 136: 35-55.

Starling, A., Gilligan, J. M., Carter, A. H. C., Foster, R. P. and Saunders, R. A., 1989. High temperature hydrothermal precipitation of precious metals on the surface of pyrite. Nature, 340: 298-300.

Talantsev, A. S. and Sazonov, V. N., 1979. Variations in compositions of coexisting dolomite-ankerite and magnesite-siderite as an index of PT-conditions of mineral formation. Akad. Nauk SSSR Ural'skii Nauchaii Tzentr, 95-103.

Taylor, B. E., 1986. Origins and isotopic characteristics of Mother Lode hydrothermal fluids in gold deposits with comparison to Archean analogues [abs]: in Chater, A.M. (ed.), Gold '86 Poster Volume, Geol. Assoc. Can., pp. 148-150.

Taylor, B. E., 1987. Stable isotope geochemistry of ore-forming fluids: In: Stable Isotope Geochemistry of Low Temperature Fluids, T. K. Kyser, (ed.), Mineral. Assoc. Canada Short Course Handbook, 13: 337-445.

Taylor, H. P., Jr., 1979. Oxygen and hydrogen isotope relationships in hydrothermal deposits. In: Barnes, H. L. (ed), Geochemistry of Hydrothermal Ore Deposits, 2nd Ed., J. Wiley and Sons, New York, pp. 236-277.

Taylor, P. N., Moorbath, S., Leube, A. and Hirdes, W., 1992. Early Proterozoic crustal evolution in the Birimian of Ghana: constraints from geochronology and isotope geochemistry. Precambrian Research, 56: 97-111.

Taylor, P. N., Moorbath, S., Leube, A. and Hirdes, W., 1988. Geochronology and crustal evolution of Early Proterozoic granite-greenstone terrains in Ghana, West Africa. International Conference and Workshop on the Geology of Ghana with special Emphasis on Gold, Program with Abstracts, Accra, Ghana.

Toure, S., Caen-Vachete, M. et Tempier, P., 1987. Nouvelles donnees petrographiques, geochimiques et geochronologiques du massif "granitique" de Bondoukou (Cote d'Ivoire) mise en evidence d'un age Burkinien, par isochrone Rb/Sr sur roches totales. Journal of African Earth Sciences, 4: pg 269.

Umeji, A. C., 1983. Archean greenstone belts of Sierra Leone with comments on the stratigraphy and metallogeny. Journal of African Earth Sciences, 1: 1-8.

United Nations Development Program, 1988. Gold and diamonds in Ghana, an investment brochure. UN/DTCD, Chief, Minerals Branch, New York.

Valley, J. W. and O'Neil, J. R., 1981. $^{13}C/^{12}C$ exchange between calcite

and graphite: a possible thermometer in Grenville marbles: Geochim. et Cosmochim. Acta, 45: 411-419.

Wada, H. and Suzuki, K., 1983. Carbon isotopic thermometry calibrated by dolomite-calcite solvus temperatures. Geochimica et Cosmochimica Acta 47: 697-706.

Winchester, J. A. and Floyd, P. A., 1977. Geochemical discrimination of different magma series and their differentiation products using immobile elements. Chemical Geology, 20: 325-343.

Wood, P. C., Burrows, D. R., Thomas, A. V. and Spooner, E. T. C., 1986. The Hollinger-McIntyre Au-quartz vein system, Timmins, Ontario, Canada; Geological characteristics, fluid properties and light stable isotope geochemistry. Proceedings of Gold '86, An International Symposium on the Geology of Gold Deposits, A. J. Macdonald (ed.), Konsult International Inc., pp. 56-80.

Wright, J. B., Hastings, D. A., Jones, W. B. and Williams, H. R., 1985. Geology and Mineral Resources of West Africa. George Allen and Unwin, London: 187 pgs.

Wu, I. and Petersen, U., 1977. Geochemistry of terahedrite and mineral zoning at Casapalca, Peru. Economic Geology, 72: 993-1016.